AI-Enabled Robots for Automated Nondestructive Evaluation and Repair of Power Plant Boilers

Principal Investigator:

Hao Zhang, Ph.D.
Colorado School of Mines
1500 Illinois St., Golden, CO 80401
Phone: 303-273-3581
Email: hzhang@mines.edu

Co-Investigators:

Yiming Deng, Michigan State University
Stephen Liu, Colorado School of Mines
Andrew Petruska, Colorado School of Mines
Lalita Udpa, Michigan State University
Zhenzhen Yu, Colorado School of Mines

DOE Award Number: DE-FE0031650

Sponsoring Program Office: Office of Fossil Energy (FE)

Date of Report: April 29, 2022

Disclaimer

Table of Contents

Table of Figures

Executive Summary

Boiler failure could cause loss of life and safety issues, cost hundreds of thousands of dollars in equipment repairs, property damage and production losses, and drive up the cost of electric power. Boiler maintenance is challenging and risky for inspectors working on scaffolding in confined hazardous spaces inside of a boiler and sometimes the space is hard to access. The operation is also time-consuming due to the large area of vertical structures for inspection and the tremendous effort needed for scaffolding. Recently, the use of robotics (e.g., drones and crawlers) in power plants for maintenance is growing rapidly. However, the existing robotics solutions show two notable technological gaps: no live repair capability, and no Artificial Intelligence (AI) for smart autonomy.

The objective of this project is to develop an integrated autonomous robotic platform that is equipped with compact non-destructive evaluation (NDE) sensors to perform live inspection, operates onboard repair devices to perform live repair, and uses AI for intelligent data fusion and predictive analysis for automated and smart spatiotemporal inspection, analysis and repair of the furnace walls in coal-fired boilers. The approach to achieve the objective includes developing NDE sensors with signal processing techniques, designing and evaluating repair devices for robots based on fusion and solid-state technologies, and an autonomous robotic platform that can attach to and navigate on boiler furnace walls using magnetic drive tracks. The robot is also powered by AI to automate data gathering (e.g., 3D mapping and damage localization) and predictive analysis.

This project has advanced the state-of-the-art by providing technological breakthroughs including compact NDE and repair tools for robots, AI capabilities for smart autonomy, and a robotic platform for automated boiler maintenance. This project has great potential to result in significant benefits including limiting or eliminating the need to send operators to assess difficult-to-access or hazardous areas, enabling automated live inspection and repair, avoiding time consuming scaffolding (especially for partial maintenance during unplanned outage), collecting comprehensive and well-organized data smartly, and avoiding or limiting the need for onsite or remote piloting technicians. The impacts can be tremendous in terms of the time and cost savings, reducing the risk for human operators, and increasing boiler reliability, usability, and efficiency.

In addition, by developing the new technologies on the autonomous inspection and repair robot, by involving multiple undergraduate and graduate students working together with the faculty members on this project, and by generating knowledge and building up collaborations with industrial partners, this effort will significantly update the education capabilities, support long-term fundamental research, and maintain the leadership of Colorado School of Mines and Michigan State University in energy fields.

I. Background and Project Objectives

1. Project Background

Boilers are the largest and one of the most critical components of a thermal power plant, which convert energy contained in fuel (e.g., coal) into high temperature steam. Damage mechanisms, including creep, thermo-mechanical fatigue, erosion, cavitation, and corrosion-induced cracking, take place in the boiler furnace chamber [1]. If damage is left unchecked, catastrophic failures could occur, causing loss of life and other serious safety issues. Boiler failures also cost hundreds of millions of dollars in equipment repairs, property damage and production losses, which drives up the cost of electric power across the U.S. As emphasized by our industrial collaborators from Xcel Energy Inc. (a utility holding company that operates all Colorado generation stations), boiler inspection and repair is one of the main focuses during scheduled overhauls.

Boiler maintenance is challenging and dangerous for inspectors working on scaffolding in the confined space inside a boiler, and sometimes the space is hard to access. The operation is also time-consuming due to the large area of vertical structures to inspect and due to the tremendous effort that is needed for mounting and dismantling scaffolding. For example, at the coal-fired Hayden Station [2] in Colorado, inspectors need to inspect 50,000 ft^2 of furnace walls (a.k.a., water walls) inside of the boiler during a single overhaul (Figure 1), which takes several days to complete.

Figure 1: Hayden Unit 1 scaffolding for manual inspection and repair.

Recently, the use of robotics in power plants for maintenance has been increasing. [3]. For example, drones (i.e., Unmanned Aerial Vehicles or UAVs) [4, 5] and robotic crawlers [6, 7] are developed to inspect boiler furnace walls. Given their promises, the existing robotics technologies have various disadvantages (Table 1). The two most notable gaps include (1) no live repair capability, and (2) no Artificial Intelligence (AI) for smart autonomy. Even after damage is detected, dangerous and time-consuming operations (e.g., scaffolding) are currently still needed for repair operations. Without autonomy and AI capabilities, well-trained pilot technicians are required to remotely control the robots or to be onsite when communication is limited, such as within a boiler. These gaps must be overcome to practically deploy robotic technologies for spatiotemporal power plant inspection and repair.

2. Research Objectives

The overarching goal of this project was to develop an integrated autonomous robotic platform that (1) is equipped with advanced non-destructive evaluation (NDE) sensors to perform live inspection, (2) operate innovative onboard devices to perform live repair, and (3) use AI for intelligent information fusion and live predictive analysis for smart automated spatiotemporal inspection, analysis, and repair of furnace walls in coal-fired boilers. The breakthroughs included compact live NDE and repair tools for robots, AI capabilities for smart autonomy, and an integrated robotic platform for automated boiler maintenance. The success of this project will now potentially result in significant benefits, including limiting or eliminating the need to send operators to assess difficult-to-access or hazardous areas, enabling automated live inspection and repair, avoiding time consuming scaffolding (especially for partial maintenance during unplanned outages), and smartly gathering comprehensive and well-organized data. These impacts will be tremendous in terms of the time and cost savings, reducing the risk for human operators, and increasing boiler reliability, usability & efficiency.

Table 1. State-of-the-practice manual and robot-assisted inspection methods and their limits

Current Practice	Limits
Maintenance by human inspectors	Safety risks caused by environmental hazards and climbing up scaffolding, time-consuming to mount/dismantle scaffolding, often slow and inaccurate inspection.
UAV/drone-based inspection	Limited payload & operation time, requirement of constant human control (autopilot not feasible yet), dependence on good wireless communication, typically only visual inspection (NDE-based inspection and repair not feasible yet).
Robotic inspection crawlers	Typically incapable of repair, requirement of constant remote control (no full autonomy yet), no AI for smart autonomy and predictive analysis.

The specific objectives of this project included:

- NDE Sensor Design: A compact NDE sensor was designed with crack detection and assessment capabilities. Signal processing methods were also developed to estimate crack sizes and improve the NDE sensor’s reliability.
- Repair Tool Design: A repair tool based on friction stir welding (FSW), one of the solid-state repair methods, was designed. By augmenting FSW with an induction heating unit, the demand for spindle torque and forging loads can be significantly reduced, enabling FSW to be used as a compact repair technique.
- Integrated Robotic Platform: A robotic system was designed that leveraged a commercial robotic platform retrofitted with a customized gantry system, sensors, cleaning, NDE sensors, and repair tools.
- Artificial Intelligence (AI) for Smart Autonomy: AI capabilities were developed to enable robots to automate data gathering (e.g., to map the environment) and perform predictive analysis (e.g., to recognize cracks using machine learning methods).

Since this project is a part of the University Coal Research (UCR) program, another major objective of the project is to inspire, educate and train PhD and MS students to address energy-related challenges. During the project, multiple PhD students from both universities and several MS/undergraduate students were included in this project. They were trained and educated in science and engineering to address the energy-related challenges. The PIs believe education is a critical component of the project, and we will integrate research with educational activities to prepare the next generation scientists and engineers for the energy industry.

II. Technical Approach, Experimental Results, and Discussion

To address the research goal and objectives, four major technical tasks were performed, including (1) NDE sensing and assessment, (2) repair device design and control, (3) robotic platform design, and (4) artificial intelligence development. Specifically, these tasks include the following subtasks:

- Task 1 – NDE sensing and assessment
    - Subtask 1.1 Probe design for robotic platforms
    - Subtask 1.2 Signal processing techniques for crack profiling
- Task 2 – Repair device design and control
    - Subtask 2.1 Integrated IHA-FSW system
    - Subtask 2.2 Repair protocol design
- Task 3 – Robotic platform design
    - Subtask 3.1 Robot retrofit for vertical navigation
    - Subtask 3.2 Cleaning mechanism design
    - Subtask 3.3 NDE integration on robot
    - Subtask 3.4 Repair integration on robot
- Task 4 – Artificial intelligence development
    - Subtask 4.1 3D mapping and data fusion
    - Subtask 4.2 Spatiotemporal damage tracking
    - Subtask 4.3 Damage analysis by machine learning

1. Task 1: NDE Sensing and Assessment

A compact NDE sensor was designed with crack detection and assessment capabilities. Signal processing methods were also developed to estimate crack sizes and improve the NDE sensor's reliability.

1.1. Subtask 1.1: NDE Probe Design for Robotic Platforms

Research in nondestructive evolution technologies have been rapidly improved due to their essential role not only in diagnostic maintenance but also in prognostic maintenance, health monitoring, quality assessment, and in manufacturing processes. Several nondestructive evolution methods, NDE, are currently being used to inspect heat exchangers, boiler structures and tubes. In this section, nondestructive evaluation methods are introduced and applied to inspect a sample from a boiler structure.

1.1.1. Literature Review

In the relevant literature, several methods have been reported for inspecting boiler structure such as, visual methods, laser-based inspection, radiography, ultrasonic, microwave near field sensing, and electromagnetic methods such flux leakage and eddy current.

- Visual inspection uses reflected or transmitted light from test object that is image with the human eye or other light sensing device. Its applications range from raw material to finished products and in-service inspection [8]. Although it can be inexpensive and simple with minimal training required, only surface conditions can be evaluated. For sophisticated visual inspection, an effective source of illumination required. For boiler inspection, visual inspection is time consuming and risky task for engineers.

- The laser optical technique (LOTIS) uses a rotating laser beam that scans the inner surface as the probe is pulled out of the tube. The reflected laser beam is picked up by a lateral detector that measures changes in proximity caused by variations on the internal diameter (ID) surface [8]. The technique is limited to ID surface inspection with a speed of up to 3 in./s. The technique also requires the tube to be cleaned to avoid any unnecessary optical scattering. It has proven applications for large diameter tubes such as those in reformers and furnaces. Because of its limitations it is mainly used as a complimentary inspection tool. LOTIS allow permanent records can be obtained from test results. It also distinguishes inner from outer diameter. Instrumentation can withstand adverse field conditions. In addition, it can detect flaws under support plates as well as flaws adjacent to end sheets [9]. However, tubes must be cleaned. Scale or deposit can fill a flaw which will make it difficult to qualify its depth. The methods are very sensitive to inspection speed. Instrumentation and probes could be very expensive. The detectability is limited to 20% and greater, and cannot accurately size discontinuities. According to [9], the method cannot inspect U-bend tubes.

- In radiography techniques, a source of radiation is directed toward the inspected object. A sheet of radiographic film is placed behind the object. It is used for pipeline inspection due to its reliability. A disadvantage associated with it is the radiation exposure and might be challenging for boiler inspection.

- Ultrasonic method has become a popular NDE method. The principle is to employ high frequency acoustic waves to probe the inspected sample. As the acoustic wave penetrates the sample, the wave is attenuated and/or reflected by any change in the density in the material. By observing the returned signal many of the characteristics of the material can be determined [10]. In [11], ultrasonic has been reported as demonstrated good performance in the determination of actual (remaining) wall thickness for large areas of tubes and sheet metal. Unlike radiography, ultrasonic NDE has no health risks. According to [11], it is possible to define defect location very accurately. The reporting accuracy regarding depth measurement for the latest generation of tools is around ±0.4 to 0.5 mm. The highest possible depth resolution that can be achieved is 0.06 mm [12]. However, ultrasonic requires an acoustic coupling and surface preparation [13]. In addition, training is necessary for ultrasonic inspection.

  Ultrasonic internal rotating inspection system (IRIS) is used for NDE evaluation [9]. This inspection method employs an ultrasonic immersion pulse echo technique. The ultrasonic transducer is contained in a test head, which fits into and is centered in the tube to be inspected. The ultrasonic pulses are emitted along a path parallel to the tube axis. A rotating 45-degree mirror then reflects these pulses so that they are directed radially on to the tube wall. It provides information on flaw profile and location i.e., on the ID or OD of the tube. With real time C-scan capabilities during data collection, pits as small as 1 mm diameter can be easily detected [8]. It has relatively slower speed of operation and enquires extensive tube cleaning. It is limited to minimum wall thickness measurement of 0.8mm for carbon steel tubes [8].

- Eddy current and flux leakage methods are the most commonly used for inspecting conductive material. In flux leakage examination methods, the probe consists of a magnet and two flux leakage sensors, which set up a flux field in the tube wall as it passes through the tube. The field fluctuates when it encounters a flaw. The flux rate fluctuation effect is picked up by the coils and displayed on the display apparatus and chart recorder [8]. A Hall effect element can be added as a combined-type probe, which is used to detect absolute flux such as gradual wall loss. The output of the Hall effect detector depends on the orientation of the sensor in the probe relative to the discontinuity and whether the location of the discontinuity is on the inside or outside surface. The output of the magnetic flux leakage coils is related to the change of flux caused by the discontinuity but not the discontinuity size [9]. The method distinguishes ID from OD flaws, can inspect ferromagnetic tubes up to 3.5 inches in diameter and 0.120 inches wall thickness, permanent records can be obtained on test results. Instrumentation can withstand adverse field conditions [9]. Flaws under support plates as well as flaws adjacent to end sheets can be detected. The method's simplicity, low cost, air coupling and non-contact application, made MFL testing suitable for the automated in-line and real time defect inspection [13].

  In eddy current testing, a time varying magnetic field is induced in the sample material by using a magnetic coil with alternating current. This magnetic field causes an electric current to be generated in conducting materials. These currents, in turn, produce small magnetic fields around the conducting materials. The smaller magnetic fields generally oppose the original field, which changes the impedance of the magnetic coil. Thus, by measuring the changes in impedance of the magnetic coil as it traverses the sample, different characteristics of the sample can be identified. Eddy current testing is an effective method to detect fatigue cracks and corrosion It is suitable for detecting for example porosity, cross and seam cracks and checking seams and butt welds. testing electrically conductive materials for the detection of surface and near-surface defects [14]. Eddy current testing is widely used for inspecting conductive material because it is cheap and can monitor subsurface defects or defects under insulating coatings without touching the surface of a specimen [11, 12, 15, 16]. In ECT, probes excited with single or multi-frequencies employed for the detection and evaluation of surface and sub-surface defects. For the detection of deep sub-surface defects, higher excitation current is necessary in single and multi-frequency techniques [14].

  For far filed sensing, remote Field Eddy Current (RFEC) is used. The remote field inspection method is based on the transmission of an electromagnetic field through the tube material. The exciter coil generates eddy currents at a low frequency in the circumferential direction. The electromagnetic field transmits through the thickness and travels on the outside surface. A receiver coil placed in the remote field zone of the exciter picks up the field. The separation between the two coils is two to four times the tube's inside diameter [9]. RFEC can be used to inspect Ferromagnetic tubes in shell and tube heat exchanger& boilers. It is well suited for the detection of the following types of corrosion: general corrosion, erosion, localized corrosion and pitting, support plate fret wear extending beyond the baffle [8]. However, evaluation of small flaws such as pits using RFEC can be difficult. Compared to near field eddy current methods, instrumentation and test probes can be very expensive and requires high inspection skills for data analysis and evaluation. In RFEC, impingement erosion and wall loss detectability is limited to approximately 20% and greater. The method needs tube cleaning and has some limitation to distinguishing inner diameter from outer diameter defects. Inaccuracy in test results could occur if a discontinuity encountered differs in geometry from calibration discontinuities. According to [8], RFEC had the highest reliability of 77% in carbon steel tube inspection.

For ferromagnetic materials, partial saturation eddy current method is used. The full saturation probe contains conventional eddy current coil and a magnet. The magnetic field of the magnet saturates the material. Once saturated the relative permeability of the material drops to one. The strength of the magnets used for saturation is very critical in this technique. Weaker magnets will not saturate the material and will produce a high noise to signal ratio. The application of a full saturation eddy current technique depends on the permeability of the material, tube thickness and diameter [9]. It could be used to size of outside surface discontinuities. However, inside surface discontinuities cannot be sized with signal phase analysis because the depth of the discontinuity does not influence the phase. The inspection speeds up to approximately 60 feet per minute. The method can distinguish between inner and outer flaws similar to conventional eddy current method. Compared to other methods it presented reliability and accuracy of test results. Moreover, it is applicable to non-ferromagnetic and slightly ferromagnetic tubes. However, instrumentation and test probes can be very expensive and requires high inspection skills for data analysis and evaluation [9]. For this method, the tube material should be fully saturated, and tubes must be cleaned.

An effective eddy current method used for conductive and nonconductive material is pulsed eddy current [17]. PEC testing can be widely used to measure the thickness and stress and to characterize crack, metal loss, and corrosion of metal materials and carbon fiber-reinforced plastic [18]. PEC testing possesses many advantages against the conventional eddy current testing, including more extended detection depth, richer information about defects and higher robustness of anti-interference. In addition, PEC testing technology taking pulse as excitation can minimize power consumption, which is more promising in the development of portable instrument [15, 16]. PEC is more economical compared to other NDT methods.

- Near-field microwave imaging method is a promising nondestructive evaluation technique that can give a quantitative measure of the surface and sub-surface profile of lossless or low-loss dielectric materials [19]. Unlike the far field technique, the resolution of the near-field measurement is not constrained by diffraction limits, since it is determined by the probe's aperture size. Thus, it is capable of providing sub-wavelength resolution. The sub-wavelength resolution microscope was first proposed by Synge in [20], with experimental designs reported in [21]. Since then, a lot of research has been focused on the improvement and development of various designs for a microscope scanning system. Cho et al. achieved millimeter level resolution with frequencies around 1 GHz by using coaxial resonators [22]. Reducing the aperture size by using a sharp probing tip achieved a spatial resolution of 100 nm, by Gao et al [23]. Bakli et al presented a scanning system that combines a vector network analyzer and a high precision interferometer which provides broadband capabilities and high measurement accuracy [24].

Based on the technical and ecumenical advantages of eddy current inspection of conductive material, in this project eddy current sensing is proposed for inspected boiler structure. For robust and reliable inspection, near field microwave sensing using open ended coaxial cable antenna is also used for inspection.

A. Eddy Current Sensors

Eddy current technique is based on electromagnetic induction. A time varying electrical current is energizing a wounded coil (primary current). A magnetic flux is generated at the center of the wounded coil as shown in Figure 2, which is adopted from [25] for illustration. Based on Faraday's induction theorem, the alternating flux generates electrical current in a conductor if it is placed perpendicular to the flux direction. As a result, circulating electrical currents flows in the conductor in forms of eddy waves, which are called eddy currents.

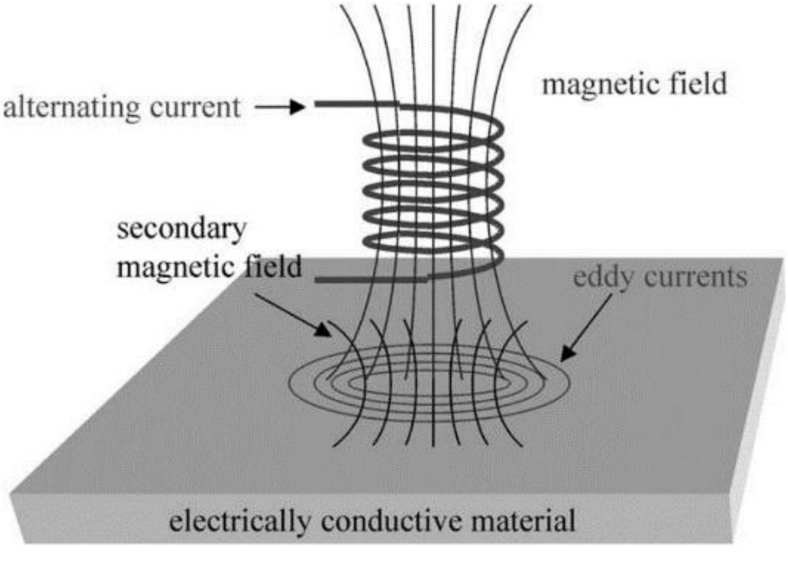

Figure 2: Primary and secondary magnetic field. Eddy current on the test piece.

The circulating eddy currents generate their own magnetic field which is opposing the primary magnetic field. The presence of the cracks in the test material disturbs the baths of the eddy currents, and the secondary marantic field. Thus, changes in secondary magnetic field are used as indications of the presence of the crack. The following measurements techniques are used to measure the marantic field in the eddy current. Induction coils and semiconductor-based device such as hall sensor, magnetoresistance, and measure are being widely used to measure magnetic field.

Impedance Variation:

The impedance of the primary coil is modeled by an inductor in series with the resistance of the wounded coil. As the coil induces electrical current in the secondary material, and the secondary magnetic field opposes the primary marantic field. The total magmatic filed seen by the coil involves the information of the secondary field changes. These changes are reflected in the impedance variation of the coil. As the sensor eddy current are disturbed by discontinuities, defects, the total impedance decreases as shown in Figure 3.

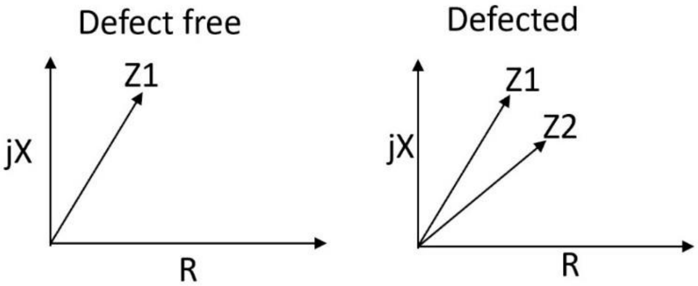

Figure 3: Impedance variation due to defects in sample under test.

Measuring the impedance variation of the excitation coil has been widely an effectively used in eddy current method [26]. An example of the single coil that is used in this experiment is shown in Figure 4 with 500 turns. Compared to other eddy current sensing methods, it involves less components and it has direct coupling with the total magmatic flux linking the coil.

Figure 4: Impedance variation sensors.

Transmitter and Receiver Coils:

To measure the field directly along with excitation coil, primary coil, another wounded coil is needed, secondary coil. The primary and the secondary coil acts like a transmitter and receiver.

The receiver coil is wounded on top of the transmitter coil of the eddy current probe as shown in Figure 5. The receiver coil of the probe is placed in time varying magmatic field. The magnetic field seen by the receiver coil is the total magnetic flux that is the magnetic field from the transmitter coil and the magmatic fields generated by the eddy currents. As a result, voltage induced across the receiver coil measures the magmatic variation of the eddy current as it encounters defects and cracks. In this project, the transmitter and receiver are consisting of 200 turns for each.

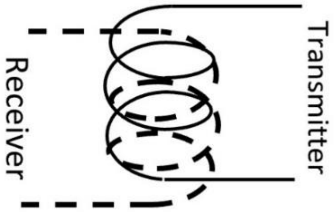

Figure 5: Eddy current Transmitter and Receiver coils.

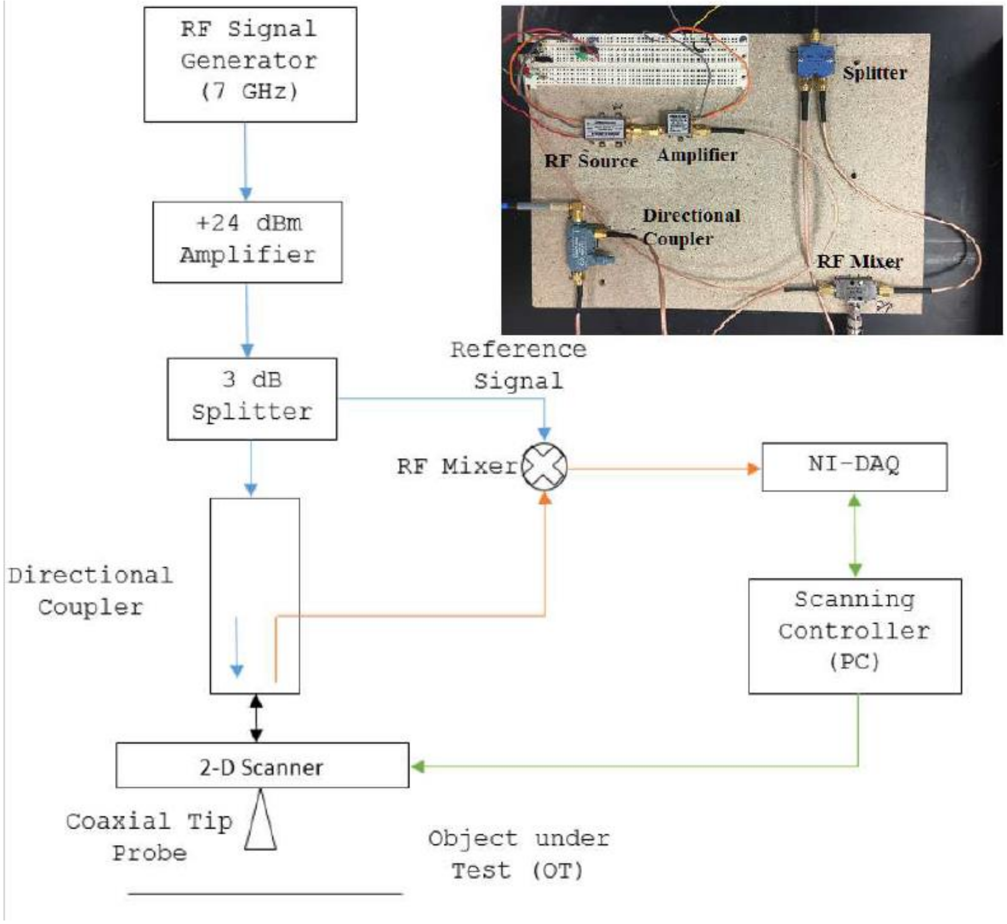

Figure 6: Near-field microwave microscopic imaging system and block diagram.

B. Near Field Microwave Sensor

A nearfield microwave imaging system consists of either a single transceiver or a multiple array of probes, which illuminates the OUT and measures the localized response from the material. The response varies with electrical properties of the material. However, to achieve high resolution images, the separation between the tip of the near-field antenna and the surface of the sample has to be small and stay constant. The precision of that distance will have a significant influence on accuracy of a near field imaging system.

The block diagram of implemented setup is shown in Figure 6. An 8 GHz RF source generator is used to feed the nearfield microwave probe. The low output of the source is amplified to +24 dBm and a 3 dB RF splitter is used to divide the amplified signal into a feed and a reference signal. The directional coupler is connected to the feed signal coming from splitter and also used to probe the reflected power. The reflected signal is mixed with the reference signal to get any changes in phase according to the changes in the properties of the object.

The probe used for imaging is a coaxial cable with an open-ended copper tip due to its simple design, easy availability and wide band frequency response. The experiments are performed by keeping the tip perpendicular to the object, where the fields are stronger and localized.

1.1.2. NDE Sensor Design

In order to embed the NDE scanning system with the robot platform, a miniaturized NDE system has been developed and tested. The new portable NDE system requires much less space and consumes lower power while maintains a similar performance compare to the pervious non-portable system.

A. Coil Array Design

Considering the technical and economic advantages of eddy current and near-field microwave sensing methods, both methods are proposed to integrate robotic scanning platform for inspecting boiler structure. For detecting millimeter and submillimeter width cracks on surface and subsurface of the inspected specimen, the following specific sensors have been investigated and implemented: transmitter-receiver (TR) and giant magneto resistive (GMR) for eddy current sensing and a small diameter tip-based coaxial cable antenna for near field sensing. Although the scanning results show the scanning system’s capability of detecting the defects with 0.2 mm width, the long scanning time become one of the constraints that prevent applying these NDE methods directly on the robot platform. In this case, sensor array which is able to cover more area in the unit time has been studied through simulation and experiment. To have a better understanding of coil array properties, a simulation has been performed.

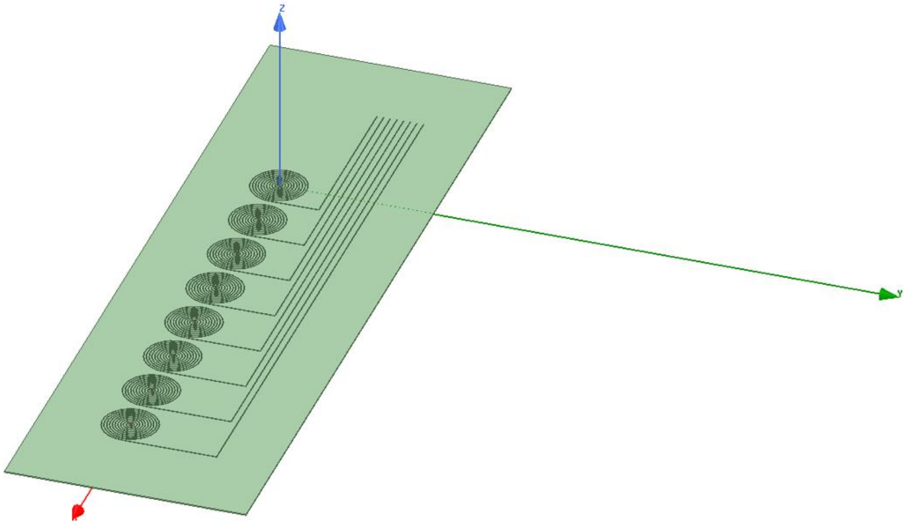

Figure 7: Simulation model of the coil array.

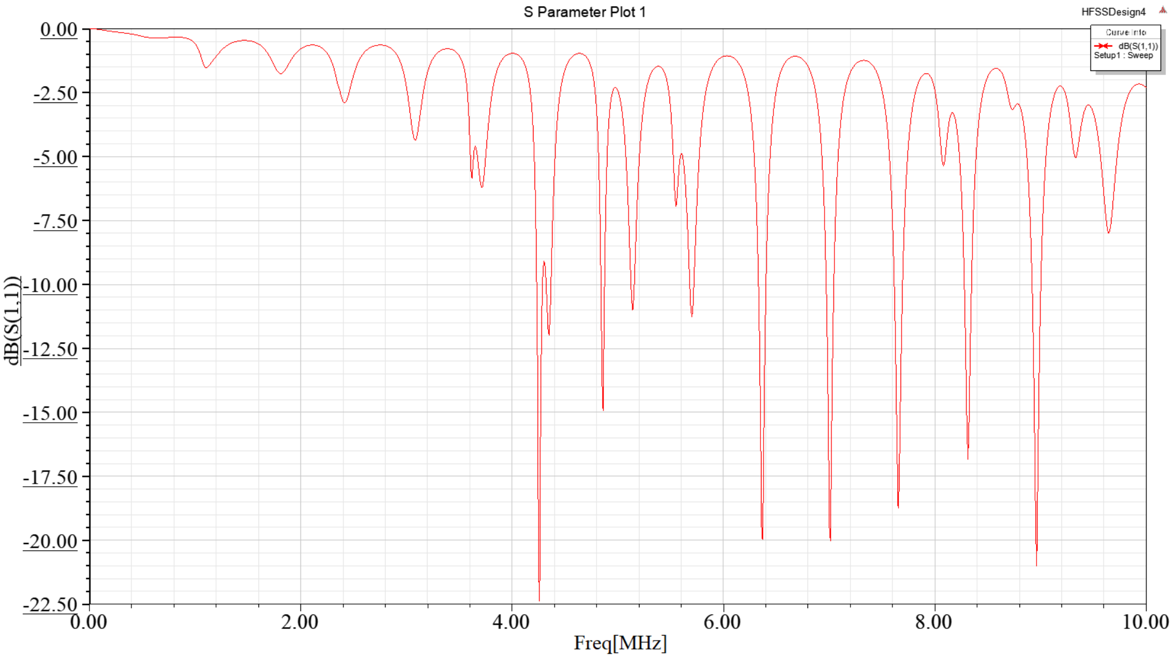

Figure 8: S11 simulation result of the coil.

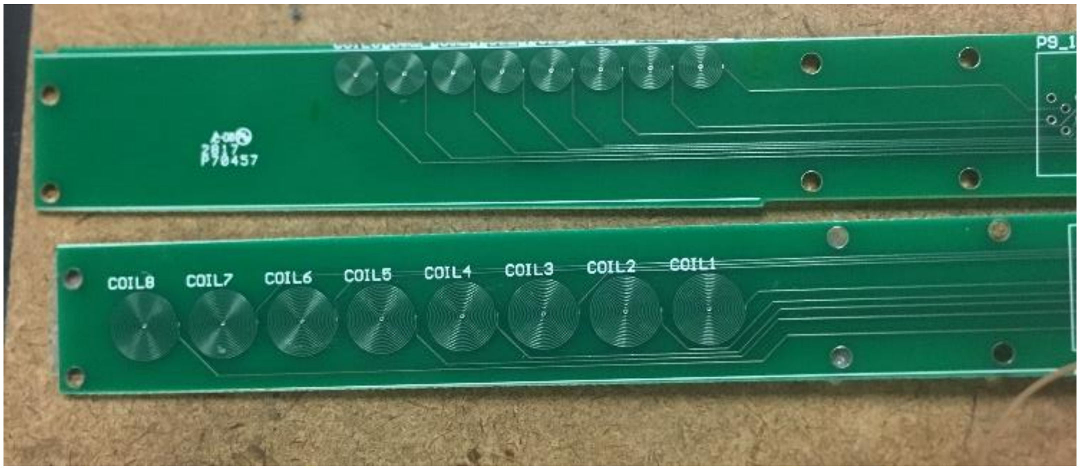

Figure 9: Coil arrays with different sizes of coils.

B. NDE Sensing System Development

A flowchart of the NDE coil array scanning system has been shown above. A dual-channel waveform generator is used as the signal source. The coil array sensor is excited by the signal from ch.1. The signal from ch.2 is used as reference and directly connect to lock-in amplifier. The lock-in amplifier demodulates the receiving signal using the reference signal and output data is sampled using a NI data acquisition device.

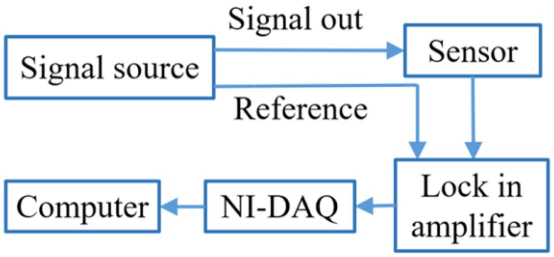

Figure 10: Flowchart of coil array scanning system.

The design of the miniaturized NDE system start with miniaturizing of the components. For the first prototype, a portable version of each part has been selected or developed.

Sine wave	0~60MHz
Square & Triangle Wave	0~15MHz
Pulse & Arbitrary Wave	0~6MHz
Square rise time	≤15nS
Pulse width adjustment range	30nS-4000S
Frequency accuracy	±20ppm
Frequency stability	±1ppm/3h

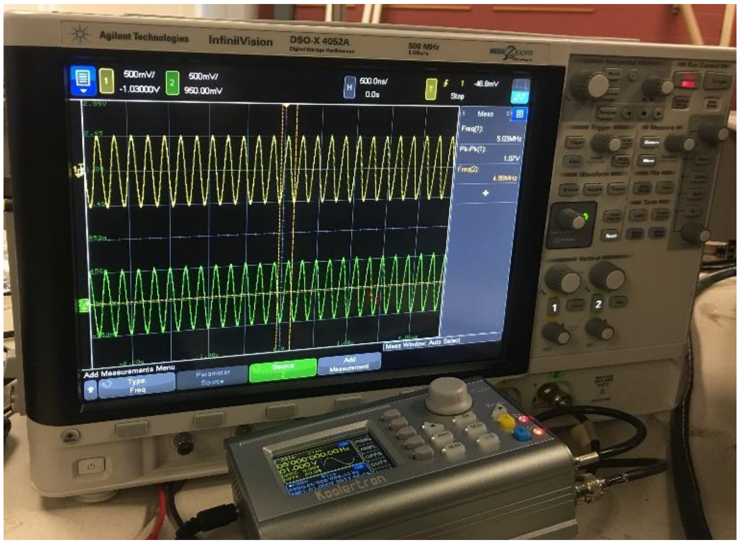

Figure 11: Spec sheet of the waveform generator.

A High Precision Direct Digital Synthesizer (DDS) based Dual-Channel Arbitrary Waveform Function Generator has been used as the signal source. The Waveform Function Generator able to provide up to 60 MHz sine wave to the coil array sensor.

In order to filter out undesired frequencies and reduce noise in the receiving data, a lock-in amplifier has been employed. Lock-in amplifier is a device that able to extract very small signals in the presence of a noisy background with the knowledge from the reference signal at same frequency.

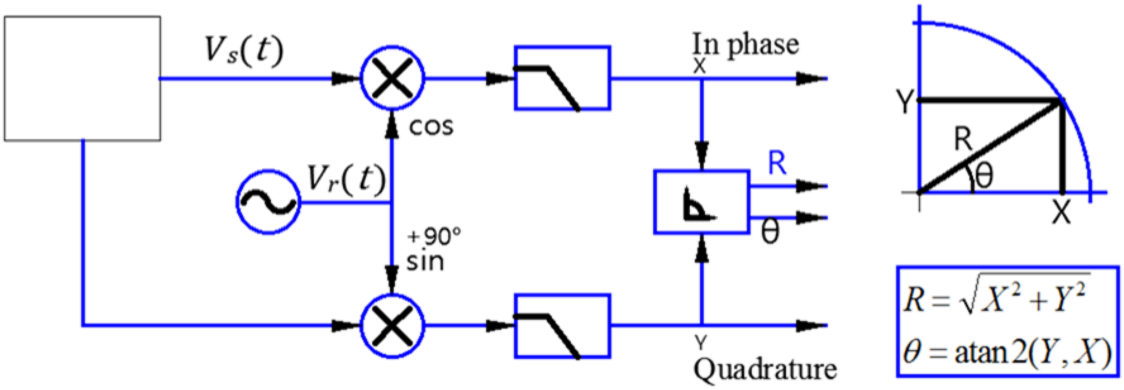

Figure 12: Block diagram of Lock-in amplifier.

As the figure shown above, a multiplication has been performed for the input signal with a reference signal. This multiplication is also termed as demodulation which isolates the specific frequency of interest from all other frequency components. An adjustable low-pass filter is then applied to the result to reject the noise and extract the DC component.

In the complex plane, the input signal Vs(t) can be express as the sum of two vectors.

$$\mathrm{V_s(t) = \sqrt{2}R \cdot \cos(\omega_s t + \theta) = \frac{R}{\sqrt{2}} e^{+i(\omega_s t+\theta)} + \frac{R}{\sqrt{2}} e^{-i(\omega_s t+\theta)}}$$

The process of demodulation can be mathematically expressed as a multiplication of the input signal with the complex reference signal $\mathrm{V_r(t)}$ where

$$\mathrm{V_r(t) = \sqrt{2}e^{-i\omega_r t} = \sqrt{2}\cos(\omega_r t) - i\sqrt{2}\sin(\omega_r t)}$$

The mixed signal is then expressed by

$$\mathrm{Z(t) = X(t) + iY(t) = V_s(t) \cdot V_r(t) = R\left[e^{i[(\omega_s-\omega_r)t+\theta]} + e^{-i[(\omega_s+\omega_r)t+\theta]}\right]}$$

with signal components calculated by the summation and subtraction of the signal frequency and the reference frequency. The averaged mixed signal is given by

$$\mathrm{Z(t) = R \cdot e^{i[(\omega_s-\omega_r)t+\theta]}}$$

When the reference signal’s frequency is same as the input signal’s $\mathrm{\omega_r = \omega_r}$, the output of the lock-in amplifier simplifies to

$$\mathrm{Z(t) = R \cdot e^{i\theta}}$$

The X and Y are the in-phase component the quadrature component obtained using Euler’s formula $\mathrm{exp(i\omega_s t) \equiv \cos(\omega_s t) + isin(\omega_s t)}$ as

$$\mathrm{X = Re(Z) = \langle V_s(t)\cos(\omega_s t)\rangle = Rcos\theta}$$
$$\mathrm{Y = Lm(Z) = -\langle V_s(t)\sin(\omega_s t)\rangle = Rsin\theta}$$

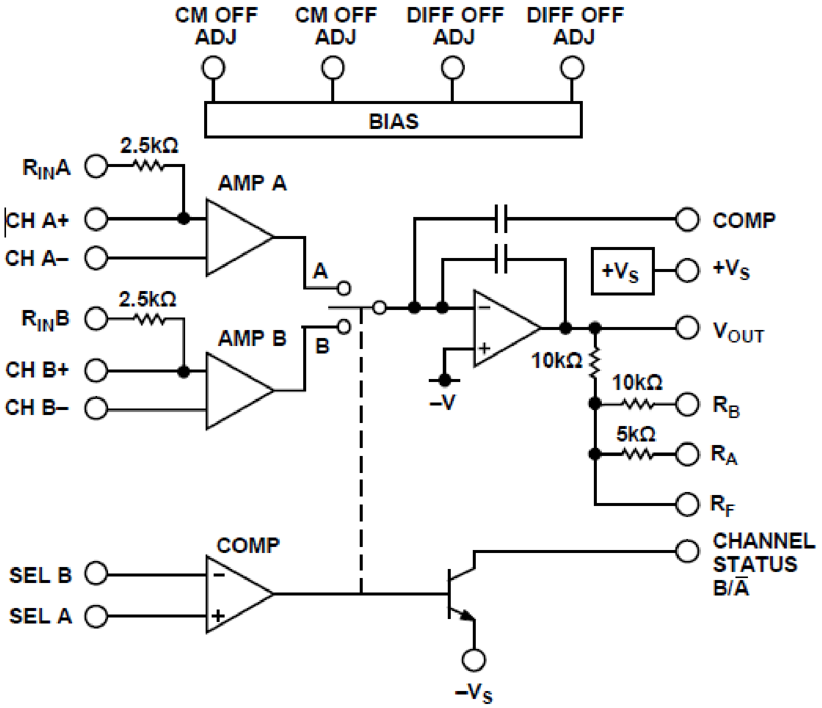

Figure 13: Functional block diagram of AD630.

For the portable lock-in amplifier, AD630 has been selected to implement the demodulation process. AD630 is a high precision balanced modulator/demodulator with 2 MHz channel bandwidth. As the functional block diagram shown above, the chip includes optional input bias current compensation resistors, common-mode and differential-offset voltage adjustment, and a channel status output that indicates which of the two differential inputs is active.

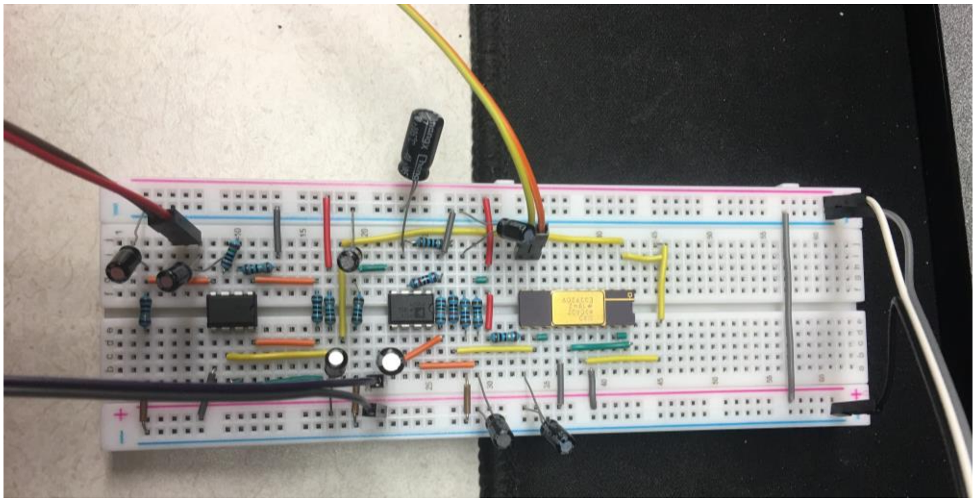

Figure 14: Breadboard based lock-in amplifier.

The portable lock-in amplifier has been designed and tested on a breadboard. Two op-amps have been used to pre-amplifying the signal. A first order low pass filter has been used at the output of the demodulator to reject the high frequency noise. A NI-Daq device has been used to sample filtered signal and convert the analog signal to digital for the further processing.

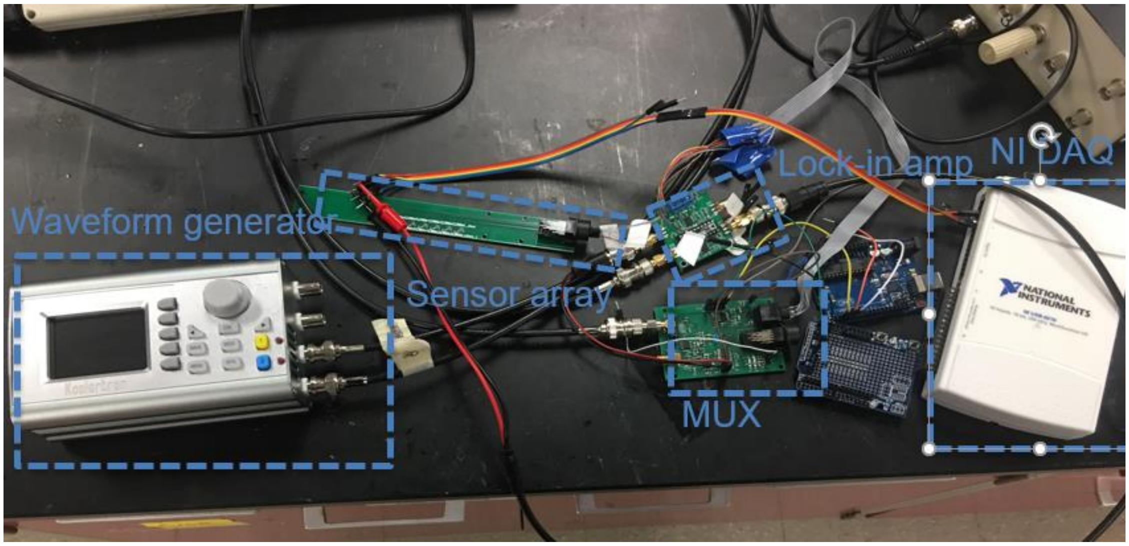

Figure 15: The first design of the portable NDE system.

The first prototype of the miniaturized NDE has been shown above. The coil array sensor is attaching on 3D CNC gantry during the scanning. A line scanning result has been shown below.

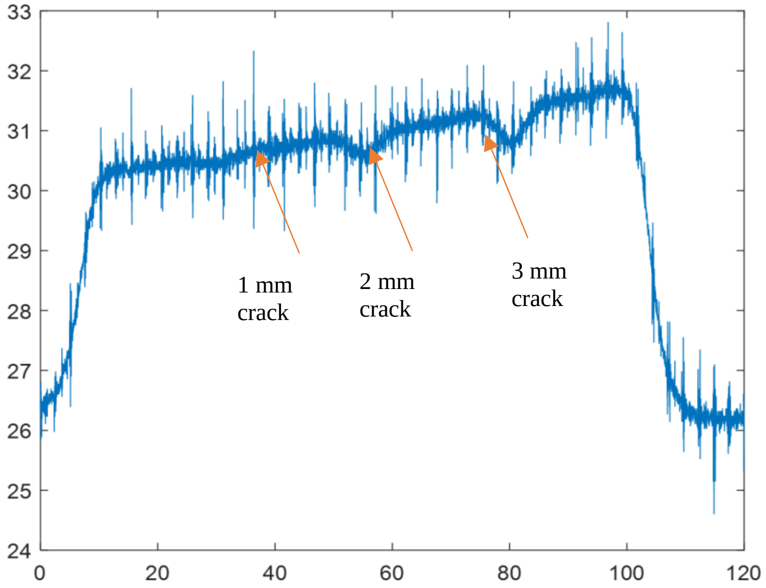

Figure 16: 1D scan of the sample using the portable NDE system.

As shown in the figure, the signal is very noisy and only the cracks with 2mm or 3 mm can be distinguished. These noises may be introduced due to the unstable jumper wire connection. Therefore, to reduce the jumper wire and improve scanning quality, a PCB that the embedded most function of the system has been designed and tested.

In order to have a better control of the system, a microcontroller unit (MCU) has been employed. As the flowchart shown below, MCU will act as a bridge between the sensing circuits and the computer. The sensing circuits provide multi-channel scanning ability and convert the analog signal to digital signal. The MCU collects the data through the I^{2}C bus and pass the data to the computer. The computer will map the data to the corresponding location of the sample and estimate the size of the defect.

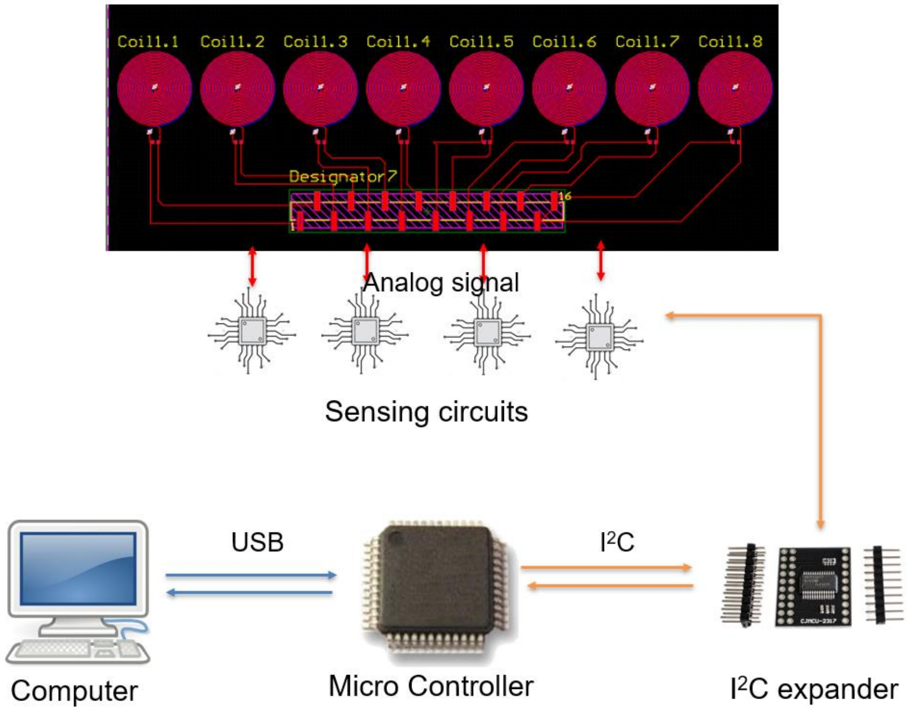

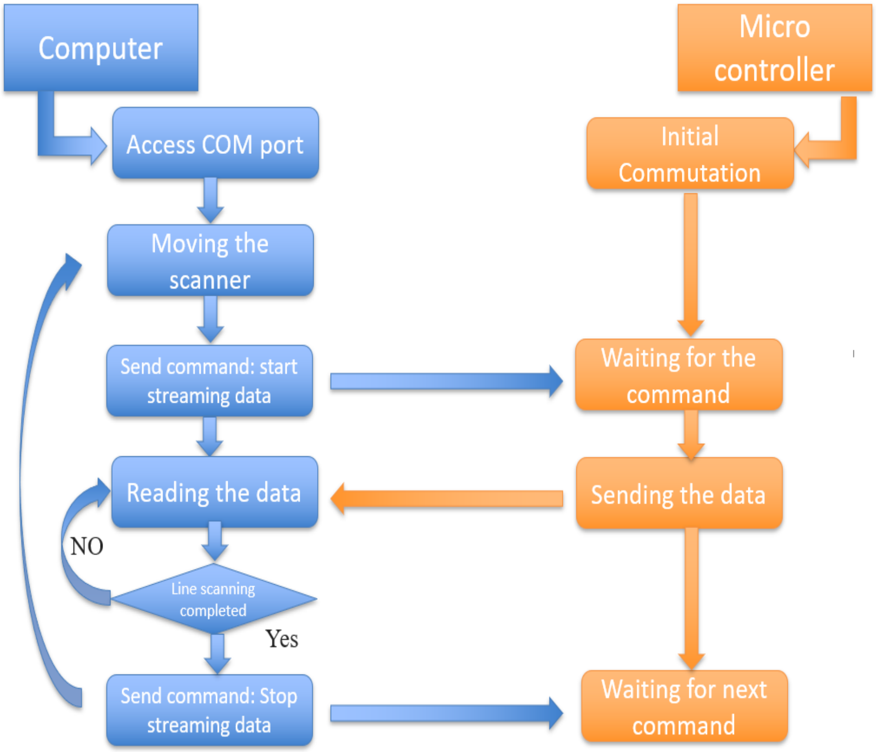

Figure 17: The flowchart of the communication between computer and microcontroller unit.

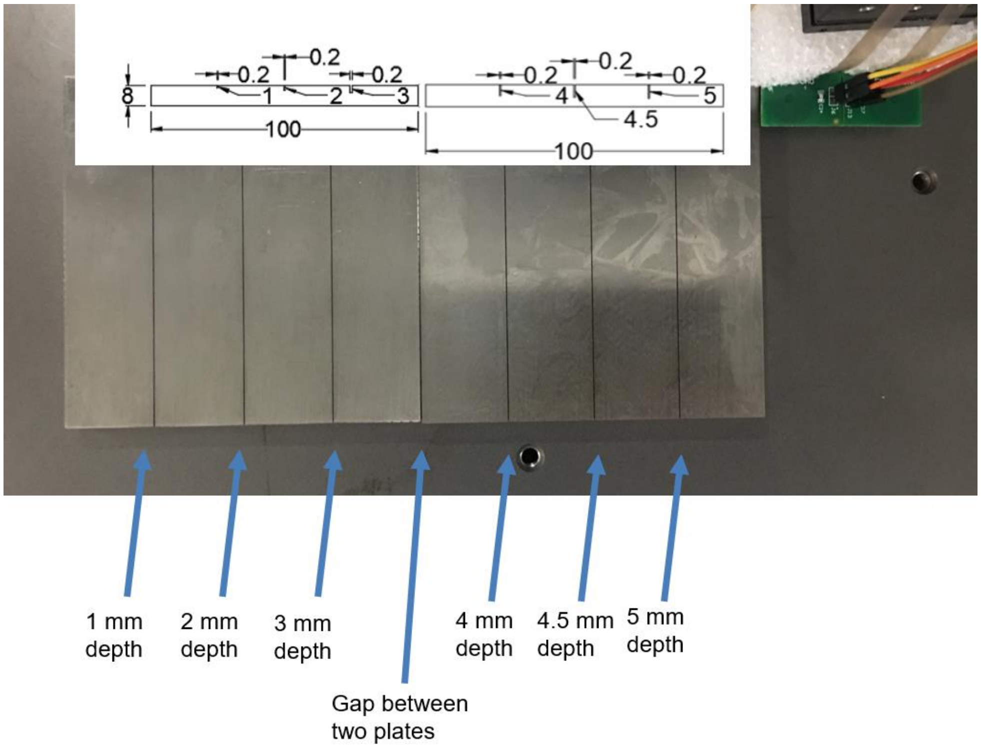

Figure 18: Two steel plates with cracks at different depth.

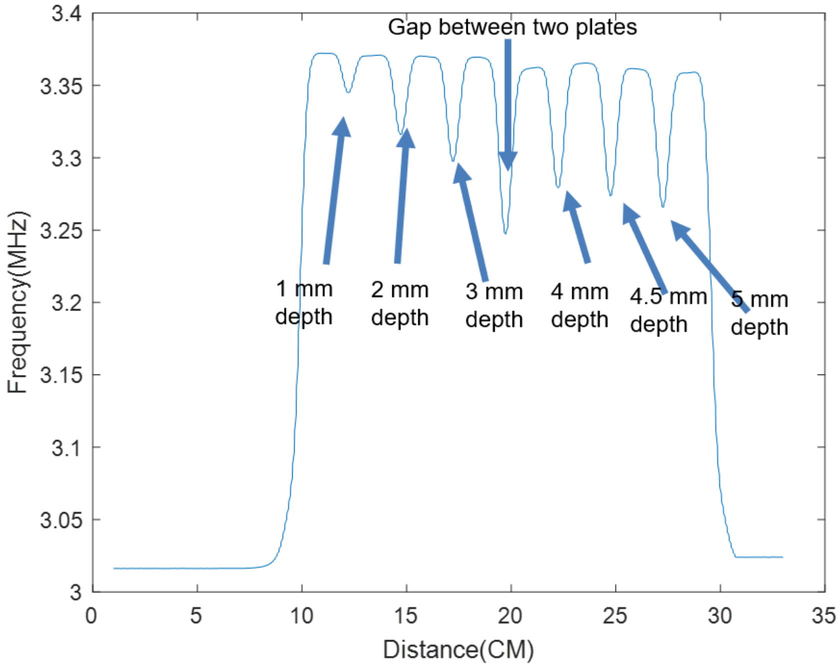

Figure 19: Line scanning result of the two steel plates.

To test the performance of the scanning, two steel plates have been placed side by side. Each of plates has 3 cracks with 0.2 mm width and different depths. As shown in the figure above, all the cracks have been successfully detected. A better signal to noise ratio has been achieved comparing to the first prototype.

Considerations of NDE Sensor Design:

Many constraints need to be considered when designing the NDE sensing system for the robot. The sensor's footprint is limited by the design of robotic system as well as the complexity of testing structures. The allowable maximum power consumption of the entire system is constrained by the available power supply unit on the robot. There are also many environmental conditions that could affect the NDE results obtained from the robotic actuating and sensing. Such would add inevitable uncertainties towards the acquired data or restrict actuation access, in turn, lowering the fidelity and resolution of NDE data used for further damage assessment and analysis. To overcome these aforementioned challenges and obtain optimized sensing outcomes, the proposed NDE sensors were customized to fit in the robotic system and workspace environment for power plant boiler inspection. These optimizations lead to a lowcost, lightweight, non-contact, and simplified NDE setup.

To achieve the optimized scanning performance, a parametric study of the coil design has been done using Ansys HFSS. The simulation studies focus on the sensor's sensitivity to the very narrow cracks (the width of the crack is less than 0.2 mm) on the boiler wall as well as the sensor’s scanning area. A sensor with better sensitivity to the interested defect will provide a better signal-to-noise ratio and a sensor with larger scanning area will reduce the scanning time. Two identical coils are simulated with steel plates present on the top of the coil. The lift-off distance is 1 mm. A crack (0.1 mm × 15 mm) has been introduced to one of the steel plates. The parametric sweep study simulates different coil dimensions such as the line space, line width, and the number of turns.

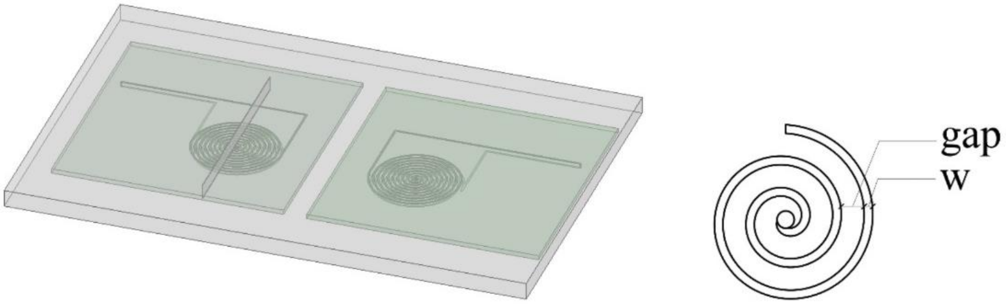

Figure 20: The simulation geometry model. Two identical coils are simulated to study the difference between the signal from the healthy region and the defective region.

The sensor's sensitivity can be depicted by resonating frequency's magnitude difference when comparing the healthy and defective regions' scanning data. A general trend can be observed that as the number of turns increases, the sensitivity of the sensor decreases. However, there is a trade-off between the scanning area and the sensor's sensitivity. Therefore, a multi-channel eddy current array has been designed and employed, which allows for surface and subsurface anomaly detection while meeting the optimization requirements.

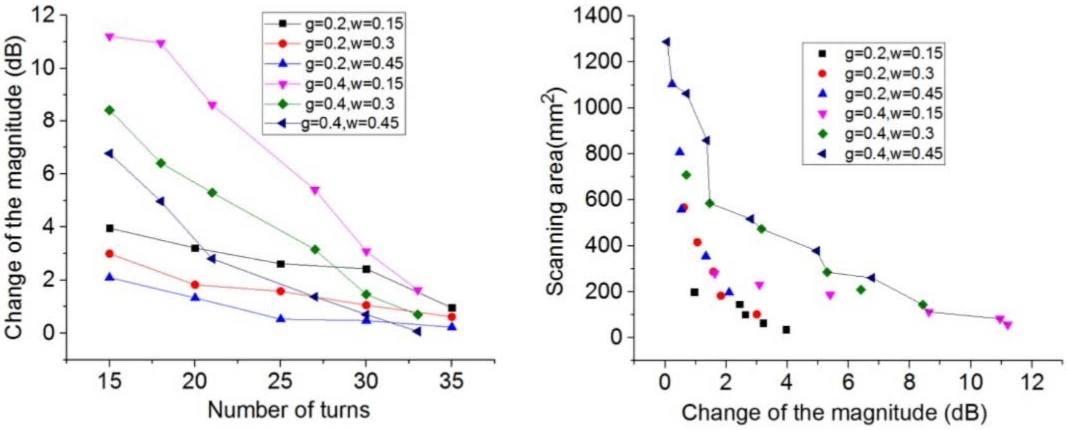

(a) (b)

Figure 21: The simulation results of the different dimensions' coils on the healthy and defective samples. (a) The magnitudes change at the resonating frequency and (b) The Pareto front of maximizing the scanning area and the sensitivity of the scanning system.

1.2. Subtask 1.2: Signal Processing for Crack Profiling

Signal processing techniques were implemented and tailored for robotic platform-based acquisition. Further, crack profiling methods were also built into the signal processing. Specifically, postprocessing and filtering methods required to eliminate the sensing noise, and learning-based crack profiling methods were developed.

1.2.1. Postprocessing for Noise Removal

A. Data Fusion for Noise Removal

Data post-processing methods were studied to achieve a better signal to noise ratio. By combining images of various sources with different physical properties, pixel-level data fusion focus on revealing complementary or redundant information about the physical and mechanical characteristics of a material. In order to improve the accuracy of detection, a method that aim to extract all the perceptually important features from different original images has been developed. This data fusion method combines the information to form a fused image in such a way that all the key features from each input image are still perceivable.

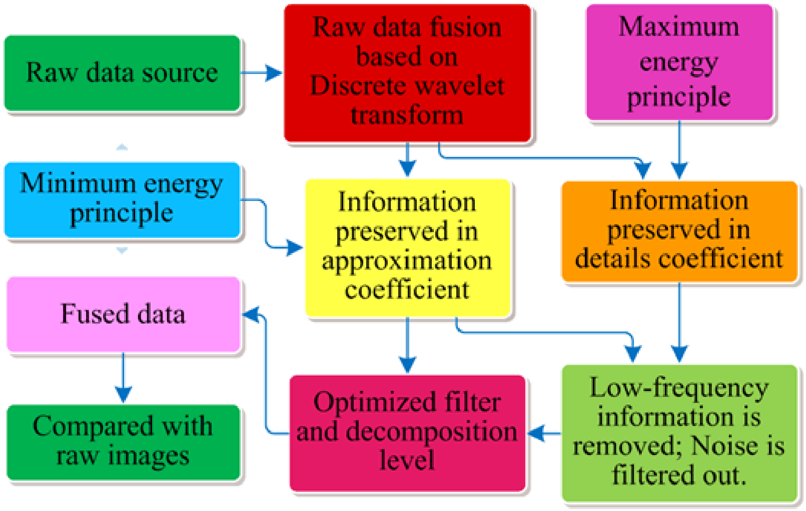

Figure 22: Flowchart of the data fusion method.

A flowchart of the data fusion method has been shown above. After selecting the input data, discrete wavelet transform (DWT) will be employed to convert the raw data. DWT based image fusion consists of two steps: selection of the proper wavelet filters and level of decomposition using formulated parameter, and selection of the proper fusion criterion in wavelet sub band. It means that fusion is operated on wavelet domain level via DWT of multiple sources combined with fusion rule and fused image is reconstructed by inverse DWT (IDWT). This method fuse images at different frequencies from the eddy current sensor.

$$I = W^{-1}[\varphi\{W(I_1) + W(I_2) + W(I_3) + \cdots + W(I_m)\}]$$

where I_1, I_2,…, I_m are the m images to fuse, φ denotes the fusion rule, and $W$and W^{-1} represent DWT and IDWT respectively. In order to achieve higher quality, wavelet filter, level of decomposition and corresponding fusion rule should be carefully selected.

Energy risk factor is adopted to select appropriate filter. $E_{min} = \min_j E_a(j)$. $E_a(j)$ is the energy of approximation coefficient at the j^{th} level of the selected wavelet filter. The wavelet energy represents the percentage of energy corresponding to the approximation and the detail coefficients. E_{min} denotes the minimum energy of the wavelet approximation coefficients (WAC) which indicate that low-frequency information is removed after decomposition. It is used to filter out noise and other low-frequency components.

Since useful information could be preserved in low frequencies mixed with noise, the maximized energy within the wavelet detail coefficients (WDCs) is considered. The energy of denoised image's WDCs cannot be higher than the original raw image. Despite of having energy stored within the WDCs of the denoised image being closer to the energy stored within the WDCs of the raw image, more importance should be given to WDCs in higher frequencies.

The A108 Steel Boiler Sample has been scanned using different kinds of sensors at different frequencies. The selected scanning area includes cracks with 200 µm and 400 µm width.

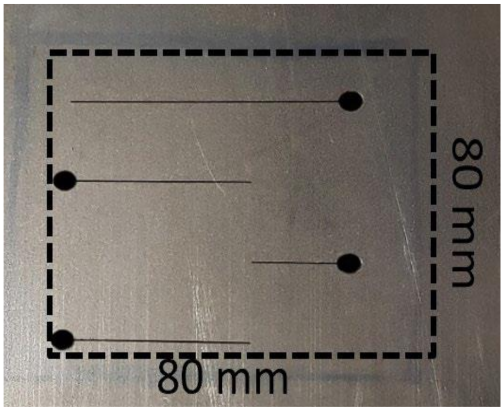

Figure 23: The scanning area of the crack sample.

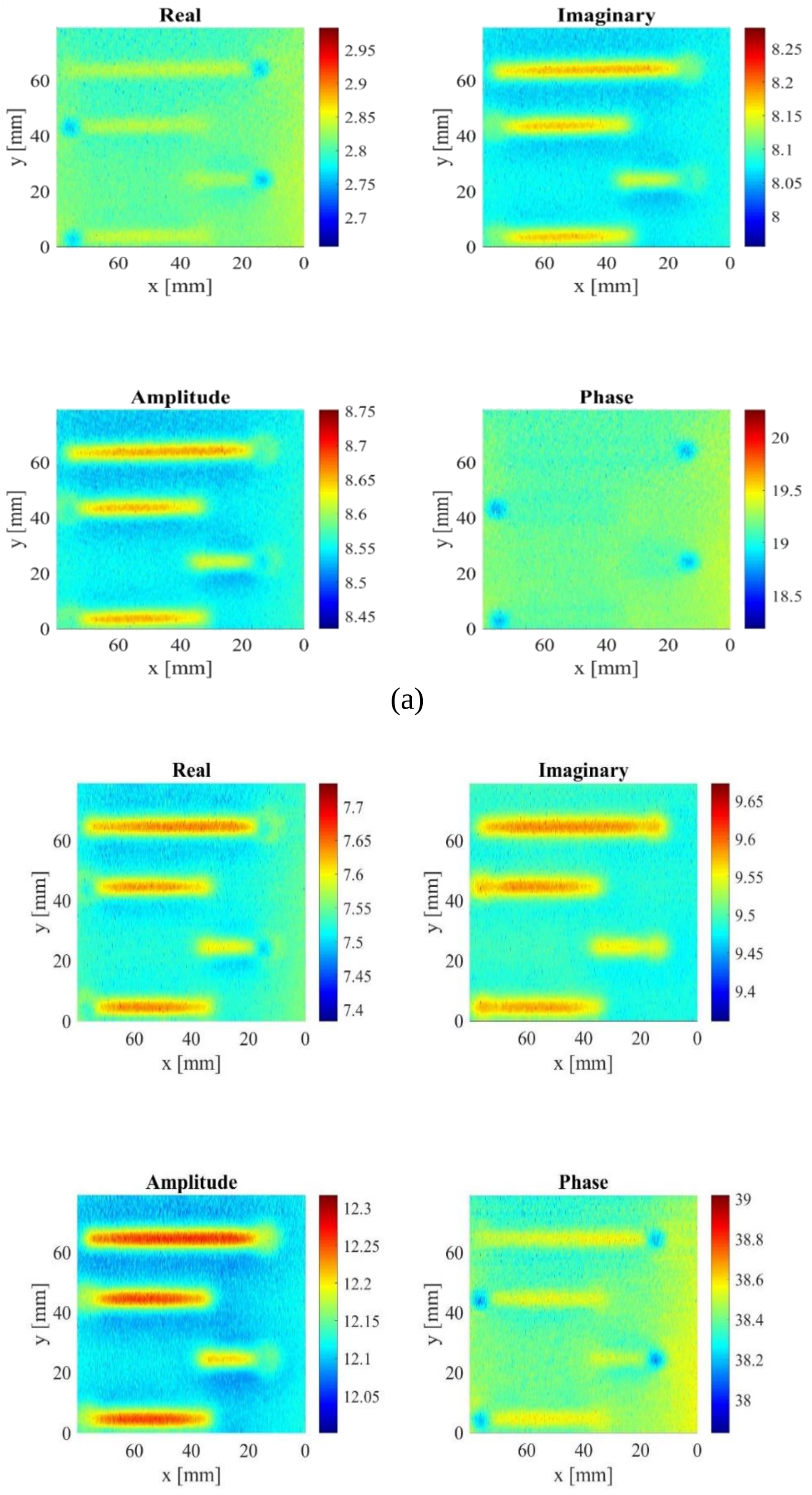
Real
Imaginary
Amplitude
Phase
y [mm]
x [mm]
0
20
40
60
2.95
2.9
2.85
2.8
2.75
2.7
8.25
8.2
8.15
8.1
8.05
8
8.75
8.7
8.65
8.6
8.55
8.5
8.45
20
19.5
19
18.5
7.7
7.65
7.6
7.55
7.5
7.45
7.4
9.65
9.6
9.55
9.5
9.45
9.4
12.3
12.25
12.2
12.15
12.1
12.05
39
38.8
38.6
38.4
38.2
38

(a)

(b)

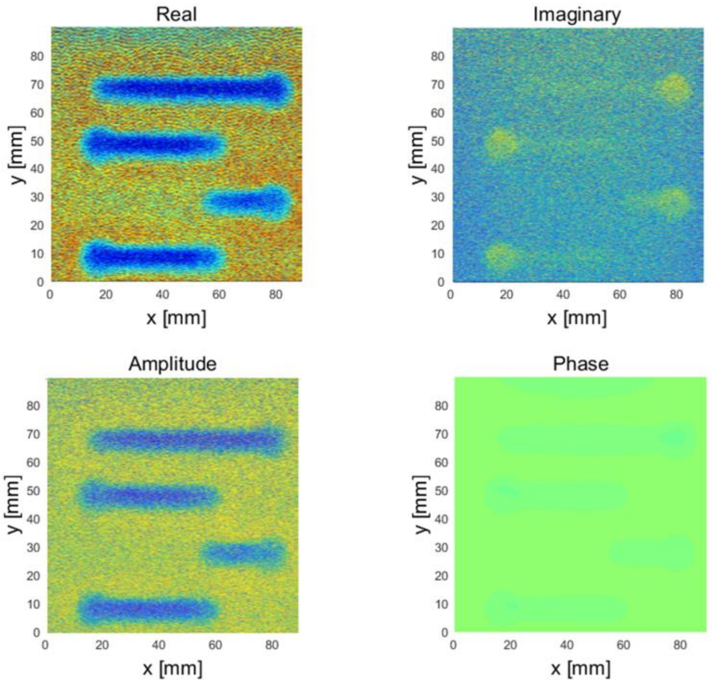

(c)

Figure 24: (a) Eddy current imaging at 30 KHz, (b) Eddy current imaging at 50 KHz, (c) GMR sensor imaging at 35 KHz.

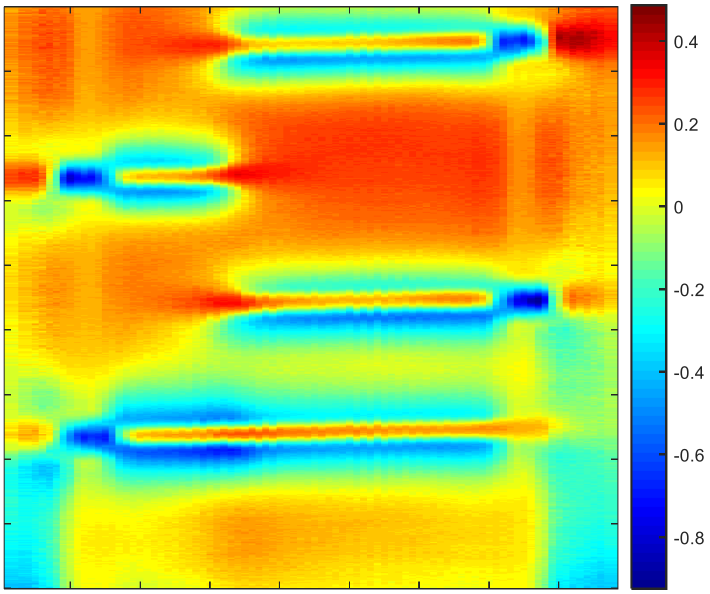

Figure 25: Data fusion result of scanning data at different frequencies.

Two 1D plots have been shown below to have a better comparison between raw data and data fusion result. From the figure, the fusion results show that with proper selection of wavelet and fusion procedure, reliability and SNR can be enhanced.

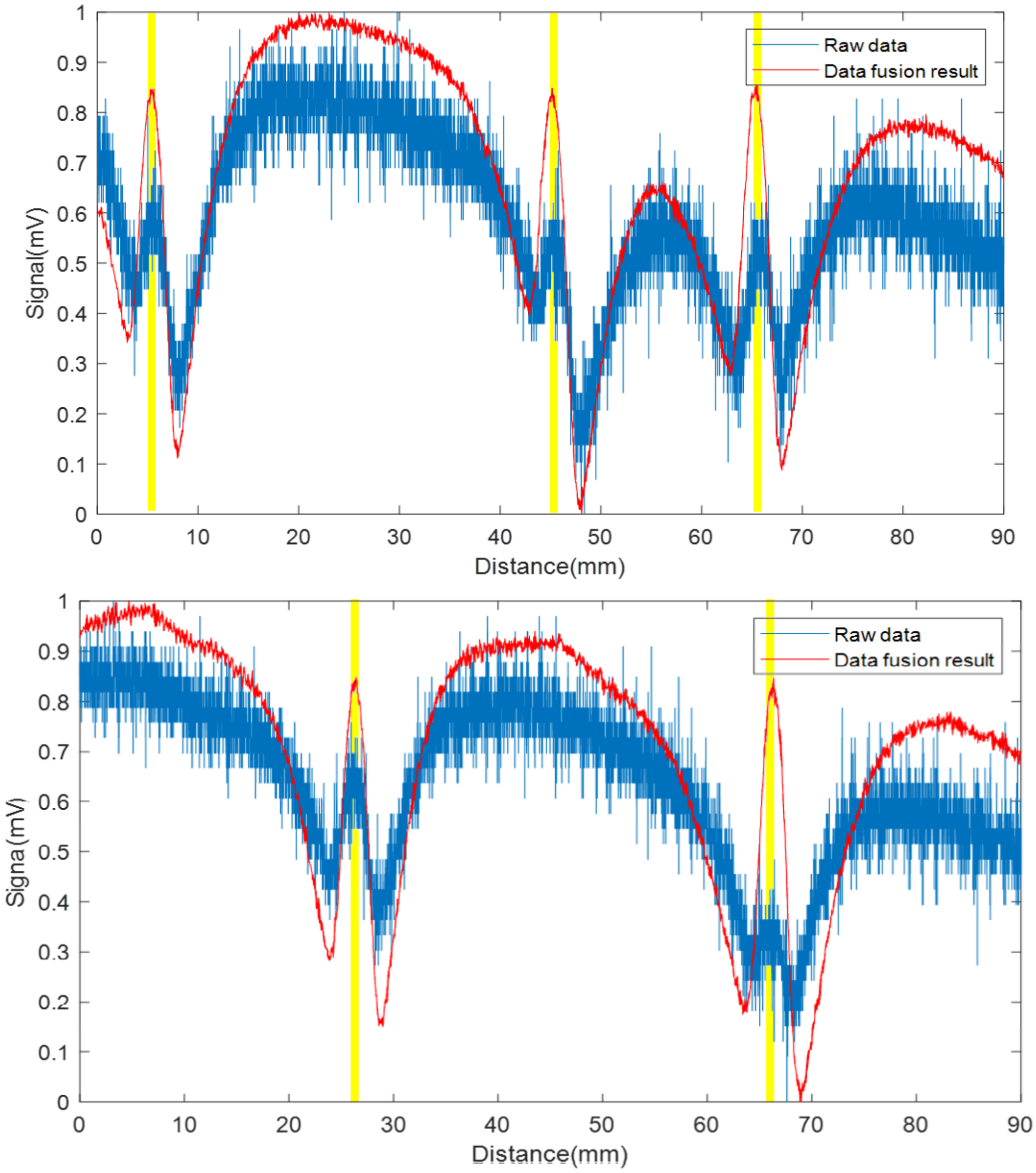

Figure 26: 1D plots that compare the raw data and data fusion result. The shading region indicates the location of sub-mm cracks.

B. Sensing Reliability Improvement

The following images show the testing samples and the 2D scanning result using the developed sensor in channel 0.

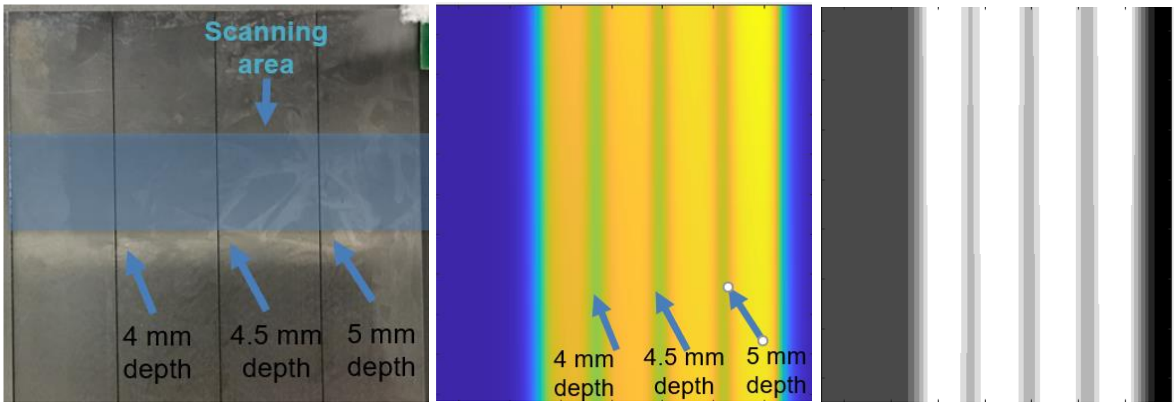

Figure 27: The 2D scanning results of the steel sample with different depth cracks.

The scanning takes 1500 steps in the X direction with step size 0.1 mm and 20 steps in the Y direction with step size 1 mm. The lift-off distance is 0.5 mm.

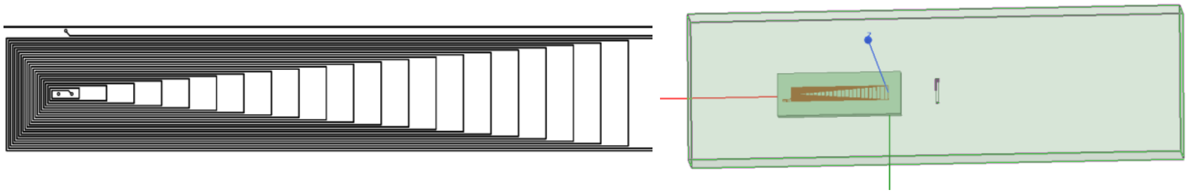

Figure 28: Schematic of the coil for the fast scanning.

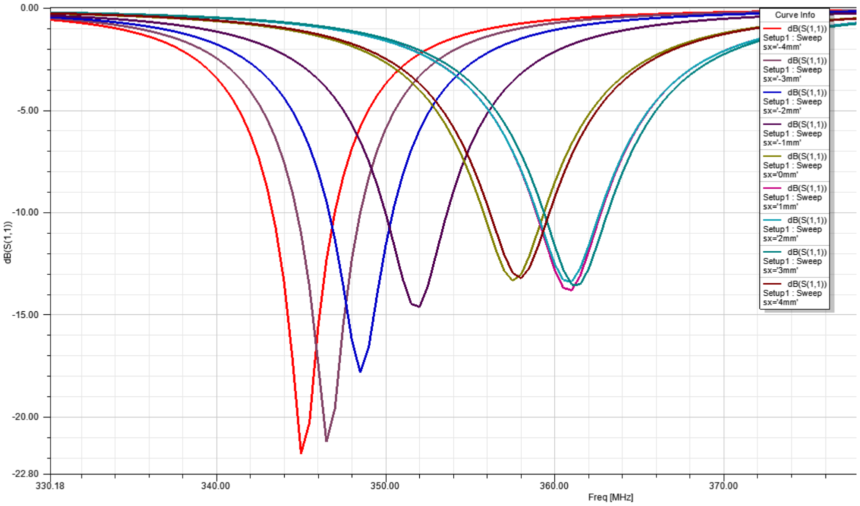

Figure 29: Specimens with a rough surface.

More data within the unit distant will provide better resolution of the scanning. However, the sampling rate is limited by the hardware and can not be increased without constraints. Therefore, a multi-channel sensor has been employed in the system to cover more scanning areas without increase the scanning time in the current design. In order to further reduce the scanning time, a bi-level sensor system is studied. The idea of this system is to use a large sensor to run a fast scan and detect the presence of the defects. Then using a small sensor to run a precise scan and obtain the detailed information of the defects.

A rectangular stretched coil has been simulated for the fast scanning. The size of the coil is 100 mm x15mm, with 23 turns. The trace and spacing of the coil are 6 mil. The coil has been placed on a steel plate with a crack on the surface. The model simulates the S11 signal when the defects are close to a different part of the coil. As shown in the Figure 28, the resonant frequency shifted when the defects present near a different section of the coil. The results indicate that the rectangular coil is able to detect the defects and also provide the estimated location information of the defects.

To estimate the reliability of NDE systems, the parameters responsible for noise, such as that is due to specimens' surface roughness the change of the lift-off distance, has been studied. Two specimens with the rough surface have been scanned to study the parameters responsible for noise,. As shown in the Figure 30, a line scan has been performed on the steel samples with rust and scratches on its surface.

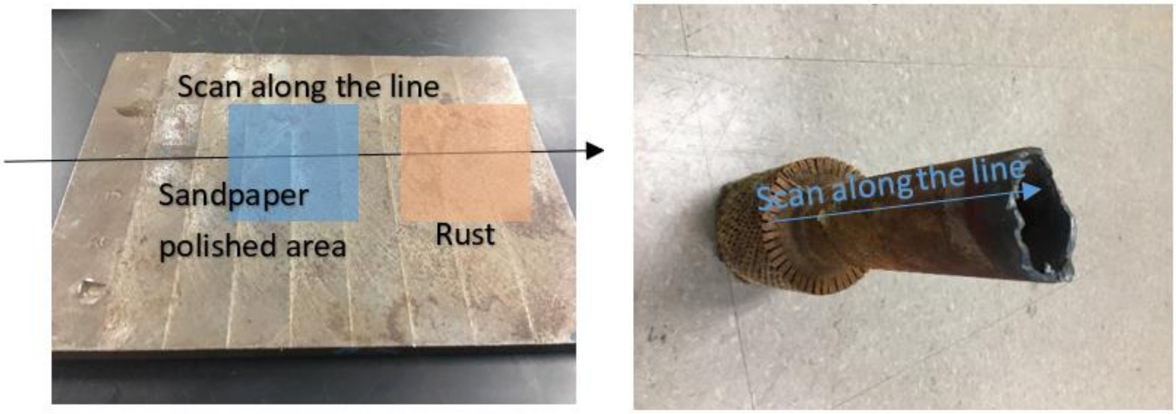

Figure 30: Specimens with a rough surface.

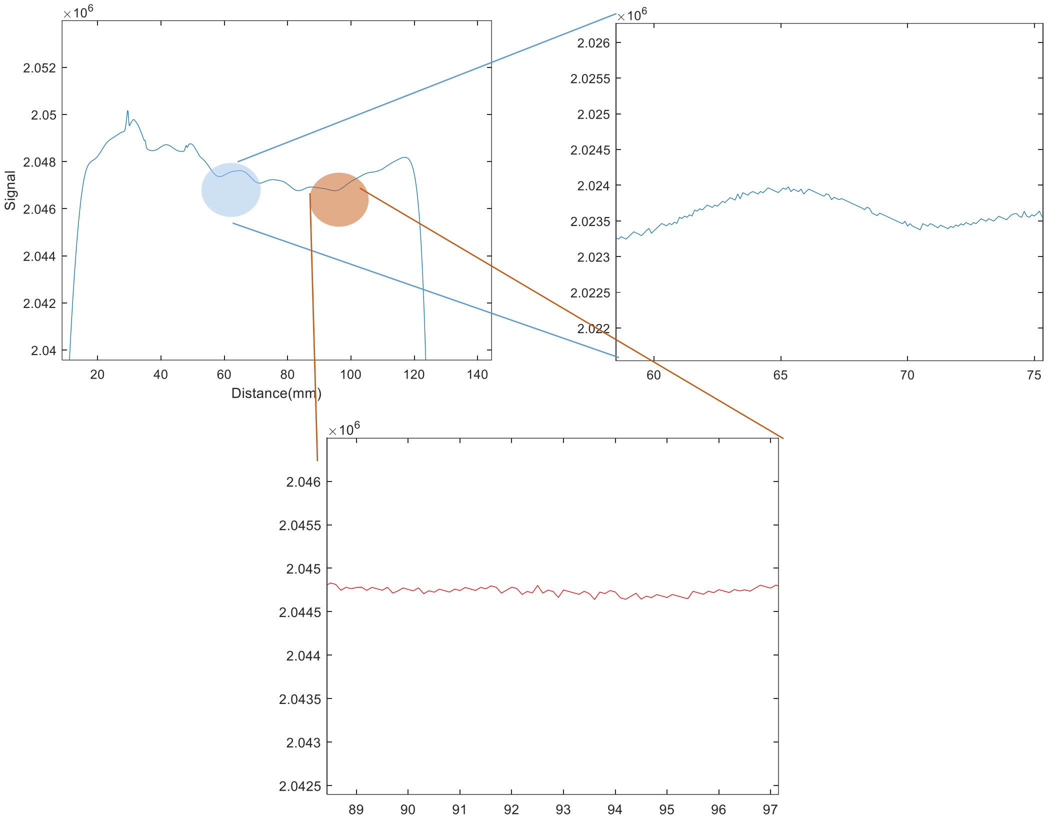

Figure 31: The line scanning signal of the steel plate with a polished area and the rusted area.

For the plate sample, the scanning takes 1500 steps in the X direction with a step size of 0.1 mm. The lift-off distance is 1 mm. As shown in the Figure 31, the noise can be observed on an average 50Hz fluctuation due to the rough surface and other factors result in the signal frequency shift on both the polished area and the rusted area. In this case, the rust does not result in the difference in the signal compared to the polished area.

When the sensor is installed on a robot platform, the lift-off distance may change during the motion of the robot. Therefore, it is necessary to study the effect of the distance between the sensor and the sample. Two steel plate samples have been placed side by side and the lift-off distance from 1mm to 50 mm has been scanned.

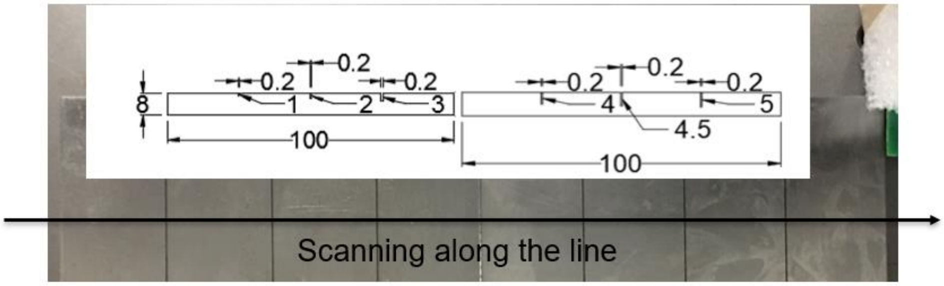

Figure 32: Steel samples with different depth of the cracks.

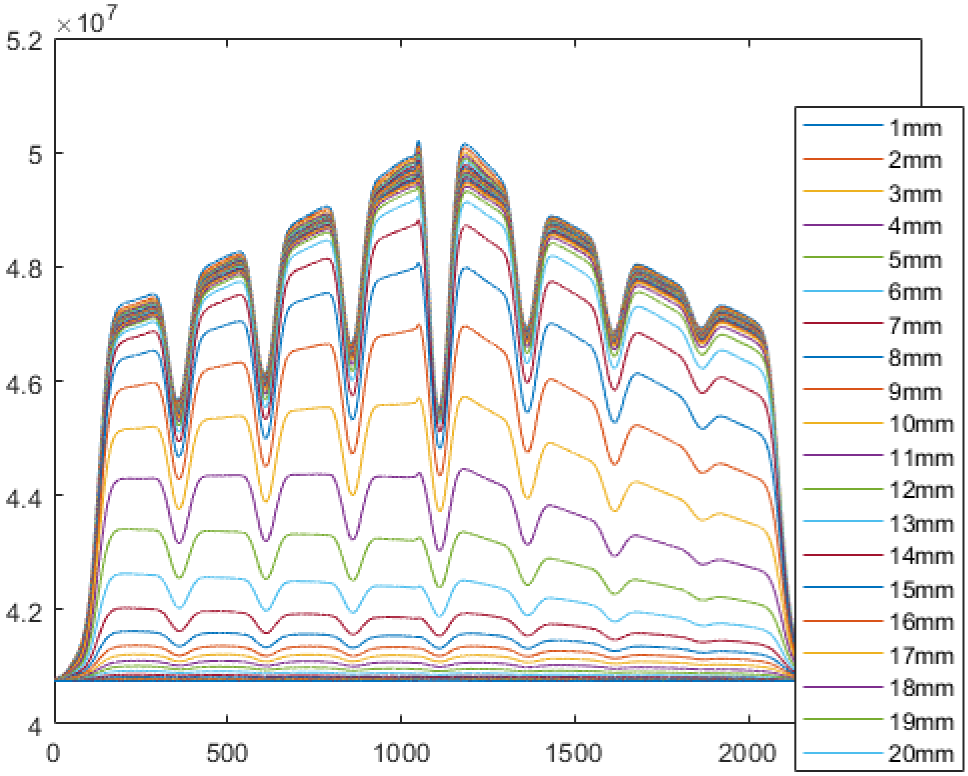

Figure 33: Line scanning of the steel plate at different liff-off distance.

As shown in the Figure 33, a better contrast of healthy area and defect area can be observed when the sensor is closer to the sample. The signal is very similar when the lift-off distance is within 1-20 mm, which indicates a small vibration will not introduce too much noise. The signal decayed very fast when the lift-off distance is increased from 21 mm to 30 mm. Although the location of the defects can still be identified from the signal, a lot of information is lost. When the distance between the sensor and the sample is more the 31 mm, it would be hard to get any useful information from the sensor.

1.2.2. Crack Profiling by Size Estimation

It is very important to know the size of the cracks. In this project, the NDE scanning system on the robot will perform a 2D scanning of the sample. With proper data processing methods, the length and the width of the defects can be accurately detected. However, the depth information of the defects is not that straightforward. In order to have a better depth estimation, both experimental tests and numerical simulations have been studied. A numerical simulation model is developed using Ansys to study the S-parameter change when the sample with different depths of cracks. The model of a single coil is shown below.

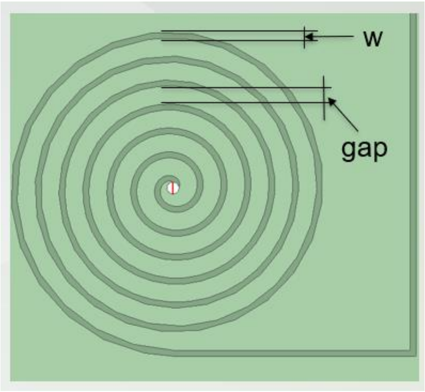

Figure 34: Coil simulation model with adjustable parameter gap and width.

A 20 X 20 X 5 (Unit: mm) sample with different depth of the cracks has been place on the top of the coil sensor as shown in Figure 34.

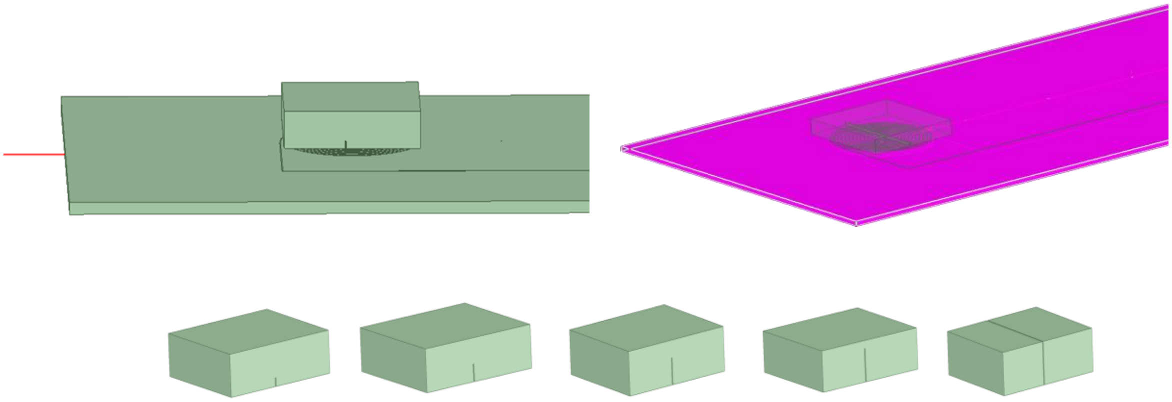

Figure 35: The steel samples with different depth of cracks on the top of sensor.

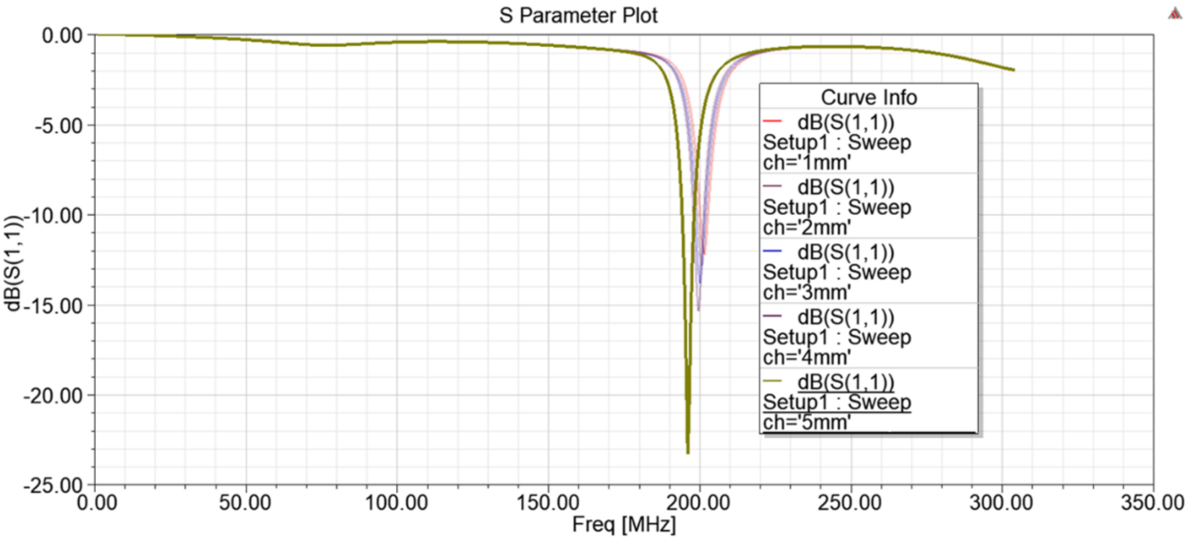

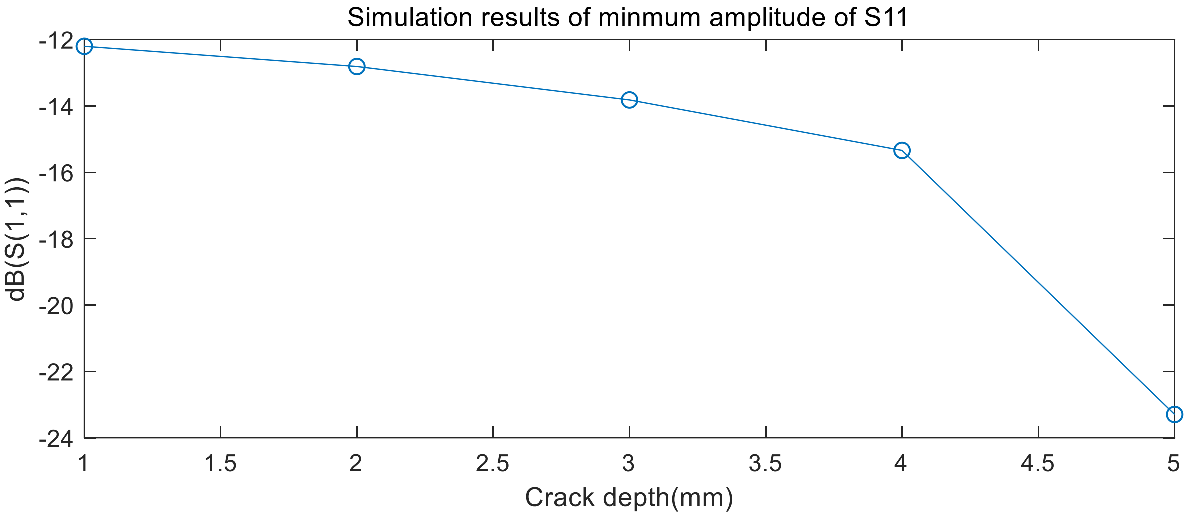

Figure 36: S11 simulation results of crack depths from 1 mm to 5 mm.

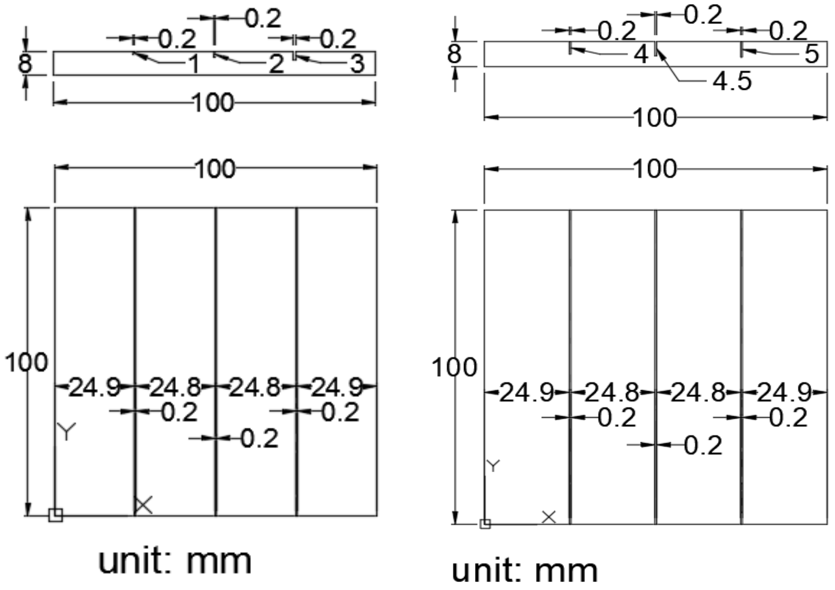

Figure 37: New sample design: A3(Q235) steel with 0.2 mm width at different depths.

The pervious sample contains only through cracks. In order to study the actual performance of the sensor on different depths, the new sample with different depths of cracks have been fabricated. The material of the sample is Q235 steel. Three 0.2 mm width cracks with depth from 1 to 3 mm have been introduced to sample 1. The cracks on sample 2 are with same width but the depths are 4, 4.5 and 5 mm respectively. The samples have been scanned using eddy current coil array sensor with 1 mm lift-off distance. As shown in the figure, the cracks with different depth can be easily distinguished. However, more study is still needed to get a good depth estimation from the data.

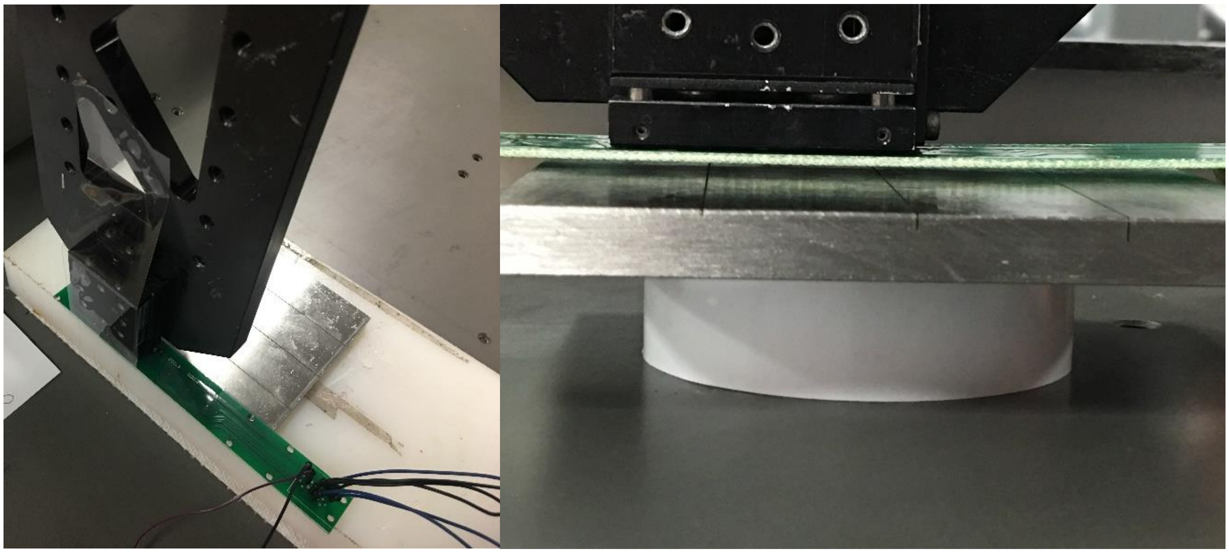

Figure 38: Experiment setup with eddy current array sensor.

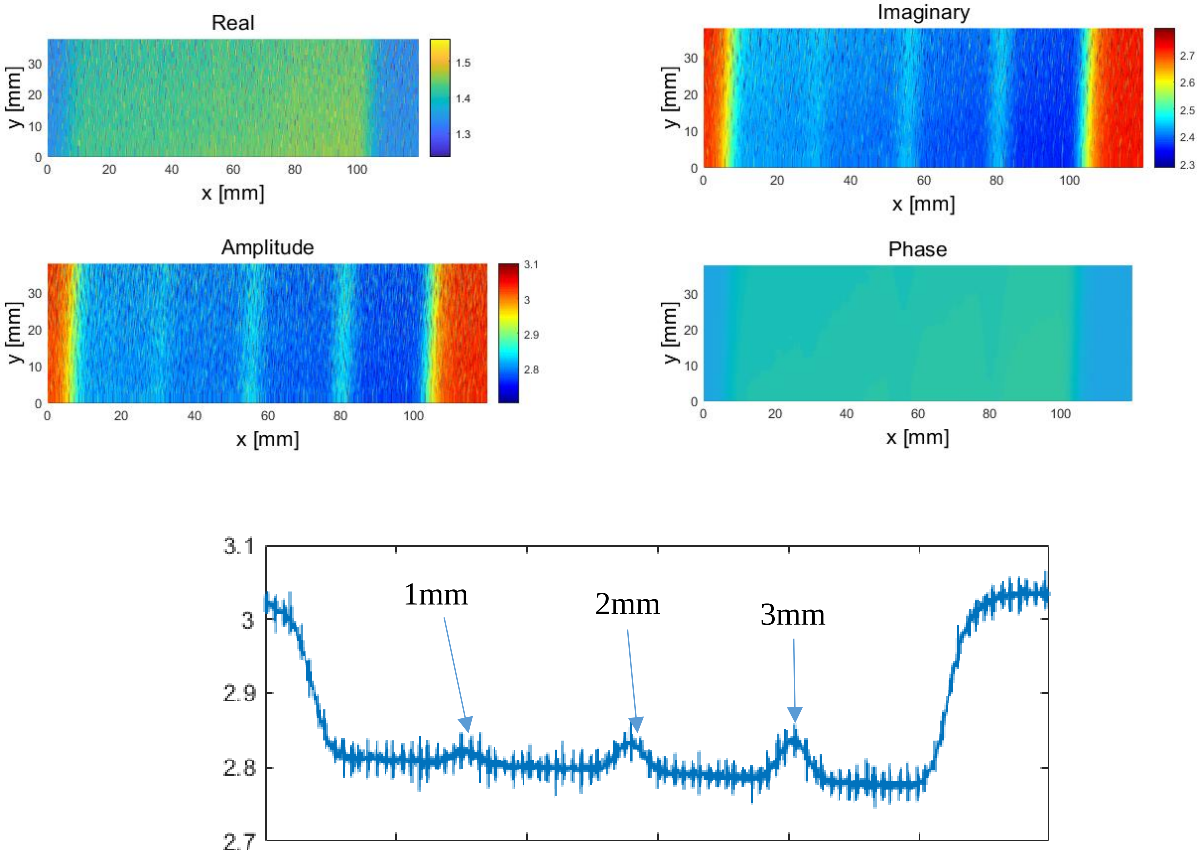

Figure 39: 2D and 1D plot of the scanning imaging.

A. Regression Model for Crack Size Profiling

A model is developed which simply mapping the inputs (signal from the sensor) to outputs (information of the cracks). In order to study the relationship between the geometry of the cracks and the raw signal, the steel plates with cracks of different depth have been placed side by side and scanned multiple times with same setup.

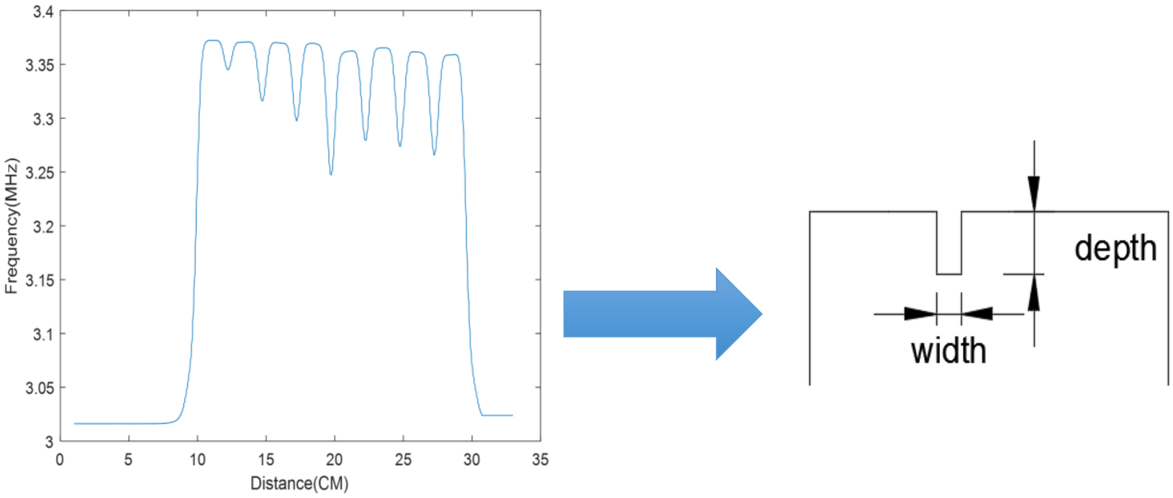

Figure 40: Extracting the crack information from raw data.

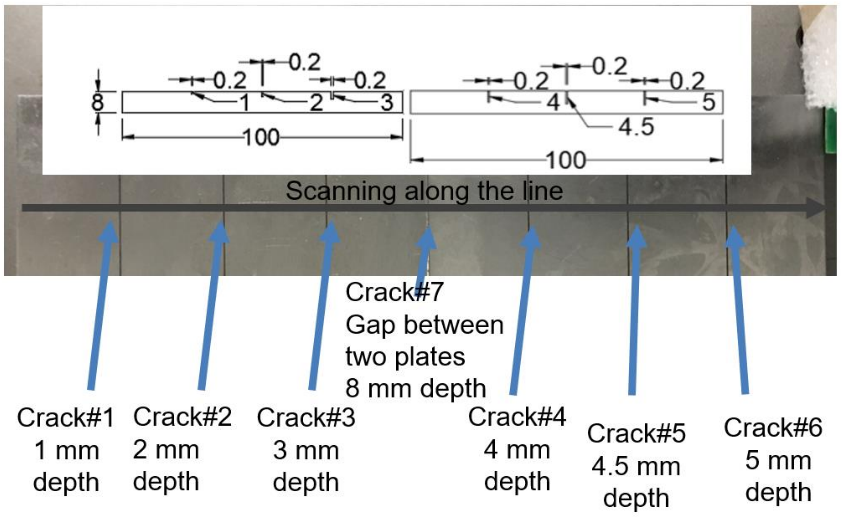

Figure 41: The steel sample setup and the schematic.

Each of plates has 3 cracks with 0.2 mm width and different depths (1mm, 2mm, and 3mm for the first plate; 4mm, 4.5mm, and 5 mm for the second plate). The gap between two plates has been considered as a through crack with 8 mm depth. This setup using two channels (Ch0 and Ch1) with same coil but scanning at different lift off distance (1mm and 1.5mm).

A model is trained to learn relationships between the inputs and outputs from the scanning dataset. During training the model is given both the features of the signal and the labels of the cracks and then create the link from the former to the latter. After training, the model is evaluated on a testing data set, where the features are given, and it makes predictions. The performance of the model is given by comparing the predictions with the known labels to calculate accuracy.

The raw data is obtained and then used to estimate the actual depth of the cracks. Considering the limited number of data points, the model has first start with simplest linear regression and then increase the complexities to prevent the overfitting.

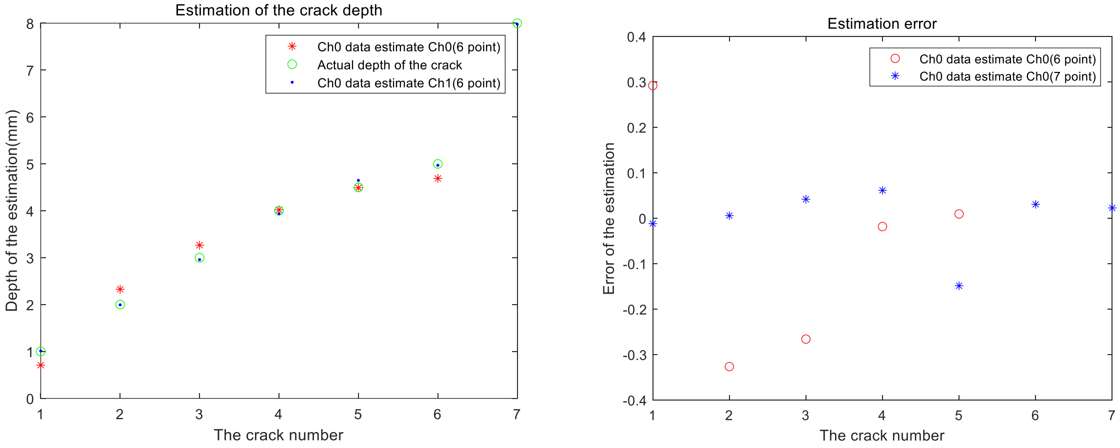

Figure 42: The prediction values and the errors using linear regression.

A huge discrepancy can be seen between the prediction value and the actual depth. The error rate of the estimation is very high which means this model is underfitted with low variance and high bias. Therefore, the polynomial degree of the model should increase which will offer a higher flexibility and a higher power to allow the model to hit as more data points.

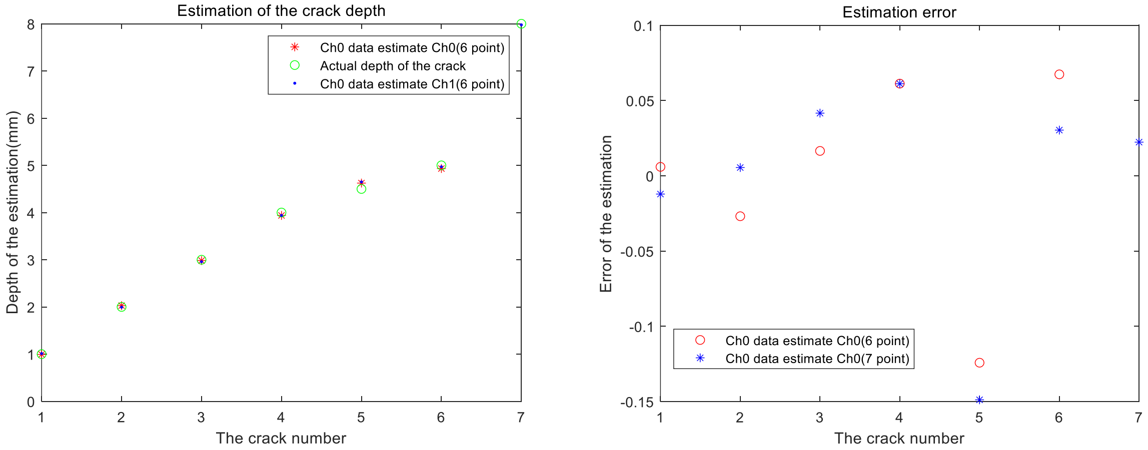

Figure 43: The prediction values and the errors using polynomial regression.

As shown in the figure, a huge improve can be seen that the errors of the prediction are much less. To further improve the prediction accuracy, more training data sets are necessary. The width information of the cracks is also important and the relationship between the raw data and the crack width has also been studied.

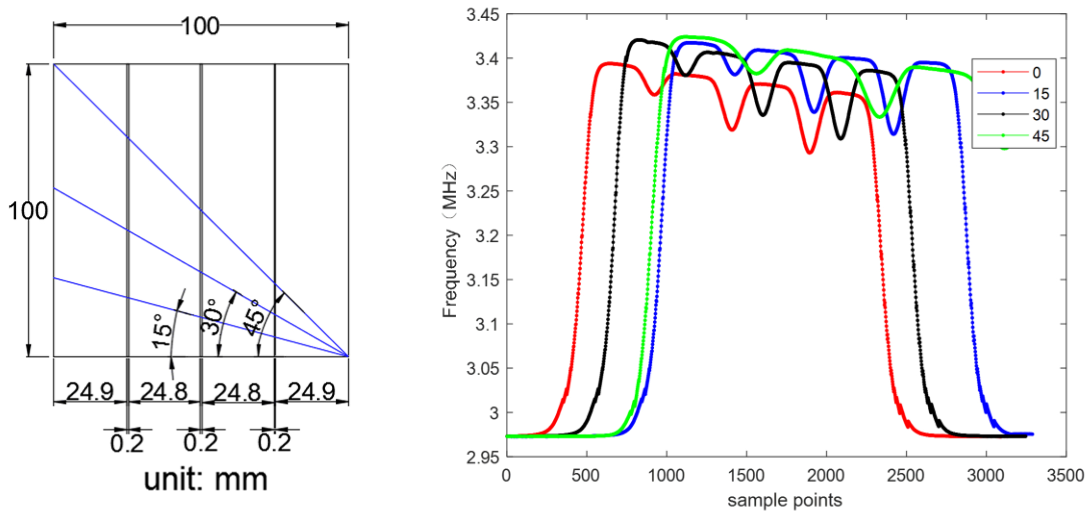

Figure 44: Scanning path with different angles and the scanning results.

The cracks of the current steel plate samples in the Lab are all having same width. In order to get different width information for the prediction, several scans have been performed along different angle of the sample. As shown in the figure, the paths parallel and have a 15º, 30º, and 45º angle with edge have been scanned. The full width at half maximum (minimum) of the signal waveform has been as the feature parameter to calculate the actual width.

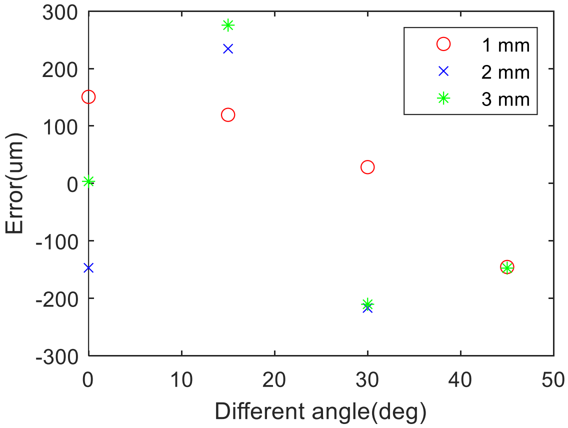

Figure 45: Error of the width estimation.

More training data sets are necessary to improve the accuracy of the prediction model. Due to the limited access to the Lab and scanning system, several simulation models have been designed and analyzed to provide a better understanding of the information extraction.

In order to study the relationship between the width of the crack and the signal, a steel plate with a triangle shape through hole has been simulated.

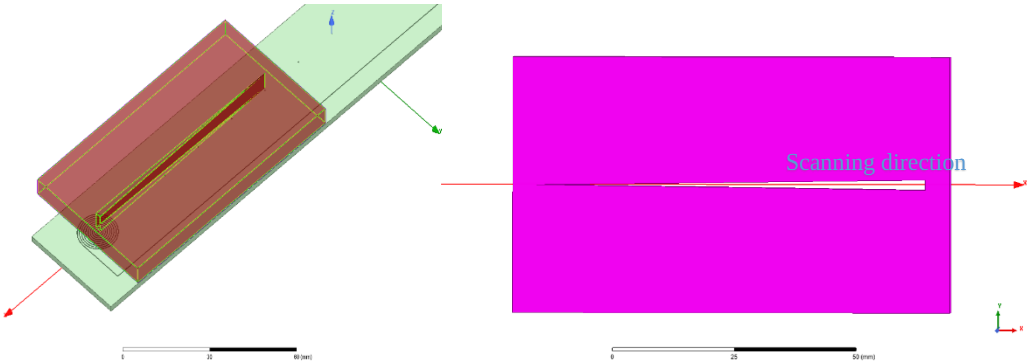

Figure 46: Simulation model for the width information study.

As shown in the figure, the size of the plate is 90 mm x 40 mm x 5 mm. The maximum width of the crack is 2 mm and the length of the crack is 80 mm. A coil sensor has been placed 1 mm away from the plate surface and moves along the positive X-direction.

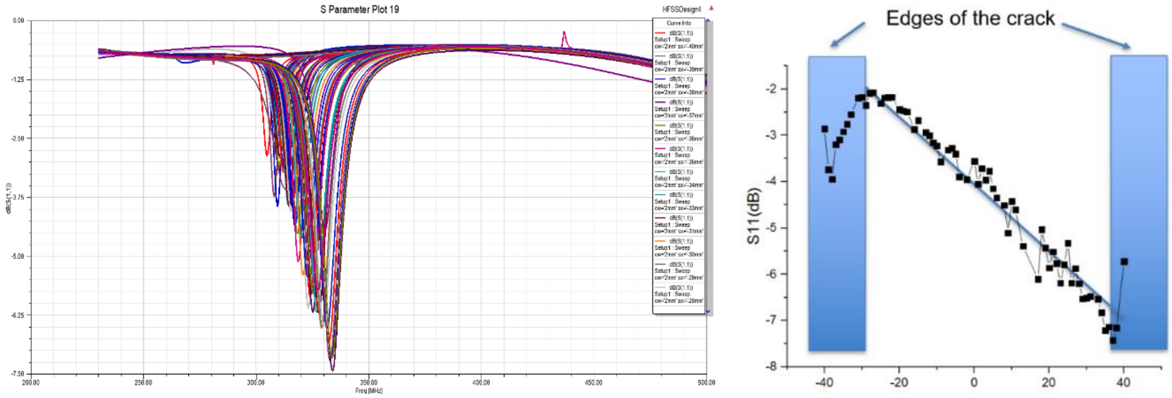

Figure 47: Simulation results for the width information study.

The S parameter simulation results are shown above. By extracting the magnitude of the resonant peak, a plot of the signal response at different location is shown above. A monotonically trend can be observed in the middle of the waveform as expected. The blue shaded parts are the data collected from the edge of the crack.

A similar model which studies the effect of the crack depth is shown below. A wedge-shaped notch with the depth changing from 5 mm to 0 mm. The simulation results of the sensor placed at different location of the notch are shown below.

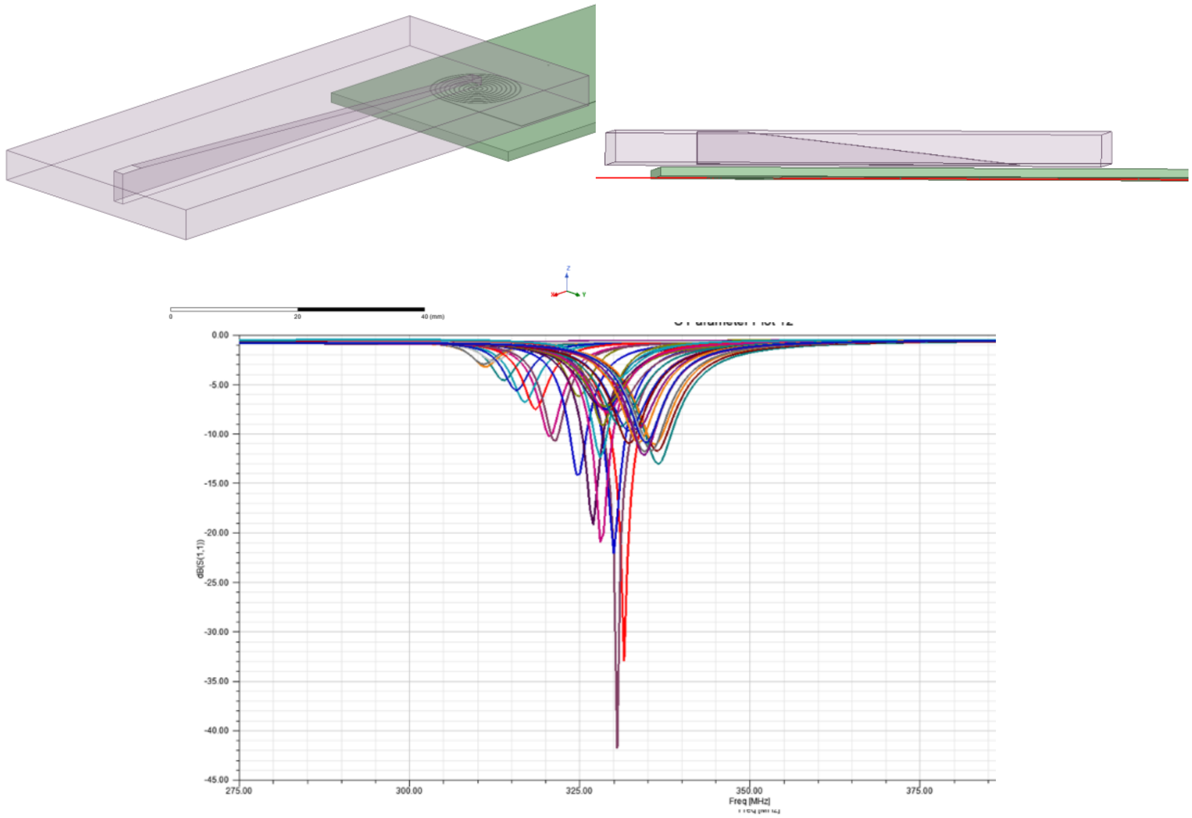

Figure 48: Simulation model for the depth information study.

During the scanning, the length of the cracks will also affect the signal. To study the relationship between the length of the crack and the signal, a steel plate with multiple cracks through hole has been simulated. These cracks are in same width and the length of them are from 20mm to 2 mm.

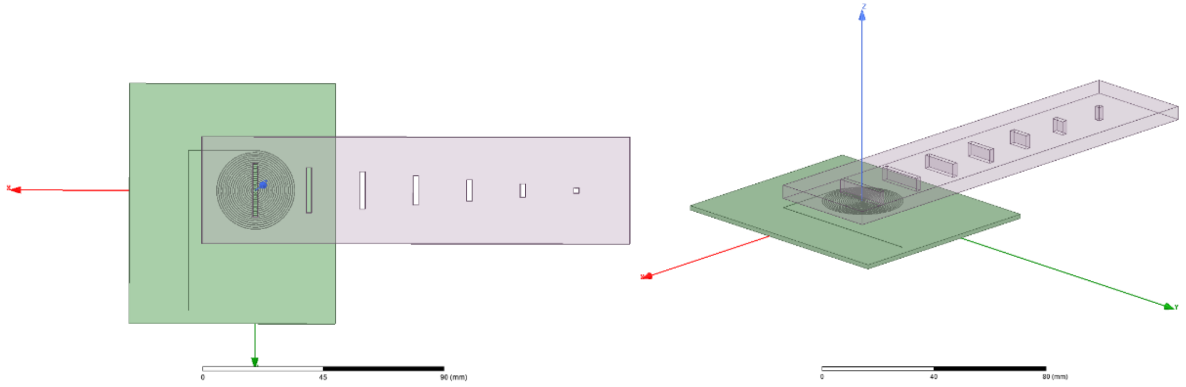

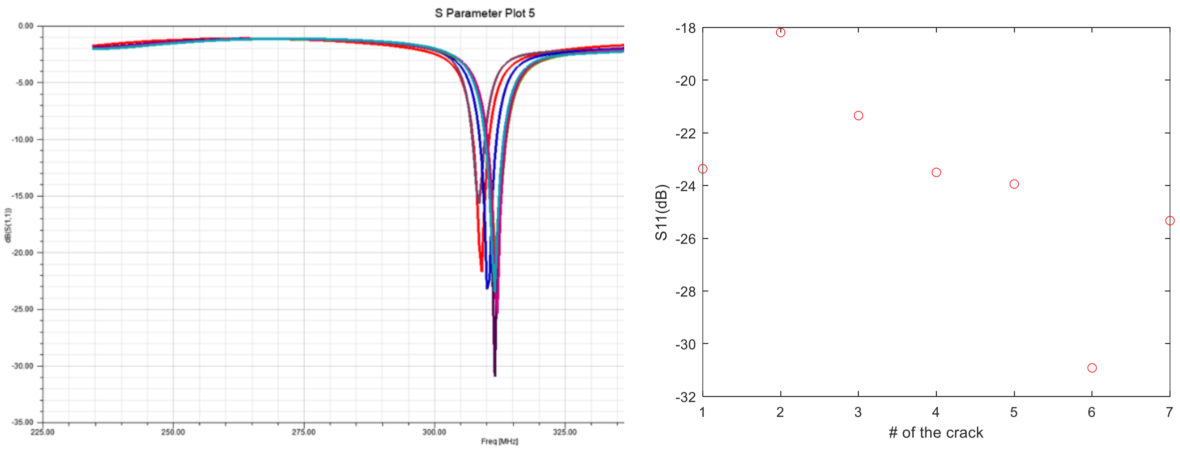

Figure 49: Simulation model and result for the length information study.

The model simulated signal when placing coil sensor on the top of each crack respectively. The plots of S11 parameter and the minimum magnitude of the resonant peak are shown above.

By clearing (removing some calculation error from the simulation) and organizing the simulation data from the models, several training data sets have been crated. An estimation error histogram of the new input data is shown below.

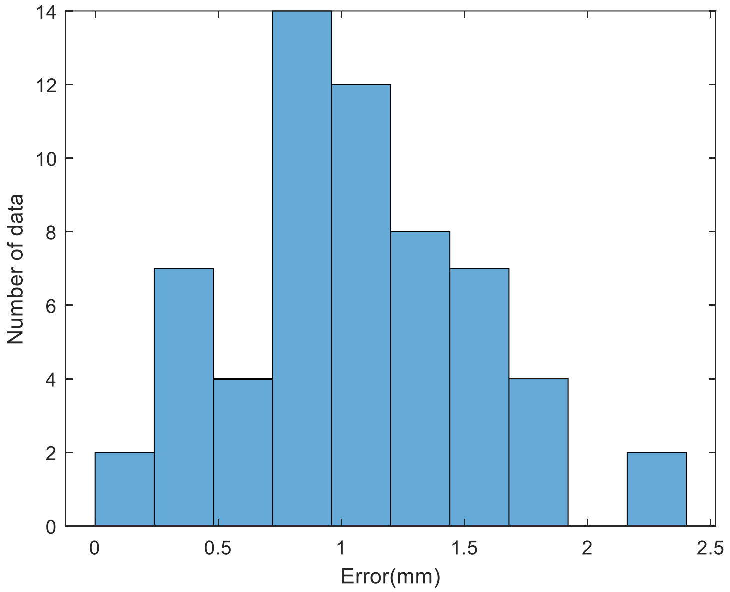

Figure 50: Estimation error for the simulation result.

The small circular coil has the advantage when s Scanning the shape of defect since it is able to provide a better resolution. When detecting the present of defect, a sensor with larger size will allow a better scanning speed since it cover larger scanning area. In this work, a coil with rectangular shape has also been studied.

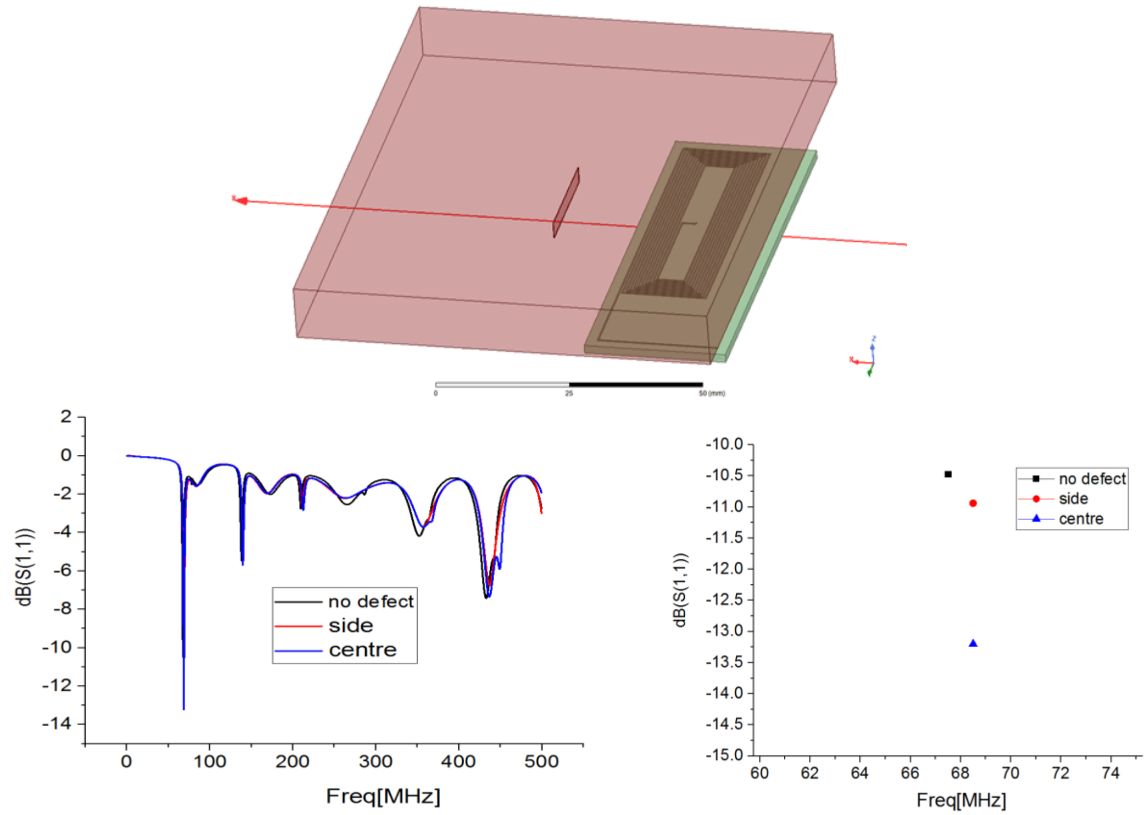

Figure 51: Simulation model and results of the rectangular shaped coil.

A crack with 0.1 mm width has been introduced to the steel plate in the model. The response signal of a rectangular coil has been simulated. The sensor has been placed at three different locations: health region, the side of the defect and on the top of the defect. When the sensor is on the top on the crack, both amplitude and phase change of the signal can be observed. The simulation results show the detecting ability of large rectangular coil and its potential to work as a complementary sensor of the circular coil.

B. Learning-Based Methods for Crack Depth Estimation

The raw signal obtained from sensor reflects the properties of the sample under test. However, the robot system needs to know the shape and location information of the cracks to perform the fixing procedure. In the previous work, several regression methods have been studied to extracting the cracks information from the raw signal. In order to improve the estimation accuracy, a machine learning approach has been studied in this work.

In recent years, more and more Neural Networks models have been developed and shown theirs promising potential in many areas. Recurrent Neural Networks architectures has shown its effective in dealing with sequential data like language recognition & processing[27-29], words sentiment analysis [30, 31], and signal processing. Several promising results and performance have been shown when Recurrent Neural Networks processing the long sequence of data.

In this project, the sensor on the robot will keep obtaining data of the scanning sample and a model that able to track the change of the signal will help the system to provide more accurate information of the defect on the sample.

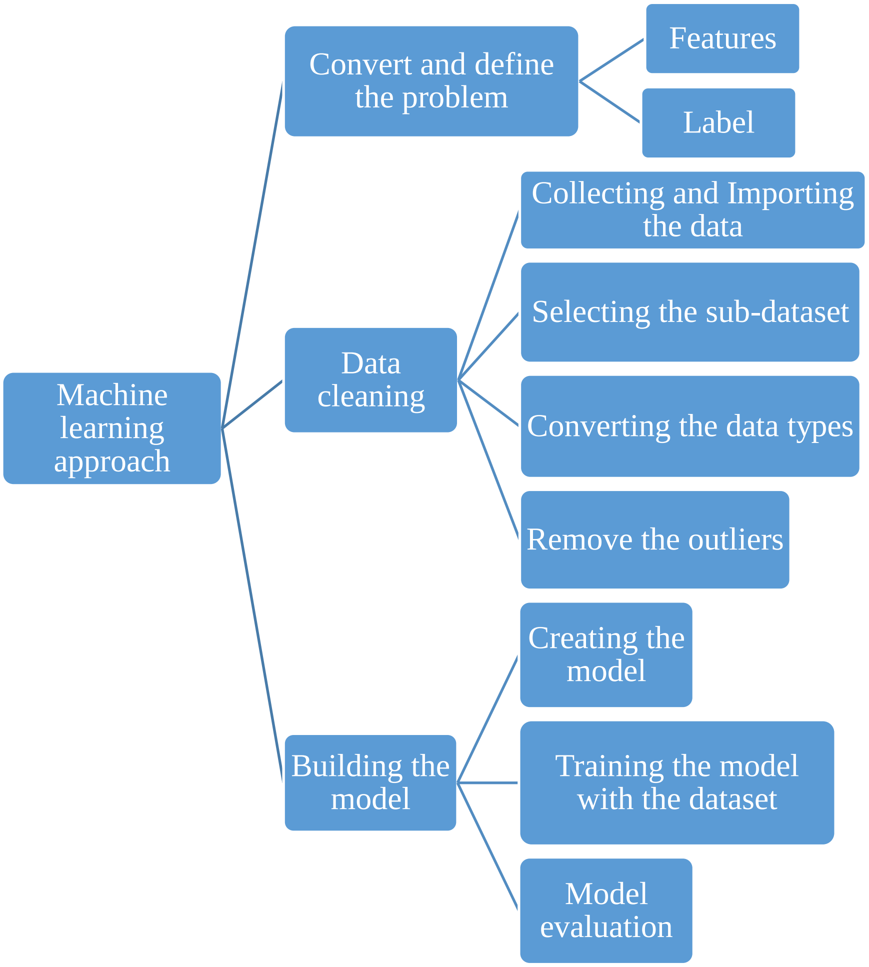

Figure 52: Flow chart of the proposed machine learning approach.

In order to achieve a better accuracy, the training time is usually very long for the large database with the data have complex internal structures which not only result in computational expense but also means that more parameters are to be learned and more structures need to be tuned. In order to reduce complexity of the model, some simplified methods are becoming more and more popular. The simple RNN train a black-box hidden state of their sequential data input. And the recurrent hidden state can be express [32]:

$$\boldsymbol{h_t = g(Wx_t + Uh_{t-1} + b)}$$

Bengio et al. [33] showed that the is difficult to training the model to remember the long-term relationship using this simple RNN. The long short-term memory (LSTM) model and its variants have been proposed by Hochreiter and Schmidhuber [34]. The standard LSTM is having 3 gates and 2 hidden states.

$$
\begin{gathered}
i_t = \sigma(W_i x_t + U_i h_{t-1} + b_i) \\
f_t = \sigma\left(W_f x_t + U_f h_{t-1} + b_f\right) \\
o_t = \sigma(W_o x_t + U_o h_{t-1} + b_o) \\
c_t = f_t \odot c_{t-1} + i_t \odot \tilde{c}_t \\
\widetilde{c}_t = g(W_c x_t + U_c h_{t-1} + b_c)
\end{gathered}
$$

One of the most famous variants of LSTM is GRU which provide desired accuracy with less structure.

$$
\begin{gathered}
h_t = (1 - z_t) \odot h_{t-1} + z_t \odot \tilde{h}_t \\
\tilde{h}_t = g(W_h x_t + U_h (r_t \odot h_{t-1}) + b_h) \\
z_t = \sigma(W_z x_t + U_z h_{t-1} + b_z) \\
r_t = \sigma(W_r x_t + U_r h_{t-1} + b_r)
\end{gathered}
$$

Different neural network methods have been designed and the tested to find the optimized structure. The networks model has been trained by a Python code which employ the Keras library with Theano as a backend. The GRU imported from Keras has been modified to GRU3. ReLU activation function is selected for all the databases.

In order to generate the data for training, a HFSS model has been designed and simulated. As shown in the figure, a steel plate with a crack at the center has been created as the sample. The size of the plate is 120 x 70 x 10 (mm) and the length of the crack is 50 (mm). The depth and the wide of the crack have been set as variables for the parametric study.

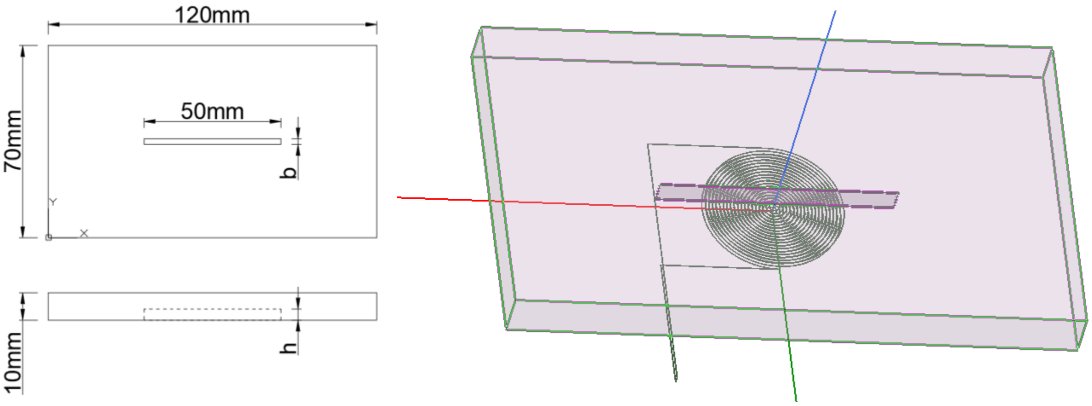

Figure 53: Schematic the steel plate model.

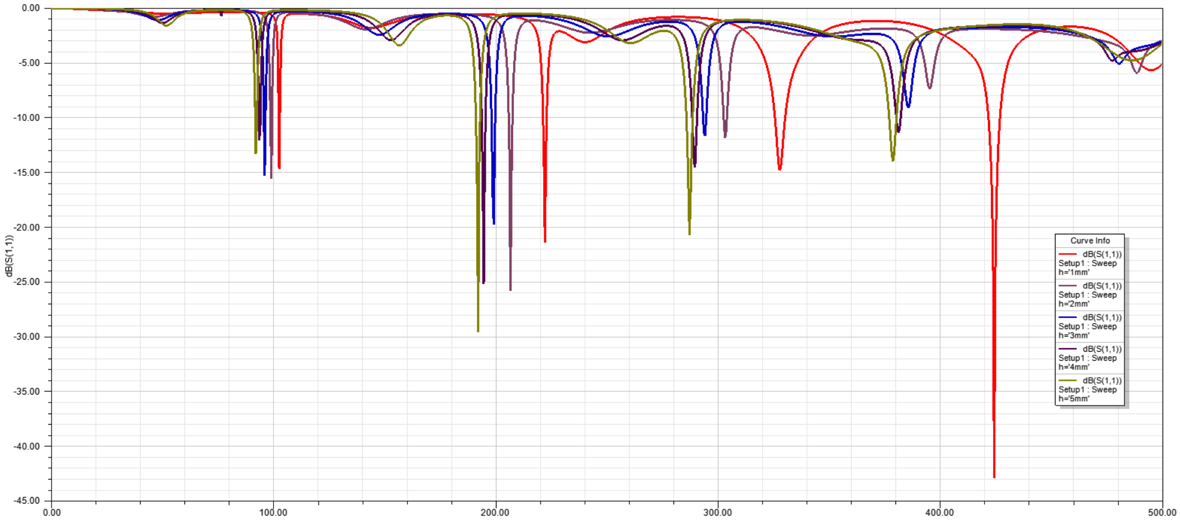

Figure 54: Simulation results of the cracks with different depth.

The training set of depth information have been generating from 0.1 mm to 5 mm with o.1 mm step size. The sensor has been placed on the top of the crack.

The data generated from the simulation needs to be convert to a dataset which includes features and labels to define the problem. The output labels in this problem are the actual depth/widths of the cracks. There are multiple parameters that can be used as the features, such as the resonant frequency, minimum magnitude, and phase change at the specific frequency. In this study, the model has been trained start from a simplified case: the first three resonant frequencies have been used as the input and the regression has been considered as a linear function. Therefore, the relationship of input and output can be written as:

$$y = f(x) = w_1 x_{fre1} + w_2 x_{fre2} + w_3 x_{fre3} + bias$$

The goal is to minimize the loss function which can be express as:

$$Loss = \sum_{i=1}^{n} |wx_i + bias - y_i|$$

The estimation results are shown below:

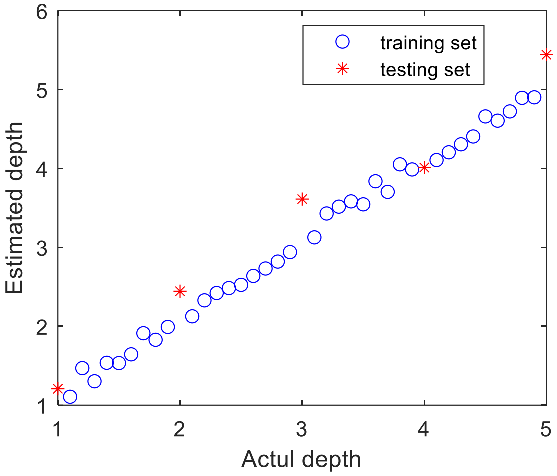

Figure 55: Depth estimation for the training set and testing set.

To further improve the accuracy of the model, more scanning data have been generated with different combination of depth and width of the crack.

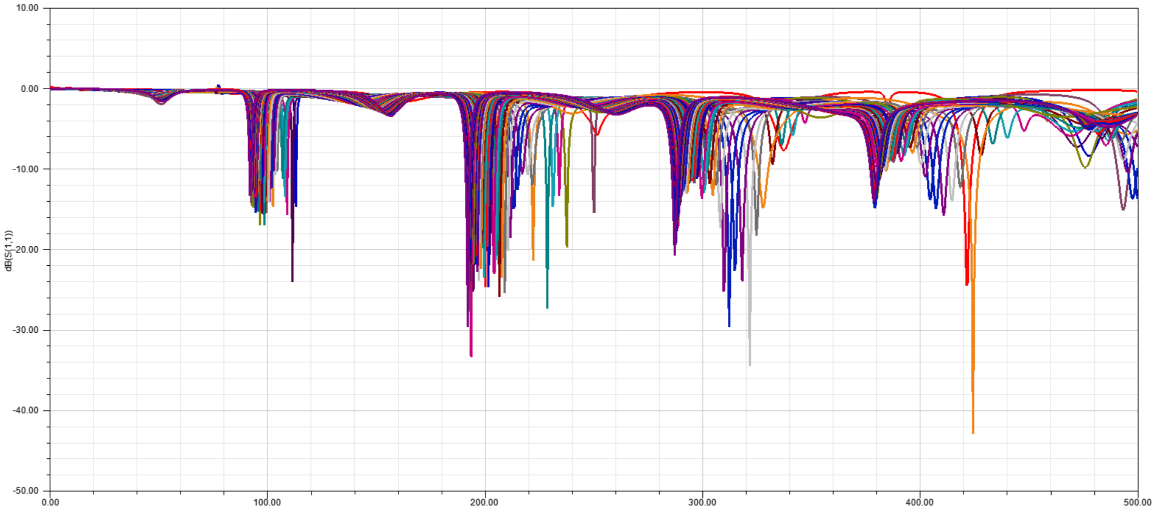

Figure 56: Simulation results of the cracks with different depth and width.

The training and testing accuracy has been shown in the figures below. As the training process repeated, the training accuracy shows an increasing trend while the testing accuracy is fluctuating. These might due to the parameters selection and also the size of the database of the model which result in an overfitted.

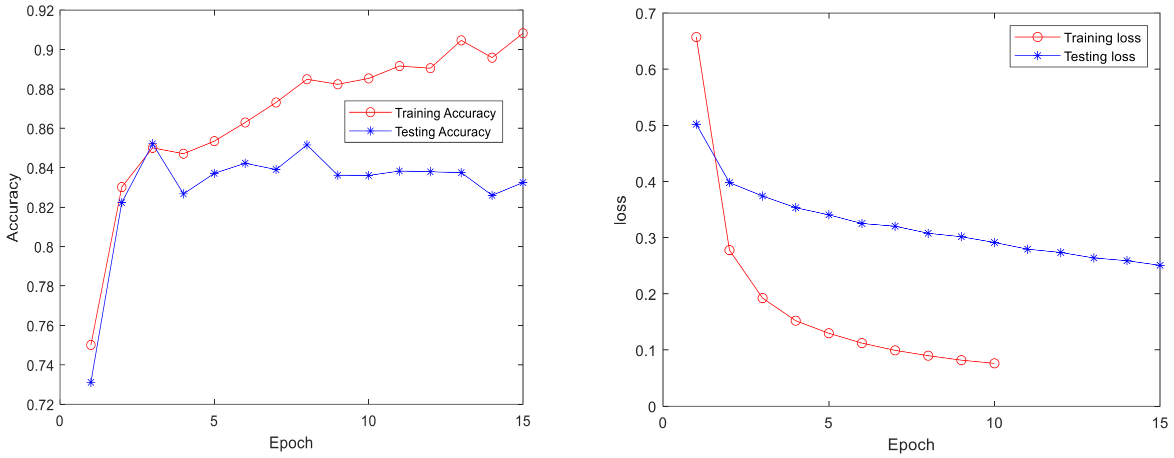

Figure 57: Training/testing accuracy and loss of GRU3 with different number of epochs.

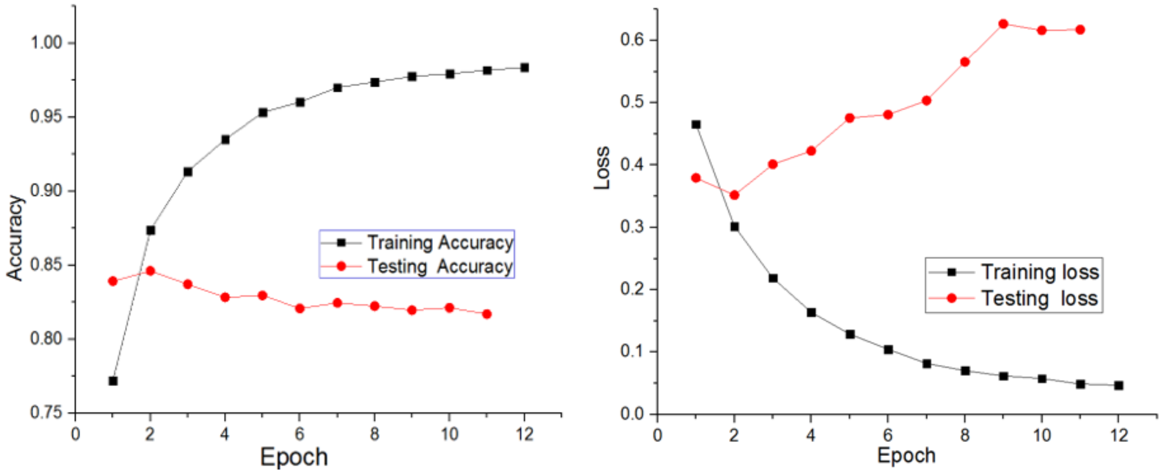

Figure 58: Training/testing accuracy and loss of LSTM with different number of epochs.

2. Task 2: Repair Device Design and Control

A repair tool based on friction stir welding (FSW), one of the solid-state repair methods, was designed. By augmenting FSW with an induction heating unit, the demand for spindle torque and forging loads can be significantly reduced, enabling FSW to be used as a compact repair tool.

2.1. Subtask 2.1: Integrated IHA-FSW System

2.1.1. Literature Review

A. FSW Baseline Parameters

First of all, literature search on typical FSW parameters without involving any preheating methods for various grades of steels were performed to establish the baseline welding parameters for the repair of boiler furnish wall steel and identify the required force as a function of welding parameters. Tables 2-4 below summarize the findings related to stainless steels (Table 2) [34-43], low carbon steels (Table 3) [44-48], and others (Table 4) [49-52].

Table 2: The FSW parameters for various grades of stainless steels.

Steel grades	Tool material	Pin length (mm)	Pin diameter (mm)	Shoulder diameter (mm)	Plunge depth (mm)	Tilt angle (°)	Rotation speed (r/min)	Travel speed (mm/min)	Vertical force (kN)
304 [34]	WC*	2.3	3.5	20	2.3	1.45	1000	63	
304 [35]	PCBN**					3.5	550	78	
304 [36]	tungsten alloy			19			300 500	102	31
304 [37]	PCBN		10	15	2.4	0	500	120	16
							800	120	14
304 [38]			6	25			300	51	25
304 [39]	WC	2.75	7	12	0.4	1.5	285	53	10
				14			355	66	10
				16			450	84	10
304 [40]	WC-Co	2.8	5			2	1180	47.5	7
430 [41]	WC-Co	pinless			0.2	2	900	96	
430 [42]	WC	2.5	5.7	16		0	1120	125	3.5
410 [43]	PCBN	3.7	9.2	25		0	450	60	20
							800	60	22

*WC: tungsten carbide; **PCBN: polycrystalline cubic boron nitride.

Table 3: The FSW parameters for low carbon steels.

Steel grades	Tool material	Pin length (mm)	Pin diameter (mm)	Shoulder diameter (mm)	Tilt angle (°)	Rotation speed (r/min)	Travel speed (mm/min)	Vertical force (kN)
AISI 1006 [44]	WC-based	2				1200	60	
1018 steel [45]	W-based	6.22		19	0	450-650	25.2-100.8	
IF steel [46]	WC	1.4	4	12	3	400	100	
1012 steel [46]	WC	1.4	4	12	3	400	100	
C–Mn 1018 steel [47]	W–0.4Re	6.22	7.9, 9.0	15, 18, 21, 24	0	300-900	25.2-126	11.6-29.8
AISI 1018 [48]	Tungsten	6.22	7.9	19	0	450	25.2	5

Table 4: The FSW parameters for other kinds of steels.

Steel grades	Tool material	Pin length (mm)	Pin diameter (mm)	Shoulder diameter (mm)	Plunge depth (mm)	Tilt angle (°)	Rotation speed (r/min)	Travel speed (mm/min)	Vertical force (kN)
X-65 [49]	PCBN	5.6					500-600	101.6-152.4	28.913
1035 [46]	WC	1.4	4	12		3	400	100	
1070 [50]	WC	1.5	4	12		3	800	400	
TRIP [51]	WC	1.9			2	0	1350	15	5
DH36 [52]	W-Re	5.7		36.8	2.5	0	500	250	40

B. FSW Force Requirements

Figure 59(a) below illustrates the vertical force profile corresponding to the FSW process at different stages [43], including (1) plunging, (2) traveling, and (3) tool retracting. Figure 59(b) illustrates that the plunging step requires the highest axial force, i.e., vertical force, during the welding process.

Based on the limited data available, it was found out that the vertical force is generally the largest forced experienced by the FSW tool. As demonstrated in Table 5 and Figure 60, the longitudinal force (F_x) is typically less than 20% of the vertical force (F_z) [53]. Also, among the three FSW parameters including travel speed, rotation speed and the pitch value, the FSW tool travel speed seems to be the dominant factor that determines the force requirements. On the other hand, J. H. Record et al. [54] performed a comprehensive study on the effect of all sorts of welding parameters on vertical force during friction stir welding process, as summarized in Figure 61. It was found out that plunge depth is the most critical factor that determines the vertical force, while rotation speed is the least.

Table 5: The FSW parameters for X80M steel.

Run No.	v(mm/min)	ω(rpm)	v/ω	F_x(N)	F_z(N)	F_x/F_z
1	100	500	0.20	3581	29778	0.12
2	100	350	0.28	3661	32848	0.11
3	100	300	0.33	3877	31893	0.12
4	80	400	0.20	2120	25864	0.08
5	80	300	0.26	2251	26352	0.09
6	120	400	0.30	3611	28242	0.13
7	120	300	0.40	4865	35798	0.136

v-Travel speed; ω-Rotational speed; F_x-Longitudinal force; F_z-Vertical force.

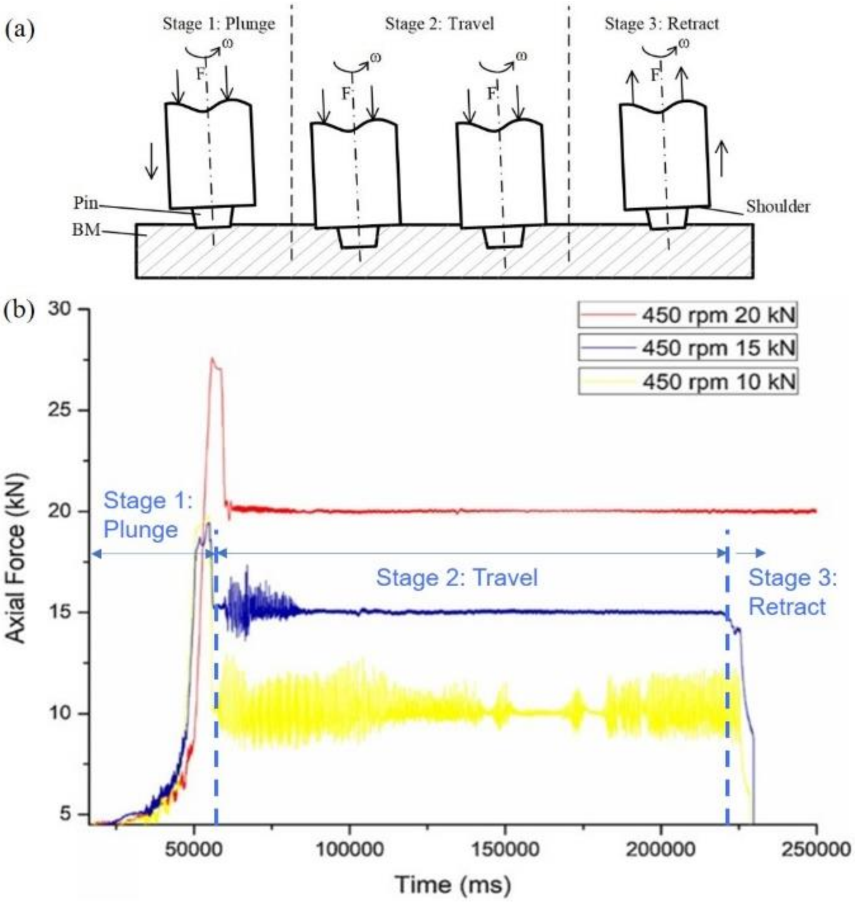

Figure 59: (a) Schematic drawing of the FSW process, and (b)the corresponding vertical force.

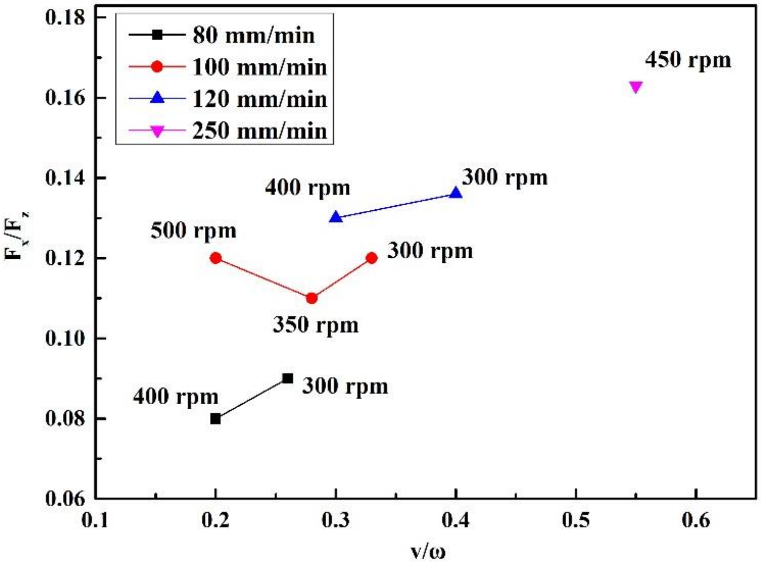

Figure 60: Fx/Fz as a function of v/ω for FSW steel.

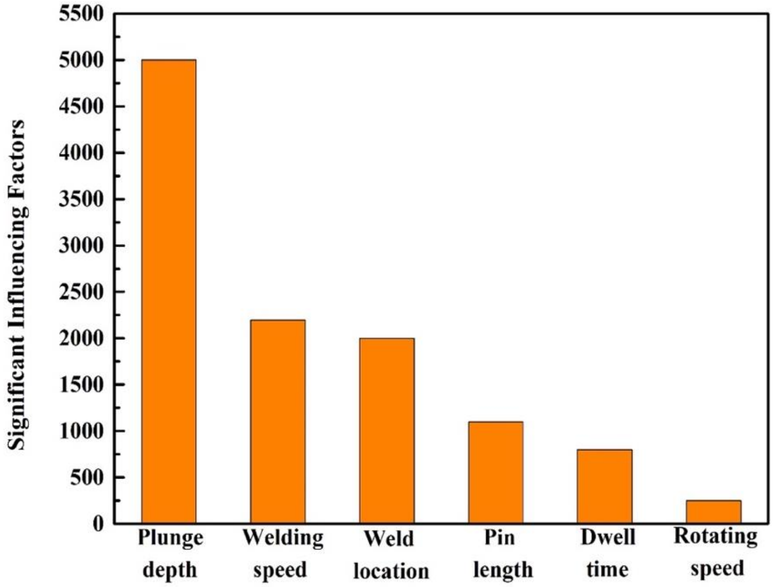

Figure 61: Pareto charts of effects of experimental inputs on the vertical force.

In order to maximize the mobility of the repair robot, a significant force/power reduction is desired (i.e., controlled within 3kN for a plunge/repair depth up to 3mm), especially at the initial plunging stage. Previous studies have demonstrated a reduction of ~30% in vertical forces for FSW of steels with the aid of induction-heating (IH) during the traveling stage, as tabulated in Table 6 [55, 56]. However, little to no literature can be found in optimization of the preheating parameters to reduce the force requirement in plunging stage to/near the level of traveling stage, which will the one of objectives in this work.

Table 6: The FSW parameters with induction heating (IH) for steels.

Steel	Tool material	Pin length (mm)	Pin Dia. (mm)	Shoulder diameter (mm)	Tilt angle (°)	Rotation speed (r/min)	Travel speed (mm/min)	Power of induction coil (kW)	Vertical force without IH (kN)	Vertical force with IH (kN)
ASTM A131 [55]	PCBN	5	8.9	23.7	0	500	50	40	36	25
Super duplex stainless [56]	PCBN	5	8.9	23.7	0	300	100	40	25	18

2.1.2. IHA-FSW System Design

A. FSW Trials with and without Preheating

Two sets of FSW experiments were performed using a pin length of 2.3mm, with and without preheating using a tungsten inert gas (TIG) welding torch. The effectiveness of force reduction by TIG preheating was evaluated preliminarily based on the recorded vertical force values.

Base Material for FSW:

Low carbon steel grade A108 was used for all the experiments. Note that the boiler water wall material is A106, but A106 is only available in pipe shape. Therefore, at this stage, we chose A108 in plate format instead for initial welding parameter evaluations. The geometric dimensions of A108 steel plates are 0.5inch thick, eight-inch wide and one-feet long. The chemical composition (wt%) of A108 steel is listed in Table 7.

Table 7 - Chemical Composition (in wt%) of A108 steel.

Steel grade	C	Mn	Si	P	S
A108	0.13-0.20	0.60-0.90	0.15-0.30	0.035	0.035

Experimental Procedure:

For FSW experiments without a preheating source, in order to reduce the tool wear, a 2.3mm deep hole with a diameter of 5mm was drilled on the top surface of the steel plate, which serves as the initial plunging hole. The geometry of the FSW tool is shown in Figure 62. Note that different pin length will be used in future study, including 1mm and 0mm.

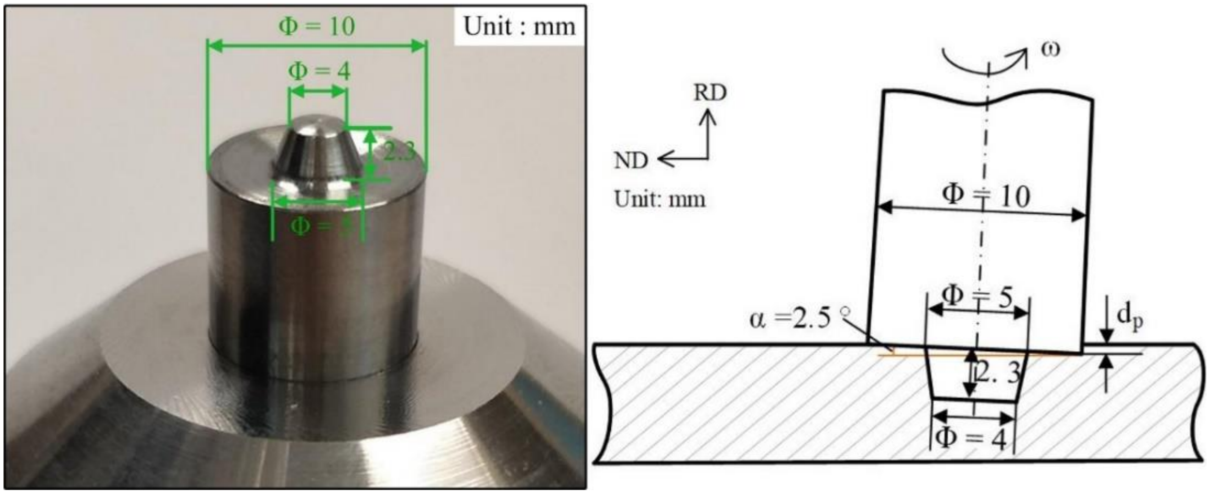

Figure 62: The schematic diagram of the tool geometric dimensions.

Figure 63: The physical diagram of the new tool holder.

In the first set of experiments including six runs, a tool holder without a cooling system was used. In all later experiments, a new tool holder with a proper cooling system was used to ensure safer long runs at high temperatures introduced by the FSW of steel plates. As shown in Figure 63, the tool holder is equipped with a cooling system and argon shielding gas was used to prevent oxidation in the steel plates during FSW. The parameters for FSW without and the corresponding vertical force during the traveling stage are tabulated in the Table 8 and Table 9. Since the welding parameters were varied to reveal their effects on the vertical forces, the weld surface quality is not yet optimized.

Table 8: Parameters for FSW without preheating before changing the tool holder.

Run No.	Rotation speed (rpm)	Travel speed (mm/s)	Plunge Depth (mm)	Tool materials	Pin length (mm)	Shoulder diameter (mm)	Tilt angle (°)	Vertical Force (kN)
1	400	50	1.00	W-Re	2.3	10	2.5	12.1
2	400	40	0.69	W-Re	2.3	10	2.5	8.5
3	400	40	0.59	W-Re	2.3	10	2.5	6.7
4	400	60	0.55	W-Re	2.3	10	2.5	5.7
5	400	60	0.34	W-Re	2.3	10	2.5	3.5
6	400	80	0.31	W-Re	2.3	10	2.5	3.1

Table 9: Parameters for FSW without preheating after changing the tool holder.

Run No.	Rotation speed (rpm)	Travel speed (mm/s)	Plunge Depth (mm)	Tool materials	Pin length (mm)	Shoulder diameter (mm)	Tilt angle (°)	Vertical Force (kN)
7	400	80	0.52	W-Re	2.3	10	2.5	5.2
8	400	80	0.45	W-Re	2.3	10	2.5	4.9
9	400	80	0.60	W-Re	2.3	10	2.5	5.8

Figure 64 illustrates a schematic drawing of the FSW process assisted by preheating. The relative distance between the welding tool and preheating source and the heat input introduced by preheating will be optimized through finite element modeling in future. Currently, a Miller TIG welding machine was used as the preheating source. As shown in Figure 65, this preheating unit was equipped with a cooling system and argon shielding gas. The TIG welding torch was fixed in front of the FSW tool, as shown in Figure 65. The relative distance between the welding torch and FSW tool head can be adjusted along all three dimensions. As an initial trial, the arcing height and distance between the TIG torch and the rotating tool were selected to be 4mm and 30mm, respectively. In order to avoid overheating during welding, the experiment was firstly carried out at relatively low TIG current of 25A. The TIG welding machine was firstly turned on, the welding torch was arced by the arc initiation of a carbon rod. Once the arc became stable, the pin rotating at 400 rpm plunged into the pre-drilled hole and stayed for five seconds to generate sufficient heat to soften the base metal. Then the pin began to travel at a set speed. All experiments were carried out under argon shielding gas. Welding parameters used in this set of experiments are summarized in Table 10.

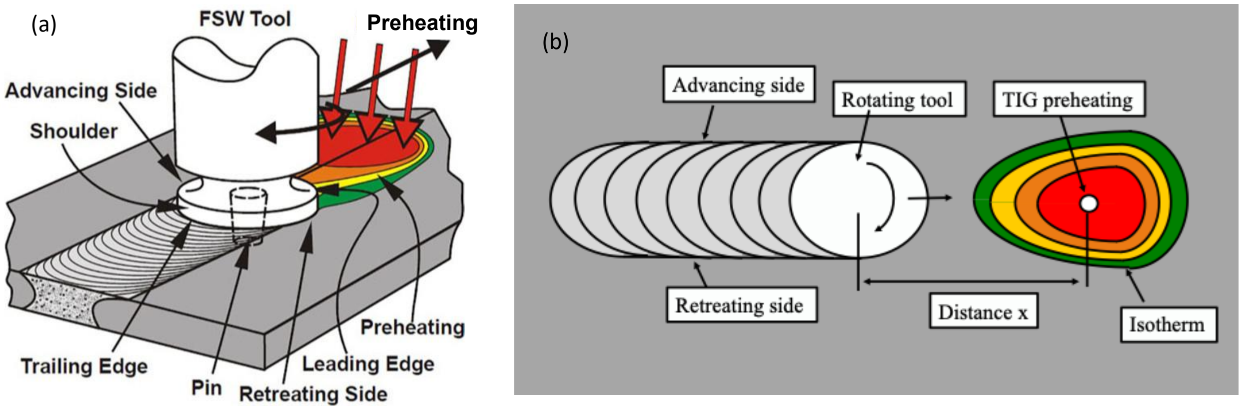

Figure 64: Schematic diagram of friction stir welding process with preheating: (a) perspective view and (b) top view.

Figure 65: The TIG preheating setup.

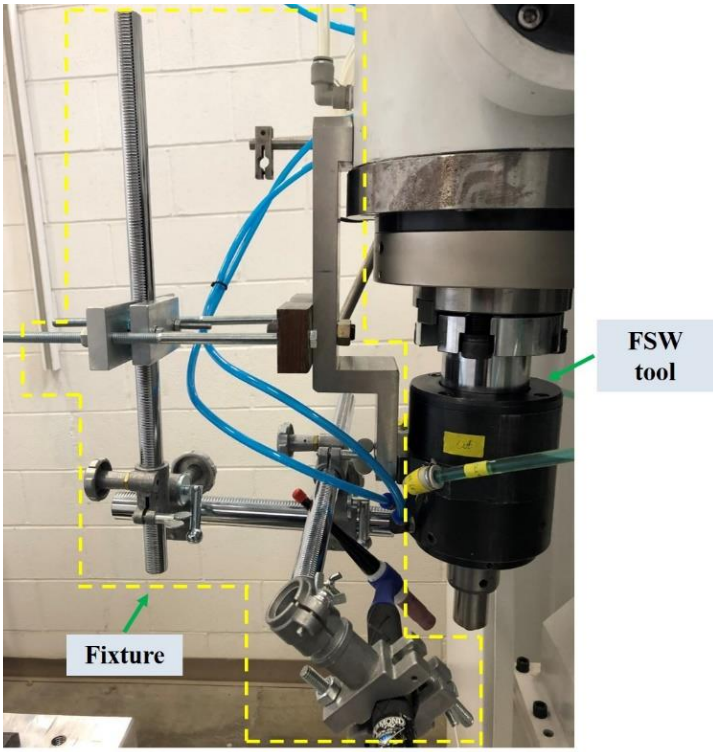

Figure 66: Mounting fixture for TIG torch in front of the FSW tool head.

Table 10: Experimental parameters for FSW with preheating after changing the tool holder.

Run No.	Rotation speed (rpm)	Travel speed (mm/s)	TIG current (A)	Plunge Depth (mm)	Tool materials	Pin length (mm)	Shoulder diameter (mm)	Tilt angle (°)	Vertical Force (kN)
10	400	80	25	0.55	W-Re	2.3	10	2.5	3.7
11	400	100	25	0.52	W-Re	2.3	10	2.5	3.9
12	400	100	20	0.50	W-Re	2.3	10	2.5	4.3

Initial Results and Discussion:

In the FSW welding experiments without preheating, keeping the travel speed and rotational speed constant, the effect of plunge depth on the vertical force was revealed by manually adjusting the plunge depth. Comparison of Sample No. 4 vs No.10, and Sample No. 7 vs No.11 were also made, to partly reveal the effect of preheating on force reduction as an initial evaluation, since each pair has the same plunge depth. As discussed in Section 1.2, plunge depth is the determining factor for vertical force.

Figure 67 summarizes the variation of vertical force as a function of the plunge depth in the first six experiments using the tool holder without a cooling system, and Figure 68 for these using the new tool holder with a cooling system. It can be seen that without preheating, the vertical force decreased with the decreasing plunge depth, although the travel speed was constantly adjusted to identify the optimal parameters for best weld appearance. The minimum vertical force was about 3.1kN.

Furthermore, by introducing TIG preheating, the vertical force of No. 10 and 11 decreased by about 25-30% in comparison with that of No. 4 and 7, which is in good agreement with the observations in literature [55, 56]. It should be noted that with the involvement of preheating, the plunge depth does not seem to be the most influential factor on the vertical force anymore, as seen in Table 10. This could be possibly caused by a deeper penetration of the TIG torch than the FSW tool pin. Instead, the influence of travel speed seems to be more significant. More systematic studies will be performed to provide more insights for such observation.

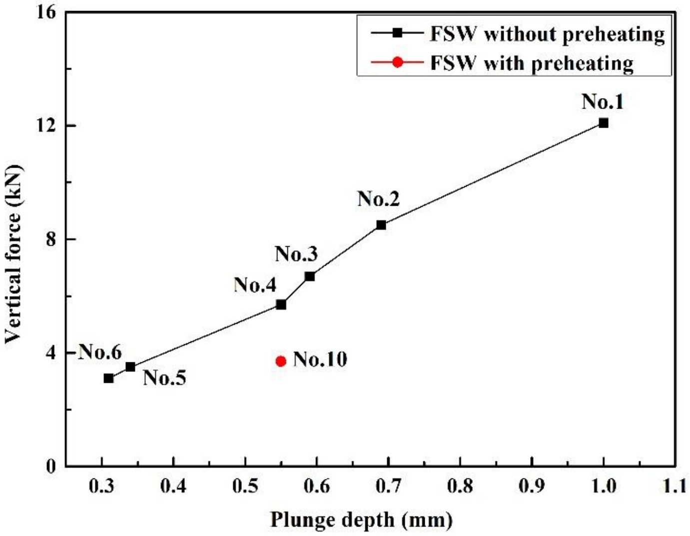

Figure 67: The variation of vertical force with the plunge depth for the No.1-6 and 10 experiments.

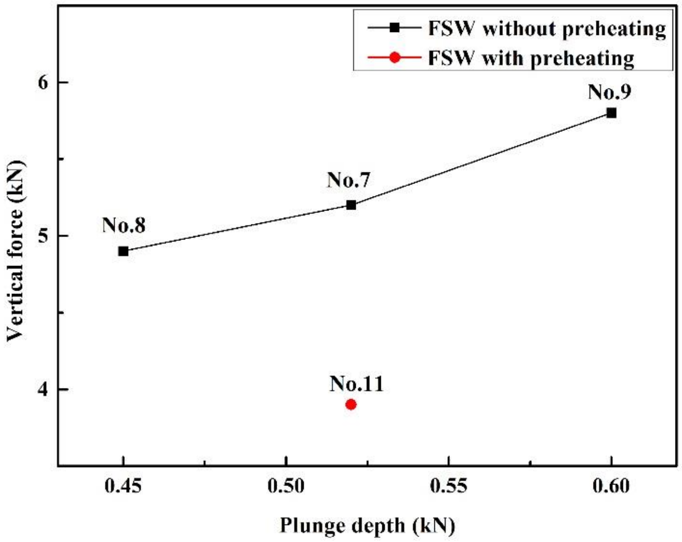

Figure 68: The variation of vertical force with the plunge depth using the tool holder with a cooling system

The set of experiments used pre-drilled holes to minimize tool wear, which required a larger plunge depth to maintain a defect-free weld. In future work, the pre-drilled holes will be eliminated to improve the weld surface quality, reduce plunge depth, and thus further reduce the vertical force.

B. Heat Analytical Modeling during FSW Process

A large amount of FSW parameters for various types of steel had already been obtained from the literature review and the experimental studies of this project. However, the experimental conditions for each study are different, so the collected parameters could only be used for specific case study. Therefore, it is necessary to understand the relation between FSW parameters (including rotational speed, travel speed, pin and shoulder geometry, preheating etc.) and power requirement (e.g., torque and vertical force), and more importantly, establish expressions that can connect all the inputs and outputs. The established correlation will provide guidance for the selection and optimization of welding parameters and predict the required power.

By establishing a heat analytical model, the input (e.g., rotational speed, travel speed, tool geometry etc.) and output parameters (e.g., vertical force) are well connected. By comparing the experimental results with the calculated results using the model, it is found that this analytical model has reasonable reliability. The stand construction was also successfully completed.

B.1. The total heat generation of the tool

We first build the analytical model of steady-state during FSW process. The total heat generation of the tool during the steady-state contains the heat generation of the shoulder, the pin side and pin head, as expressed below:

$$Q_{tool} = Q_{shoulder} + Q_{pin\_side} + Q_{pin\_bot}$$

where Q_{tool} is the total frictional heat generation of the welding process between workpiece and tool surface profile, $Q_{shoulder}$, Q_{pin_side} and Q_{pin_bot} are the heat generations from shoulder bottom surface, pin side and pin bottom surfaces, respectively.

Heat generation of shoulder:

Figure 69(a) shows the bottom view of the shoulder, which is the ring region between R_2 and R_1. It is assumed that the vertical force is applied uniformly to the shoulder and does not change with the radius r_1. In this figure, r1 is the radius of any rings on shoulder bottom surface, and dr1 is the infinite small radius increase from this ring; (b) Side view of the tool., r2 is the radius of micro-circular truncated cone in side surface, ds is the side length of the micro-circular truncated cone, dh is the vertical length of the micro-circular truncated cone, h is the distance between the micro-circular truncated cone, H is the pin length, and α is the angle between pin side and vertical direction.

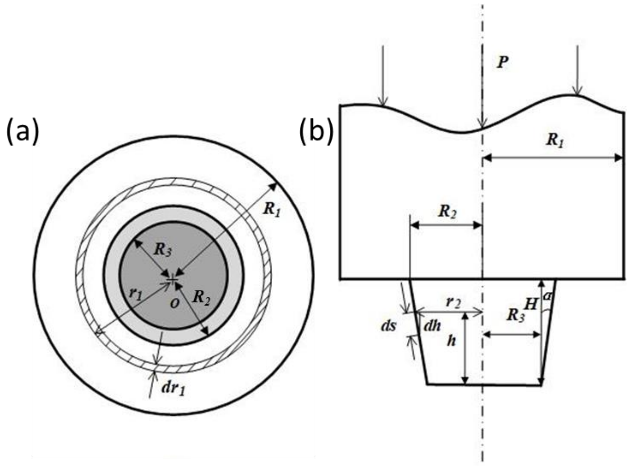

Figure 69: Schematic diagram of the tool: (a) Bottom view of the tool. R1, R2 and R3 are the radius of shoulder bottom surface, pin top surface and pin bottom surface respectively.

The frictional force on the micro-ring with radius r_1 and width dr_1 is [57]:

$$df = \mu F = \mu P dA = \mu P \cdot 2\pi r_1 dr_1$$

where μ is the friction coefficient ($\mu = 0.4$) [58], P is the vertical pressure(Pa), dA is the area of the micro-ring (m^2), r_1 is the radius of the micro-ring (m), dr_1 is the width of the micro-ring (m), and df is the frictional force (N). Thus, the torque dM ($N \cdot m$) on micro-ring can be written as [59]:

$$dM = r_1 df = 2\pi P \mu {r_1}^2 dr_1$$

The total torque of the shoulder $M_{shoulder}$ ($N \cdot m$) is then obtained by integrating dM:

$$M_{shoulder} = \int_{R_2}^{R_1} dM = \int_{R_2}^{R_1} 2\pi P \mu {r_1}^2 dr_1 = \frac{2\pi \mu P (R_1^3 - R_2^3)}{3}$$

Heat generation of the shoulder in unit time $q_{shoulder}$ (J/s) can be obtained by multiplying angular velocity ω and torque [60, 61]:

$$q_{shoulder} = \omega M_{shoulder} = \frac{2\pi \omega \mu P (R_1^3 - R_2^3)}{3}$$

Assuming the rotating tool travel forward a micro-distance dl (m) at a certain speed v (m/s), the heat generation from the tool shoulder during this time period can be written as:

$$Q_{shoulder} = q_{shoulder} \times \frac{dl}{v} = \frac{2\pi \omega \mu P (R_1^3 - R_2^3)}{3} \times \frac{dl}{v}$$

Heat generation of the pin side:

The shape pin side is a circular truncated cone, whose cone angle is 2α, where α is the angle between pin side and vertical direction (°), As shown in Figure 69(b). The side area of the micro-circular truncated cone *dA* is:

$$dA = 2\pi r_2 ds$$

where r_2 (*m*) and *ds (m)* are radius and side length of the micro-circular truncated cone, respectively. *ds* can be written as:

$$ds = \frac{dh}{\cos\alpha}$$
$$r_2 = R_3 + h\tan\alpha$$

where *dh* is the vertical length of the micro-circular truncated cone (*m*), R_3 is the radius of the pin bottom surface (*m*), *h* is the distance between the micro-circular truncated cone and the pin head (*m*). Then, side area of micro-circular truncated cone *dA* is:

$$dA = \frac{2\pi(R_3 + h\,tan\,\alpha)dh}{\cos\alpha}$$

The side area A_{side} (m^2) of the pin can be integrated as:

$$A_{side} = \int_0^H \frac{2\pi(R_3 + h\tan\alpha)}{\cos\alpha} dh = \frac{2\pi R_3 H}{\cos\alpha} + \frac{2\pi\tan\alpha}{\cos\alpha} \cdot \frac{H^2}{2}$$

In Figure 69(b), the pressure on the side and bottom of the pin, and the bottom of the shoulder are all assumed to be P_1. The balance of the forces in the vertical direction is as follows:

$$P_1 \pi R_3^2 + P_1 \pi (R_1^2 - R_2^2) + P_1 A_{side} \sin\alpha = P\pi R_2^2$$

where *P* is the pressure applied to the tool (*Pa*). It turns out that $P_1 = P$.

The frictional force acting on the micro-circular truncated cone is [57]:

$$df = \mu P_1 dA = \mu P dA$$

Then the torque on micro-circular truncated cone *dM* becomes [59]:

$$dM = r_2 df = \frac{2\pi\mu P \tan(R_3 + h\tan\alpha)^2 dh}{\cos\alpha}$$

And the total torque of the pin side M_{pin_side} (*N·m*) can be integrated as:

$$M_{pin_{side}} = \int_0^H dM = \int_0^H \frac{2\pi\mu P \tan(R_3 + h\tan\alpha)^2 dh}{\cos\alpha}$$

$$= \frac{2\pi\mu PH}{3\cos\alpha}(3R_3^2 + 3R_3H\,tan\,\alpha + H^2\tan^2\alpha)$$

So the heat generation of the pin side q_{pin_side} in unit time is [60, 61]:

$$q_{pin\_side} = \omega M_{pin\_side} = \frac{2\pi\mu\omega PH}{3\cos\alpha}(3R_3^2 + 3R_3H\tan\alpha + H^2\tan^2\alpha) = \frac{2\pi\omega\mu P(R_2^3 - R_3^3)}{3\sin\alpha}$$

where ω is angular velocity of the tool (*rad/s*).

Therefore, when the rotating tool travel forward a micro-distance dl (*m*) at a certain speed v (*m/s*), the total heat generation from the pin side during this time period will be

$$Q_{pin\_side} = q_{pin\_side} \times \frac{dl}{v} = \frac{2\pi\omega\mu P(R_2^3 - R_3^3)}{3\,sin\,\alpha} \times \frac{dl}{v}$$

Heat generation of the pin head:

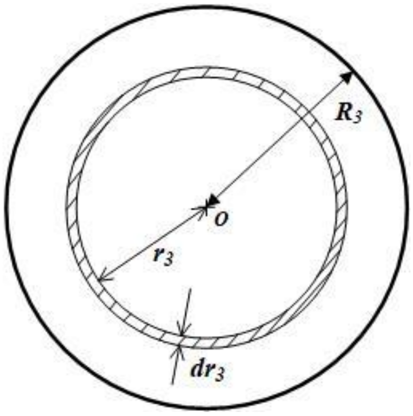

Figure 70: Schematic diagram of the pin bottom surface.

Similar to the bottom surface of shoulder, the heat generation of the bottom surface of pin can be analyzed as follow. The frictional force df (*N*) on the micro-ring with radius r_3 and width dr_3 is [57]:

$$df = \mu F = \mu PdA = \mu P \cdot 2\pi r_3 dr_3$$

where μ is the friction coefficient, P is the vertical pressure stress (*Pa*), dA is the area of the micro-ring (m^2), r_3 is the radius of the micro-ring (*m*), and dr_3 is the width of the micro-ring (*m*).

Thus, the torque on micro-ring dM (*N·m*) is [59]:

$$dM = r_3 df = 2\pi P\mu {r_3}^2 dr_3$$

The torque of the pin bottom M_{pin_bot} (*N·m*) is integrating as:

$$M_{pin\_bot} = \int_{R_2}^{R_1} dM = \int_{R_2}^{R_1} 2\pi P\mu {r_3}^2 dr_3 = \frac{2\pi\mu P R_3^3}{3}$$

The heat generation of the pin bottom in unit time can be obtained by multiplying angular velocity by torque [60, 61]:

$$q_{pin\_bot} = \omega M_{pin\_bot} = \frac{2\pi\omega\mu P R_3^3}{3}$$

When the rotating tool travel forward a micro-distance *dl* (*m*) at a certain speed *v* (*m/s*), the heat generation from the pin bottom surface during this time period will be:

$$Q_{pin\_bot} = q_{pin\_bot} \times \frac{dl}{v} = \frac{2\pi\omega\mu P R_3^3}{3} \times \frac{dl}{v}$$

To sum up, the total heat generation Q_{tool} during the time period of *dl/v* is:

$$Q_{tool} = \left(\frac{2\pi\omega\mu P (R_2^3 - R_3^3)}{3 \sin\alpha} + \frac{2\pi\omega\mu P R_3^3}{3} + \frac{2\pi\omega\mu P (R_1^3 - R_2^3)}{3} \right) \times \frac{dl}{v}$$

B.2. Heat input in the stir zone

The heat required to raise a homogeneous substance to a certain temperature is [62]:

$$\Delta Q = C_p \times m \times \Delta T$$

where ΔQ (*J*) is the amount of heat needed to uniformly raise the temperature of the substance by ΔT (*K*), C_p ($J \cdot kg^{-1} \cdot K^{-1}$) is the specific heat capacity of the substance, *m* (*kg*) is the mass of the substance.

Assuming the rotating tool travel forward an infinite small distance *dl (m)*, the temperature increase within the distance *dl* is *dT (K)*, and the temperature gradient is *dT/dl (K/m)*, the heat input Q_{input} (J) into the stir zone is:

$$Q_{input} = C_p \times m \times \left(\frac{dT}{dl} \right) \times dl$$

Take low carbon steel as an example, the heat capacity and density of low carbon steel are as follows [58, 63]: For $T < 1073K,\ C_p = 347.27 + 62.34e^{T/471.706}$; For $T > 1073K$, $C_p = 962.32\ J \cdot kg^{-1} \cdot K^{-1}$; $\rho = 7850\ kg/m^3$.

And the mass is product of density and volume V (m^3):

$$m = \rho \times V$$

Then the total heat input of the stir zone is:

$$Q_{input} = C_p \times m \times \frac{dT}{dl} \times dl = C_p \times \rho \times V \times \frac{dT}{dl} \times dl$$

The calculation of the volume of the flowable metal around the pin is as follows:

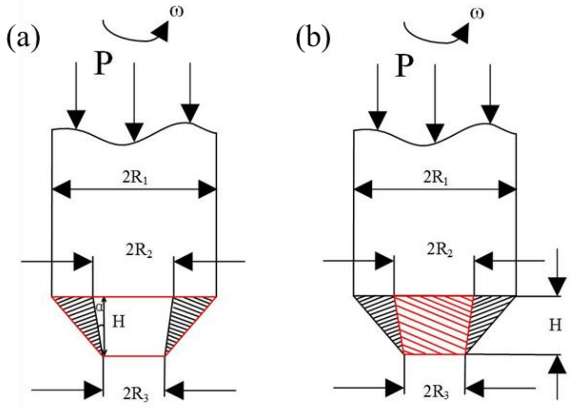

Figure 71: Schematic diagram of the side view of the tool.

The red box in Figure 71(a) indicates the total volume of the pin and flowable base metal around the pin V_{total} (m^3):

$$V_{total} = \frac{\pi H}{3}(R_1^2 + R_1 \times R_3 + R_3^2)$$

And the red shaded area (b) indicates the volume of the pin V_{pin} (m^3):

$$V_{pin} = \frac{\pi H}{3}(R_2^2 + R_2 \times R_3 + R_3^2)$$

The volume of flowable metal around the pin V (m^3) is:

$$\mathrm{V} = \frac{\pi H}{3}(R_1^2 + R_1 \times R_3 + R_3^2) - \frac{\pi H}{3}(R_2^2 + R_2 \times R_3 + R_3^2)$$

Then, the heat input becomes:

$$Q_{input} = C_p \times \rho \times \left(\frac{dT}{dl}\right) \times$$
$$\left(\frac{\pi H}{3}(R_1^2 + R_1 \times R_3 + R_3^2) - \frac{\pi H}{3}(R_2^2 + R_2 \times R_3 + R_3^2)\right) \times dl$$

It is assumed that there is no loss of heat generated during the welding process and all the heat is used to increase the temperature of the base metal. Therefore, heat input can be approximately equal to the heat generation during the welding process:

$$Q_{input} = Q_{tool}$$

Then *dT/dl* can be expressed as:

$$\frac{dT}{dl} = \frac{\left(\frac{2\pi\omega\mu P(R_2^3 - R_3^3)}{3\sin\alpha} + \frac{2\pi\omega\mu P R_3^3}{3} + \frac{2\pi\omega\mu P(R_1^3 - R_2^3)}{3}\right) \times \frac{1}{v}}{C_p \times \rho \times (\frac{\pi H}{3}(R_1^2 + R_1 \times R_3 + R_3^2) - \frac{\pi H}{3}(R_2^2 + R_2 \times R_3 + R_3^2))}$$

The vertical pressure can be expressed as:

$$P = \frac{C_p \times \rho \times \left(\frac{dT}{dl}\right) \times (\frac{\pi H}{3}(R_1^2 + R_1 \times R_3 + R_3^2) - \frac{\pi H}{3}(R_2^2 + R_2 \times R_3 + R_3^2)) \times dl}{\left(\frac{2\pi\omega\mu(R_2^3 - R_3^3)}{3\sin\alpha} + \frac{2\pi\omega\mu R_3^3}{3} + \frac{2\pi\omega\mu(R_1^3 - R_2^3)}{3}\right) \times \frac{dl}{v}}$$

Then the vertical force is

$$\frac{F}{\pi R_1^2} = \frac{C_p \times \rho \times \left(\frac{dT}{dl}\right) \times (\frac{\pi H}{3}(R_1^2 + R_1 \times R_3 + R_3^2) - \frac{\pi H}{3}(R_2^2 + R_2 \times R_3 + R_3^2)) \times dl}{\left(\frac{2\pi\omega\mu(R_2^3 - R_3^3)}{3\sin\alpha} + \frac{2\pi\omega\mu R_3^3}{3} + \frac{2\pi\omega\mu(R_1^3 - R_2^3)}{3}\right) \times \frac{dl}{v}}$$

So

$$F = \frac{\pi R_1^2 \times C_p \times \rho \times \left(\frac{dT}{dl}\right) \times (\frac{\pi H}{3}(R_1^2 + R_1 \times R_3 + R_3^2) - \frac{\pi H}{3}(R_2^2 + R_2 \times R_3 + R_3^2)) \times dl}{\left(\frac{2\pi\omega\mu(R_2^3 - R_3^3)}{3\sin\alpha} + \frac{2\pi\omega\mu R_3^3}{3} + \frac{2\pi\omega\mu(R_1^3 - R_2^3)}{3}\right) \times \frac{dl}{v}}$$

The vertical force can thus be calculated by plugging the parameters into the above equation.

Table 11: The experimental FSW parameters.

Run No.	Rotation speed (rpm)	Travel speed (mm/min)	Plunge Depth (mm)	Pin length (mm)	Shoulder diameter (mm)	Measured vertical Force (N)	dT/dl (K/mm)	Calculated vertical force (N)	Standard Deviation (N)
1	400	80	**0.42**	2.3	10	4700	408	5001	320
2	400	80	**0.45**	2.3	10	4900	421	5056	324
3	400	80	**0.52**	2.3	10	5200	436	5184	332
4	400	80	**0.60**	2.3	10	5800	473	5331	341

The table summarizes four sets of experimental welding parameters. *dT/dl* was therefore calculated for each run and a mean value of 435(±28) (K/mm) was obtained. The *dT/dl* mean value was then used to estimate the vertical forces. The vertical force from experimental measurement and theoretical calculation are compared. It indicates that the calculation results fall approximately within the standard deviation range, which shows the reliability of the analytical model.

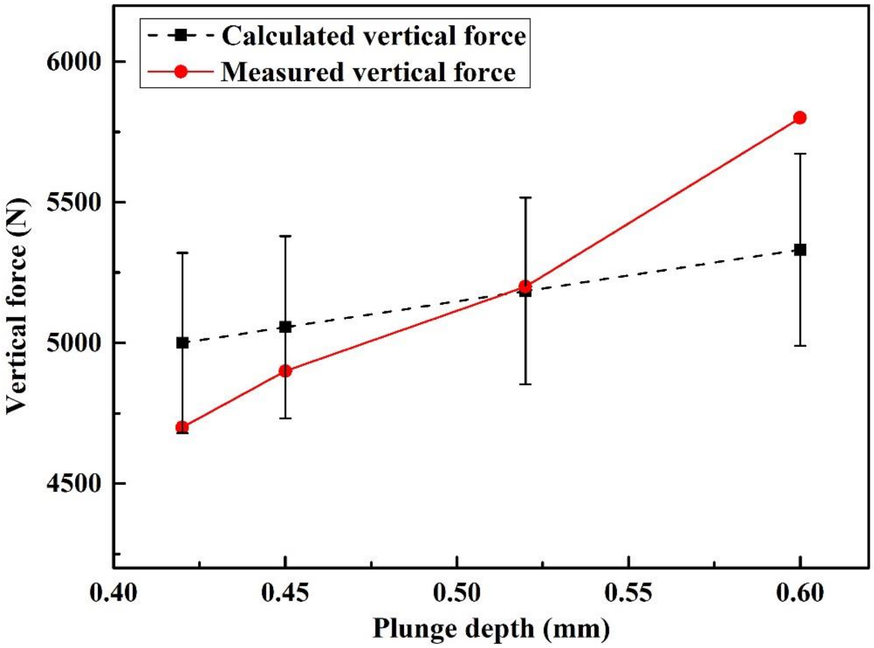

Figure 72: Calculated vertical force and measured vertical force as a function of plunge depth under 2.3 mm pin length condition.

As for the FSW process with pinless tool, one experiment has been carried out so far for initial evaluation. It is found that the force calculated using the analytical model, 5.5kN, is comparable to the experimentally measured value 5.2kN, as shown in Table 12.

By using the validated analytical model, it can be estimated that reducing the shoulder diameter by half, from 10mm to 5mm, can effectively reduce the vertical force from 5.5kN to 2.8kN. Further reduction in power and force requirement can achieved by introducing preheating, which has been incorporated into the analytical model.

Table 12: Parameters for FSW using pinless tool and calculated vertical force from analytical model.

Run No.	Rotation speed (rpm)	Travel speed (mm/min)	Plunge Depth (mm)	Tool materials	Pin length (mm)	Shoulder diameter (mm)	Tilt angle (°)	Measured Vertical force (N)	Calculated vertical force (N)
1	400	80	0.22	W-Re	0	**10**	2.5	**5200**	**5509**
2	400	80	0.22	W-Re	0	**5**	2.5	-	2755

2.2. Subtask 2.2: Repair Protocol Design

2.2.1. Identification of Prototype Repair Protocol

The prototype friction stir welding (FSW) repair parameters using a pinless tool were identified for conditions with and without the assistance of induction preheating, namely, FSW and induction-heating-assisted friction stir welding (IHA-FSW) processes based on the surface morphology inspection. Preliminary metallurgical characterizations were carried out to reveal the effects of repairing process on the base material microstructure.

A. Base material

Low carbon steel grade A108 was used as the base metals for repair experiments. Note that the boiler water wall material is A106, which can only be found in pipe shape. Therefore, in this study, A108 in plate format was chosen instead for repair parameter evaluation. The dimensions of A108 steel plates were 0.5 inch thick, 8 inches wide and 12 inches long. The chemical composition (wt%) of A108 steel is listed in Table 13.

Table 13: *Chemical Composition (in wt%) of A108 steel*

Steel grade	C	Mn	Si	P	S
A108	0.13-0.20	0.60-0.90	0.15-0.30	0.035	0.035

B. Experimental procedure

A pinless W-Re tool with a shoulder diameter of 10mm was employed to carry out the FSW repair trails, which eliminates the exit hole. Note that the need for repair width and depth will determine the proper tool geometry with various pin lengths in future, and exit hole can be eliminated by existing technologies such as a retractable pin tool. The prototype parameters for FSW and IHA-FSW processes are tabulated in the Table 14.

Table 14: Parameters FSW and IHA-FSW

Sample	Rotation speed (rpm)	Travel speed (mm/min)	IH power (kW)	Plunge depth (mm)	Tilt angle (°)
FSW (one trial)	500	80	-	0.15	2.5
IHA-FSW (two trials)	400	70	15	0.15	2.5

Preliminary characterizations were performed in the welding trials including profilometry measurement on weld surfaces, and optical microscopy and hardness mapping on the weld cross-sections. The metallurgical inspections were performed on the cross-section of the welds after grinding, polishing and etching with 3 % nitric acid and 97 ml methanol solution. Optical microscope with the capability of profilometry measurement was also used to obtain the surface profiles of the welds. Vickers hardness mapping were performed on the transverse cross-sections, i.e., the plane perpendicular to the welding direction, with a relative distance of 500 μm between the indents and using a 500 g load and a dwelling time of 10 s.

In terms of the preheating system, a Miller TIG welding machine was previously used as the preheating source. Our preliminary evaluation on TIG torch preheating indicated that the minimum safe distance between the torch and the tool limited the amount of heat input as a preheating source, which was insufficient to influence the FSW process (e.g., to reduce tool rotation speed for less heat input while maintaining a good repair). Therefore, induction heating method was selected for further investigation.

Figure 73 shows the Miller induction heating (IH) power source equipped with a cooling system. The copper coil was mounted in front of the FSW tool, as shown in Figure 74 with a minimum distance of 20mm. The distance between the coil and steel plate during repair was about 8.5mm. Laser pyrometer was used to monitor the peak temperature as a function of IH power between 20kW and 5kW. Based on the preliminary laser pyrometer measurement, to provide a preheating temperature between 700°C and 900°C, a power of 15 kW was selected for further experiment. Note that the key input parameter for laser pyrometer measurement, i.e., emissivity of steel as a function of temperature, was greatly influenced by the level of oxidation, since argon shielding gas was mainly applied surrounding the FSW tool. Therefore, calibration is currently being conducted for emissivity value in order to provide a more accurate measurement of temperature profile introduced by IH in future.

The induction preheating was started after turning on the cooling water system. The programming of IHA-FSW process included:

(1) Preheating for 20s at the weld start point, which is underneath the center of the coil;
(2) Moving the rotating tool to the start point at a speed of 70 mm/min, plunging into the base metal with a depth of 0.15mm, and dwelling for five seconds to generate sufficient frictional heat. Note that this dwelling time is much shorter than the FSW process, which is 28s, in order to generate sufficient frictional heat to soften the material.
(3) Initiating tool travel for a total distance of 70mm.

Finite element (FE) modeling will be performed in future to quantify the heat contribution from FSW tool and IH, respectively, and potentially further optimize the relative distance between the welding tool and coil.

Figure 73: The induction heating source.

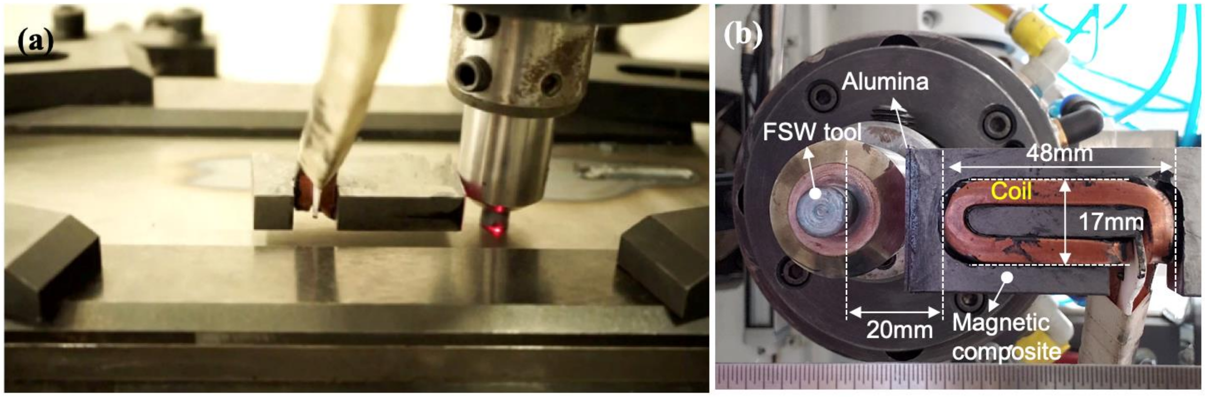

Figure 74: The set up for the IHA-FSW process a) side view; b) bottom view.

C. Results and Discussion

Vertical force profile:

Figure 75 demonstrates the vertical force profile of FSW process exhibiting three distinct regions including: (1) an initial rise as the tool shoulder becomes in contact with the workpiece, (2) force reduction as the tool rotates and continues to plunge as softening of material occurs due to heating, and (3) a rise again as the tool travels forward after dwelling for 28s.

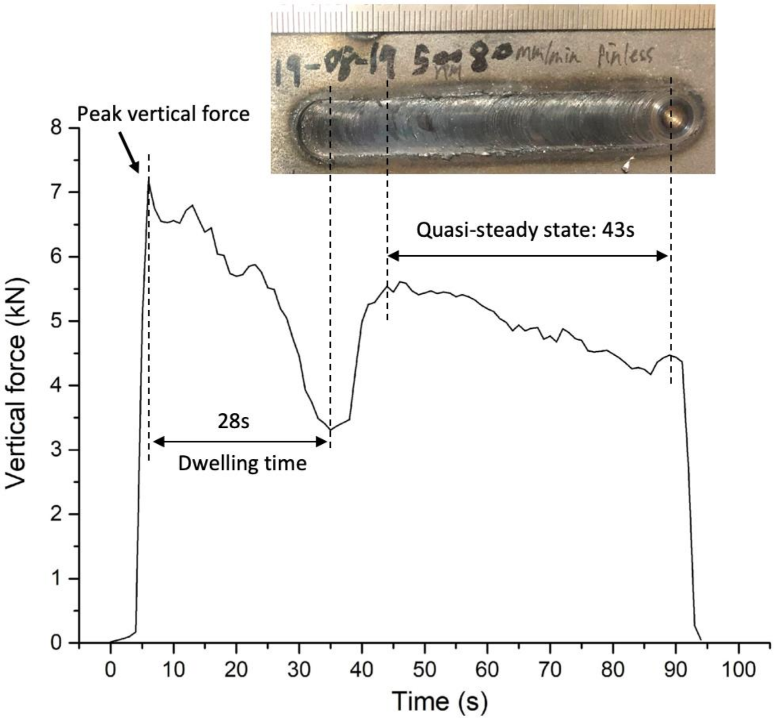

Figure 75: The vertical force profile as a function of time during FSW.

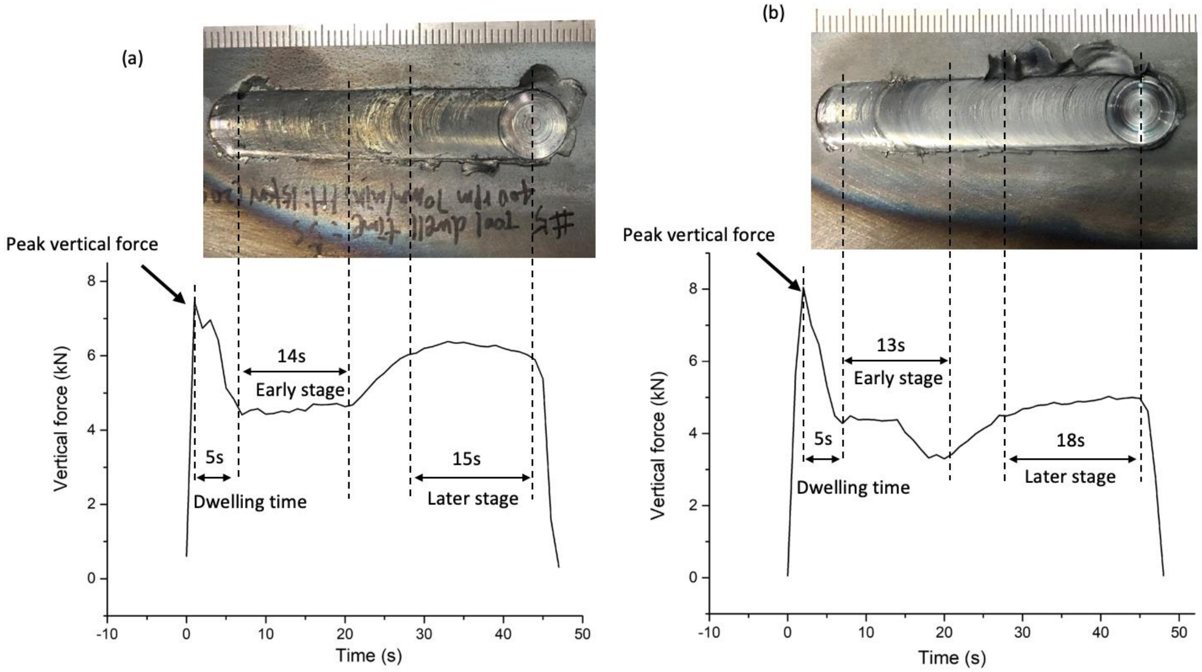

Figure 76: The vertical force profiles as a function of time during IHA-FSW (a) trial 1 and (b) trial 2.

Figure 76 summarizes the vertical force profiles of IHA-FSW trials. Note that after trial 1 (Figure 76a), it is noticed that the tool had base metal materials sticking in the grooves and thorough cleaning by grinding was performed before trial 2 (Figure 76b). Moreover, trial 1 was performed close to the edge of the steel plate and the plate had many trials runs on it, leading to slight distortion in the plate. In comparison, trial 2 was performed in the center of a new plate without any previous welding trials and using a carefully cleaned tool. Therefore, data obtained from trial 2 would be more trustworthy. Trial 1 is still presented here since all the preliminary characterizations were performed on trial 1.

As shown in Figure 76, the peak vertical force of IHA-FSW is comparable to that of FSW as the tool first touched the workpiece, which could be caused by a slow initial moving speed of 70mm/min for the tool to move to the start point. In other words, the slow-moving speed to the start point may have led to excessive heat loss. In addition, the rotating speed in FSW (500rpm) is higher than that of IHA-FSW (400rpm). Therefore, in the initial pressing stage (1-3 seconds), the frictional heat generation in FSW were greater than the sum of frictional heat and induction heat in IHA-FSW. For the next step, the speed of the tool moving to the initial point will to be maximized in order to minimize the loss of the initial preheating, and thus reduce the peak vertical force to a value comparable to that of later stages in IHA-FSW.

As shown in Figure 76(b), when the tool started to move forward after a dwelling time of 5s, the vertical force of IHA-FSW reached a temporary quasi-steady state at a force level of ~4.5kN, without going through a valley as in FSW in Figure 75. The reason could be that during FSW the tool dwelled for 25 seconds at the start point while during IHA-FSW it dwelled for 5 seconds. The extra 20 seconds at a fast rotational speed of 500 rpm enabled accumulation of frictional heat, leading to more severe softening of the base metal at the start point.

Note that while the tool dwelled at the starting point, IH sitting in front of the tool continuously provided heat input, which caused the force valley present near the end of the early stage of IHA-FSW in Figure 76(b). After dwelling and as the coil moved along with the FSW tool, a quasi-steady state was reached again in the later stage of IHA-FSW. The presence of force valley indicates that to further reduce the vertical force associated IHA-FSW overall. It might be worthwhile to further investigate the effect of higher power input from IH or lower tool travel speed, but there would be concerns of surface quality and repair strength as excessive heat is introduced.

Surface morphology of the repairs:

Periodic band structure is a typical surface morphology of friction stir welds and it is the direct evidence of periodic plastic deformation. A schematic drawing in Figure 77 demonstrates the formation mechanism of periodic band structure [66]. During FSW, the rotating tool with a slight tilt angle enables the rigid metal in front of the tool to plastically flow around the tool and eventually deposit behind it.

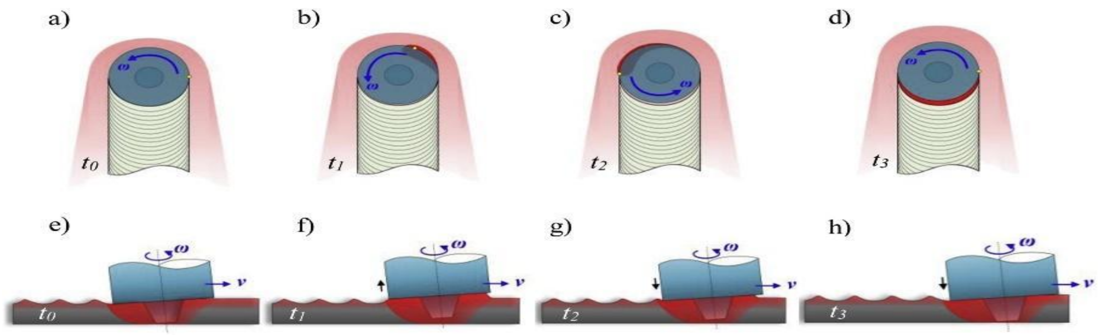

Figure 77: Formation mechanism of the periodic bands: a)-d) top view at different moments, and e)-h) the corresponding longitudinal sections.

Figure 77 a) and e) illustrate the position of the tool at t_0, i.e., the last revolution has just finished and the shoulder is located at the trough. In the next moment t_1-t_3, the rotating tool will press the fresh rigid material at the advancing side (AS) (Figure 77 b and f), extrude it to the retreating side (RS) (Figure 77 c and g), eventually deposit it behind the tool (Figure 77 d and h), and then a new revolution starts [66].

At the beginning, the temperature of the fresh rigid material is low, resulting in a higher yield strength, the fresh rigid material is initially very difficult to be pressed down. Hence, the tool needs to slightly lift up, as shown in Figure 77 f). When the material flows from the AS to RS, it is softened sufficiently due to the frictional motion between the tool and base metal (Figure 77 c). As a result, the tool is able to fall back down (Figure 77 g), meanwhile, the plastic material flows behind the rotating tool and deposits in the trailing edge until the shoulder reaches the lowest position, that is, the wave trough (Figure 77 h).

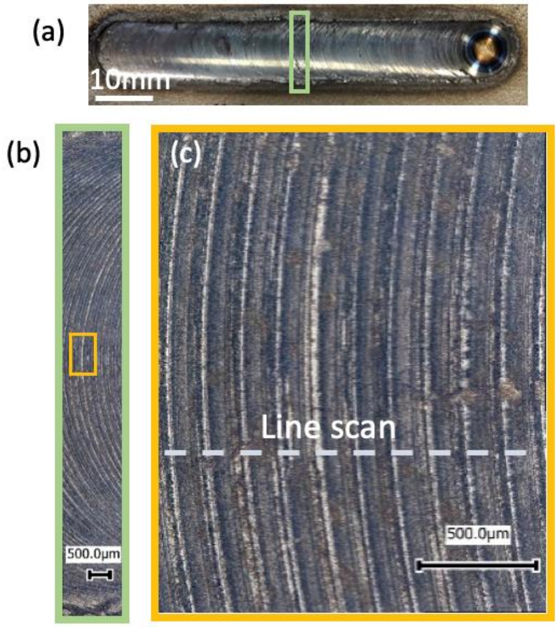

Figure 78: Surface appearance of the FSW specimen.

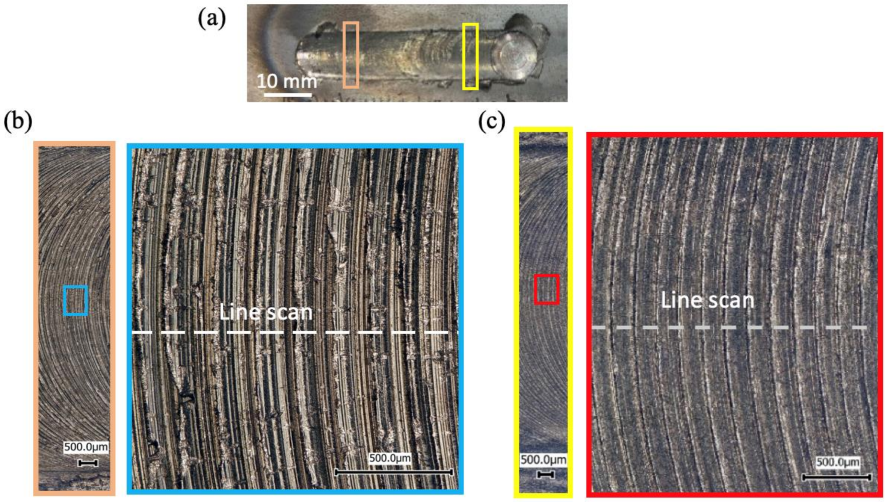

Figure 79: (a) Surface appearance of the IHA-FSW trial 1 specimen, and the local morphologies in (b) early stage and (c) later stage.

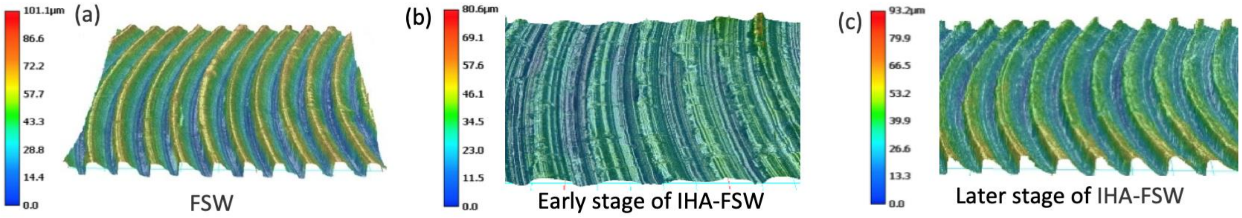

Figure 80: Surface morphology of (a) FSW and IHA-FSW trial 1 (b) early stage and (c) later stage.

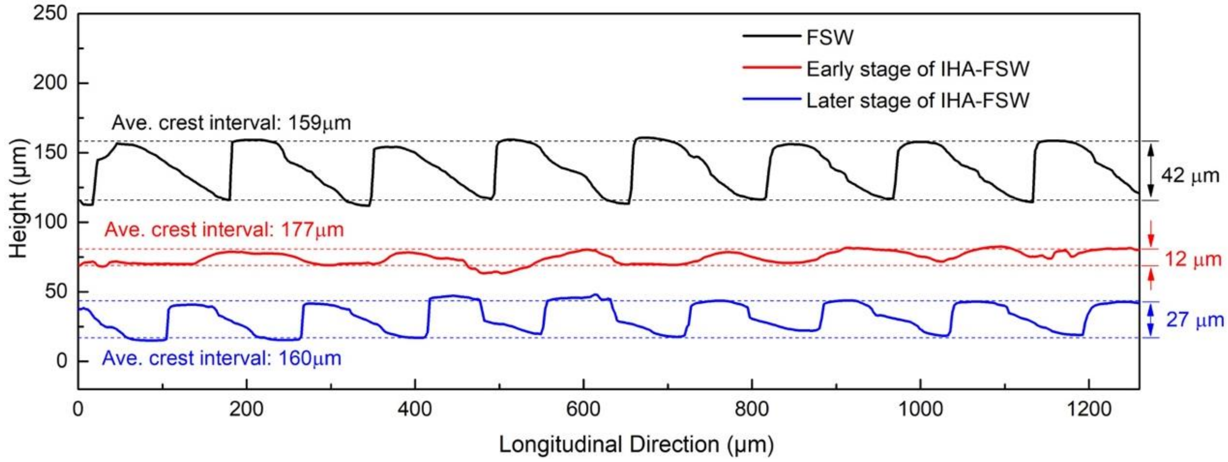

Figure 81: Line scan results of the surface morphology of FSW and IHA-FSW trial 1 early stage and later stage.

Figure 78 and Figure 79 demonstrate the repair surfaces from FSW and IHA-FSW trial 1, respectively. Periodic band structure (sometimes called onion ring structure) appears on the weld surface in both of them. Note that waterjet cutting introduced some minor corrosion pits on the top surface of FSW specimen, as seen in Figure 78 (c). Therefore, all the other specimens were cut by LECO MSX sectioning machine instead. Figure 80 summarizes and compares the line scan results for the three-dimensional periodic patterns of the bands in FSW and IHA-FSW trial 1 specimens.

As the tool moves forward, the process described above occurs periodically, and a periodic band structure on the weld surface is formed. The intervals between neighboring wave crests or troughs on the weld surface can be calculated by the following equations:

$$\text{FSW: } d=v/\omega= (80\text{ mm/min}) / (500\text{ rev/min}) =160\ \mu\text{m/rev}$$
$$\text{IHA FSW: } d=v/\omega= (70\text{ mm/min}) / (400\text{ rev/min}) =175\ \mu\text{m/rev}$$

Figure 81 summarize the line scan results on the surface profiles of FSW and IHA-FSW trial 1 specimens. The measured average crest intervals for FSW is 159μm, and 177μm and 160μm for the early stage and later stage of IHA-FSW trial 1 sample, respectively. The measured crest interval of FSW sample is approximately equal to the distance traveled during one revolution of the tool. The variation in crest interval in the early and later stage of IHA-FSW trial 1 specimen is under further investigation. Note that characterizations will be performed on IHA-FSW trial 2 specimen to further confirm the presence of such variations.

Moreover, it can be seen that for the weld surface of FSW, the amplitude from wave crest to trough is 42 μm. However, after applying induction heating, the value of the amplitude is reduced to 12 μm in early stage and 27 μm in later stage. As mentioned earlier in the section of vertical force profile, since the induction copper coil dwelled at the initial point for 20 seconds of preheating before welding, the total heat input in the base metal at the early stage is larger than that at the later stage. The higher heat input led to excessive softening of materials under the took, and thus resulted in the flattest band structure.

2.2.2. Metallurgical Characterizations

A. Metallurgical characterizations of FSW specimen:

Figure 82 shows the hardness mapping result from a transverse cross-section (i.e., perpendicular to the welding direction) machined in the middle of FSW sample. It is observed that stir zone (SZ) exhibits is the highest hardness in comparison to the other regions such as heat-affected zone (HAZ) and base metal (BM). The significant increase in hardness is mostly likely attributed to the grain refinement during FSW[70], as demonstrated in Figure 83 by comparing Figure 83 g to e. On the other hand, the hardness of the HAZ is the lowest due to grain coarsening associated with the heat input during welding process.

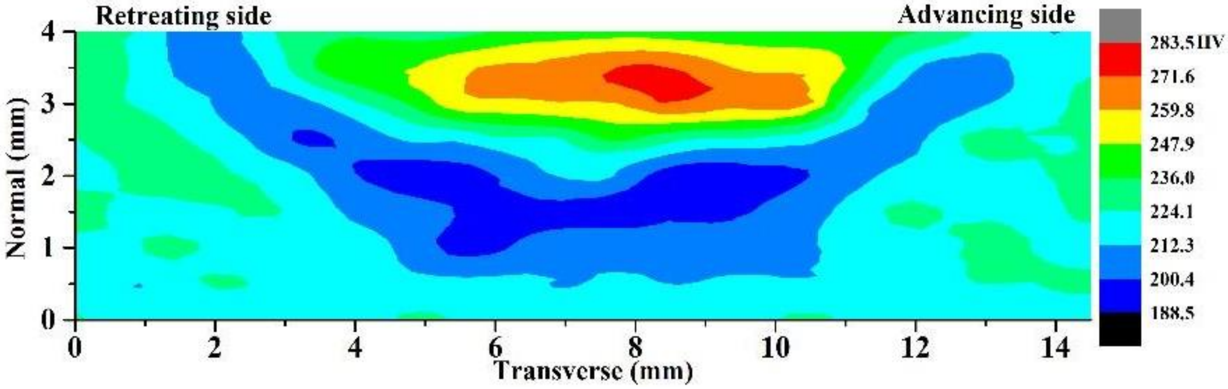

Figure 82: The hardness mapping on the weld cross-section of the FSW.

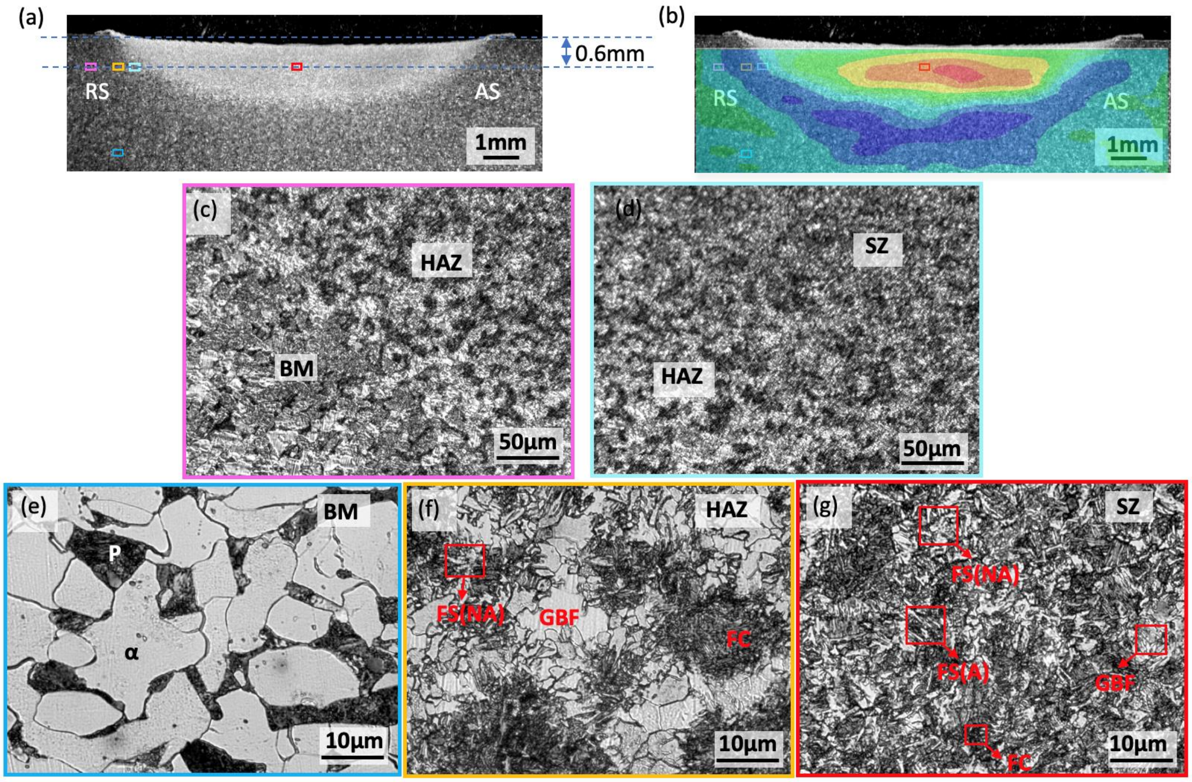

Figure 83: FSW specimen: (a) low-magnification optical micrograph of the weld cross-section, (b) overlapped images of weld cross-section macrograph and hardness map, and the optical micrographs of transition between BM and HAZ, and transition between HAZ and SZ.

Figure 83 summarizes the microscopic examination results on the FSW cross section. The BM exhibits a typical microstructure of low carbon steel, which consists of ferrite (light area) and pearlite (dark area). The SZ contains fine grains due to dynamic recrystallization (DRX) induced by frictional heat generated and severe plastic deformation [67]. The Fe-C phase diagram in Figure 84 can be used to further explain the observed microstructure and the red broken line indicates the composition of A108 steel [68], although during FSW, equilibrium phase transformation may not be representative. In SZ, the material could experience a temperature above 70% of the melting point, which is way above the A_3 temperature of A108 of 850°C. Therefore, SZ experienced complete austenization at peak temperature, and then during cooling it transformed to a mixture of *grain boundary ferrite (GBF), ferrite with aligned second phases (FS(A)) and nonaligned second phases (FS(NA)), and ferrite/carbide aggregate* (*FC*), as shown in Figure 83 (g). The HAZ microstructure is highly dependent on the local thermal cycle experience during FSW. As illustrated in Figure 83 (f), a grain-coarsened HAZ is observed, where GBF, fc and FS(NA) were observed.

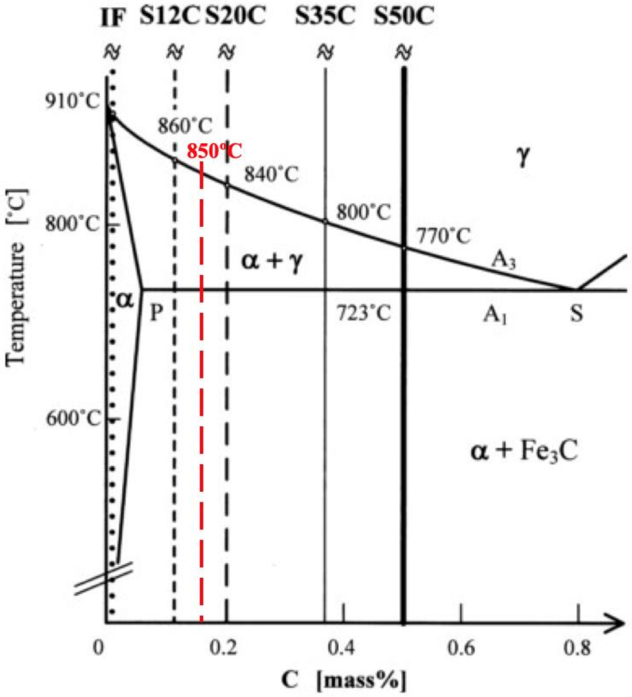

Figure 84: Fe–C phase diagram with various carbon steel compositions marked out.

B. Metallurgical characterizations of IHA-FSW specimen:

Figure 85 shows the hardness mapping result from a transverse cross-section of IHA-FSW sample. Different from the results of FSW, it was found that the hardness of the stir zone is comparable to the BM. But similar to the FSW result is that the hardness of the HAZ is still the lowest due to grain coarsening associated with the heat input during welding process. The wide region of hardness reduction on the retreating side is caused by the excessive heat from the wide induction coil, which can be controlled by an optimized coil geometry. The slight increase in hardness on the advancing side is caused by work hardening introduced during machining process, since it is close to the edge of the steel plate.

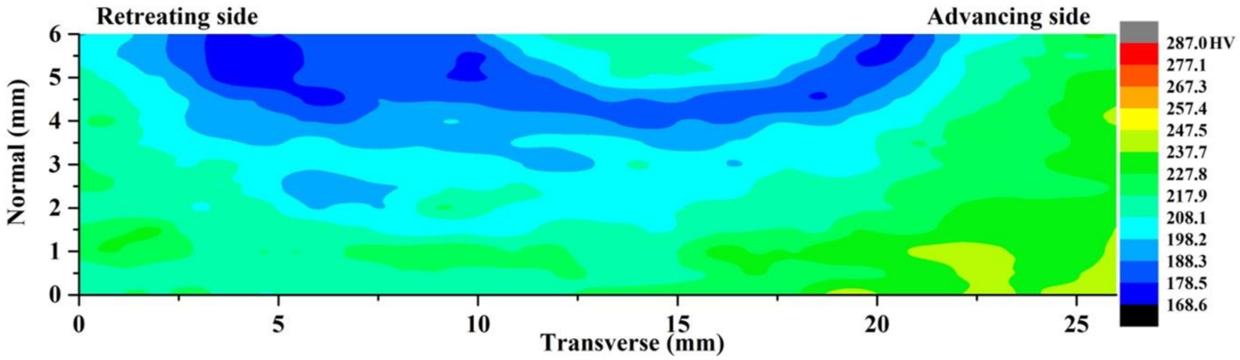

Figure 85: Hardness mapping on the weld cross-section of the IHA-FSW.

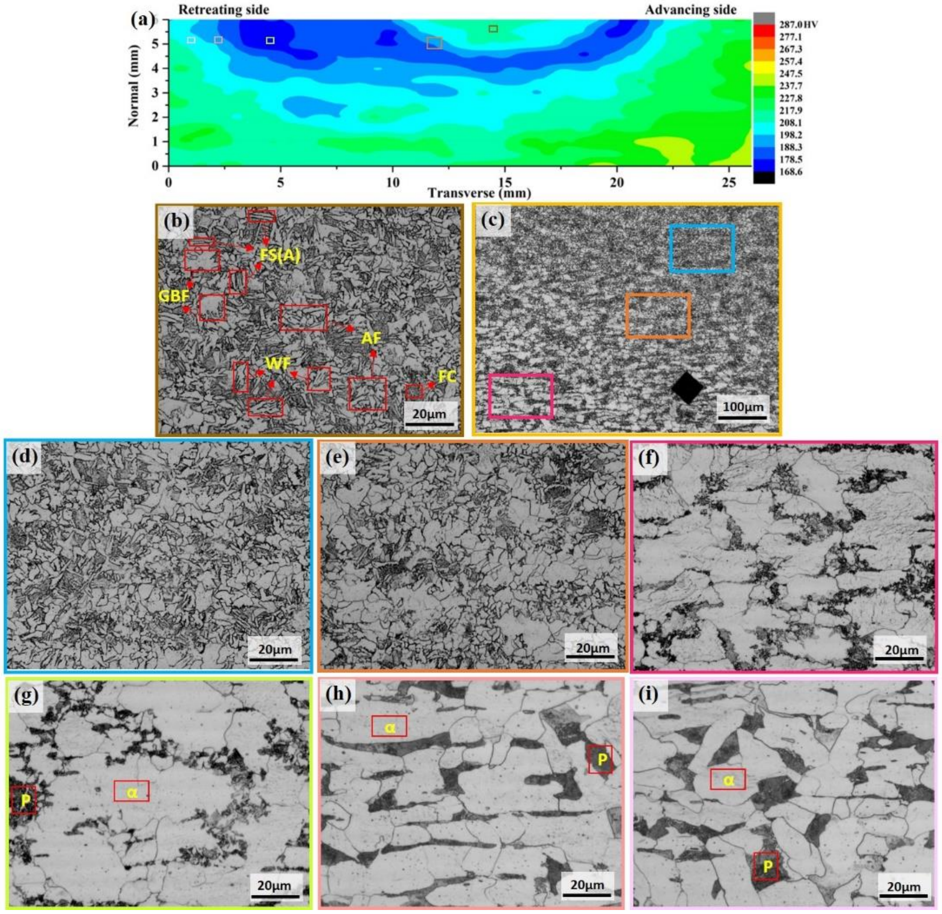

Figure 86: IHA-FSW specimen: (a) overlapped images of weld cross-section macrograph and hardness map, and the optical micrographs of (b) SZ, (c) transition from SZ to HAZ using 200 magnification, (d-f) transition from SZ to HAZ using 500 magnification, (g) HAZ, (h) transition from HAZ to BM using 500 magnification and (i) BM, where SZ, HAZ and BM represents stir zone, heat-affected zone and base metal, respectively. GBF: grain boundary ferrite; FS(A): ferrite with aligned second phases; AF: acicular ferrite; WF: Widmanstatten ferrite; FC: ferrite-carbide aggregate; α: α-ferrite; P: pearlite.

Figure 86 summarizes the optical micrographs on the IHA-FSW cross-section. The SZ contains fine grains due to dynamic recrystallization (DRX) induced by frictional heat generated, induction preheating and severe plastic deformation. According to the Fe-C phase diagram, in SZ, the material could also experience a temperature above 70% of the melting point and then above the A_3 temperature of A108 of 850°C with the auxiliary of induction preheating. Therefore, SZ austenitized completely at peak temperature, and then during cooling it transformed to a mixture of grain boundary ferrite (GBF), ferrite with aligned second phases (FS(A)), acicular ferrite (AF), Widmanstätten ferrite (WF), and ferrite/carbide aggregate (FC), as shown in Figure 86(b). The HAZ shows coarsened grains due to the slow cooling rate affected by double thermal cycle from frictional heat and induction preheating, as illustrated in Figure 86(g), where ferrite (α) and pearlite (P) are observed. The BM exhibits a typical microstructure of low carbon steel, which consists of ferrite (light area) and pearlite (dark area).

Comparison of metallurgical characterization of FSW and IHA-FSW:

Considering all the above experiments, the prototype friction stir welding (FSW) parameters have been determined to be 500 rpm and 80 mm/min without preheating and 400 rpm and 70 mm/min with 15kW induction heating power (IHA-FSW). Comparing FSW and IHA-FSW, it is observed that the grain size in SZ of IHA-FSW is larger than that of the FSW. Correspondingly, the hardness in SZ of IHA-FSW is lower than that of the FSW. Similar phase constituents were observed in the SZs of FSW and IHA-FSW specimens, but there was a small amount of bainite forming in SZ of FSW, which indicates that the cooling rate of FSW is slightly higher than that of IHA-FSW. This may be because under the condition of IHA-FSW, the weld would experience dual thermal cycles from the induction preheating and the frictional heat, which might lead to a slower cooling rate during IHA-FSW. The higher cooling rate also makes the grain size of SZ of FSW a little bit smaller than that of IHA-FSW.

3. Task 3: Robotic Platform Design

A robotic system was designed that leveraged a commercial robotic platform retrofitted with a customized gantry system, sensors, cleaning, NDE sensors, and repair tools.

3.1. Subtask 3.1: Robot Retrofit for Vertical Navigation

The original robotic platform was the Clearpath Jackal robot. However, the Jackal robot is a wheel-based robotic platform. Retrofitting the Jackal robot wheels with magnetic tread did not provide enough attachment force to facilitate welding operations on the vertical furnace wall surface. A search for a treaded robot was conducted, with the ideal robot selection being the Reebotic treaded rover platform. A comparison image is shown below with the previous Jackal robot on the left and Reebotic Rover on the right.

Figure 87: Jackal wheeled rover (left) and Reebotic treaded rover (right).

After selecting a robotic platform, we began a physics simulation utilizing COMSOL simulation software to evaluate the pull-force of the robot against the furnace wall surface. Placing 5x1.75" length bar magnets in between each tread "nub" on the reebotic rover platform results in a total of 150 magnets total. Attaching the magnets with alternating polarity provides the maximal amount of force.

Magnetic Track Design:

Figure 88 below illustrates the magnetic field obtained with alternating bar magnet polarity (left) and magnet arrangement in the footprint of the reebotic rover platform (right).

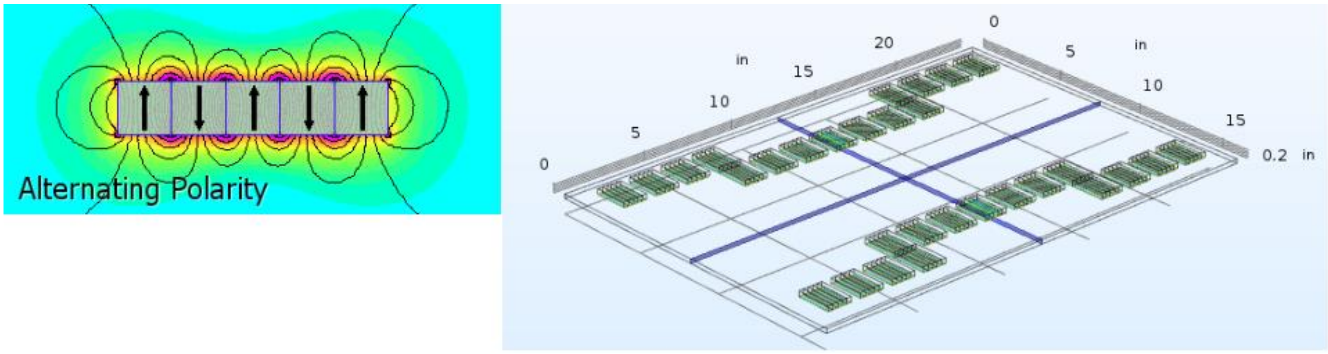

Figure 88: Alternating polarity magnetic field and rover footprint magnet arrangement.

This magnet arrangement yields a 7kN pull force on flat steel. However, on the furnace wall surface, the pull force is 1.3kN when the treads are parallel to the tube direction. When the treads are at a 45-degree rotation relative to the tubes, the force is 1.4kN. Figure 89 below shows the magnet footprint parallel to the tube direction (top) and treads at 45-degree rotation relative to the tubes (bottom).

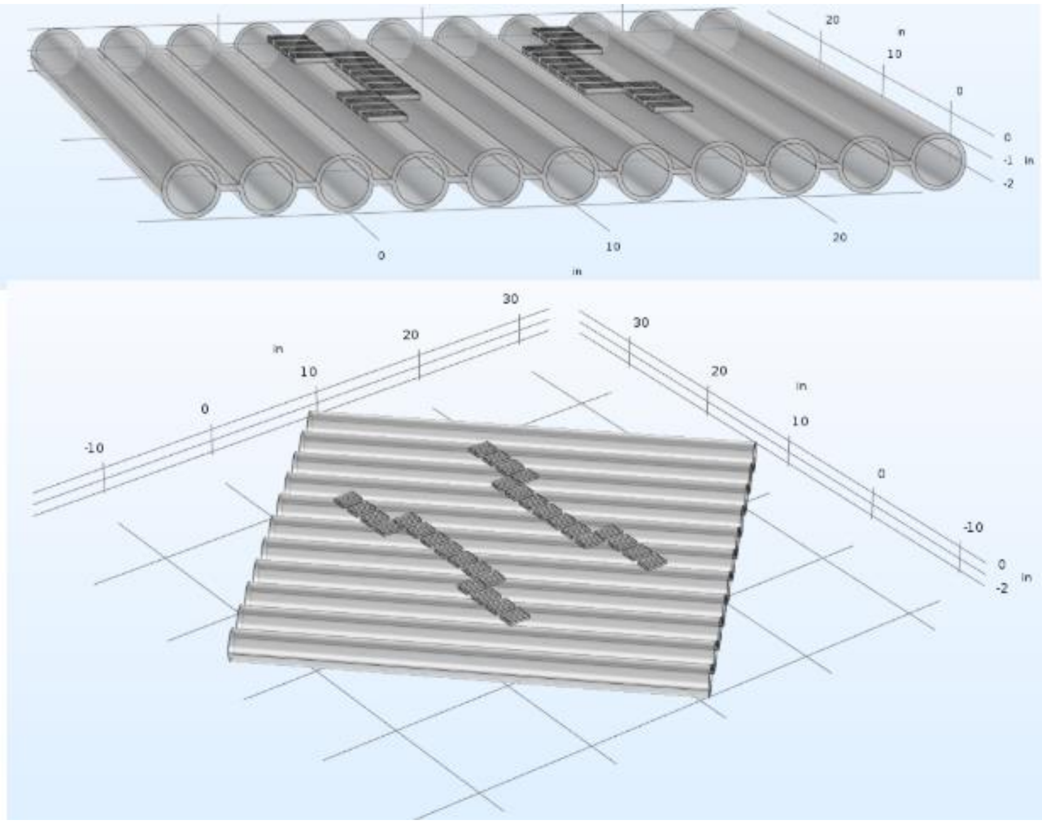

Figure 89: Footprint parallel to tubes and footprint at 45-degree rotation to tubes.

To better evaluate the magnetic force at different rotations, a simulation was conducted that rotated the magnetic footprint at 6-degree increments. The results from the rotating simulation are shown below in Figure 90. The minimum force is 0.73kN at 171 degrees and the max is 2.36 kN at 99 degrees.

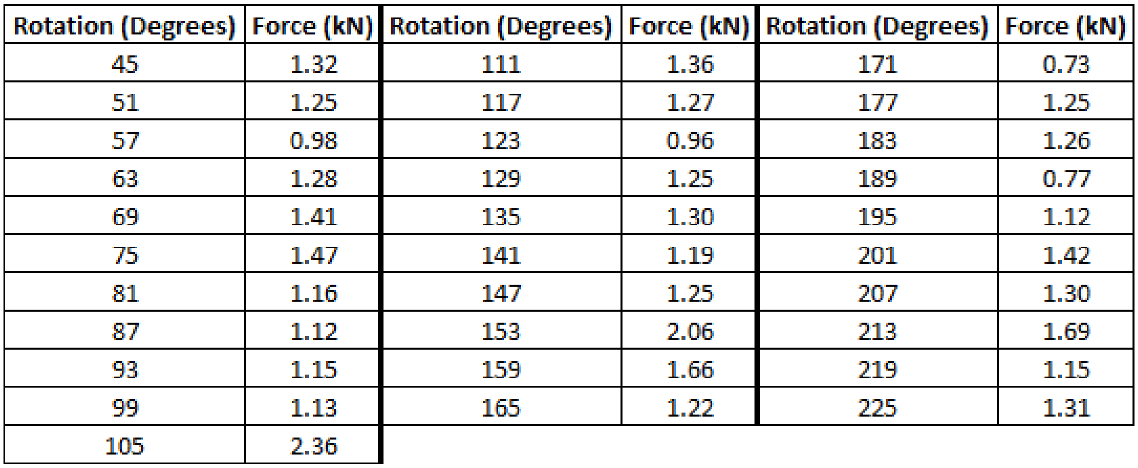

Rotation (Degrees)	Force (kN)	Rotation (Degrees)	Force (kN)	Rotation (Degrees)	Force (kN)
45	1.32	111	1.36	171	0.73
51	1.25	117	1.27	177	1.25
57	0.98	123	0.96	183	1.26
63	1.28	129	1.25	189	0.77
69	1.41	135	1.30	195	1.12
75	1.47	141	1.19	201	1.42
81	1.16	147	1.25	207	1.30
87	1.12	153	2.06	213	1.69
93	1.15	159	1.66	219	1.15
99	1.13	165	1.22	225	1.31
105	2.36				

Figure 90: Magnetic footprint rotation vs force.

It was estimated that we may need a minimum of 3kN of attachment force when performing welding operations when the robot is parallel to the tube direction. To achieve this force, the magnet footprint can be augmented with 4x 4” by 4” square packs of similar bar magnets placed at the edges of the footprints.

Figure 91 below shows that footprint modification with the square magnet packs attached. This augmentation yields a force of 3.3kN when the treads are parallel to the tubes. This is enough for welding operations. It is an ongoing effort to determine how to mount and manipulate these 4 magnet packs.

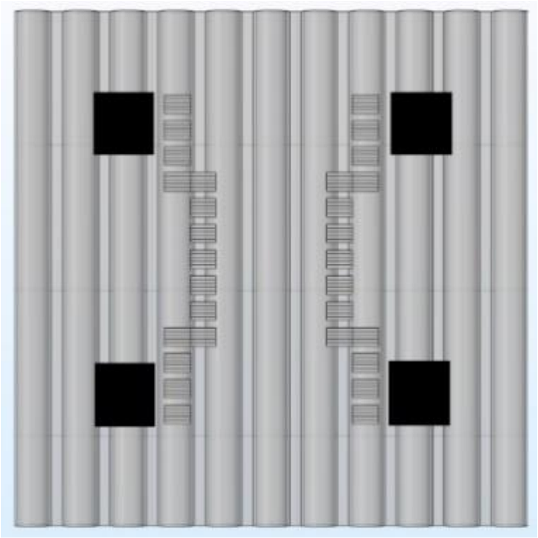

Figure 91: Magnet footprint with 4" x 4" magnet packs.

Magnetic Track Construction:

To construct the magnetic track system, room temperature vulcanizing (RTV) silicone was selected to attach the magnets. The used product was chosen for the 1,025 psi tensile strength, 825% elongation and 60 lbf/in peel strength. Of these qualities, percent elongation and peel strength are most important because the magnets must be able to travel around the radii of the tracks. As the magnets are being lifted off the steel surface, the leading edge of the magnet experiences strong peeling forces. To further improve the holding forces on the magnets, a layer of steel wire cloth was sandwiched between the tracks and magnets. The wire cloth was sized to maximize magnetic attraction, flexibility and allow silicone adhesive to flow through the mesh. For this purpose, 30 x 30 steel mesh with a 0.012 inch wire diameter and 0.021 inch opening size was suitable. Plastic spacers were installed between the individual magnets to decrease the mutual attraction and improve track flexibility. However, some of the spacers were ejected during the driving test from poor adhesion to the silicone. The gaps were later filled with more adhesive to form a flexible, permanent spacer. The magnets were arranged into blocks of 5 with alternating polarity to maximize attraction force to the wall. Whenever possible, these blocks were arranged to attract to their neighboring blocks to maximize wall attraction and minimize construction difficulty. Closeups of track and construction process are shown below.

Magnets arranged, cloth cut & surfaces cleaned with xylene

Adhesive applied in rows to completely fill gaps

Wire cloth ready for application

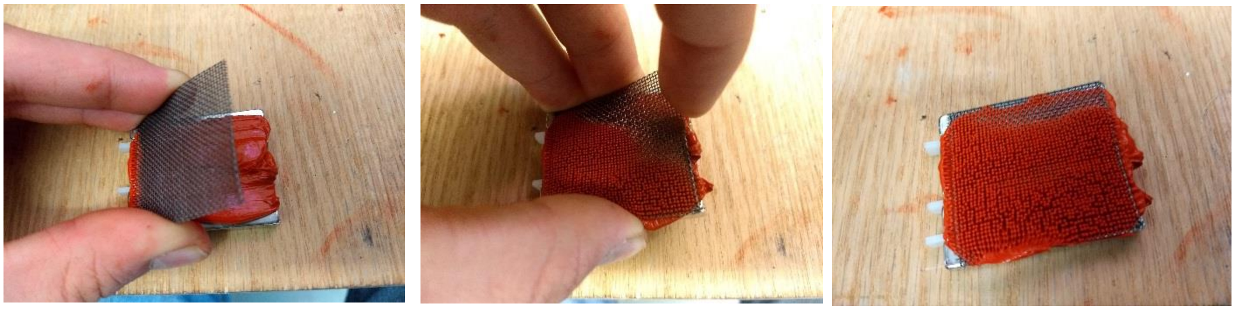

Wire cloth started at edge to maintain control

Wire cloth carefully laid down through adhesive

Magnet block ready for application to track

Figure 92: Illustration of the gluing processes.

The magnets afforded excellent traction and firmly locked the robot against the surface. It was necessary to drive the robot onto an aluminum plate (pictured) to disengage from the steel wall. Because turning relies on slippage of the tracks, the turning radius of the robot is under investigation. After conducting the test, it was discovered that two blocks of magnets had peeled off the track surface. This was due to a layer of paint that separated from the track surface. These isolated instances were fixed by scraping the remaining paint off and reapplying the magnets. Repairs of this nature will be made on an as-needed basis unless the problem becomes more frequent.

During the driving test, the robot had little difficulty climbing up or down the wall. The motors were able to drive the tracks despite the weight of the robot and resistance from peeling magnets off the steel surface. However, the robot drove in a jerking motion and undulated with respect to the wall. Depending on the accuracy needed to position different pieces of equipment, driving alone may not be precise enough.

Figure 93: Illustration of the modified magnetic track closeup.

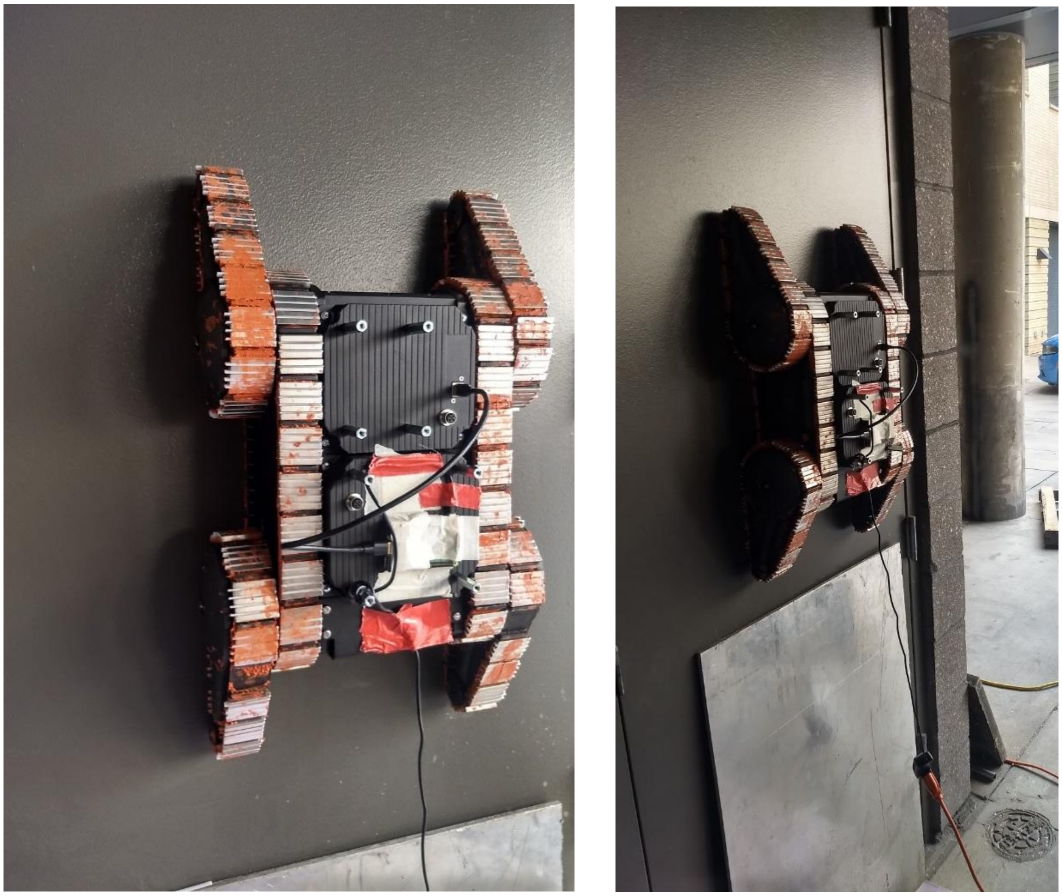

Figure 94: Illustrations of robot navigation on vertical testing walls.

The progresses allowed for a successful test of vertical driving capabilities. Several pictures of the experiments are shown above. A cable can be seen going to the robot, but it only served to power the device receiving control commands. An on-board battery was used for power during testing. In the final robot this will be infeasible and replaced with a cable. Consequently, more weight will be shed and an increase in torque may be possible. During the system integrating phase, further testing is needed to determine the maximum torque available for carrying a load up the wall without the battery. However, calculations show that at least one-foot pounds of torque will be required for every four pounds of weight. The manufacturer of the base robot platform was unable to give a maximum torque output for the drivetrain and experimentation is needed. Figure 95 depicts the robot driving vertically on the water wall boiler tube surface under its own power, attached to wall via magnets on the robot treads.

Figure 95: The robotic platform has been demonstrated traversing a vertical waterwall using magnets for attachment.

3.2. Subtask 3.2: Cleaning Mechanism Design

For the non-destructive evaluation (NDE) sensors scanning system to accurately detect defects the surface must be consistently clean and free of defects. To accomplish this, a cleaning mechanism was affixed to the mobile robot platform. This system removes built-up surface contaminants to provide a consistent surface for inspection and prepares areas requiring repair for a weld devoid of contaminant defects. The design integrates a stainless-steel wire brush powered by a commercially available angle grinder as shown in Figure 96. The mechanical design of the system ensures rapid prototyping and modularity to accommodate future iterations while remaining rigid.

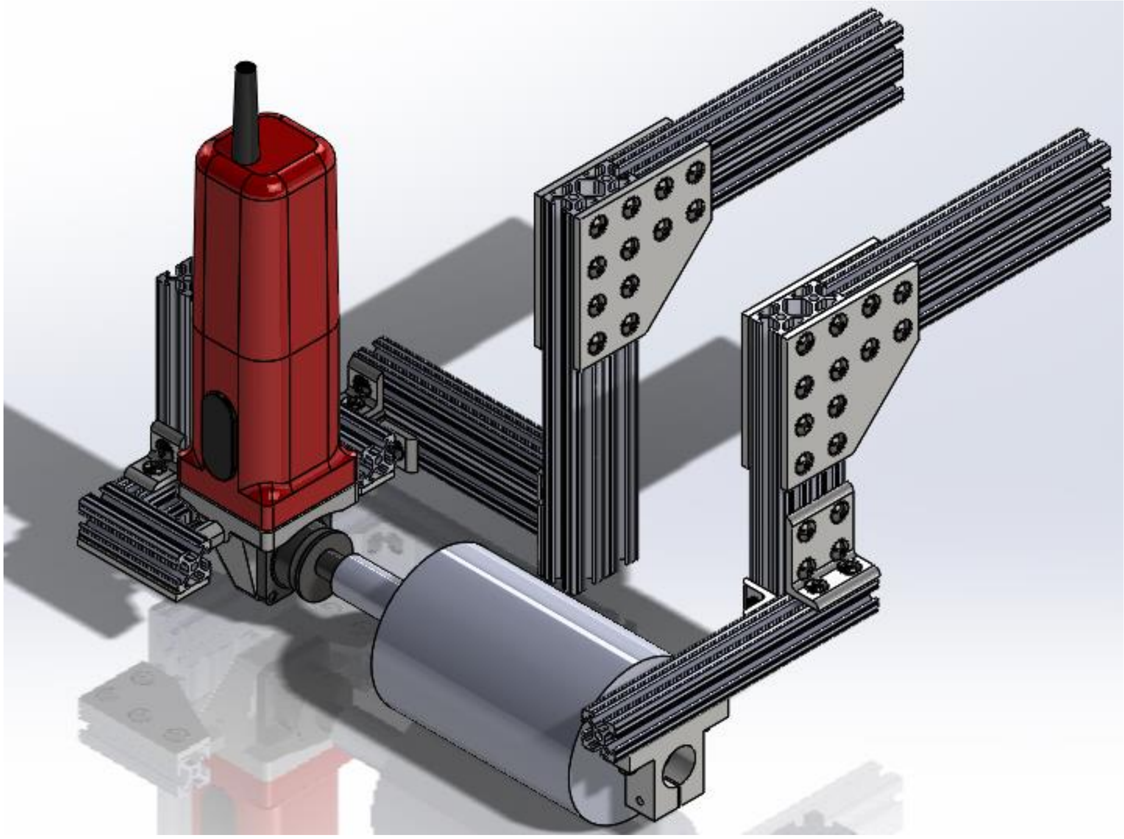

Figure 96: Wire cleaning mechanism initial design. A commercially available angle grinder powers a stainless-steel wire brush to remove debris from the water wall surface.

Economical, mechanical, and electrical constraints were placed upon the design of the cleaning mechanism. With consideration to the overall project objective, the design of the wire cleaning brush system must assimilate with the mobile robot platform and control can be integrated with a centralized controller. It was desired the mechanism apply a constant force to the water wall to provide a consistent cleaning action along the length of the brush.

Starting with the initial idea that a wall containing rust and other contaminants needs to be cleaned in preparation for any cracks in the pipe’s exterior could be fixed. As the brush system may be used in conjunction with the NDE sensor system the overall width of the brush assembly was designated to be 6-inches, allowing for single-pass precleaning and evaluation. The brush wires were designated to be made from stainless steel as this provides the longest life cycle of commercially available wire brushes while also having a lower potential for contaminant transfer. With consideration to future system integrations and modifications it was desired the frame be modular.

Mechanical Design:

An angle grinder provided a ready-made platform designed for wire brush metal cleaning. One would provide the desired rotational speed and torque of the brushes while protecting the motor from dust and debris, while the right-angle gear case provides a compact form factor. To account for the increased width of the brushes compared to the typical application an 11.0 A DeWalt DWE402N with a 5/8”-11 threaded arbor was specified.

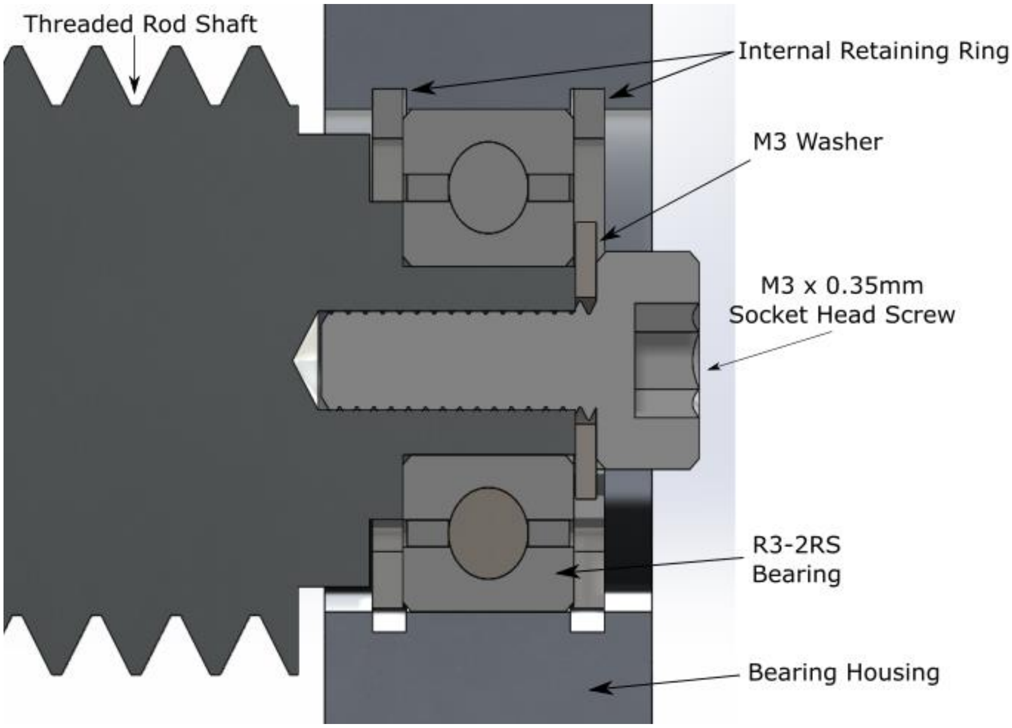

Figure 97: Depiction of the brush shaft stepped shoulder design and interface with the bearing housing.

A 6-inch wide brush adaptable to an angle grinder is only available as a custom solution which is costly and has a long lead time. Moreover, when any one section is damaged the entire custom brush must be replaced. A modular, readily repairable solution was developed by utilizing standard 4” diameter stainless steel wheel brushes with a 5/8”-11 arbor thread stacked in series on a 5/8”-11 stainless steel threaded rod. To evenly space and secure the wire brushes jam nuts were placed between successive wheel brushes and on either end. Sharing the same thread size, the angle grinder arbor and brush shaft were connected via a coupling nut with a jam nut to ensure the assembly does not back out. On the opposite end of the shaft a shoulder step was machined to mate with a R3-2RS sealed 440C stainless steel ball bearing. An M3 x 0.35mm internal thread was placed axially and an 8mm long socket head cap screw with a washer were used to axially fix the shaft to the bearing. The bearing was placed in a bearing housing and held axially by internal retaining rings. The shaft-bearing mating is depicted in Figure 97.

By fixing the bearing housing and angle grinder to a frame the brush assembly is fully supported, enabling parallelism to the work surface thereby creating a consistently clean surface along the length of the brush. The angle grinder was affixed to the frame by utilizing the two threaded holes in the body of the angle grinder initially intended for a side handle. The frame was made from 10 series 80/20 Inc. T-slotted framing rails, an imperial sized system, but the angle grinder had M8 x 1.25mm threaded holes. To facilitate attachment of the two male-female hex thread adapters with an M8 x 1.25mm male thread and ¼"-20 female thread was used. For additional support the angle grinder's cylindrical body was affixed to a vertical stanchion of the frame with a hose clamp. The mounting of the angle grinder and the brush assembly can be seen in Figure 98.

Figure 98: Attachment of angle grinder to frame. Vertical stanchion and hose clamp at center and the two male-female hex thread adapters with an M8 x 1.25mm male thread and ¼"-20 female thread on sides of angle grinder body.

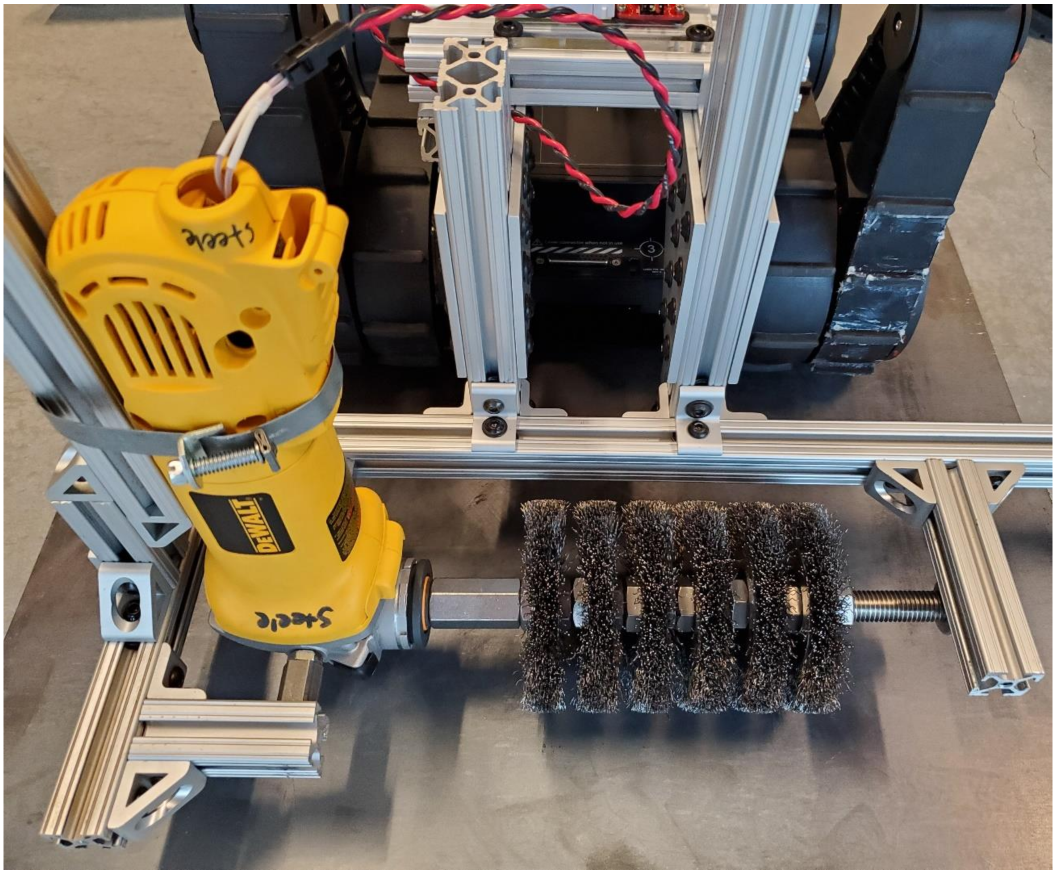

Figure 99: Angle grinder and brush assembly fully supported and mounted to the 10 series 80/20 Inc. frame.

Keeping with the initial design intent of a modular system to accommodate future improvements the frame was manufactured using 10 series 80/20 Inc. T-slotted framing rails. The orientation of the framing rails allows for a variable width brush assembly, change in height of the brush with respect to the water wall surface, and the brush assembly can be shifted laterally from its centerline position. To install the frame to the RoboteX Avatar III platform a T-slotted framing rail was mounted to the preexisting threaded inserts with standoffs to place the rail clear of the I/O ports of the robot platform. The mounting of the frame to the robot can be seen in Figures 99 and 100.

The finalized frame design simplified the mounting of the angle grinder and employed a single profile rail aft of the brush assembly as opposed to the initial decoupled design. These changes reduced the potential points of failure, created a more ridged mounting platform and increased the vibrational dampening. Due to the viscoelastic behavior screws exhibit in a vibrational environment, particularly in the high frequency produced by the brush cleaning mechanism, thread locker was applied to all screws to prevent them coming loose during operation.

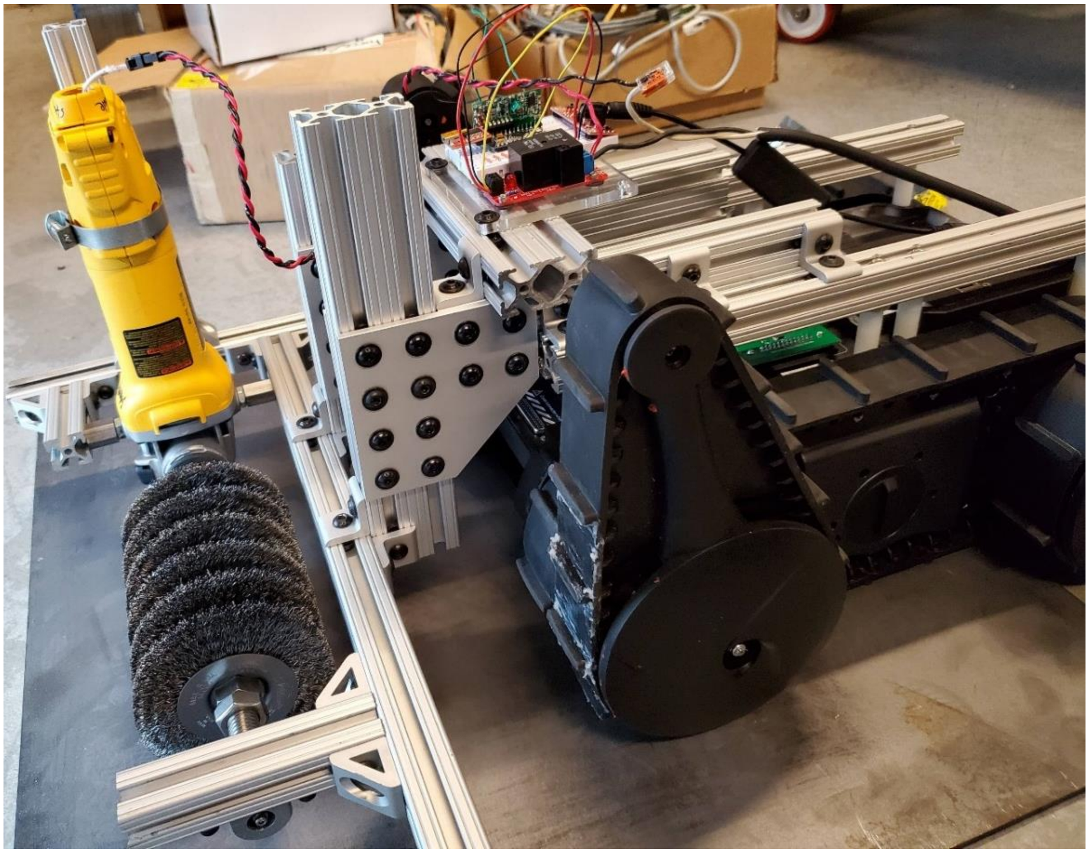

Figure 100: Overview of wire brush cleaning mechanism.

Electrical Design:

To facilitate teleoperation of the brush system the components of the manual paddle switch were removed and replaced by an electromagnetic relay. This relay is essentially a switch which we can control via a control signal rather than a tactile depression of the standard switch. The 20A/10A SPDT relay was wired onto the positive leg of the power cable input, between the power cable and motor. For this particular relay a 5V signal is required. We utilized a 5V 16MHz Arduino for this version. A 4-channel wireless RF remote control was wired into the Arduino, providing us with the safety and ease of use of untethered remote control over the brush system. Typically, there is signal noise associated with triggering a microcontroller from an external source, particularly with this RF system. To ensure reliably safe control of the brush cleaning mechanism actuation a 1kΩ resistor voltage divider was added. Additionally, with the relatively high current of the angle grinder the Arduino is unable to provide a current source high enough to retain constant solenoid contact. Therefore, a 5V breadboard power supply was utilized to power both the Arduino microcontroller and the relay. The wiring diagram is included in Figure 101. The 5V reference for the relay would also be transferred to the Jetson, eliminating the need for the additional external power supply currently being utilized. A bill of materials for the wire brush cleaning mechanism is shown in Table 15. the finalized PCB was created as shown in Figure 102.

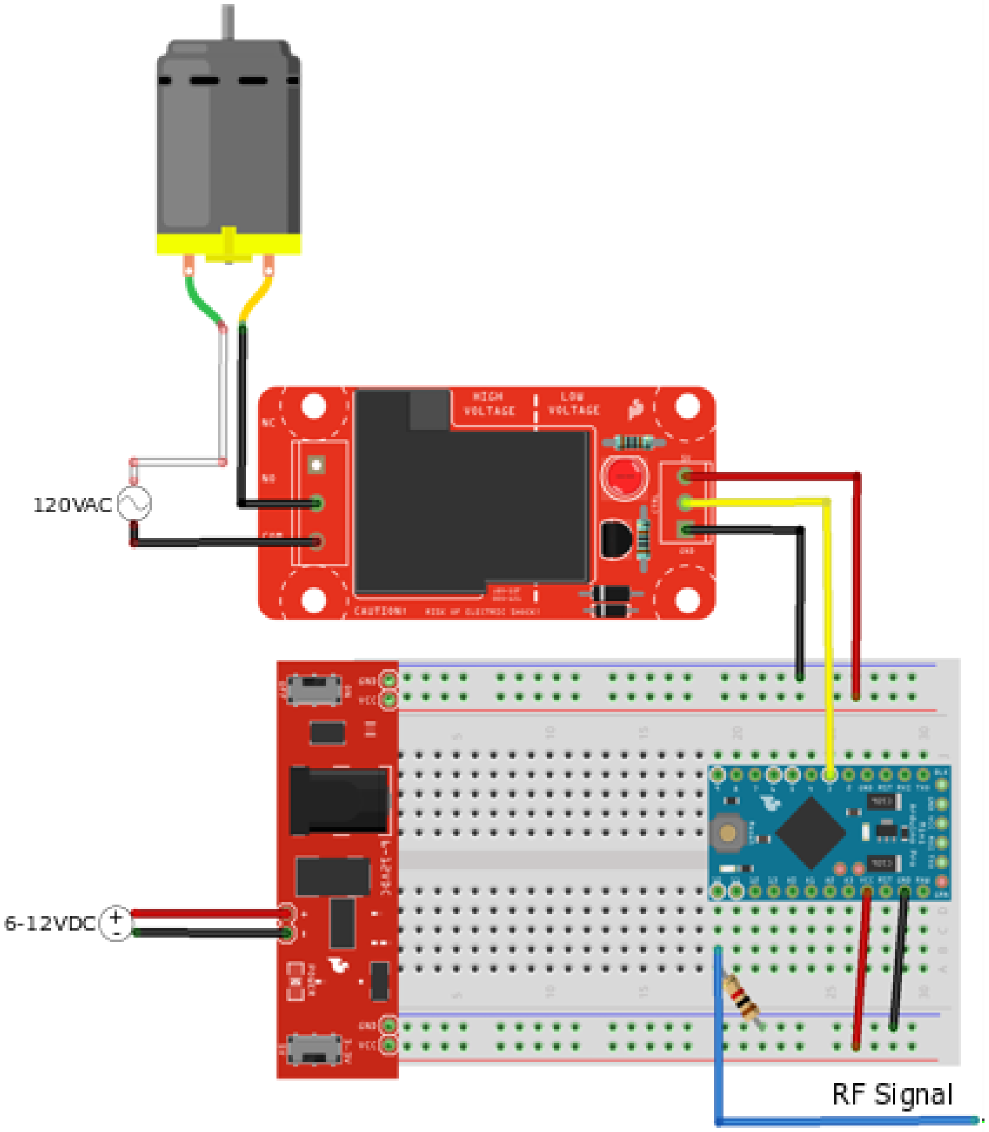

Figure 101: Electrical wiring diagram depicting the connections to remotely control the brush cleaning system.

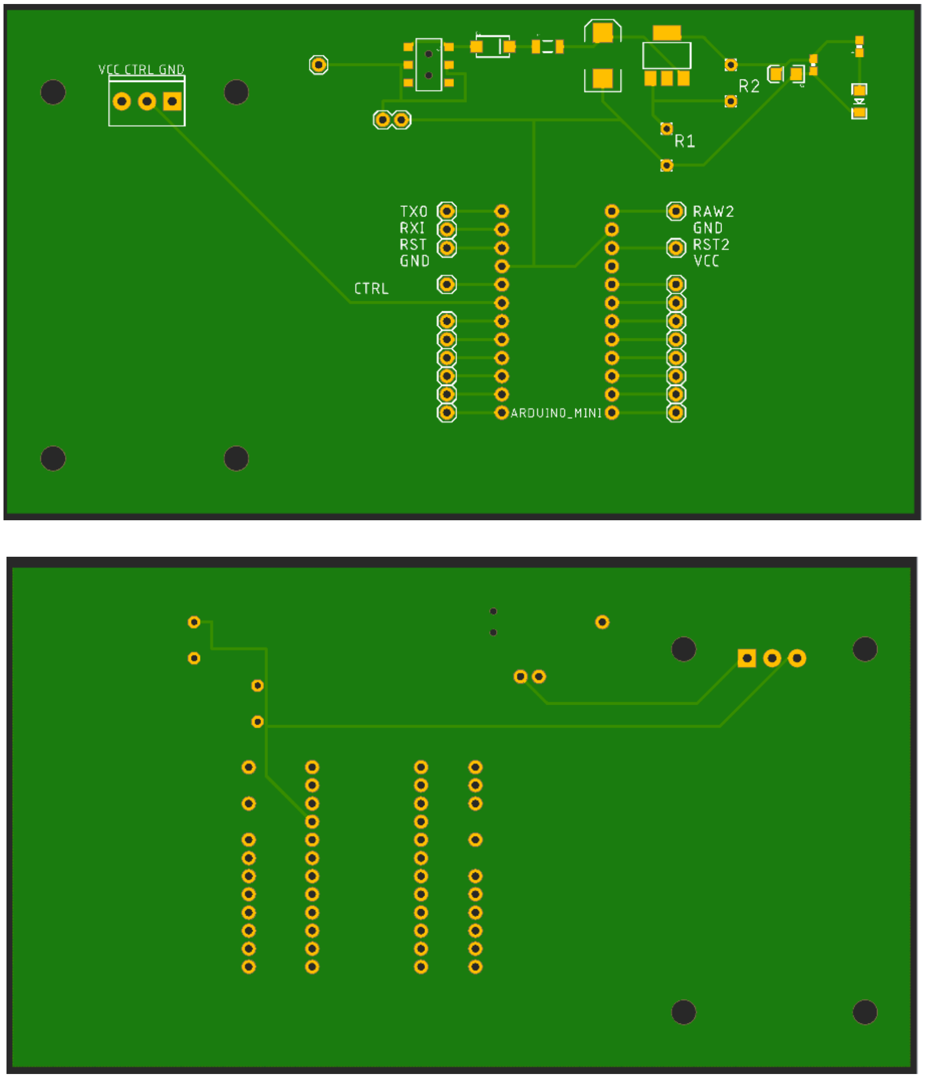

Figure 102: Top and bottom of completed PCB.

Experimental Results:

Testing of the mechanism went as expected. The cleaning mechanism withstood the torque of the motor and stayed mounted to the robot. The grinder was able to power the rotation of the brush while being pressed into a metal sheet. Once removed from the metal it was evident that the mechanism had removed most of the built-up grime. While the brush system cleaned the surface, it was inconsistent due to less than required preload force of the brush on the surface plate, as shown in Figure 103. This lessened preload did not force the bristles at the outer diameter to splay out as designed. To remedy this additional preload force was applied. Additionally, the space between each wire wheel could be decreased and/or the static system currently controlling the downforce could be made to be dynamic with a hinge and spring system.

Table 15: Bill of materials for cleaning mechanism.

ITEM	Quantity	Purpose	Source	Part #
18-8 Stainless Threaded Rod, 5/8”-11	1 Foot	Brush Shaft	McMaster-Carr	98804A123
Wire Wheel Brush, 4” Diameter 5/8”-11 Thread	6	Brush	McMaster-Carr	4896A71
18-8 Stainless Steel Coupling Nut, 5/8”-11 Thread	1	Shaft-Grinder Coupler	McMaster-Carr	90268A035
18-8 Jam Nut, 5/8”-11, Packs of 10	1	Brush Securement	McMaster-Carr	91847A540
R3-2RS Sealed Ball Bearing	1	Shaft Support	McMaster-Carr	6138K64
Ball Bearing Housing	1	Bearing Support	McMaster-Carr	2829N2
12L14 Carbon Steel Hex Bar, 5/8” Wide	1 Foot	Grinder Attachment	McMaster-Carr	6606K212
Pipe Clamp, Smooth Band, 1” to 5” Clamp ID	1	Grinder Attachment	McMaster-Carr	5420K4
¼-20 x 7/8” SHCS, Washer, Economy T-nut	2	Brush Support Frame	80/20 Inc.	3471
10 S 1” Single Horizontal Base	1	Brush Support Frame	80/20 Inc.	5860
1” x 2” T-Slotted Extrusion	5 Feet	Brush Support Frame	80/20 Inc.	1020
1” x 1” T-Slotted Extrusion	3 Feet	Brush Support Frame	80/20 Inc.	1010
10 S 12 Hole 90 Degree Joining Plate	4	Brush Support Frame	80/20 Inc.	4128
¼-20 x ½” FBHSCS & ECON T-nut	86	Brush Support Frame	80/20 Inc.	3321
10 S 4 Hole Inside Corner Bracket	1	Brush Support Frame	80/20 Inc.	4113
10 S 6 Hole Inside Corner Bracket	1	Brush Support Frame	80/20 Inc.	4175
10 S 2 Hole Inside Corner Bracket	6	Brush Support Frame	80/20 Inc.	4119
10 S 4 Hole 90 Degree Joining Plate	2	Brush Support Frame	80/20 Inc.	4150
10 S 4 Hole Joining Plate	1	Brush Support Frame	80/20 Inc.	4167
DeWalt Angle Grinder	1	Brush Rotational Motor	Amazon	DWE402N
SparkFun Beefcake Relay Control Kit (Ver. 2.0)	1	Motor Control	SparkFun	KIT-13815
Arduino Pro Mini 328 – 5V/16MHz	1	Relay Control	SparkFun	DEV-11113
4 Channel Wireless RF Remote Control	1	Remote Relay Control	Amazon	XY-DJM-5V
SparkFun FTDI Basic Breakout – 5V	1	Serial Communication	SparkFun	DEV-09716
Breadboard	1	Wire Connections	SparkFun	PRT-12002
SparkFun Breadboard Power Supply	1	Relay Power	SparkFun	PRT-13032
Wall Adapter Power Supply – 9VDC, 650mA	1	Relay Power	SparkFun	TOL-15314

Figure 103: Brush system removing mill scale from an A36 steel plate.

3.3. Subtask 3.3: NDE Integration on Robot

The NDE sensor and the enclosure was designed and integrated with the robot. The enclosure is 5.25” L x 5” W x 0.75” H, all parts non-conductive. The housing is made out of Acetal homopolymer (Delrin) and the glass is reinforced with nylon 6/10 fasteners. Currently a Jetson TX2 is being utilized to control the system. At the moment, this size of this device doesn’t currently fit with in the specifications that are being tested. The team is currently considering switching to a Jetson Nano for a smaller form-factor solution.

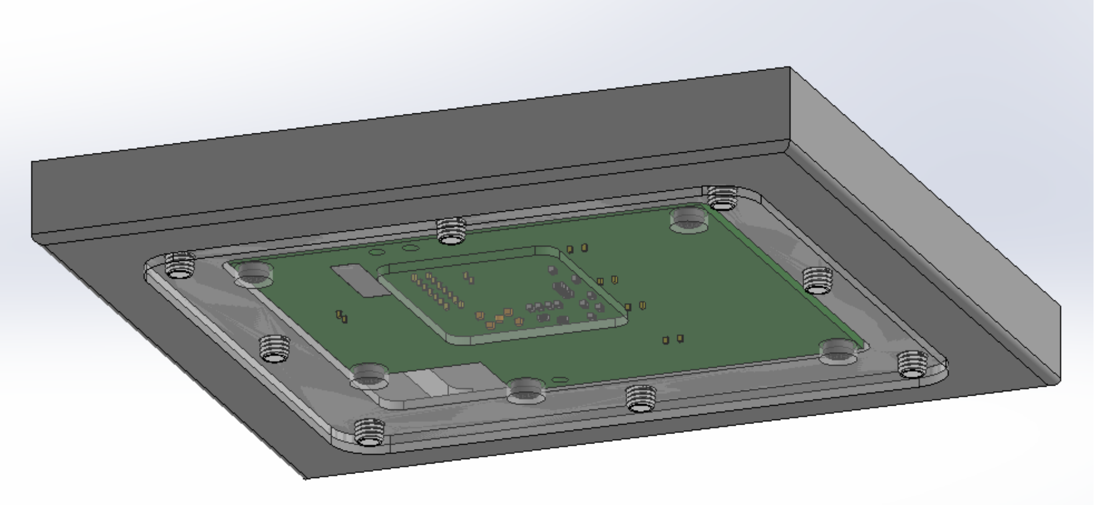

Figure 104: Enclosure design visualization.

The enclosure is 6.28” L x 6.01” W x 0.69” H, all parts non-conductive. The housing is made out of Acetal homopolymer (Delrin). On the top of the enclosure (Figure 105), there are 12 ¼-20 holes for securing to the enclosure to the RoboteX Avatar III. Thermal inserts will be placed into these holes. Securing the cover plate will be Nylon socket cap head screws. On the bottom of the enclosure (Figure 106), the plastic wear plate will be secured with double-sided foam tape for easy access to the sensor as well as replacing the wear plate once damaged. The plate has a thickness of 1/16th” to ensure the best detection. An indentation was created for the foam tape so that the distance from the wear plate and the sensor was as close to 1/16th as possible.

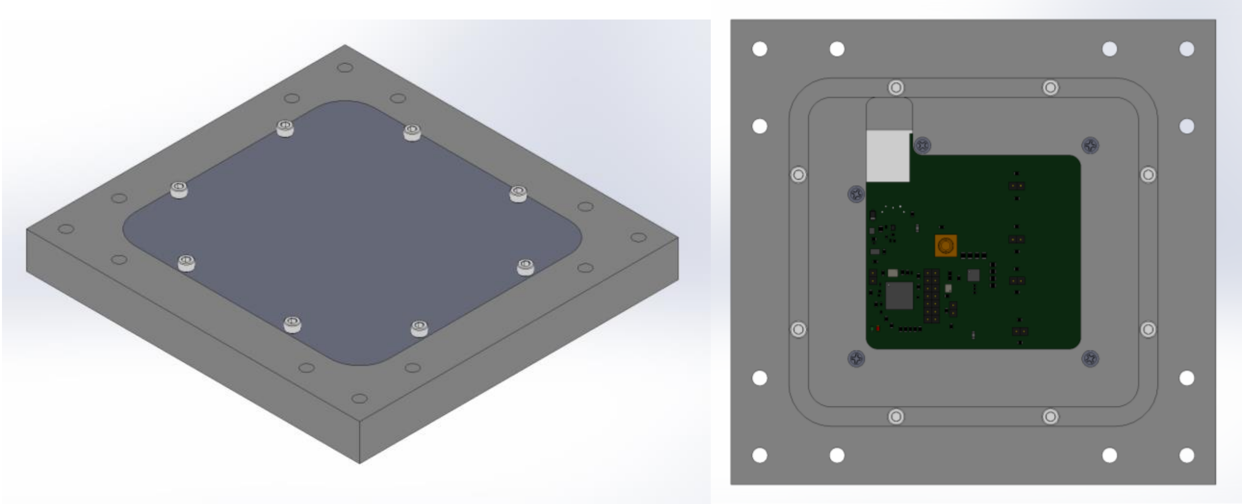

Figure 105: Top of enclosure top of PCB Sensor.

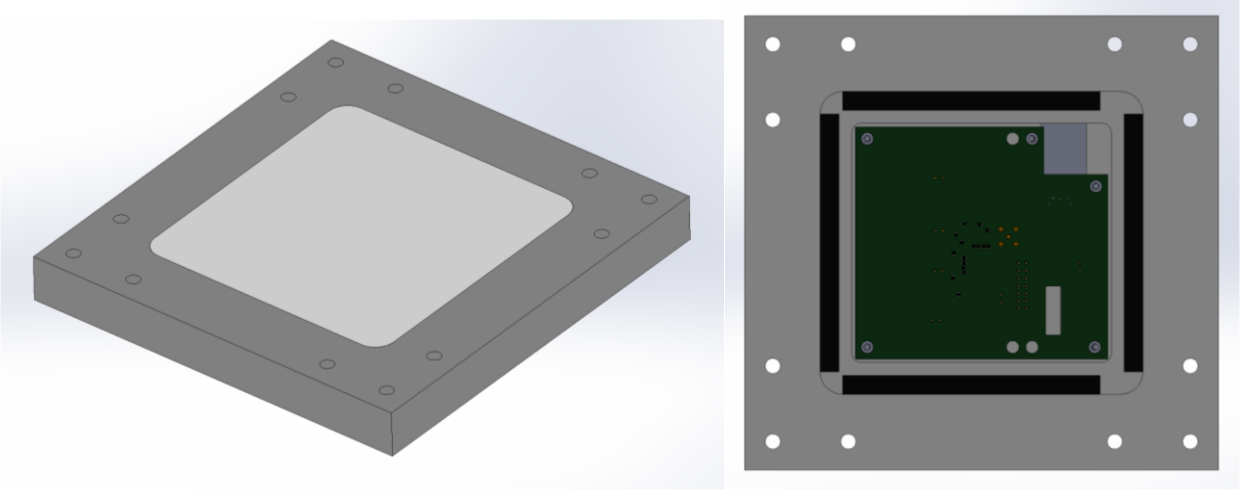

Figure 106: Bottom of enclosure and bottom of PCB Sensor.

Without a gantry system, the NDE sensor can be mounted to the underside of the mobile robot, as shown in Figure 107, where it is pressed against and swept along the steel surface by a spring-loaded mechanism. By keeping the sensor close to the surface during operation, variations in lift-off are minimized which in turn increases NDE data reliability.

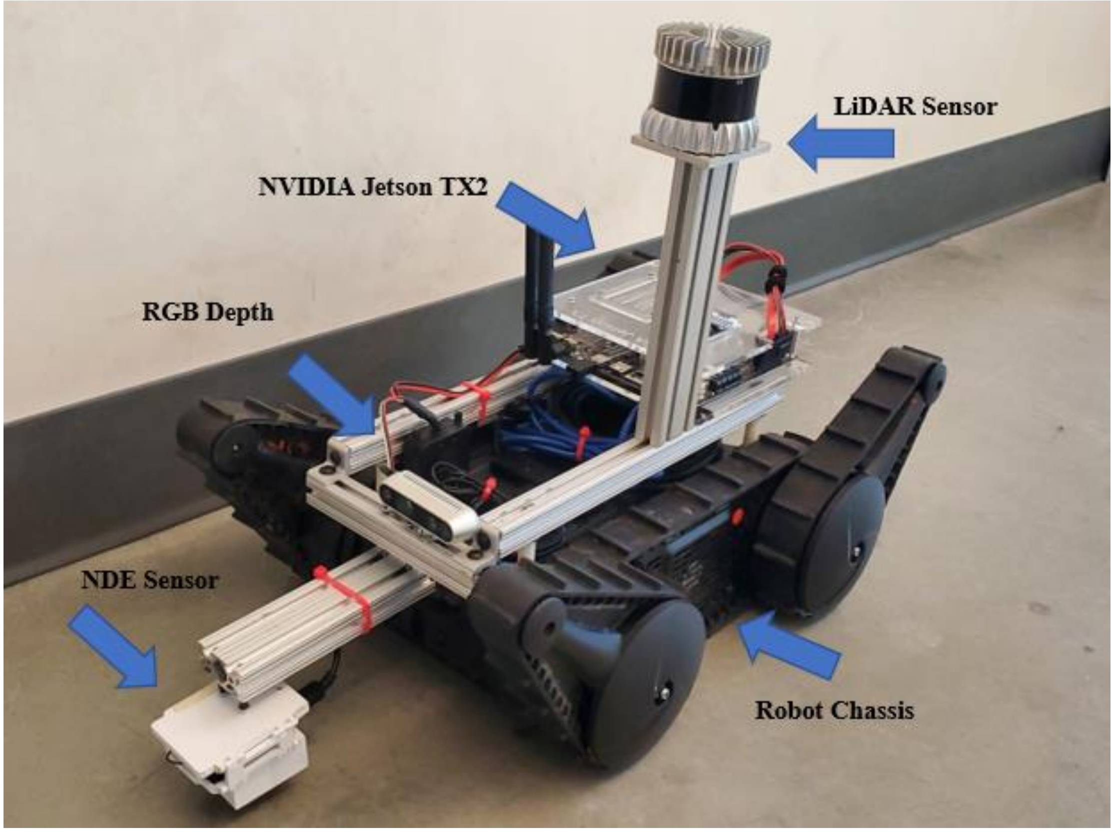

Figure 107: Example of installing the NDE sensor on the robotic platform.

Figure 108 depicts the assembly of a gantry system with NDE capability (the gantry design is discussed in the next section). The system has a sub-millimeter scanning resolution along a single axis and has repair capability along the two-dimensional repair plane. The NDE sensor has an eight channel, two-layer, staggered eddy current coil array which sends data over two separate USB ports to the robots main Nvidia Jetson TX2 computer. The gantry system is controlled via a low-level Latte Panda computer which communicated with the Jetson TX2 over ethernet and controls the motors which give the gantry its xyz freedom of movement. Mounted to the gantry mechanism are four electromagnets seen on its corners. When the robot needs to execute a repair, these magnets are energized so the gantry will remain adhered to the boiler wall while the welding tool plunges into the material.

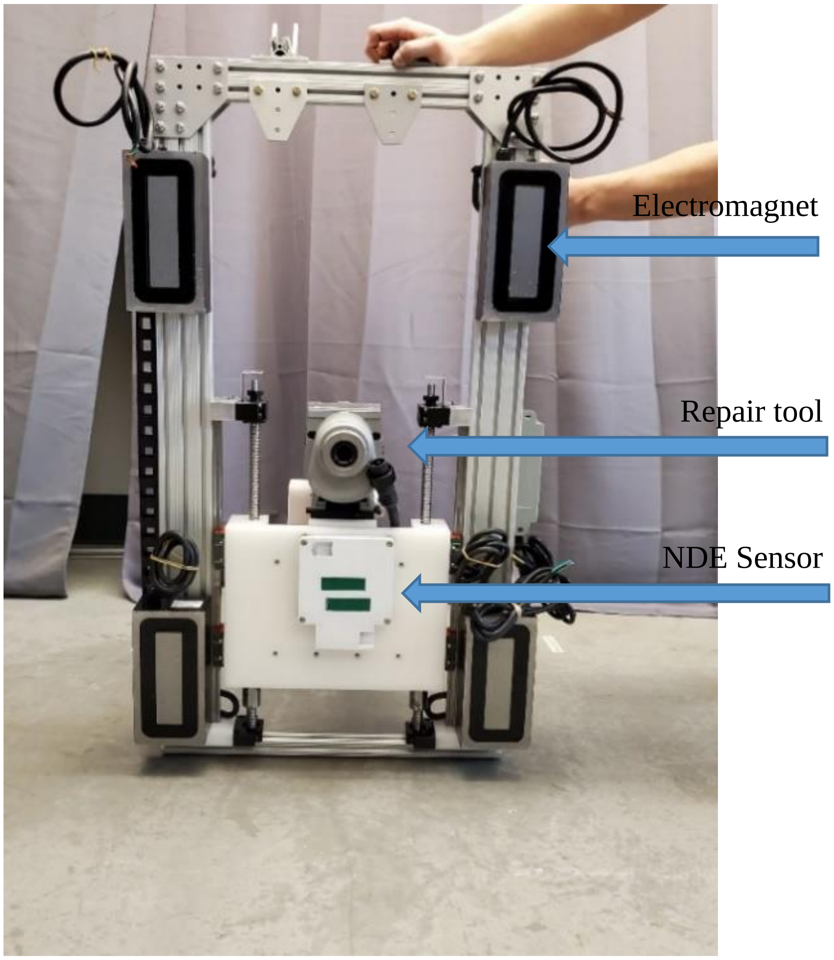

Figure 108: NDE sensor installation.

3.4. Subtask 3.4: Repair Integration on Robot

To effectively perform the FSW task on the robot, the repair system must meet the following specifications:

- Spindle power of 1.5 kW
- Spindle speed of 450 RPM
- Minimum plunge force (Z-axis) of 8.25 kN (5.5 kN specified by welding group, 1.5 safety factor)
- 450 N traverse force in X, Y-axis
- The X, Y, Z axis shall be autonomous and controllable from a single central controller
- The frame and method of X, Y, Z axis control shall be rigid enough to prevent tool fracture

A. Gantry System Design Analysis

We first developed the CAD model of the gantry system. It uses of ball screws and railed carriages due to their high accuracy and resistance to back drive, as well as high factors of safety towards dynamic loading. Further design to the gantry system came in the form of electromagnets at the base of the system, so that the system can ground itself to the climbing surface while the stir welding process is active. The electromagnets specified are capable of 2400 lbs of force, achieving a factor of safety of 1.3. The gantry has also been significantly improved within its compactness, achieving the necessary range of motion for the drill press while being less than half the size within its forward and lateral dimensions (49x47x57 cm versus 17x27x24 cm). This is achieved through more efficient use of the ball screw and rail systems. A final gantry design is the capability of mounting the NDE sensor about its bottom lateral strut. This will allow for rescanning of the crack surface, removing any accuracy of the sensor lost while the robot drives forwards.

All components of the design are subject to high reaction forces from the stir welding process, and as such were checked thoroughly using solid mechanics concepts. The gantry will also undergo comprehensive finite element analysis when the CAD model and part selection have been finalized. As demonstrated within Table 16, all components have sufficient factors of safety. These have been calculated using:

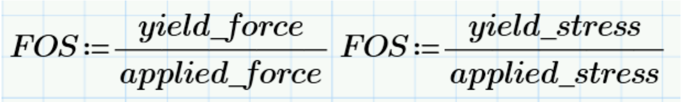

$$FOS := \frac{yield\_force}{applied\_force} \quad FOS := \frac{yield\_stress}{applied\_stress}$$

Table 16: Factors of safety for the gantry system design.

Part	**Applied Forces**	**Dynamic Loading Capacity**	**Factor of Safety**
Carriage and Rail	8 kN Vertical Force	2,400 lbs	1.3
Ball Screw	450 N Axial Force	85,000 psi	14.7
Ball Nut	450 N Axial Force	150 lbs	1.5

Further improvements to the gantry were made through motor reselection for the ball screw travelling systems. Crucially, using a geared brushed motor with an encoder yields the necessary gantry travel accuracy (+/- 0.05 mm, with desired accuracy being +/- 0.5 mm, as described in the following equation), while being lower cost, lower amperage, and lower voltage:

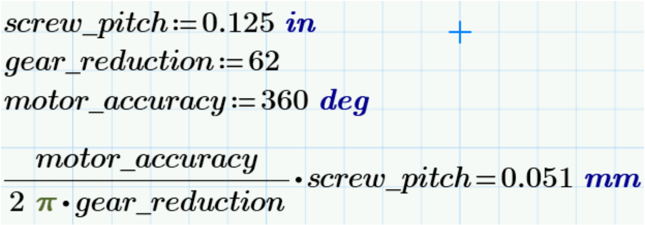

$$screw\_pitch := 0.125\ in$$
$$gear\_reduction := 62$$
$$motor\_accuracy := 360\ deg$$
$$\frac{motor\_accuracy}{2\,\pi \cdot gear\_reduction} \cdot screw\_pitch = 0.051\ mm$$

The performance of the selected motors falls within the torque necessary with a factor of safety of 2.0, while also being capable of eight times faster rpm at lower torque such that the gantry can travel quickly:

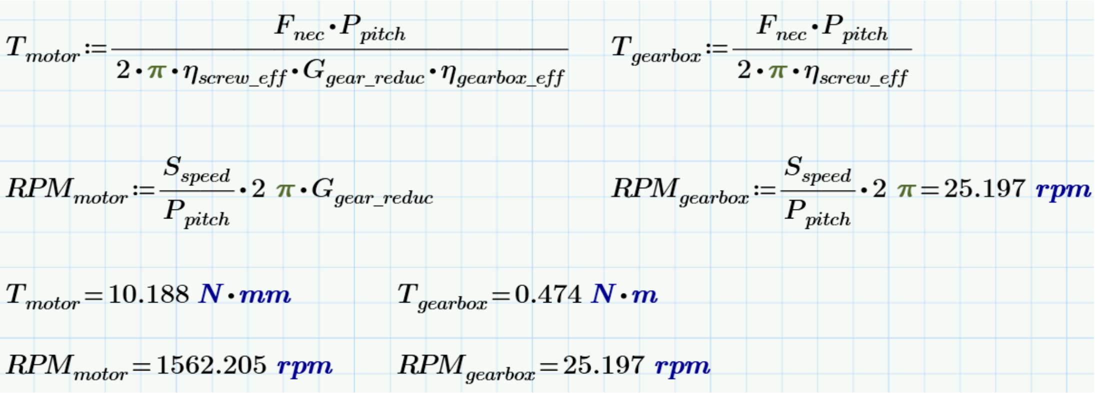

$$T_{motor} := \frac{F_{nec} \cdot P_{pitch}}{2 \cdot \pi \cdot \eta_{screw\_eff} \cdot G_{gear\_reduc} \cdot \eta_{gearbox\_eff}} \qquad T_{gearbox} := \frac{F_{nec} \cdot P_{pitch}}{2 \cdot \pi \cdot \eta_{screw\_eff}}$$

$$RPM_{motor} := \frac{S_{speed}}{P_{pitch}} \cdot 2\ \pi \cdot G_{gear\_reduc} \qquad RPM_{gearbox} := \frac{S_{speed}}{P_{pitch}} \cdot 2\ \pi = 25.197\ rpm$$

$$T_{motor} = 10.188\ N \cdot mm \qquad T_{gearbox} = 0.474\ N \cdot m$$

$$RPM_{motor} = 1562.205\ rpm \qquad RPM_{gearbox} = 25.197\ rpm$$

With the motors being of a lower voltage and amperage, smaller positional drivers are also now viable, allowing use of an Arduino and Adafruit motor shield to control the entire gantry system.

Table 17: Reselected motor specifications.

Motor Properties	**Motor Values**
Necessary Voltage	12 V
Max Speed at high load	130 rpm
Max Continuous Torque	0.23 N*m
Required Continuous Torque	0.115 N*m
Max Continuous Current	0.64 A

The designed parameters of the gantry system are listed as follows:

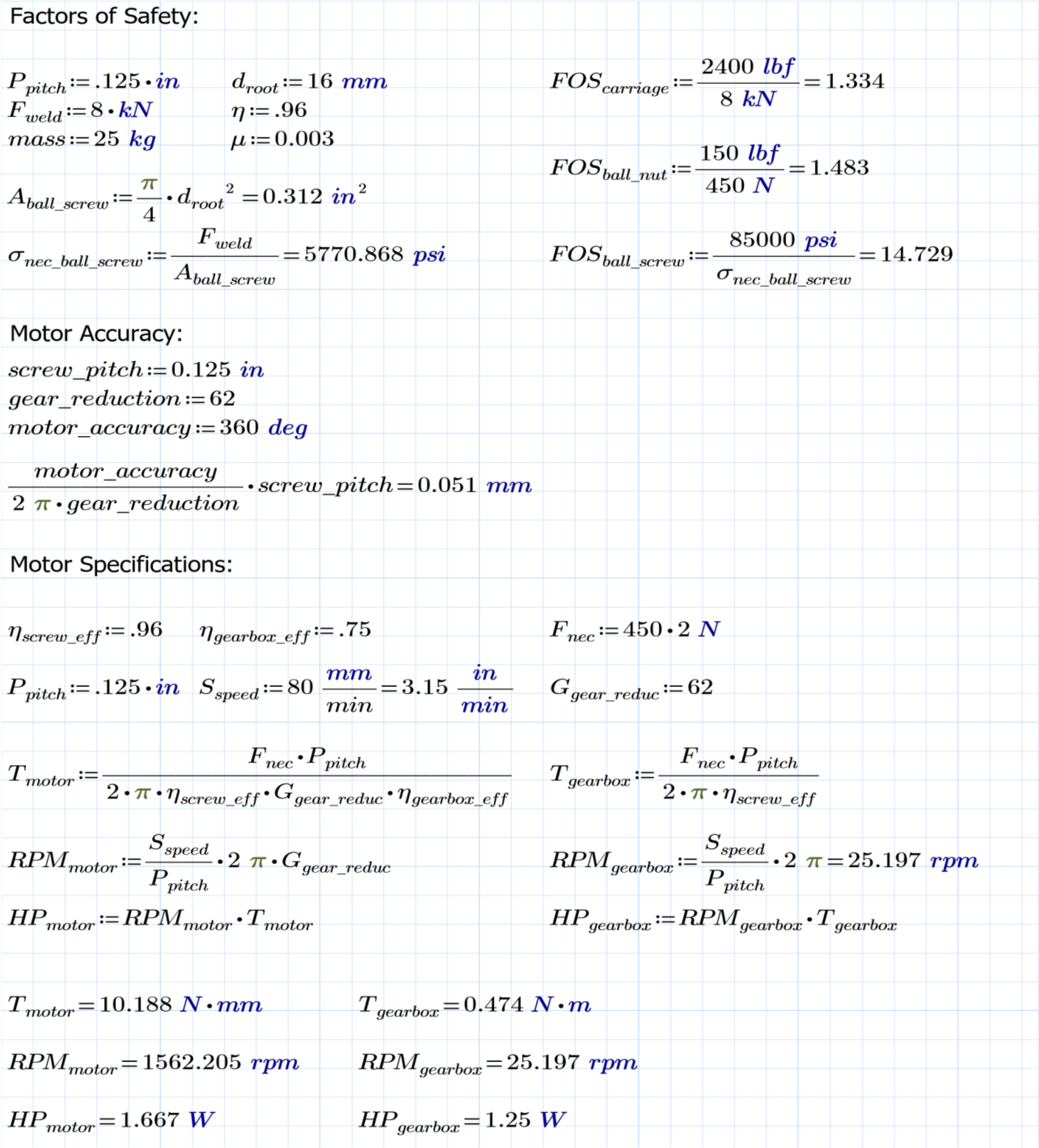

Factors of Safety:

$P_{pitch} := .125 \cdot in$ $\quad d_{root} := 16\ mm$

$F_{weld} := 8 \cdot kN$ $\quad \eta := .96$

$mass := 25\ kg$ $\quad \mu := 0.003$

$$A_{ball\_screw} := \frac{\pi}{4} \cdot {d_{root}}^{2} = 0.312\ in^{2}$$

$$\sigma_{nec\_ball\_screw} := \frac{F_{weld}}{A_{ball\_screw}} = 5770.868\ psi$$

$$FOS_{carriage} := \frac{2400\ lbf}{8\ kN} = 1.334$$

$$FOS_{ball\_nut} := \frac{150\ lbf}{450\ N} = 1.483$$

$$FOS_{ball\_screw} := \frac{85000\ psi}{\sigma_{nec\_ball\_screw}} = 14.729$$

Motor Accuracy:

$screw\_pitch := 0.125\ in$

$gear\_reduction := 62$

$motor\_accuracy := 360\ deg$

$$\frac{motor\_accuracy}{2\ \pi \cdot gear\_reduction} \cdot screw\_pitch = 0.051\ mm$$

Motor Specifications:

$\eta_{screw\_eff} := .96$ $\quad \eta_{gearbox\_eff} := .75$ $\quad F_{nec} := 450 \cdot 2\ N$

$P_{pitch} := .125 \cdot in$ $\quad S_{speed} := 80\ \dfrac{mm}{min} = 3.15\ \dfrac{in}{min}$ $\quad G_{gear\_reduc} := 62$

$$T_{motor} := \frac{F_{nec} \cdot P_{pitch}}{2 \cdot \pi \cdot \eta_{screw\_eff} \cdot G_{gear\_reduc} \cdot \eta_{gearbox\_eff}} \qquad T_{gearbox} := \frac{F_{nec} \cdot P_{pitch}}{2 \cdot \pi \cdot \eta_{screw\_eff}}$$

$$RPM_{motor} := \frac{S_{speed}}{P_{pitch}} \cdot 2\ \pi \cdot G_{gear\_reduc} \qquad RPM_{gearbox} := \frac{S_{speed}}{P_{pitch}} \cdot 2\ \pi = 25.197\ rpm$$

$$HP_{motor} := RPM_{motor} \cdot T_{motor} \qquad HP_{gearbox} := RPM_{gearbox} \cdot T_{gearbox}$$

$T_{motor} = 10.188\ N \cdot mm$ $\quad T_{gearbox} = 0.474\ N \cdot m$

$RPM_{motor} = 1562.205\ rpm$ $\quad RPM_{gearbox} = 25.197\ rpm$

$HP_{motor} = 1.667\ W$ $\quad HP_{gearbox} = 1.25\ W$

B. CAD Modeling of the Gantry System for Repair Tool Integration

The section discusses refining, verifying and finalizing the gantry design shown below. This included locating and ordering items with long lead times, identifying viable drivers and other electronic components, modifying the previous design to conform to the prepared drill press, running FEA on all load bearing components and improving the quality of selected components where it was deemed necessary.

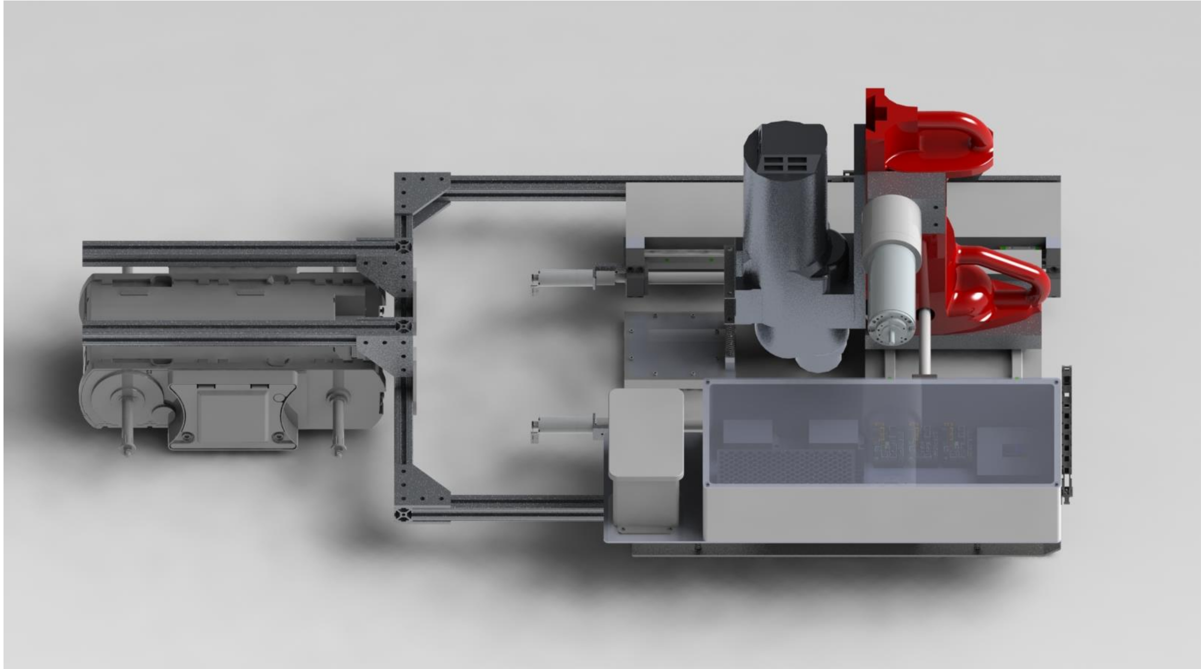

Figure 109: Side view of gantry system design.

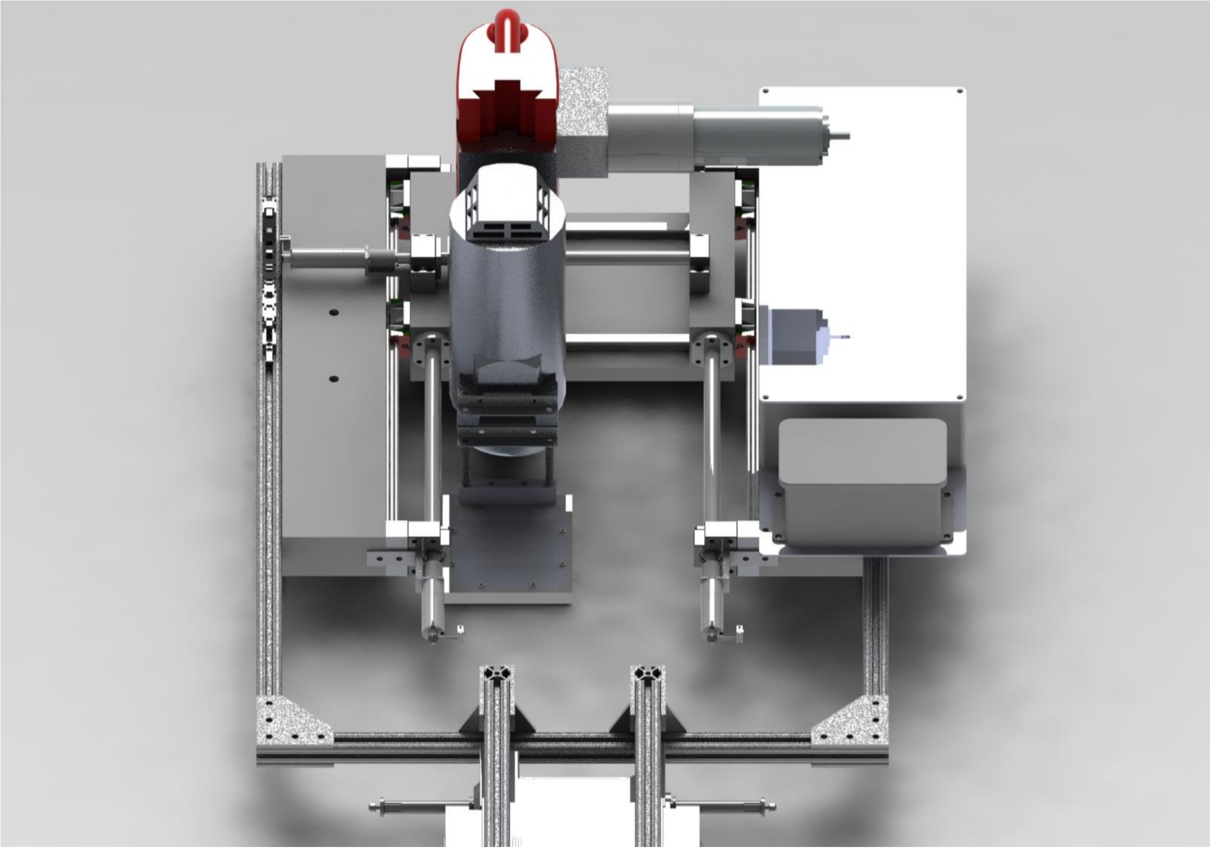

Figure 110: Front view of gantry system design.

The final design modularly interfaces with the robot casing using a reinforced 8020 frame. The design is able to stir weld within a range of 5.9 x 5.3in forward and laterally using high precision ball screws to orient the stir welder. The drill press that is used to stir weld, shown in greater detail below, has been modified with a 113 N*m geared motor so that it can be autonomously lowered with 8 kN of force, as well as a ball screw attachment to allow it to travel laterally.

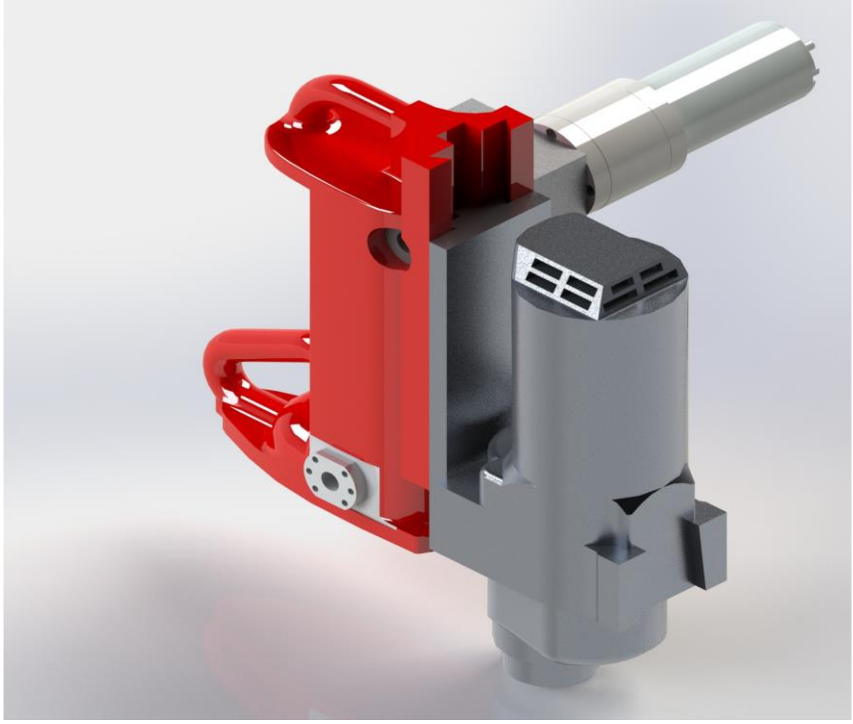

Figure 111: Detailed view of a modified drill press.

Given that the gantry is expected to endure large forces (8 kN vertical loading and 450 N horizontal loading) during the stir welding process, all load bearing machined components have been tested through FEA. Alongside the ordered components part documentation, satisfactory factors of safety have been verified:

Table 18: Finalized factors of safety for the gantry system design.

Part	**Applied Forces**	**Dynamic Loading Capacity**	**Minimum Factor of Safety (FOS)**
Carriage and Rail	8 kN Vertical Force	2,400 lbs	2.7
Ball Screw	450 N Axial Force	85,000 psi	14.7
Ball Nut	450 N Axial Force	150 lbs	1.5
Electromagnets	8kN Vertical Force	1,700 lbs	1.9
Cast Iron Drill Press	113 N*m Torque & 8 kN Vertical Force &	via FEA	1.6

	450 N Axial Force		
Gantry Center	8 kN Vertical Force & 450 N Axial Force	via FEA	4.7
Gantry Siding	8 kN Vertical Force & 450 N Axial Force	via FEA	5.0

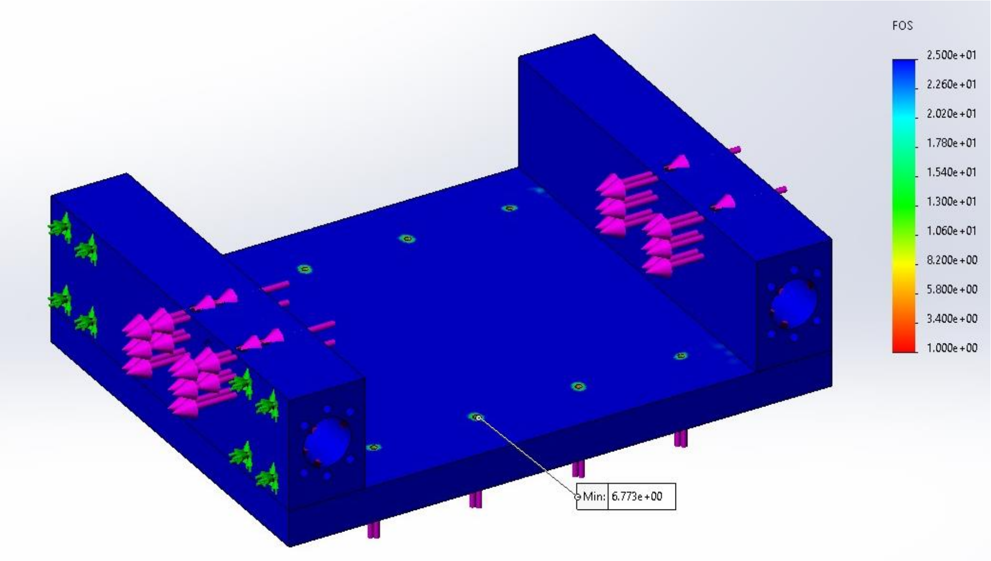

Figure 112: FEA of the factor of safety for the gantry center.

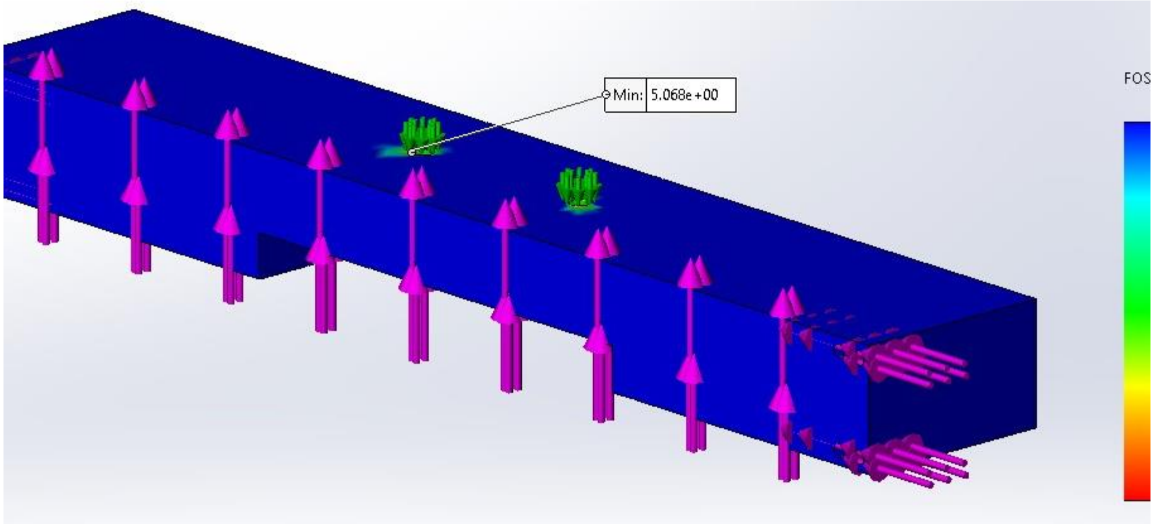

Figure 113: FEA of the factor of safety for the gantry siding.

This gantry system has also been designed to address rough terrain, with suspension being applied to both the sides of the gantry (Figure 114), as well as the NDE sensor (Figure 115). This will allow for a minimum of 1in of suspension, though this can be easily adjusted by replacing the suspension springs with springs of different stiffness or shortening their available length with spacers. The electromagnets, seen at the center of Figure 114, have been strengthened, yielding a factor of safety of 1.9.

Figure 114: Gantry sleds.

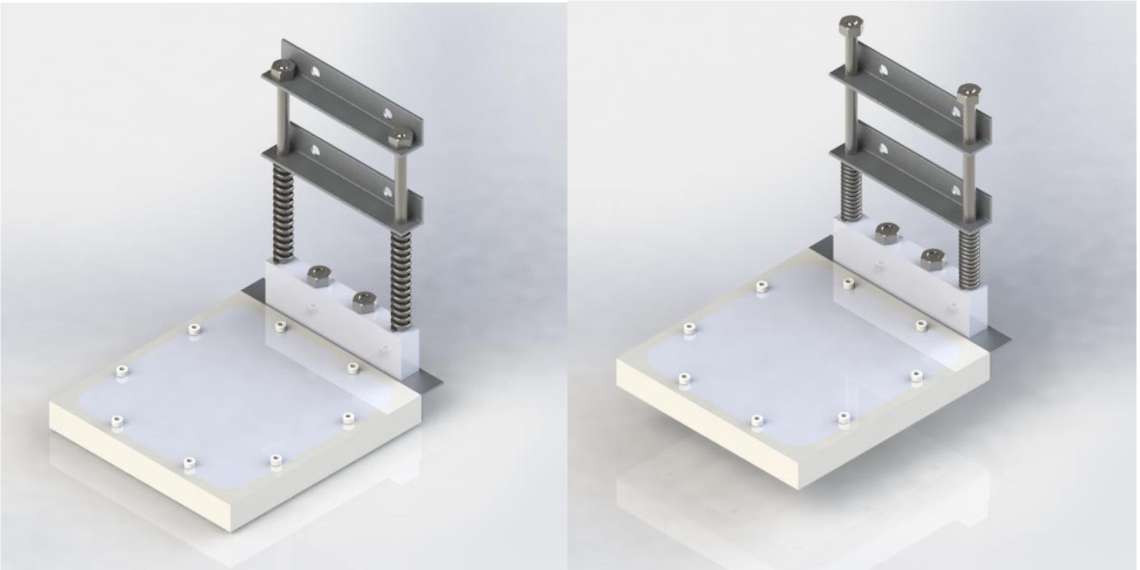

Figure 115: States of suspension applied to the sensor mounting.

We then designed and integrated an electronics box that can autonomously and safely control the electromagnets, positioning motors and drill press. A second critical focus was within refining the repair tool design to be both lightweight and sturdy. The finalized CAD design of the gantry system is shown in Figure 116.

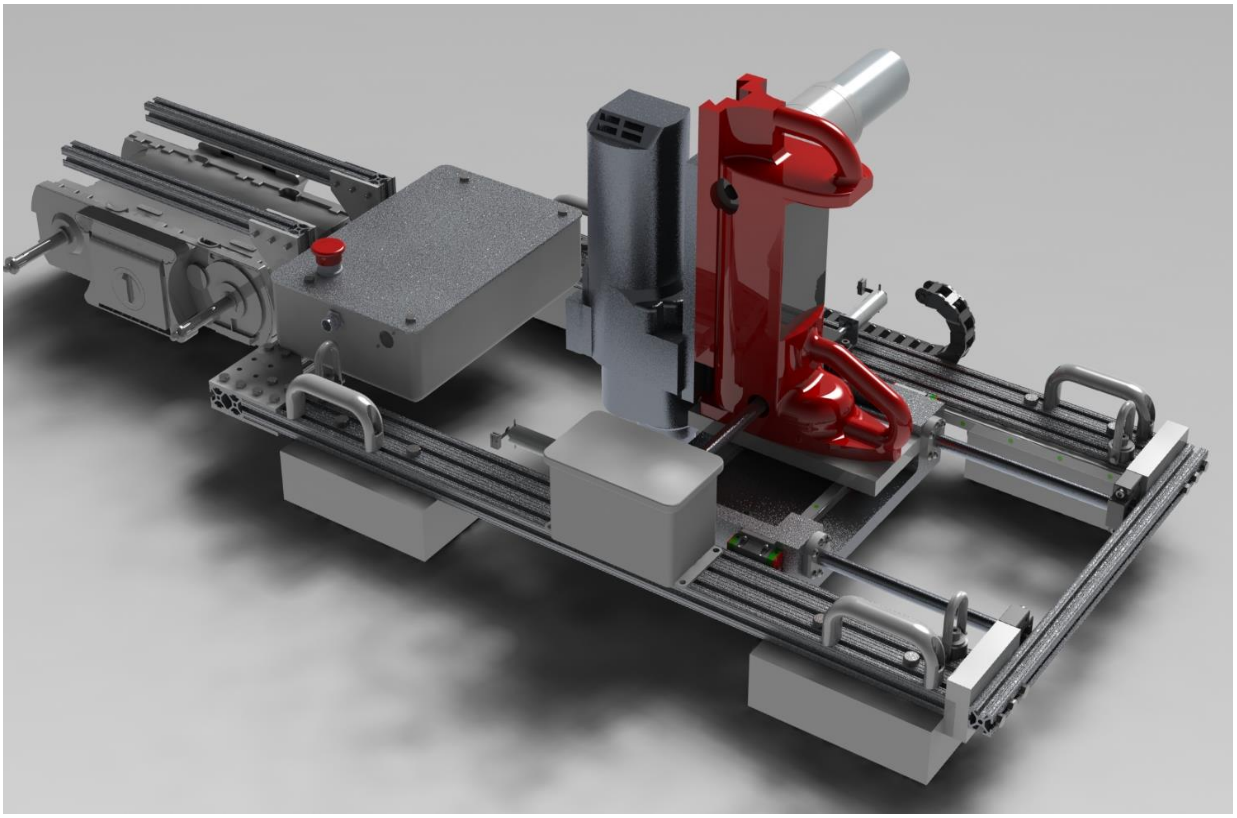

Figure 116: Finalized CAD design of the repair tool and gantry system.

C. Repair Tool and Gantry System Assembly

Actuation of the Repair Tool:

The drill press selected as a repair tool for the gantry system is from Milwaukee tools, and hosts a 1600 lbs of drill point pressure and 400 drill rpm, which are within necessary specifications. The X and Y axis movement of the repair tool bit is propelled by three C7 accuracy grade ball screws (two in parallel on the Y axis). These ball screws are mounted through BK12 and BF12 Pillow Block Type Supports, with a custom 3D printed component to reduce axial play and vibration when the system is welding, shown within Figure 118. This component is mounted to the brushed DC 30:1 gearmotors which drive the ball screws, which allow for accuracy within ~+/- 0.5mm linear travel with a maximum thrust of 900N (twice as much on the Y axis due to it being driven by two motors in parallel).

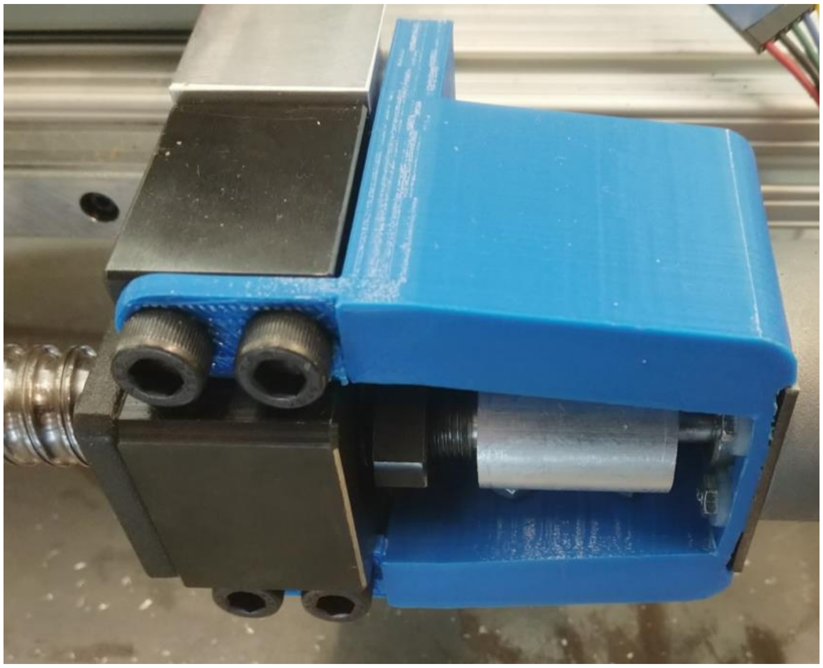

Figure 117: Ball screw mounting and custom 3D printed stabilizing component.

Z axis movement of the repair tool is produced by automating the manually controlled rack and pinion within the Milwaukee 41208-1 drill press. A Maxon brushed DC gearmotor has been installed in place of the standard user operated handle, shown in Figures 119. This gearmotor, alongside the further gear reduction via the rack and pinion, can allow for plunging force in excess of 8000N.

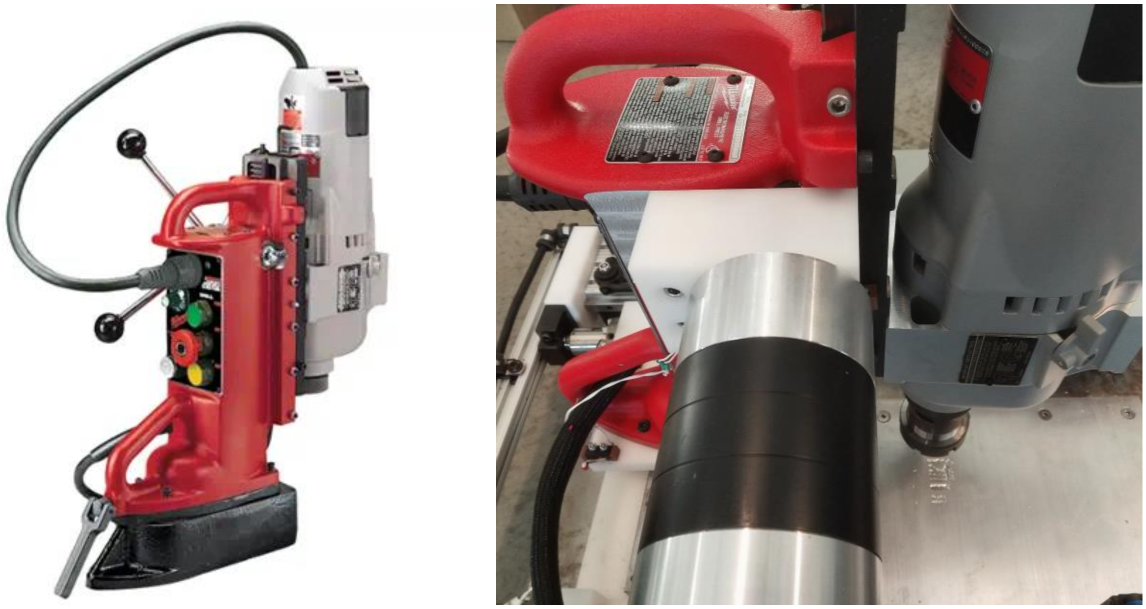

Figure 118: Milwaukee 4208-1 Electromagnet Drill Press with manual handle and custom Maxon motor.

Movement on the X, Y and Z axes is controlled from the arduino and accompanying BTS7960 motor drivers using PID. This is not necessary to prevent overshoot or manage acceleration given the high gear ratios produced through the motor gearing, X and Y axis ball screws and Z axis rack and pinion. However, PID in this case can allow for a target velocity that the motors try to reach and maintain. As a result, if the motors are travelling at an ideal rpm and encounter an increase in resistance, the PID will provide more current to the motor to compensate and maintain the ideal rpm. This is done in code by having a dynamic target position that is constantly incrementing away from the current position. When the dynamic target position reaches the actual final position, it will stop incrementing and allow the current position to catch up. At higher desired velocity, the target position will increment away faster. As a result of this code, if the motor encounters resistance and it begins slowing down, the gap between the dynamic target position and current position will increase, leading to more current being provided until the gap begins to close.

This can be analogized to a man running towards a tree while being accompanied by their dog. The man (or dynamic target position) will continue at a regular pace until they reach the tree (or final position). The (well behaved) dog will not try to outrun the man, and will keep at a constant distance unless the man speeds up, in which case the dog will proportionally speed up. If the dog is having more trouble walking (let’s say there’s snow), they will put in more effort to keep at a normal pace with their owner.

Electromagnets & Frame:

The majority of the repair tool frame is composed of 3”x1” 8020 stock with framing brackets, shown in Figure 119. This allows for reduced weight and 8020 tracks to be used for non load bearing components (For example, mounting of the electronics box, electromagnet transformer, and hose clamps for wire management). Load-bearing joints use ¼-20 bolts or larger for a minimum 20 FOS alongside lock nuts to avoid issues from system vibration. Gantry motion is stabilized and reinforced through HIWIN 15mm linear rails mounted onto the 8020. The central delrin piece (delrin being chosen over aluminum or steel after rigorous FEA analysis for the sake of modifiability, weight and price) is mounted through the linear rails to the 8020 frame, and is propelled using ball nuts on the aforementioned ball screws.

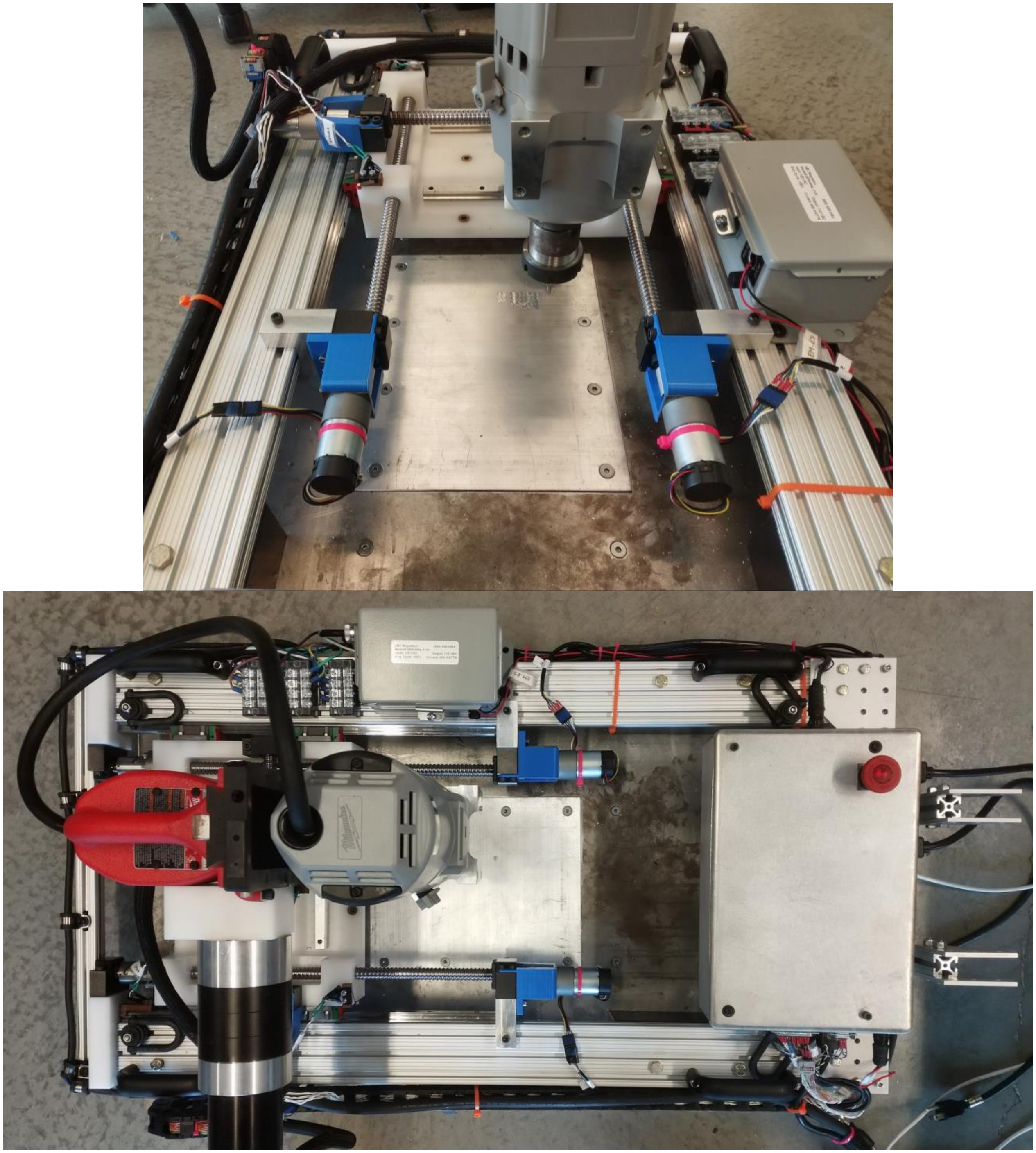

Figure 119: Repair tool frame on the gantry system.

The system can be magnetized to steel using four 120V AC electromagnets shown in Figure 120 to prevent backlash from the welding process. In response to the maximum backlash of 8000N, these electromagnets have a FOS of 1.9. To prevent residual magnetization causing the gantry to be stuck to the steel after welding is complete, these electromagnets are controlled via a transformer shown within Figure 120, which temporarily flips the magnetic current to quickly separate the electromagnets and steel.

Figure 120: Electromagnets and transformer.

Electronics:

The repair tool is controlled via a combination of electronics placed within the enclosure seen in Figure 121, and the wiring diagram within Figure 122. The brain of the electronics is an arduino MEGA ADK, selected for it's large number of pins. A LattePanda was previously used, and is compatible with the current system. However, after it was damaged from a miswire during testing, it was decided to replace it with a less expensive control board, with the MEGA ADK being fully capable of handling the system requirements (the reason the LattePanda was initially selected was that it could handle the main program, which the MEGA ADK currently receives over serial through a laptop. If the system needed to be fully wireless like it might within a production model this would be unviable, but for current prototyping it is reasonable). As seen within Figure 122, the MEGA ADK controls power to the drill and electromagnets using relays, and controls the gantry (X and Y axis) motors and vertical (Z axis) motor using BTS7960 drivers. It also receives data from the five limit switches, shown in Figure 121, installed on the gantry to shut down motors if the gantry tries to go beyond its bounds. To prevent miswiring or shorting, a custom PCB shown within Figure 121 has been designed to mount to the MEGA ADK and connect through ribbon cable to all other electronics.

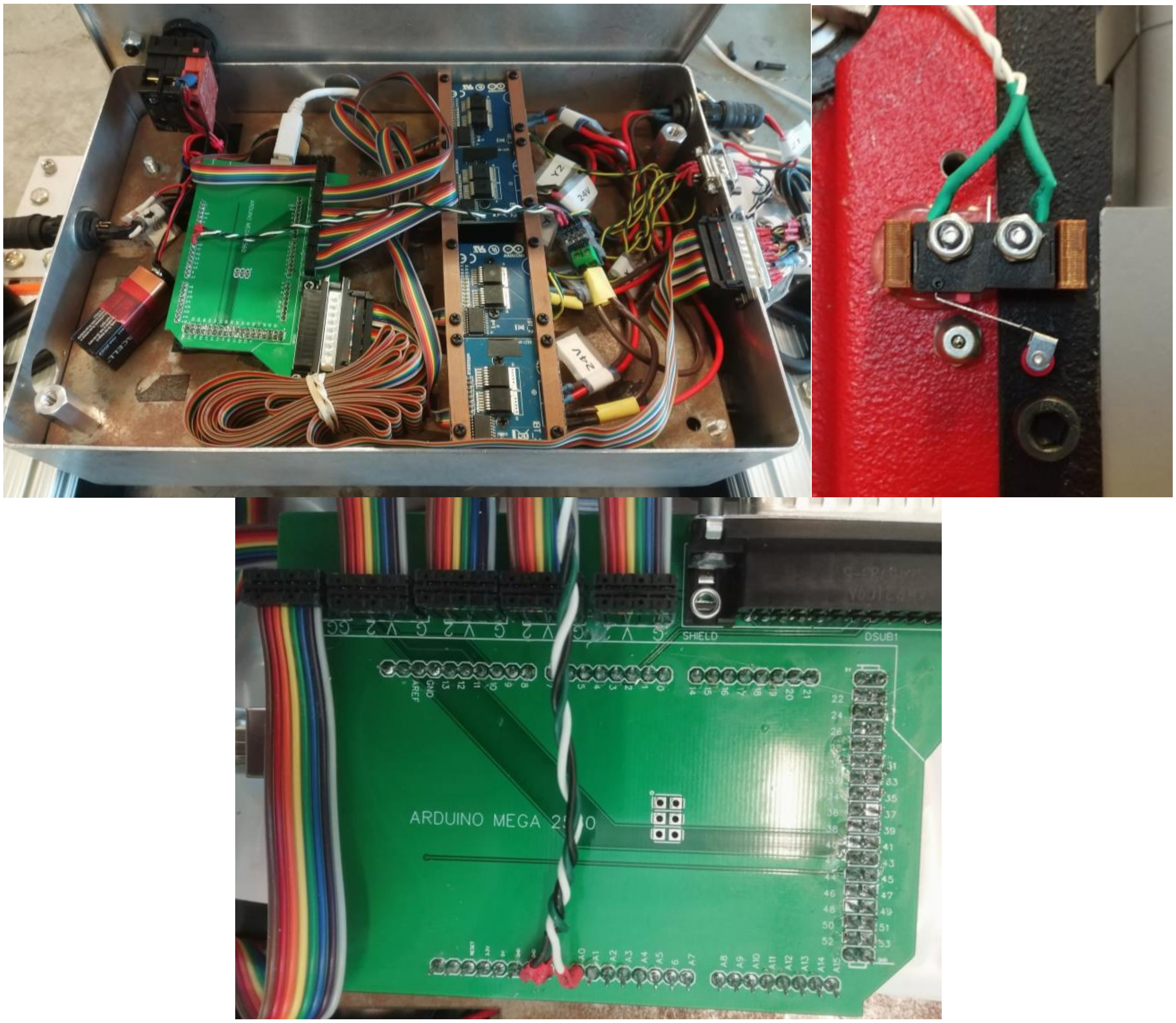

Figure 121: Electronics case, limit switches and custom PCB.

We also integrate motor controllers onto the gantry mechanism. They are designed to move the end effector of the repair tool in vertical direction, as well as, along the surface of the material under repair. We focused on integration of the motor controllers onto the system. Initially it was intended to control the motors using a Basic Micro MCP236 DC motor controller. However due to numerous challenges and ineffective troubleshooting in configuring the controller over the serial bus, we instead decided to use a EPOS4 micro 24/5 CAN module instead, which offers the appropriate hardware for control of the gantry mechanisms motors.

The assembled repair tool on the gantry system is shown by Figure 123. Stabilizing 8020 bracing has been added to the front of the design, as well as hoist rings and handles to allow for manageable lifting, which is critical given the cumulative weight of the frame, motors and electromagnets (~90lbs in total). Though considerable, this level of weight is lower than the previous iteration which used comparatively heavy aluminum blocks for the frame. The current design preserves the strength of the system while reducing weight through the use of 1”x3” 8020 framing. This framing also allows for greater customizability of wiring mounts and other features through the use of T-nuts.

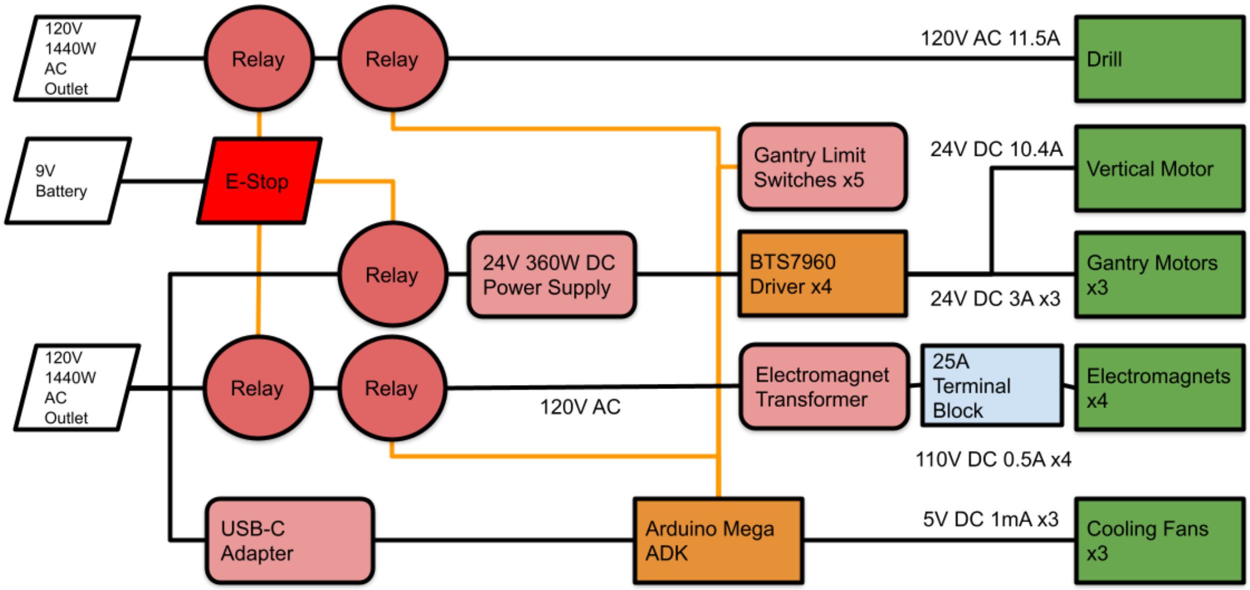

Figure 122: Repair tool wiring diagram.

Figure 123: Assembled repair tool on the gantry system.

Experimental Results in Lab Environments:

We focused on designing the larger steel plate, and designing and machining the material inserts in house (of which there are five of each material - delrin, aluminum and steel). The aluminum backing seen within Figure 124 also had to be machined in house, and allow for the material inserts to be bolted onto the larger steel plate. The testing plate is large enough to cover the repair tool's electromagnets, with the material inserts covering the entirety of the repair tools range. The testing plate being composed of steel allows for activation of the electromagnet systems, which also allows for safe testing of the welding process. Furthermore, the material inserts are able to be quickly removed and reinserted without removal of the repair tool, allowing for a streamlined testing process.

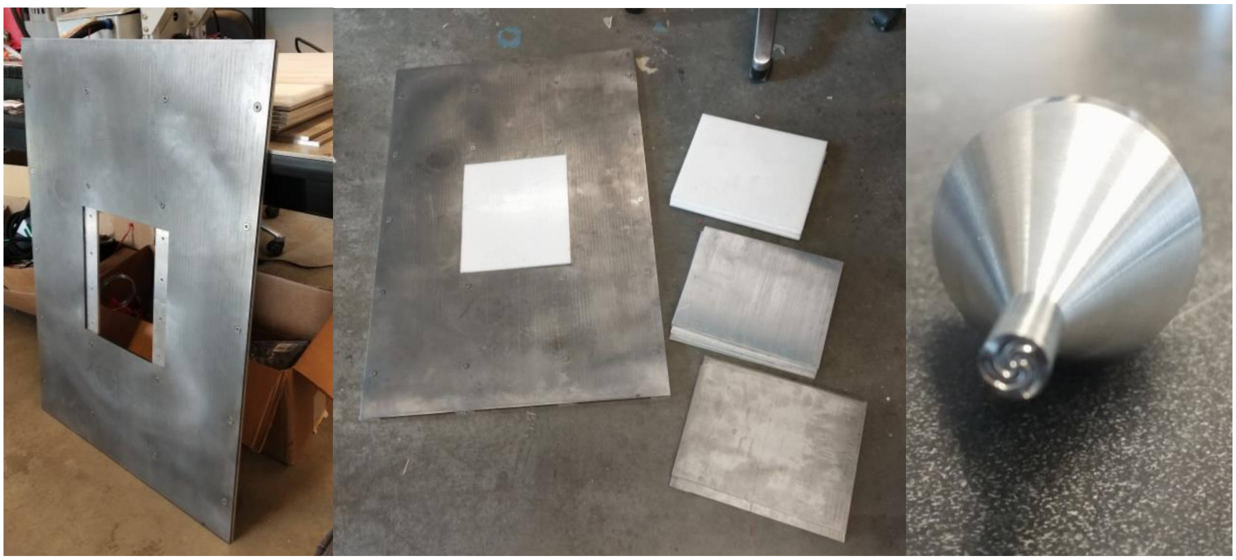

Figure 124: Testing plate, material inserts and stir welding bit.

The gantry operates on an arduino in communication with a Windows PC (further referred to as the PC). On queuing from the PC the gantry will initialize arduino code alongside electromagnets and cooling fans. On a second queuing the gantry will begin a homing sequence. From here, positional data and related target velocities can be sent to the arduino, with the gantry completing these tasks to produce welds on previously cracked plates. On failure of any of these tasks or the startup and homing processes, the arduino will send a descriptive error code to the PC and shut down safely.

Figure 125: Close up of X direction results, and X (left) and Y (right) welding passes.

The designed repair tool on the gantry system is able to apply ~8000N of drill pressure to a 15cmx15cm section of aluminum or delrin testing material using a stir welding bit shown within Figure 124, and using that pressure alongside the drill itself, can weld together previously cracked sections of that testing material.

As can be seen from Figures 125, the repair tool is capable of multiple welding passes in both the X and Y direction. Figure 125 shows that X direction welding is more stable (given that the bit has less vibration while travelling, leading to a less crooked weld). This is due to one of two possibilities - one is that moving along the grain of the metal material yields less vibration, and two is that the overall gantry frame better supports X travel. This could be tested by using material that has grain travelling in the Y rather than X direction, or rotating the repair tool ninety degrees (which would require it to be locked to the floor manually rather than with its electromagnets given that the testing plate does not support the repair tool in that orientation). A second current issue can be seen with the thinner starting weld on the top weld, and multiple other welds in Figure 125. This is due to the drill not moving immediately following the plunge, likely due to too much initial pressure on the plate. As a result, the bit first sits at the start of the weld, then following the PID code described in the following actuation section ‘jumps ahead’ in order to maintain the overall desired velocity. This can be resolved by adjusting the starting plunging force, as well as improving the PID algorithm.

4. Task 4: Artificial Intelligence Development

In this task, artificial intelligence (AI) capabilities were developed to enable robots to automate data gathering (e.g., to map the environment) and perform predictive analysis (e.g., to track cracks across multiple inspections and to recognize cracks using machine learning methods).

4.1. Subtask 4.1: 3D Mapping and Data Fusion

Algorithms for 3D mapping and data fusion were developed and analyzed. The goal is to create a mapping algorithm capable of accurately mapping industrial boiler environments and capture multi-layer information such as surface defects or navigation landmarks. A custom, voxel-based loop closure detection technique has been developed and an over simultaneous localization and mapping (SLAM) package was also developed.

Simultaneous localization and mapping (SLAM) can be thought of as two components: the front end and back end. The front end is responsible for data acquisition and data fusion. The back end is responsible for error minimization and maintaining an accurate, global representation of the world. Loop closure detection described above is a component of the back-end of SLAM. In order to enable SLAM on the boiler inspection and repair rover, it is critical to develop a full SLAM package that includes both a front end and a back end.

A key component of enabling simultaneous localization and mapping for robots is loop closure detection. Loop closure detection describes the capability of mobile robots to recognize previously visited locations. This recognition helps to minimize accumulated error encountered during navigation. Figure 126 below visualizes the loop closure detection problem. The green trajectory might illustrate the robot’s path in the real-world while the red trajectory might illustrate the estimated robot path. Notice how the amount of difference between the red and green paths increases as the robot navigates; this is because the error compounds as navigation occurs. Enabling a robot to recognize the red dot as the green dot can enable the robot to correct the error accumulated during navigation.

In support of this capability, the team developed a novel loop-closure detection capability called Voxel-Based Representation Learning (VBRL). VBRL utilizes only point cloud data collected from a LiDAR sensor for loop closure detection. It is capable of learning both voxel importance and feature extraction modality importance for the loop closure detection task. Figure 127 below illustrates the VBRL method.

Given a set of 3D point clouds acquired during robot navigation, VBRL learns which 3D voxels are important to differentiating between point clouds as well as which feature extraction modality is most important. Weighting the place recognition algorithm with these learned weights yields more accurate loop closure detection results than simply using the feature extraction modalities alone. The team is confident that this loop closure detection method will provide accurate loop closure detection results in the industrial boiler wall environment.

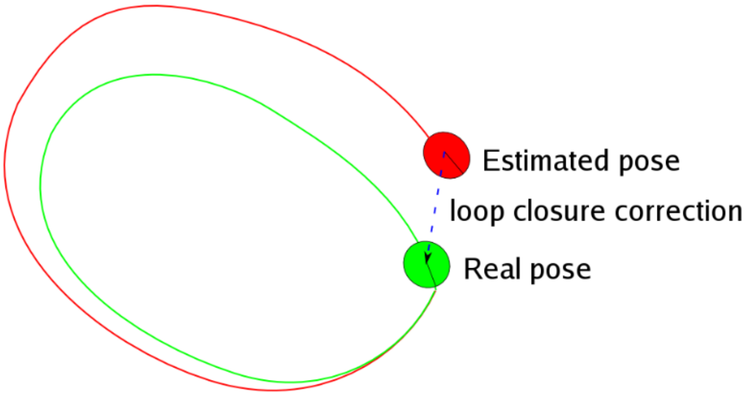

Figure 126: Loop closure detection visualized.

The latest release of MATLAB (R2019B) includes a navigation toolbox with a graph-based representation of 3D navigation data. In addition, MATLAB has a few built-in functions for point cloud registration. A preliminary SLAM software package has been developed this project that uses normal distribution transform for point cloud registration, MATLAB navigation toolbox algorithms for maintaining a graph data structure, and VBRL for loop closure detection.

For boiler repair and inspection the capability of tagging surface defects to the navigation map is critical. MATLAB's pose graph data structure in the navigation toolbox can easily be augmented to contain more metadata about the environment. Tagging pose graph nodes with information ranging from surface defects, navigation landmarks, to plain text is possible.

A. Problem Formulation

Notations: Given a matrix $\mathbf{M} = \{\mathrm{m}_{ij}\} \in \Re^{\mathrm{u}\times\mathrm{v}}$, we refer to its *i*-th row and *j*-th column as $\mathbf{m}^{i}$ and $\mathbf{m}_{j}$. Its Frobenius norm is computed by $\| \mathbf{M} \|_{\mathrm{F}} = \sqrt{\Sigma_{i=1}^{u}\Sigma_{j=1}^{v} m_{ij}^{2}}$. Given a vector $\mathbf{m} \in \boldsymbol{\Re}^{v}$, its ℓ_2-norm is defined as $\| \mathbf{m} \|_2 = \sqrt{\mathbf{m}^{\mathrm{T}}\mathbf{m}}$

Given a set of point cloud instances acquired during long-term LiDAR-based navigation over different scenarios, each point cloud is divided into a set of voxels. Then, multiple feature types are extracted from each of these voxels and we defined a modality as the features computed from a specific feature descriptor. The multi-modal features extracted from all voxels are denoted as **X** = $[\mathbf{x}_1, \ldots, \mathbf{x}_n] \in \boldsymbol{\Re}^{d\times n}$. $\mathbf{x}_i \in \boldsymbol{\Re}^{d}$ is the vector of features extracted from all the voxels of the *i*-th 3D point cloud, which is a concatenation of features from all *m* modalities, such that $d = \Sigma_{i=1}^{m}\Sigma_{j=1}^{v} d_{ij}$, where d_{ij} is the dimensionality of the *i*-th feature modality in the *j*-th voxel, and v is the total number of voxels. The corresponding long-term scenarios (e.g., summer and winter) are represented as $\mathbf{Y} = [\mathbf{y}_1, \dots, \mathbf{y}_n] \in \boldsymbol{\Re}^{\boldsymbol{n\times c}}$, where c denotes the number of scenarios and $\mathbf{y}_i$ is the scenario indicating vector, with each element $y_{ij} \in \{0, 1\}$ denoting that the i-th 3D point cloud is collected from j-th scenario. Then, we formulate place recognition based on 3D point clouds as a regularized optimization problem:

$$\min L(\mathbf{X}, \mathbf{Y}; \mathbf{W}) + \lambda R(\mathbf{W})$$

where $\mathcal{L}(.)$ is the loss function, $\mathcal{R}(.)$ is the sparsity-inducing regularization term, and $\lambda \geq 0$ is a trade-off hyperparameter to balance the loss function and the regularization term. The model parameter $\mathbf{W}$ is a weight matrix, which represents the importance of the features in $\mathbf{X}$ to represent the scenarios $\mathbf{Y}$ in general. By learning the weight matrix $\mathbf{W}$ in Eq. (1), we learn features that are more important towards place recognition. That is, the features that are more important towards place recognition have higher weights and the less important features have weights closer to zero. The loss function is designed to encode the error of using the learned model to represent the scenarios, which can be defined as $L(\mathbf{X}, \mathbf{Y}; \mathbf{W}) = \ min_W \parallel X^T W - Y \parallel_F^2$.

The solution to the optimization problem defined in Eq. (1) $\mathbf{W} = [\mathbf{w}_1, \dots, \mathbf{w}_c] \in \mathcal{R}^{d\times c}$ where $\boldsymbol{w}_i \in \Re^d$ denotes the weights of features from all views and modalities to represent the i-th scenario. Since $\mathbf{w}_i$ contains the weights of features from m-modalities in all voxels, it can be further denoted as $\mathbf{w_i} = [\mathbf{w_i^1}, \dots, \mathbf{w_i^m}]^\mathbf{T}$.In addition, since each w_i^j includes the weights of features (extracted from the j-th modality with respect to the i-th scenario) from all voxels, it can be further divided into v parts as $\mathbf{w_i^j} = \left[\mathbf{w_i^{j^1}}, \dots, \mathbf{w_i^{j^v}}\right] \in \Re^{d_{ij}}$ where $w_i^{j^k}$denotes the weights of features extracted from the k-th voxel and j-th modality with respect to the i-th scenario.

Learning Representative Voxels and Feature Modalities:

When performing place recognition, we hypothesize that some voxels within the 3D point cloud are more representative than others. To identify representative voxels for place recognition, we introduce a regularization term called a voxel norm. Formally this norm is a sparsity-inducing norm that can be mathematically defined as $\mathcal{R}_V(\mathbf{W}) = \Sigma_{i=1}^{v} \parallel \mathbf{W}^i \parallel_F$. This voxel norm $\mathcal{R}_V$ is used as a regularization term in our optimization formulation to enforce the grouping effect of the multimodal features shared among different scenarios and promote sparsity among different voxels.

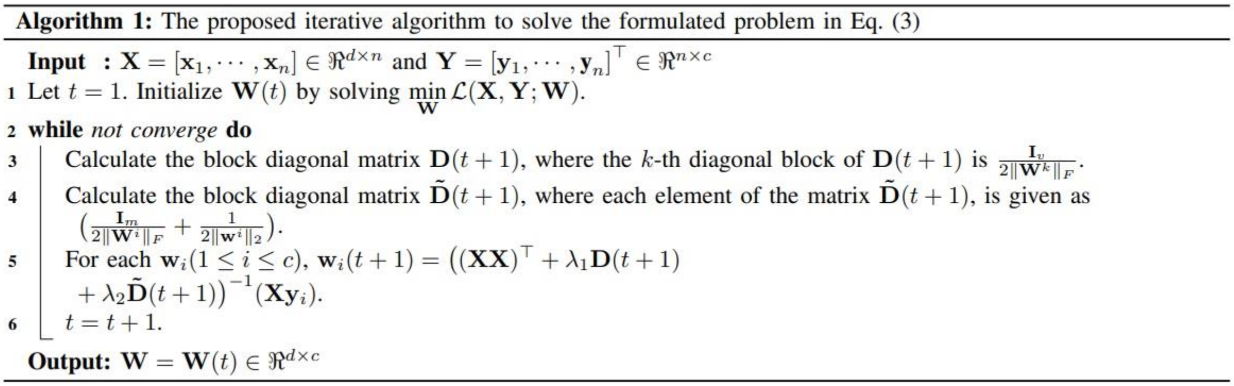

```
Algorithm 1: The proposed iterative algorithm to solve the formulated problem in Eq. (3)
Input  : $\mathbf{X} = [\mathbf{x}_1, \cdots, \mathbf{x}_n] \in \Re^{d\times n}$ and $\mathbf{Y} = [\mathbf{y}_1, \cdots, \mathbf{y}_n]^\top \in \Re^{n\times c}$
Let $t = 1$. Initialize $\mathbf{W}(t)$ by solving $\min_{\mathbf{W}} \mathcal{L}(\mathbf{X}, \mathbf{Y}; \mathbf{W})$.
while not converge do
    Calculate the block diagonal matrix $\mathbf{D}(t+1)$, where the $k$-th diagonal block of $\mathbf{D}(t+1)$ is $\frac{\mathbf{I}_v}{2\|\mathbf{W}^k\|_F}$.
    Calculate the block diagonal matrix $\tilde{\mathbf{D}}(t+1)$, where each element of the matrix $\tilde{\mathbf{D}}(t+1)$, is given as
     $(\frac{\mathbf{I}_m}{2\|\mathbf{W}^i\|_F} + \frac{1}{2\|\mathbf{w}^i\|_2})$.
    For each $\mathbf{w}_i (1 \leq i \leq c)$, $\mathbf{w}_i(t+1) = \big((\mathbf{X}\mathbf{X})^\top + \lambda_1 \mathbf{D}(t+1)$
     $+ \lambda_2 \tilde{\mathbf{D}}(t+1)\big)^{-1} (\mathbf{X}\mathbf{y}_i)$.
    $t = t + 1$.
Output: $\mathbf{W} = \mathbf{W}(t) \in \Re^{d\times c}$
```

Different feature modalities usually capture different characteristics of a place. Some feature modalities can be more representative to describe a place than others. Thus, it is also beneficial to identify the importance of feature modalities to improve long-term place recognition performance. Accordingly, we also propose a regularization term to identify representative feature modalities under the unified regularized optimization framework, which is named modality norm. It is mathematically defined as:

$$\mathcal{R}_M(\mathbf{W}) = \Sigma_{i=1}^{m} \parallel \mathbf{W}^i \parallel_F + \Sigma_{i=1}^{d} \parallel \mathbf{W}^i \parallel_2$$

which is a combination of two structured sparsity-inducing norms. The first term applies the Frobenius norm within each modality and then applies a group ℓ_1-norm across different modalities. By enforcing sparsity among modalities, this term allows the VBRL method to identify representative modalities that have larger weights, and to make the weights of non-representative features tend towards 0. The second term in Eq. (2) denotes the $\ell_{2,1}$-norm (i.e., a ℓ_2-norm for each column and ℓ_1-norm across different columns) used to enforce the sparsity of the columns of $\mathbf{W}$ and grouping effect of the weights in each column. By enforcing sparsity of individual features, this norm helps recognize representative individual features and assign a zero value to the weights of non-representative features (e.g., from noise).

Incorporating both of the regularization terms to identify representative voxels and feature modalities, our final formulation of learning voxel-based multimodal representations for place recognition can be defined as the following regularized optimization problem:

$$min_w \, L(\mathbf{X}, \mathbf{Y}; \mathbf{W}) + \lambda_1 R_V\,(\mathbf{W}) + \lambda_2 R_M\,(\mathbf{W})$$

where λ_1 and λ_2 denote trade-off hyperparameters to govern the balance between the loss function and the structured sparsity-inducing norms.

Voxel-Based Multimodal Place Recognition:

Once the formulated regularized optimization problem in Eq. (3) is solved based on Algorithm 1, the optimal weight matrix $\boldsymbol{W}^*$ is obtained. Given the feature vector $x \in \Re^d$ that is extracted from all voxels and feature modalities in a query 3D point cloud, and a feature vector from a template 3D point cloud $\tilde{x} \in \Re^d$, we compute a similarity score between this query and template point clouds as follows:

$$\boldsymbol{s} = \sum_{\boldsymbol{i=1}}^{\boldsymbol{m}} \sum_{\boldsymbol{j=1}}^{\boldsymbol{v}} \boldsymbol{w_M(i)} * \boldsymbol{w_V(j)} * (|\boldsymbol{x_{ij}} - \boldsymbol{\tilde{x}_{ij}}|)$$

where $\mathbf{x}_{ij}$ denotes the vector features from the i-th modality and the j-th voxel, $w_M\,(i)$ is sum of all weights of features in the i-th feature modality, and $w_V\,(j)$ is sum of all weights of features in the j-th voxel. When this score is above a user-defined threshold, the query 3D point cloud is determined as a match with the template 3D point cloud.

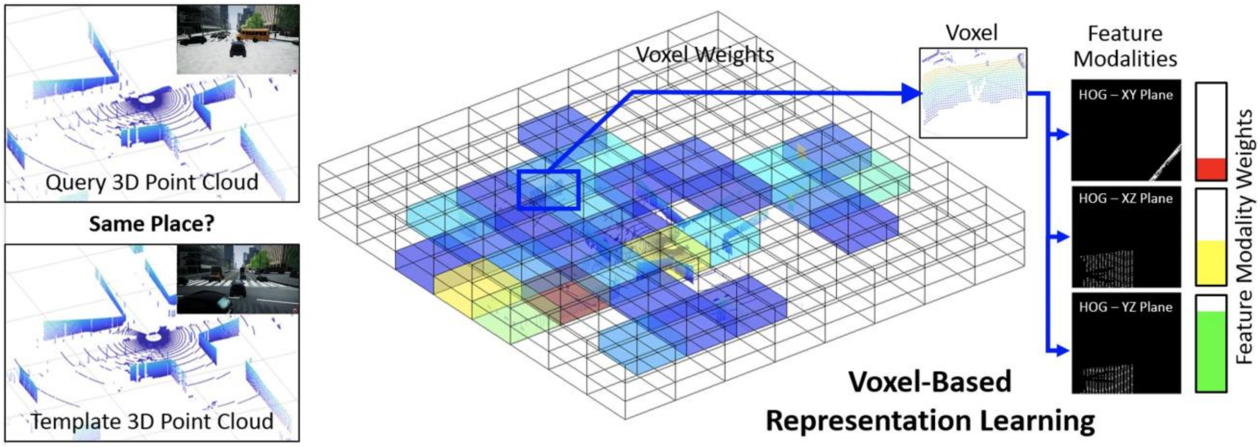

Figure 127: Illustration of the VBRL approach for loop closure detection in SLAM on 3D point cloud data.

B. Experimental Results

In our implementation, each 3D point cloud scan from LiDAR is divided into many voxels. From each voxel five different feature descriptors are extracted including (1) covariance of points contained within the voxel, (2) Histogram of Oriented Gradients (HOG) features of a snapshot of the point cloud in the XY plane, (3) XZ plane, (4) YZ plane, and (5) Subvoxel Occupancy.

The subvoxel occupancy feature is obtained simply by dividing a voxel into 8 equal subvoxels. If the subvoxel is occupied by any points, a 1 is written to the feature matrix. Otherwise a 0 is written. As opposed to concatenating these features together from each voxel, VBRL operates with the intuition that learning a shared representation of the overall scene from multiple data instances and weighting the feature matrix accordingly will fuse the feature modalities more effectively for loop closure detection.

Experiments are evaluated both qualitatively and quantitatively. To showcase that VBRL learns a better representation of a LiDAR scan than feature extraction alone, we compare VBRL ($\lambda_1 = 10$ and $\lambda_2 = 0.1$) to performing loop closure detection with features concatenated together ($\lambda_1 = 0$ and $\lambda_2 = 0$), voxel learning only ($\lambda_1 = 10$ and $\lambda_2 = 0$), and modality learning only ($\lambda_1 = 0$ and $\lambda_2 = 0.1$).

Results on Autonomous Driving Simulation:

At first, we evaluate the performance of our VBRL approach to perform 3D point cloud based long-term place recognition by extensive experimenting on data obtained from the AirSim simulator. AirSim [71] is an autonomous driving simulator developed by Microsoft to facilitate the development of self-driving vehicle methods in a virtual environment. We collect the dataset in AirSim's cityscape environment with roads, skyscrapers, parks, and dynamically moving cars and pedestrians. A virtual LiDAR sensor is installed on top of a vehicle to record the point cloud data from the virtual environment. The point cloud based LiDAR scans are collected from 210 unique locations within the environment. These scans are first collected in clear, sunny weather.

This set of point cloud scans constitute one scenario of training our VBRL approach. Then, point cloud scans are collected from these locations from the self-driving vehicle during snow and fog conditions forming the second scenario. All of the 210 locations were distinctive to one another and there was no overlap. To perform the experiments on simulated data and evaluate our approach, we used 160 point cloud scans for training and a disjoint set of 50 point clouds are designated for testing. It is to be noted that the training and testing data doesn't have any overlap to make sure that our approach can learn a robust weight matrix **W**, that can be used to perform place recognition in new and unseen locations.

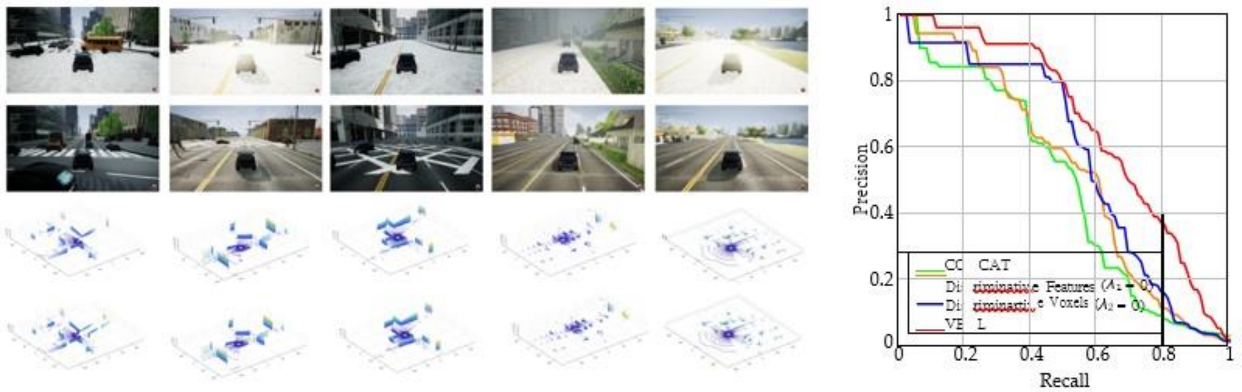

(a) Examples of matched point clouds

(b) Precision-recall curves

Figure 128: Qualitative and quantitative experimental results over the AirSim simulations.

The main challenges associated with this dataset are the dynamic cars and pedestrians. The LiDAR scans are robust to changes in lighting conditions and are not affected by the virtual snow. However, because fog, as well as snow, could reflect lasers, certain LiDAR points may be represented as noise, affecting the representation of the scene adversely. This is a key challenge in present-day place recognition using point clouds because autonomous vehicles need to operate in snow, fog, rainy seasons. However, this dataset doesn't provide data with variation in vegetation. Illustrated in Figure 128 are the place recognition results based on our VBRL approach and its comparison to baseline approaches. The qualitative results on 3D point cloud scan matches are illustrated in Figure 128(a) The template point clouds from the snow scene that obtain the maximum matching score are shown in the top row, while the query scenes from the clear scene are shown in the bottom row. It is observed that our VBRL approach can match point clouds, despite changes in lighting conditions and weather, thus proving the capability to perform long-term place recognition.

The classification problem is analyzed quantitatively using the standard precision-recall curve. Figure 128(b) shows the precision-recall performance of VBRL when compared with features concatenated together, discriminative voxels alone, and discriminative features alone. We observe that using feature concatenation alone we achieve minimal performance in point cloud-based place recognition. Using discriminative features increases the performance, as the area under the curve increases. Introducing the discriminative voxel learning approach increase the performance even more. Finally, we observe the performance of our VBRL approach, where it obtains the maximum area under the curve when compared with previous methods, indicating the

best performance. Therefore, by fusing multiple feature modalities together and weighting them based on importance, the VBRL approach yields the best results for loop closure detection.
The modality weights learned automatically for the AirSim dataset are shown in Figure 130(a). The Subvoxel Occupancy feature is the most important with a weight of 30% and the covariance feature is the second most important with a weight of 29%. The three HOG feature importance range from 4% for HOG-XY to 28% for HOG-XZ.

The learned voxel weights are shown via a color map above in Figure 130. Voxels occurring more towards the center of the workspace are learned to be weighted as more important in place recognition. This makes sense as the center voxels are most likely to be occupied because they are closest to the sensor origin and in a LiDAR scan point clouds are more populated in the center. Apart from this, we also analyze the relative importance of the different layers of voxels (top, middle, and bottom) when performing place recognition using point clouds in the AirSim dataset. It was observed that the relative importance of bottom, middle and top layer was 37.08%, 42.22%, and 20.72% respectively. This indicated that the bottom and middle layer were critical towards point cloud based place recognition.

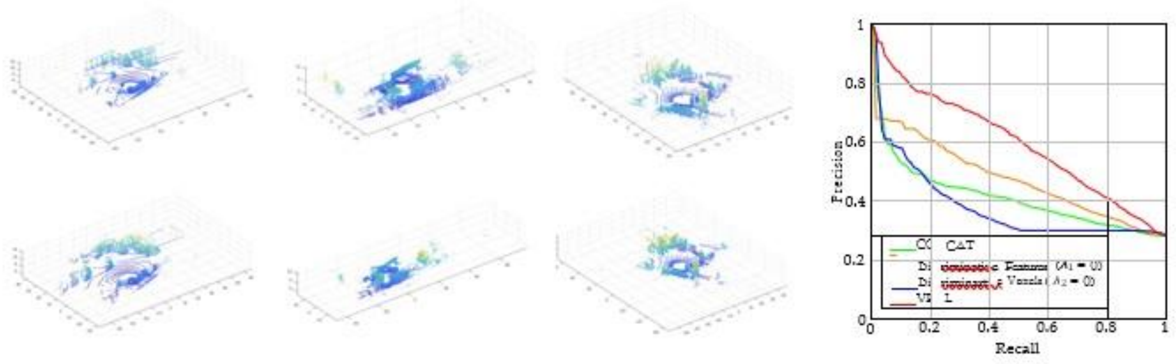

(a) Examples of matched point clouds (b) Precision-recall curves

Figure 129: Experimental results over the NCLT dataset for long-term 3D point cloud-based place recognition in different seasons.

Results over the NCLT Dataset:

The North Campus Long Term (NCLT) [72] dataset is collected at the University of Michigan by a mobile robot driven around the campus. There are 27 separate sessions with varying robot routes in the dataset, which occur over the course of 15 months and span multiple times of day and seasons. The dataset contains long-term changes in lighting conditions, vegetation, and weather. Two sessions are chosen: one collected in June and the other in December. These seasons are selected as they have overlapping routes and seasonal changes. A Velodyne HDL-32E LiDAR sensor was used to collect 3D point cloud data of the environment and was mounted on the mobile robot.

This dataset has dynamic pedestrians and also has vegetation changes. Change is vegetation is typically observed with seasonal changes and is important to be addressed in the LAC problem, to perform long term place recognition. The NCLT dataset includes 850 LiDAR scans from the month of June and a corresponding 850 LiDAR scans from the month of December. For this set of experiments, we choose 700 instances of point clouds for training and for testing a disjoint set of 150 point cloud scans are taken. Again, it is to be noted that the training and testing data doesn't have any overlap in order to make sure that our approach is robust.

The qualitative results of the performance of our VBRL approach are provided in Figure 129(a) in which query scans from the data collected in June are shown on the bottom row and resulting matches from December are shown in the top row. Our VBRL approach is able to recognize scenes from 3D point cloud data despite vegetational, seasonal and structural changes (such as leaves falling off of trees).

Figure 129(b) shows the qualitative precision-recall analysis of VBRL on the NCLT dataset. Once again, it is observed that VBRL yields greater area under the precision-recall curve than discriminative voxels, discriminative features, or feature concatenation. Additionally, the learned modality weights obtained are shown. The learned voxel weights are also shown in Figure 130(b) and results obtained are similar to the AirSim dataset in that the center voxels are learned to be of more importance than the outer voxels.

The learned voxel weights are also shown in Figure 130(b). An analysis of weights of the different voxel layers showed that the bottom, middle and top layer have their relative importance as 33.92%, 54.62%, and 11.46% respectively. Quite contrasting to the results obtained in the AirSim dataset, we see that the top layer has very little importance. The bottom layer's importance also decreases. However, the middle layer plays a major role in place recognition. The NCLT dataset was majorly collected when the robot traverses over open areas and didn't have any tall structures throughout its route. Thus, the bottom and top layer's importance is less, whereas the middle layer has the most importance as it has the maximum number of important features that are critical in place recognition as opposed to the AirSim point cloud data which had point cloud scans of tall buildings nearby.

Discussion:

We performed additional experiments to further analyze our approach. The results are shown in Figure 130. Figure 130(a) shows the importance of feature modalities for the AirSim simulations. Figure 130(b) shows the importance of voxels for long-term place recognition using the NCLT dataset, where the robot is located in the center of the point cloud at position (0, 0). Figure 130(c) illustrates the performance variations of our VBRL approach given different hyperparameter values over NCLT.

Importance of Voxels and Feature Modalities: Our VBRL approach can automatically estimate the importance of each of the voxels and feature modalities while training. The relative importance of voxels is illustrated in Figure 130(b). Intuitively, points closer to us are more important towards performing place recognition. It is analogous to the fact that humans also use nearby points such as street signs and buildings to recognize places rather than using mountains in the distance. Accordingly, our approach indicates that point clouds near the center are of more importance. On the other hand, voxels far away from the center are of least importance and thus their weights are close to zero. The importance of feature modalities are illustrated in Figure 130(a). The pie chart here indicates the relative importance of different feature modalities towards performing voxel- based place recognition. It is observed that Subvoxel occupancy, Covariance and HOG-XZ have an importance of 30%, 29% and 28% respectively and are equally important in general, whereas HOG-XY is of least importance.

Hyperparameter Selection: The hyperparameters λ_1 and λ_2 in our formulation of the final objective function, Eq.(3) are designed to control the strength of regularization norms over learning descriptive voxels and feature modalities respectively. Their optimal values can be determined using cross-validation during training. From the result in Figure 130(c) we observe that when $\lambda_1 = 10$ and $\lambda_2 = 0.1$, VBRL statistically obtains the best accuracy while performing 3D point cloud based place recognition. In general, the range $\lambda_1 \in \{1, 100\}$ and $\lambda_2 \in \{0.01, 1\}$ can result in satisfactory results, which demonstrates that both of the regularization terms are useful to improve performance.

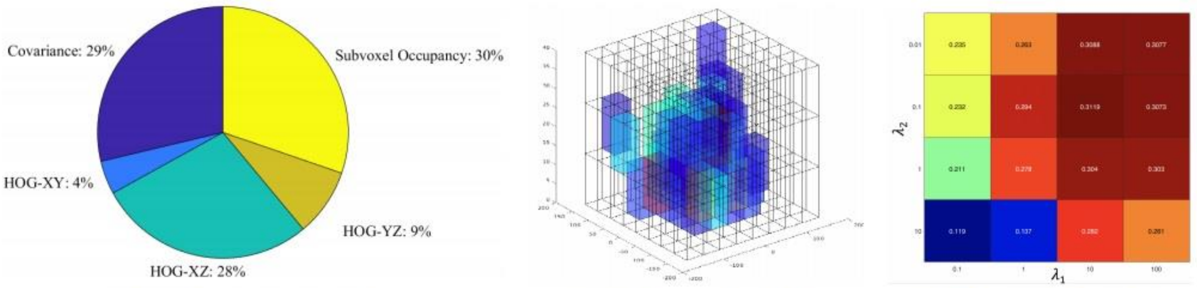

(a) Modality importance for AirSim (b) Voxel weights for NCLT (c) Hyperparameter analysis

Figure 130: Experimental results over the NCLT dataset in different seasons.

C. Robot Mapping

We also implemented Simultaneous Localization and Mapping (SLAM) methods based on LiDAR data. The place recognition methods can be used to close the loop in the constructed map thus increasing the mapping accuracy.

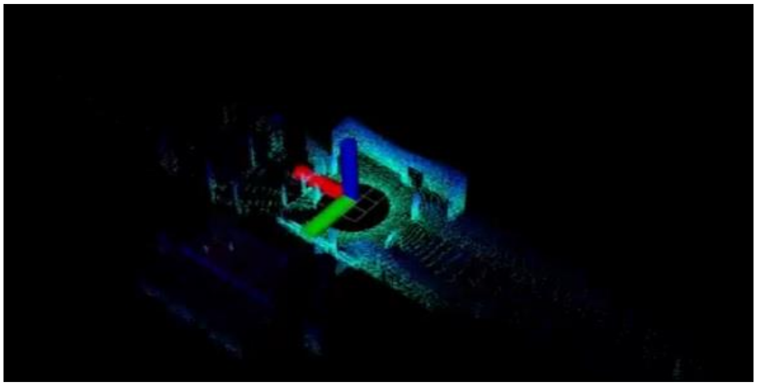

Figure 131: LiDAR observation.

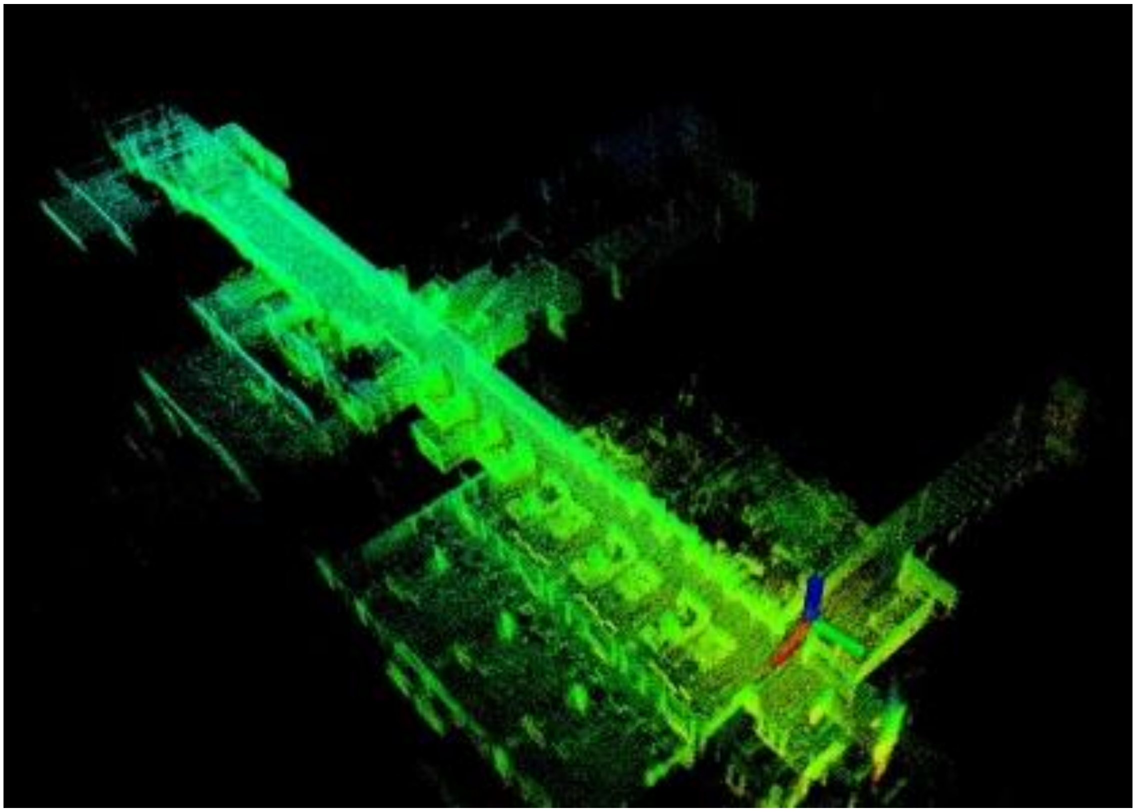

Figure 132: Example of 3D robot mapping.

4.2. Subtask 4.2: Spatiotemporal Damage Tracking

Given the previous designed SLAM algorithm, we can figure out if the current place we used to visited before. Given the damages recorded in the previous observation and the current observation of the same place, we need to identify the correspondences of the damages recorded at different times but the same place. In this task, we aim to achieve the tracking of damages, which is a process of associating individual or multiple damages over time at the same place. We split the tracking problem into two situations, including the tracking of the single damage and multiple damages. Thus, we designed two algorithms for the two situations separately.

A. Single Damage

Nowadays, re-identification attracts wide attention in computer vision and robotics, which is defined as the process of determining whether a given individual object has already appeared in other observations.

For the tracking of the single damge, we can treat it as the re-identification of the single object, because both of the problems aim to determinate the same object from different perspectives. For a single damage, the perspective of observing it varies over time. Thus, the re-identification technique can be used to decide if the current damage is the previous damage we observed in order to associate individual damage recorded at different times but the same place.

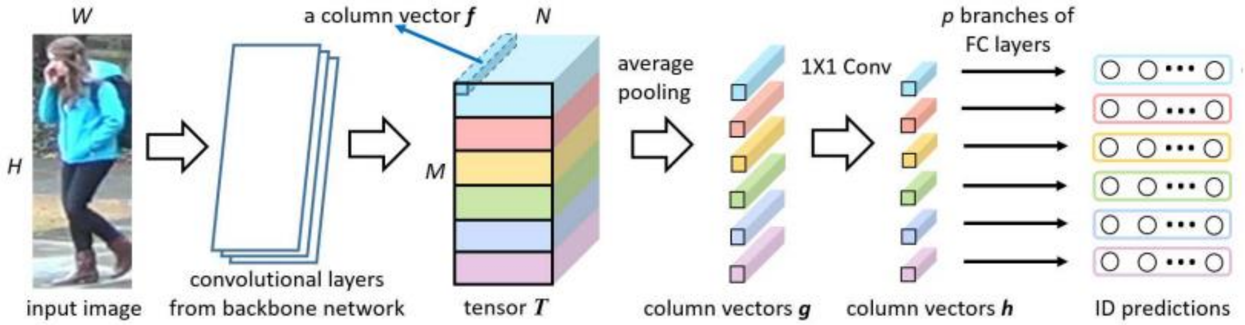

Figure 133: Structure of single object/crack re-identification.

The process of re-identification is presented as above, which includes 4 main steps:

Step1: The input image pass through the backbone network (ResNet50) to extract high-level features of the original image. The extracted features are encoded in the tensor **T.**

Step2: Given the tensor **T**, we split it into M (M=6) parts associating with 6 parts of the object (e.g, head, shoulder, arm, waist, leg, feet). Afterwards, we average all the column vector $\boldsymbol{f_i}, i = 1,2,\dots,M$ in each part into a single column vector $\boldsymbol{g_i}, i = 1,2,\dots,M$ in order to downsample the high-dimension input tensor **T.**

Step3: In order to futher downsample the feature vector to reduce the computing cost, we employ a 1X1 convolutional layer to reduce the dimension of $\boldsymbol{g_i}$ into $\boldsymbol{h_i}, i = 1,2,\dots,M$.

Step4: Given the downsampled feature vector $\mathbf{h_i}$, we can predict the ID of the each part of the original object as follows:

$$\mathrm{ID} = \mathrm{softmax}(W_i^T \mathrm{h_i}) = \frac{\exp\,(W_i^T \mathrm{h_i})}{\sum_{\{\mathrm{j=1}\}}^{\mathrm{M}} W_j^T \mathrm{h_i}}$$

where W_i is the learnable parameters for each part in the classifer defined above. During testing, we can easily concatenate all features $\boldsymbol{h_i}, i = 1,2,\dots,M$ in to a big one $H = [h_1, h_2, \dots, h_m]$, and the final preciditon is similarly defined as softmax$(\mathbf{W^T}\boldsymbol{H})$

B. Multiple Damages

If there exist multiple objects (e.g., damages) in an observation, the tracking of multiple objects with identical or similar appearance is very challenging, as shown in Figure 134. In each of the observation of the same place, the objects denote damages with similar appearance (e.g., apples or banana). The tracking of multi damages over time is equivalent to identify the correspondences of objects between the two observations.

We proposed a graph matching method for the tracking of multiple objects that integrates visual and spatial information describing the objects to identify the correspondence of objects between two perspectives. From one of the perspectives, we represent multiple detected objects as a graph, where each node corresponds to a detected object, where edges between nodes describe the spatial distance between objects and an attribute vector associated with each node describes the object's visual appearance. We represent the other perspective with a similar graph. Thus, our graph representation integrates both visual and spatial information about the detected objects in both observations.

Given these two graph representations generated from the two observations, we formulate the tracking of multiple objects as a graph matching problem, which uses constrained optimization to identify corresponding objects between two views based on the similarity of the visual and spatial information of the objects encoded in each graph as shown in the below figure.

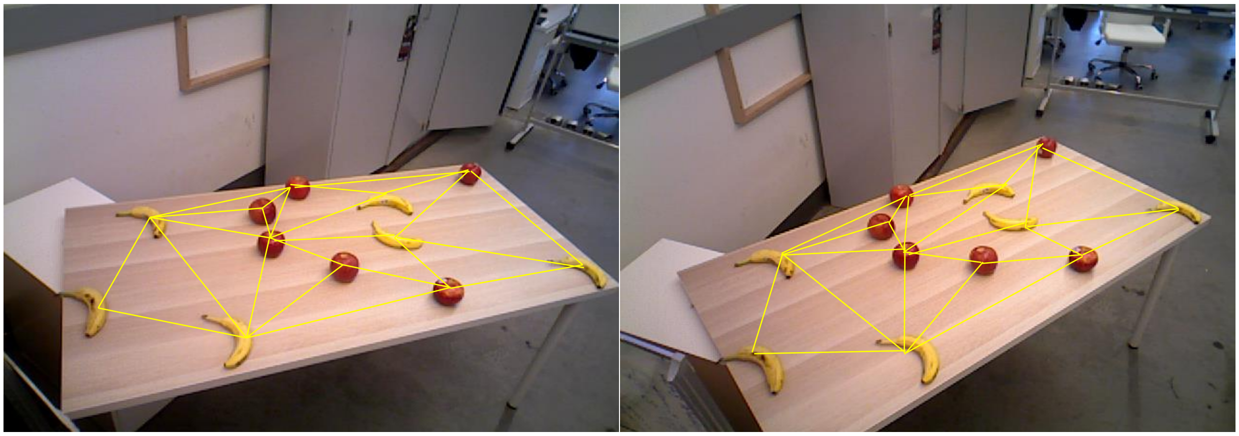

Figure 134: Graph representations of the observation with multiple objects.

In order to track the correspondences between two graphs $\mathbf{G} = \{\mathbf{V}, \mathbf{F}, \mathbf{E}\}$ and $\mathbf{G}' = \{\mathbf{V}', \mathbf{F}', \mathbf{E}'\}$ objects. $\mathbf{V} = \{\mathbf{v_1}, \mathbf{v_2}, \dots, \mathbf{v_n}\}$ is the nodes set, where v_i denotes the position of objects and n is the number of objects in graph **G**. $\mathbf{F} = \{\boldsymbol{f}_\mathbf{1}, \boldsymbol{f}_\mathbf{2}, \dots, \boldsymbol{f}_\mathbf{n}\}$ is the feature set, where f_i denotes the visual feature of the i-th object in graph **G**. $\mathbf{E} = \{\boldsymbol{e}_{\boldsymbol{i},\boldsymbol{j}}, \boldsymbol{i} = \mathbf{1}, \mathbf{2}, \dots, \boldsymbol{n}, \boldsymbol{j} = \mathbf{1}, \mathbf{2}, \dots, \boldsymbol{n}, \boldsymbol{i} \neq \boldsymbol{j}\}$ is the edge set, where $\boldsymbol{e}_{\boldsymbol{i},\boldsymbol{j}}$denoting the distance between node v_i and v_j in graph G. Finally, we formulate the tracking problem as the following graph matching problem:

$$\max_{X} \boldsymbol{A}^{\boldsymbol{T}}\boldsymbol{X} + \boldsymbol{X}^{\boldsymbol{T}}\boldsymbol{S}\boldsymbol{X} \quad s.t.\, \boldsymbol{X}\mathbf{1}_{\{\boldsymbol{n}'\times\mathbf{1}\}} \leq \mathbf{1}_{\{\boldsymbol{n}\times\mathbf{1}\}}, \quad \boldsymbol{X}^{\boldsymbol{T}}\mathbf{1}_{\{\boldsymbol{n}\times\mathbf{1}\}} \leq \mathbf{1}_{\{\boldsymbol{n}'\times\mathbf{1}\}}$$

where $\mathbf{X} = \{\mathbf{X}_{\{\mathbf{ii}'\}} \in \{\mathbf{0}, \mathbf{1}\}^{\{\mathbf{nn}'\}}\}$ denotes the correspondence matrix, with $\mathbf{X}_{\{\mathbf{ii}'\}} = \mathbf{1}$ denoting that the i-th node in **G** and the i'-th node in **G'** are matched, and 1 is a vector with all elements equal to 1. $\boldsymbol{A} = \left\{\boldsymbol{A}_{\{\boldsymbol{ii}'\}}\right\} \in \boldsymbol{R}^{\{\boldsymbol{nn}'\}}$ denotes the visual similarity between visual feature $\boldsymbol{f}_{\boldsymbol{i}} \in \boldsymbol{F}$ of the i-th object in graph **G** and $\boldsymbol{f}'_{\boldsymbol{i}} \in \boldsymbol{F}'$ of the I'-th object in graph **G**'. And $\boldsymbol{S} = \left\{\boldsymbol{S}_{\{\boldsymbol{ii}',\boldsymbol{jj}'\}}\right\} \in \boldsymbol{R}^{\{\boldsymbol{nn}'\times\boldsymbol{nn}'\}}$ denotes the spatial similarity between edge $\boldsymbol{e}_{\boldsymbol{i},\boldsymbol{j}} \in \boldsymbol{E}$ in graph **G** and edge $\boldsymbol{e}'_{\boldsymbol{i}',\boldsymbol{j}'} \in \boldsymbol{E}'$in graph **G'**. Formally, the visual and spatial similarities can be calculated as follows:

$$\mathbf{A}_{\{\boldsymbol{ii'}\}} = \frac{\boldsymbol{f_i f'_{i'}}}{||\boldsymbol{f_i}||\ ||\boldsymbol{f'_{i'}}||}$$

$$\mathbf{S}_{\{\mathbf{ii',jj'}\}} = \exp\left(-\left(e_{\{i,j\}} - e'_{\{i',j'\}}\right)^2\right)$$

The first term in our designed formulation represents the accumulated similarity between visual appearances of the objects in the two graphs, which sums all visual appearance similarities. The second term denotes the accumulated spatial similarities of the objects in two graphs, which sums all distance similarities of edges between two graphs.

4.3. Subtask 4.3: Damage Analysis by Machine Learning

A. Machine Learning for Crack Classification

Two machine learning approaches were developed for crack classification using our collected simulated NDE data. We first developed a regularized ridge classification method as follows:

$$min_w \|y^T - w^T x\|_2^2 + \alpha \|w\|_2^2$$

The goal is to minimize the objective function. Where x is our feature vector, w is our learned weight matrix and y are the observations. Alpha is a hyperparameter multiplied into the regularization term to avoid overfitting. Alpha was selected as one for this implementation. The target variables are then converted to positive and negative one and a binary classification is achieved based on positive or negative regression.

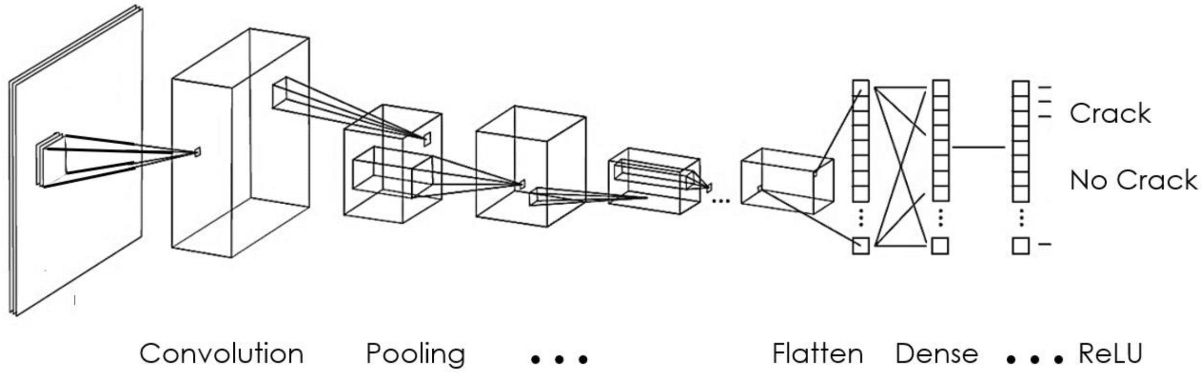

Figure 135: CNN architecture for crack classification.

We also implemented a convolutional neural network (CNN). The network architecture can be seen in Figure 135. The network has a total of 11 layers and utilized the “adam” gradient descent optimization algorithm. Four layers are convolutional utilizing a rectified linear activation function. Three layers are maximum pooling layers, there is one flatten layer and 3 dense layers. The model was trained for 5 epochs.

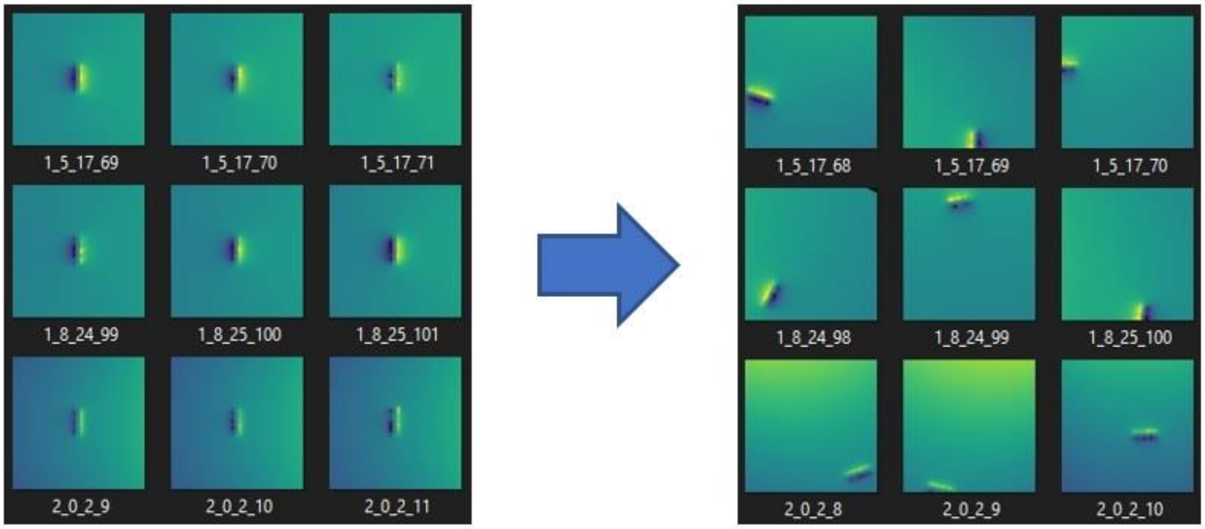

Figure 136: Date generation through randomization for model training.

The data set consists of 60,000 data instances of 10 separate crack depths of three separate scan velocities at four different levels of vibration. The eddy current scans were collected from the Michigan State University's scanning gantry system. Each instance is a text file where each row represents an array of resonating frequencies at that rows position of the scan. To work with our models these files are first converted to 227x227 RGB images. A crack can be seen as a sharp change in contrast. Furthermore, the models are supervised, and thus data need to be labeled "positive" or "negative" for model training. This was done by taking a cropped subsection of each image that represents a healthy region and a damaged region. Initially both models yielded poor results as the images were cropped in the same location for all the data, thus a randomized offset anywhere in the range that the damage would still occupy the image as well as a random rotation angle between 0 and 180 degrees were generated and applied to each image before taking the cropped subsection (Figure 136).

Table 19: Experimental results from the ridge classifier and CNN.

	Ridge Model				Convolutional Neural Network			
	Precision	Recall	F1-Score	Support	Precision	Recall	F1-Score	Support
0	0.95	0.95	0.95	29920	0.98	0.99	0.98	29920
1	0.94	0.94	0.94	30080	0.99	0.98	0.98	30080
Accuracy			0.95	60000			0.98	60000
Macro avg	0.95	0.95	0.95	60000	0.98	0.98	0.98	60000
Weighted avg	0.95	0.95	0.95	60000	0.98	0.98	0.98	60000

We first evaluated the ridge classifier. This approach requires some data preprocessing and feature extraction. Each image is first converted to greyscale. We then utilize the canny edge detection method to find sharp changes in gradient. We then crop teach image at its bounding rectangle and extract the histogram of oriented gradients (HOG) feature. We then flatten this image into a one-dimensional feature vector. Then two machine learning methods were applied to classify the feature vectors. From the results listed in Table 19, it is clear that the deep learning approach outperforms the regularization approach, thus this is the model we selected for crack classification.

B. Machine Learning for Crack Localization and Estimation

As a unique challenge to execute effective repairs, it is not only necessary to classify damage accurately, but also feed damage locations into the global map of robot's environment through data fusion. To achieve this goal, simple classification approaches such as the ridge classifier or traditional convolutional neural networks are not adequate for this application because they are only able to classify whether an object is within an image, but have no awareness of where the object is within the image. To address this, an instance-based semantic segmentation method is utilized. This approach differs from traditional semantic segmentation in that it can detect the number of instances of a certain class instead of grouping them together as a single object. As this approach is only concerned with a single object class (damaged area) inside the entire scan region and there may exist multiple cracks within the same scan, the proposed instance-based approach is ideal for this particular application.

Our approach utilizes a two-staged mask region-based convolutional neural network (mask RCNN) as shown in Figure 137. First, data are fed into a traditional CNN for a cropped subsection, called an anchor, of each NDE scan image. To support training multiple images per batch, all images are resized such that the shortest edge is 800 pixels, but the aspect ratio of the original image is preserved. For each, or any, anchor where crack instances are detected, a proposal of its bounding box is generated and stored in memory. The next stage merges each anchor containing the same instance of detected damage region as a single instance. Lastly, a pixel mask is generated for each predicted instance of the damage class.

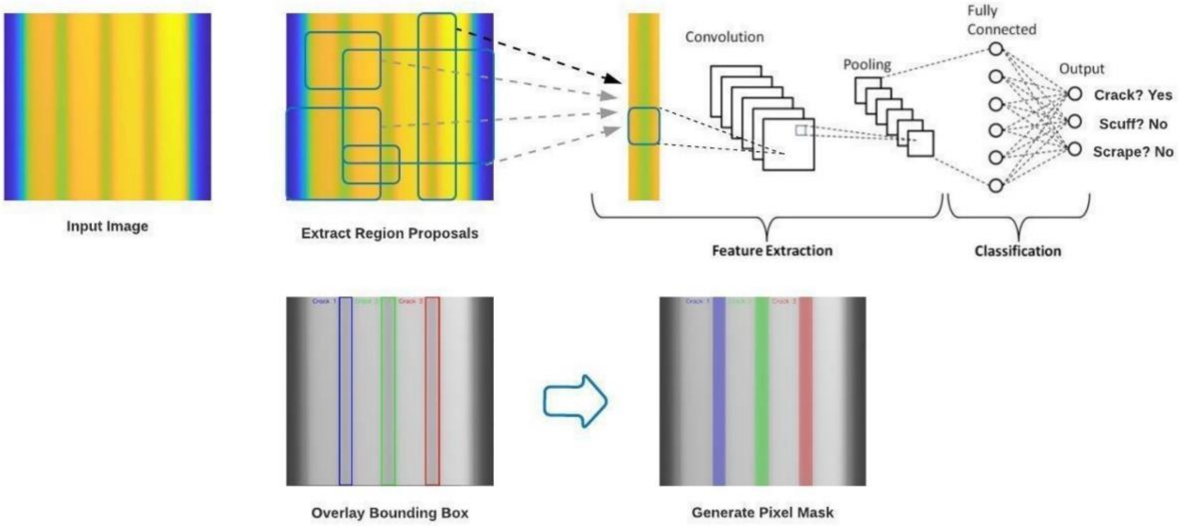

Figure 137: Mask R-CNN process, architecture, and pixel mask generation.

To train any neural network model, a sufficiently large training dataset, and for this application, NDE data of representative cracks for power plant boiler structures are needed. A dataset with the number of required samples is currently not feasible to obtain. This would require NDE scans to be collected from hundreds of thousands of naturally occurring cracks in steel plates which is too difficult and expensive to carry out at this time. Therefore, a transfer learning approach which builds off the Resnet101 pre-trained model is utilized. Resnet101 is a 101- layer CNN, which has been pre-trained on dataset containing over 15 million labeled images.

Utilizing this model allows us to build off learned features from other data eliminating the need to retrain an entire model. 100 images of representative data instances were annotated and given to the model for training, which is implemented on 8 GPUs for 160,000 iterations with a learning rate of 0.02, a weight decay of 0.0001 and momentum of 0.9. These parameters were chosen because, in addition to minimizing the chance of overfitting, they have been shown to provide an optimal balance between training time and premature convergence to a sub-optimal solution. Once the model is trained, given an NDE scan containing a damaged region, the model will find the location of the damage and generate a pixel mask overlaid onto the scan image at the precise location of the damage.

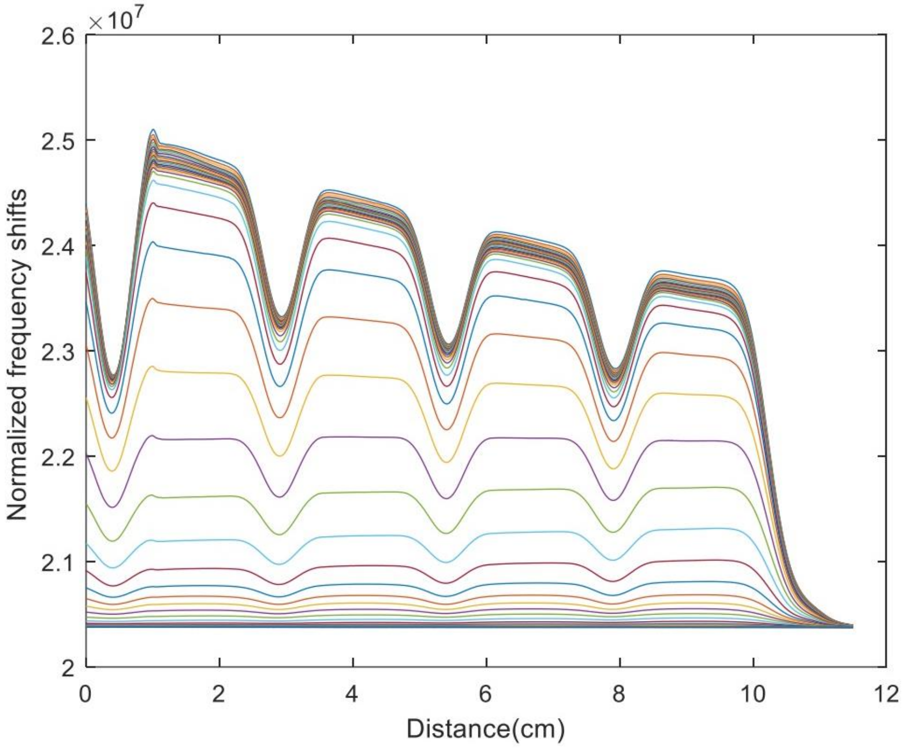

Figure 138: Normalized frequency shifts with different lift-off distance of the NDE sensor.

After the model has generated pixel masks over boiler damage instances, the location of each instance is calculated. The coordinates of a centroid are calculated by dividing the range of pixels that the masks occupy in horizontal and vertical directions by two. These image plane locations and the distance per pixel in the scan region correspond to where the damage exists on the boiler wall. With this information, the robot can then accurately position itself such that its repair probe is able to reach the region in need of repair. The steam corrosion, oxygen corrosion, alkali corrosion, and corrosion under the scale are ever-present in a power plant boiler. The rough surfaces caused by the corrosions result in the vibration during the movement of the robot. Therefore, the lift-off distance of the eddy current coil array may change due to the vibration during the inspection, which challenges the reliability of the NDE data.

The eddy current coil array is placed with the lift-off distance in the range from 0 mm to 5 mm with a step size of 0.1 mm and 6 mm to 50 mm with a step size of 1 mm to inspect the sample 2. As shown in Figure 138, all cracks have been successfully detected quantitatively, where the different normalized shifts of the resonance frequency of the eddy current sensor are correlated with the different depths of the narrow cracks. The normalized frequency shift decreases slightly with the increase of the lift-off distance of the eddy current sensor. According to the results, the crack detection capability of the sensor is basically not influenced by the lift-off distance in the range from 0 mm to 5 mm.

A crack depth prediction algorithm based on the kernel-based Gaussian Process Regression (GPR) is performed to estimate the depth of the cracks obtained at different lift-off distance range from 0 mm to 5 mm. There are 50 crack signals obtained at each depth of the cracks. 35 crack signals are randomly selected from the 50 crack signals in each depth of the cracks to form a training dataset. The GPR model is expressed as $\mathrm{y} = \mathrm{b}(x)^T\beta + l(x)$, where:

$$l(x) \sim GP\big(0, k(x, x')\big), \mathrm{b}(x) \in R^p$$

and $\mathrm{l}(x_i)$ is the latent variable. The Matern 5/2 kernel:

$$\mathrm{k}\big(x_i, x_j \big| \theta\big) = \sigma_f^2 \left(1 + \frac{\sqrt{5}r}{\sigma_l} + \frac{5r^2}{3\sigma_l^2}\right) exp\left(-\frac{\sqrt{5}r}{\sigma_l}\right)$$

is used as the covariance function of the Gaussian process, where i is the number of the dataset, σl is the characteristic length scale, σf is the signal standard deviation, and:

$$r = \sqrt{\big(x_i - x_j\big)^T \big(x_i - x_j\big)}\ .$$

The trained GPR predicts the values of depths of the testing dataset, which consists of the rest 15 crack signals of the 50 crack signals in each depth of the cracks. Figure 139 shows the estimated depth of the crack obtained from the testing sets using the trained GPR model. Meanwhile, the true depth of the crack is also shown in Figure 139 for the comparison. The mean absolute error and the root mean square error are as low as 0.0018 mm and 0.002mm. The result shows that the developed GPR model can estimate the crack depth with a low estimation error and a high degree of prediction accuracy and stability.

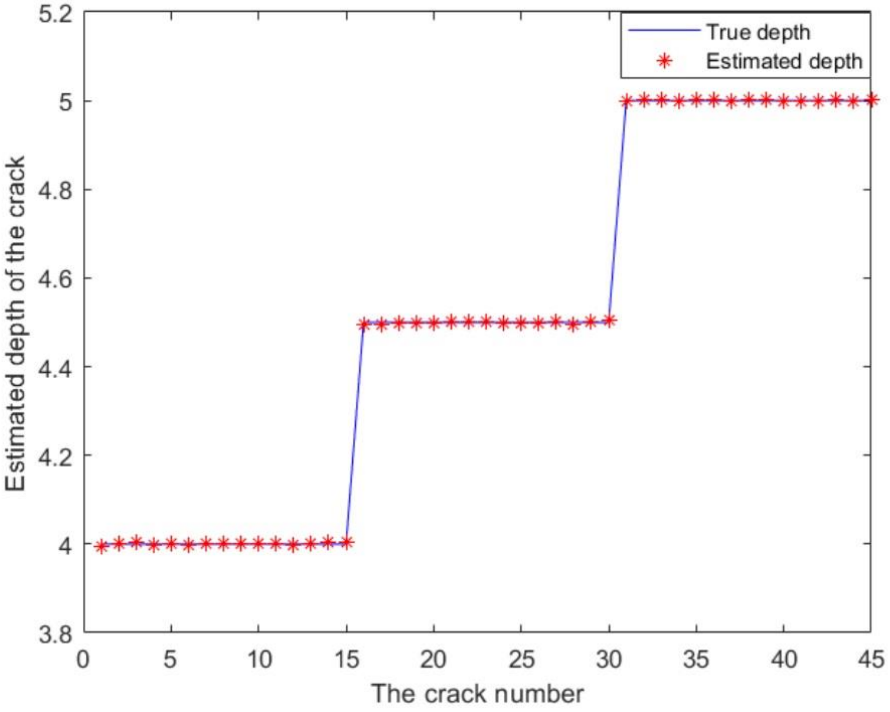

Figure 139: The true and prediction values using GPR method.

Software System Integration:

All software is managed through the Robot Operating System (ROS). ROS provides a convenient framework for managing robotic software. Code is organized into segments called “nodes”. ROS then allows for communication between these processes in the form of “publishing” or “subscribing” to a certain “topic”. Figure 140 displays the design.

The architecture is a three-layer system depicted by the colored boxes. The ovals within each layer represent the nodes and the arrows between them represent the topics. All sensing and low-level perception is handled in the perception layer. The color depth node handles the RGB depth processing from an Intel Realsense D435 depth camera. The Lidar node handles the low-level processing of a 3D laser scan from an Ouster lidar sensor. The IMU node processes the data obtained from an inertial measurement unit and the encoder node reads odometry data from the robots built in wheel encoders.

All higher-level processing such as robot reasoning through machine learning is handled in the cognition layer. Data from all the robotic perception sensors are published and read by the odometry fusion node. The odometry fusion node uses a ROS package utilizing an extended Kalman filter which eliminates sensor noise as well as provides a better state estimate of the robots’ location by fusing the odometry data from the robot’s perception sensors. NDE data from the NDE sensor alone are not compatible with our machine learning approaches as a 2-dimentional image representation of the scan region is needed. Thus, the reconstruction node subscribes to the topics published by the NDE sensor and odometry fusion. The node then uses this information to fuse the data to the appropriate format. The machine learning algorithm is implemented in the classification node. This node uses a machine learning method to classify the damage. The localization node subscribes to both the odometry fusion node and classification node. It is the responsibility of this node to track where in the robots local and global map damage exists and to command the nodes in the action layer.

The action layer contains two nodes which handle all the physical maneuverability of the robot and its repair mechanism. The motor control node is the node which commands the robots built in motors which navigate the boiler. The tooling controller node sends commands to the robots the low-level Latte Panda computer which handles the xyz motion of the NDE sensor and the repair tool end effector.

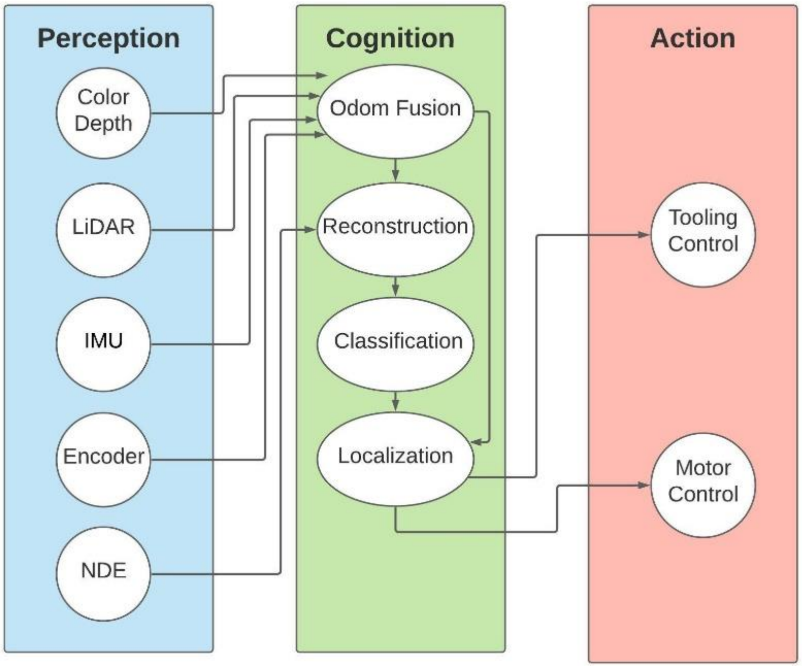

Figure 140: Robotic software architecture.

III. Summary and Future Work

Boiler failure could cause loss of life and safety issues, cost hundreds of thousands of dollars in equipment repairs, property damage and production losses, and drive up the cost of electric power. Boiler maintenance is challenging and risky for inspectors working on scaffolding in confined hazardous spaces inside of a boiler and sometimes the space is hard to access. The operation is also time-consuming due to the large area of vertical structures for inspection and the tremendous effort needed for scaffolding. Recently, the use of robotics (e.g., drones and crawlers) in power plants for maintenance has been growing rapidly. However, the existing robotics solutions show two notable technological gaps: no repair capability, and no Artificial Intelligence (AI) for smart autonomy.

The overarching goal of this project focused on developing an integrated autonomous robotic platform that is equipped with compact non-destructive evaluation (NDE) sensors to perform inspection, operate onboard repair devices in order to perform repair, and use AI for intelligent data fusion and predictive analysis for automated and smart spatiotemporal inspection, analysis and repair of the furnace walls in coal-fired boilers. The approach to achieve the objective includes developing NDE sensors with signal processing techniques, designing and evaluating repair devices based on fusion and solid-state technologies, and an autonomous robotic platform that is integrated with the NDE sensor and the repair tool. The robot will also be powered by AI to automate data gathering (e.g., 3D mapping and damage localization) and predictive analysis.

This project well aligns with the Fossil Energy Objective: “Advance technologies to improve the efficiency, reliability, emissions, and performance of existing fossil-based power generation,” by developing “advanced sensors and controls to help increase coal plant efficiency, reduce forced outages, and avoid downtime related to equipment failures.” Maturing this developed robotic technology has the potential to make great impacts in terms of time and cost savings, reducing the risk for human operators, and increasing boiler reliability, usability, and efficiency. In addition, by developing involving multiple students and faculty members in this research, and by generating knowledge and building up collaborations with industrial partners, this project has improved the education capabilities, supported long-term fundamental research, and enhanced the leadership of the involved universities in energy fields.

This project performs fundamental research to prove the concept of an AI-enabled robot with integrated nondestructive evaluation sensors and repair tools. The technological components were integrated into a robot system, and we performed system evaluation and validation in the laboratory environment. Although the developed system is a good starting point for a further robotic solution for boiler wall damage evaluation within power plants, there are still many technical gaps existing with further development desired to make this developed system feasible in the field. Future follow-up projects may address several future topics:

(1) A major consideration is that many powerplant boiler house walls consist of an array of water tubes in addition to simple uniform steel surfaces. These surfaces present a challenge given the non-uniform distance of the NDE coil array which results in distorted sensor readings that cannot be accurately evaluated by the AI model. Similarly, further improvements are needed to address this non-uniform distance for repair.

(2) Improving NDE sensing technology to detect multiple types of damages is a necessary future topic. The developed NDE sensor basically only uses a single sensing technology based on eddy current and mainly only considers cracks in this project. Several other sensing technologies, e.g., based on acoustic sensing and magnetic flux leakage (MFL), can be further developed and used together to improve detection accuracy. Improved controls of the sensors are also needed to address the issue that the scan along a crack occurs parallel to robot’s direction of travel. In this case, the sensor in this project would detect a minimal change in uniformity which may lead to damages becoming unclassified. This problem may be addressed by designing an improved sensing control method for performing multiple scans along the same surface but in perpendicular directions.

(3) Further improvement requires the need for a large-scale dataset of representative damages for power plant boiler inspection, which requires a large number of NDE data instances for training. Relative to what was possible for this project, obtaining this large number of datasets was not feasible, nor is the number of datasets to achieve a properly trained system known. Another difficulty is the computational complexity of deep learning methods. Deep learning methods typically requires significant overhead during training due to the need to run an individual deep networks over various regions of the same image. More data-efficient deep learning methods are needed to identify cracks, other damages, and in general, anomalies.

(4) It is also possible to further extend the concepts and methods in this project to use a similar robotic system for other structural analysis applications from other various energy or civil related fields. A closer approximation for full autonomy would in turn significantly improve the results from required maintenance within power plants and other energy facilities, in terms of decreasing time used to obtain a damage analysis and repair of the system under test, enhancing quantitative results for objectifying damages, decreasing the likelihood of cataclysmic system failure, and overall improvements in human safety by minimizing human interaction within hazardous regions that require inspection.

IV. Reference

[1] J. Pikula, M. Lomozik and T. Pfeifer, "The influence of manual metal arc multiple repair welding of long operated waterwall on the structure and hardness of the heat affected zone of welded joints," Archives of Metallurgy and Materials, vol. 62, no. 1, pp. 327-333, 2017.

[2] Xcel Energy Inc, "Hayden Generating Station," [Online]. Available: https://www.xcelenergy.com/energy_portfolio/electricity/power_plants/hayden. [Accessed 31 3 2018].

[3] G. Caprari, A. Breitenmoser, W. Fischer, C. Hürzeler, F. Tâche, R. Siegwart, O. Nguyen, R. Moser, P. Schoeneich and F. Mondada, "Highly compact robots for inspection of power plants," Journal of Field Robotics, vol. 29, no. 1, pp. 47-68, 2012.

[4] conEdison, "Con Edison Testing Drones For Energy Inspections," [Online]. Available: https://www.coned.com/en/about-con-edison/media/news/20160620/drone-testing.

[5] U. Aerobotics, "Magnabot for boiler inspection," [Online]. Available: http://www.udc.net/Dot_page.asp?Dotid=56. [Accessed 31 3 2018].

[6] Inspection Robotics, "Inspection Robotics," [Online]. Available: https://inspection-robotics.com/bwci-boiler-wall-cleaning-inspection/. [Accessed 31 3 2018].

[7] Gecko Robotics, "Gecko Robotics," [Online]. Available: https://www.geckorobotics.com/. [Accessed 31 3 2018].

[8] Vivekanand, K. and K. Venkataraman. Nde techniques for reliable inspection of carbon steel tubes. in National Seminar on Non-Destructive Evaluation. 2006.

[9] Sadek, H.J.I.-W.T.N.-. NDE technologies for the examination of heat exchangers and boiler tubes-principles, advantages and limitations. 2006. 48(3): p. 181.

[10] Annila, L., Non-destructive testing of pipelines. 2001.

[11] Orfanoudakis, N. and K. Krallis. Selection of the optimum NDT methods for determination of steam boiler remaining life. in The 8th International Conference of the Slovenian Society for Non-Destructive Testing. 2005.

[12] Beller, M.J.P.P. and S. Association, Pipeline inspection utilizing ultrasound technology: on the issue of resolution. 2007. 2.

[13] Zhou, D., et al., Stress detection and measurement in ferromagnetic metals using pulse electromagnetic method with U-shaped sensor. Measurement, 2017. 105: p. 136-145.

[14] Arjun, V., et al., Optimisation of pulsed eddy current probe for detection of sub-surface defects in stainless steel plates. 2015. 226: p. 69-75.

[15] Ali, K., et al., A Review on System Development in Eddy Current Testing and Technique for Defect Classification and Characterization. 2017. 11(4): p. 330-343.

[16] Javier, G.M., G.G. Jaime, and V.S.J.S. Ernesto, Non-destructive techniques based on eddy current testing. 2011. 11(3): p. 2525-2565.

[17] He, Y., et al., Defect classification based on rectangular pulsed eddy current sensor in different directions. Sensors and Actuators A: Physical, 2010. 157(1): p. 26-31.

[18] Kai, Z., Y. He, and Z.J.J.o.S. Dong, ,, Pulsed Eddy Current Nondestructive Testing for Defect Evaluation and Imaging of Automotive Lightweight Alloy Materials. 2018. 2018(1): p. 1-11.

[18] Deng, Y. and X.J.S. Liu, Electromagnetic imaging methods for nondestructive evaluation applications. 2011. 11(12): p. 11774-11808.

[20] Synge, E.J.T.L., Edinburgh,, D.P. Magazine, and J.o. Science, XXXVIII. A suggested method for extending microscopic resolution into the ultra-microscopic region. 1928. 6(35): p. 356-362.

[21] Ash, E. and G.J.N. Nicholls, Super-resolution aperture scanning microscope. 1972. 237(5357): p. 510.

[22] Cho, Y., et al., New Functions of Scanning Nonlinear Dielectric Microscopy–Higher-Order Measurement and Vertical Resolution–. 2001. 40(5S): p. 3544.

[23] Gao, C., et al., High spatial resolution quantitative microwave impedance microscopy by a scanning tip microwave near-field microscope. 1997. 71(13): p. 1872-1874.

[24] Bakli, H., et al., Interferometric technique for scanning near-field microwave microscopy applications. 2014. 63(5): p. 1281-1286.

[25] POHL, et al., NDT techniques for railroad wheel and gauge corner inspection. 2004. 37(2): p. 89-94.

[26] Chen, G., Two Novel Information Entropy Indices for Analysis of the Eddy Current Distribution. Entropy, 2018. 20(9).

[27] K. Cho, B. van Meri¨enboer, C. Gulcehre, D. Bahdanau, F.Bougares, H. Schwenk, Y. Bengio. Learning phrase representations using RNN encoder-decoder for statistical machine translation. In Proceedings of the 2014 Conference on Empirical Methods in Natural Language Processing, Association for Computational Linguistics, Doha, Qatar, pp. 1724–1734, 2014.

[28] I. Sutskever, O. Vinyals, Q. V. Le. Sequence to sequence learning with neural networks. In Proceedings of Advances in Neural Information Processing Systems 27, NIPS, Montreal, Canada, pp. 3104–3112, 2014.

[29] Huang, Z., Tang, J., Xue, S., & Dai, L. (2016). Speaker adaptation OF RNN-BLSTM for speech recognition based on speaker code. Paper presented at the 5305-5309. doi:10.1109/ICASSP.2016.7472690.

[30] Cheng, J., Li, P., Ding, Z., Zhang, S., & Wang, H. (2016). Sentiment classification of chinese microblogging texts with global RNN. Paper presented at the 653-657. doi:10.1109/DSC.2016.65.

[31] ZHANG Yangsen JIANG Yuru TONG Yixuan. (2016). Study of sentiment classification for chinese microblog based on recurrent neural network. 25(4), 601-607. doi:10.1049/cje.2016.07.002.

[32] S. Hochreiter, J. Schmidhuber. Long short-term memory. Neural Computation, vol. 9, no. 8, pp. 1735–1780, 1997.

[33] Bengio, Y., Simard, P., and Frasconi, P. Learning Longterm Dependencies with Gradient Descent is Difficult. IEEE Trans.Neural Networks, 5(2):157–166, 1994. H. Simpson, Dumb Robots, 3rd ed., Springfield: UOS Press, 2004, pp.6-9.

[34] Meran C, Kovan V, Alptekin A. Friction stir welding of AISI 304 austenitic stainless steel. Materialwissenschaft und Werkstofftechnik 2007;38:829-35.

[35] Thomas WM, Threadgill PL, Nicholas ED. Feasibility of friction stir welding steel. Science & Technology of Welding & Joining 1999;4:365-72.

[36] Reynolds AP, Tang W, Gnaupel-Herold T, Prask H. Structure, properties, and residual stress of 304L stainless steel friction stir welds. Scripta Materialia 2003;48:1289-94.

[37] Plaine AH, Alcântara NGd. Prediction of Friction Stir Welding defect-free joints of AISI 304 austenitic stainless steel through axial force profile understanding. Materials Research 2014;17:1324-7.

[38] Chansoria P, Solanki P, Dasgupta MS. Parametric study of transient temperature distribution in FSW of 304L stainless steel. The International Journal of Advanced Manufacturing Technology 2015;80:1223-39.

[39] Siddiquee AN, Pandey S. Experimental investigation on deformation and wear of WC tool during friction stir welding (FSW) of stainless steel. The International Journal of Advanced Manufacturing Technology 2014;73:479-86.

[40] Meran C, Canyurt OE. Joint strength of friction stir welded AISI 304 austenitic stainless steels. International Journal of Materials Research 2013;104:1197-204.

[41] Kim KH, Bang HS, Bang HS, Kaplan AFH. Joint properties of ultra thin 430M2 ferritic stainless steel sheets by friction stir welding using pinless tool. Journal of Materials Processing Technology 2017;243:381-6.

[42] Bilgin MB, Meran C. The effect of tool rotational and traverse speed on friction stir weldability of AISI 430 ferritic stainless steels. Materials & Design 2012;33:376-83.

[43] Caetano GdQ, Silva CC, Motta MF, Miranda HC, Farias JP, Bergmann LA, et al. Influence of rotation speed and axial force on the friction stir welding of AISI 410S ferritic stainless steel. Journal of Materials Processing Technology 2018;262:430-6.

[44] Shunmugasamy VC, Mansoor B, Ayoub G, Hamade R. Friction Stir Welding of Low-Carbon AISI 1006 Steel: Room and High-Temperature Mechanical Properties. Journal of Materials Engineering and Performance 2018;27:1673-84.

[45] T. J. LIENERT, W. L. STELLWAG, JR., B. B. GRIMMETT, AND R. W. WARKE. Friction Stir Welding Studies on Mild Steel. Welding Research 2003.

[46] Fujii H, Cui L, Tsuji N, Maeda M, Nakata K, Nogi K. Friction stir welding of carbon steels. Materials Science and Engineering: A 2006;429:50-7.

[47] De A, Bhadeshia HKDH, DebRoy T. Friction stir welding of mild steel: tool durability and steel microstructure. Materials Science and Technology 2014;30:1050-6.

[48] Nandan R, Roy GG, Lienert TJ, Debroy T. Three-dimensional heat and material flow during friction stir welding of mild steel. Acta Materialia 2007;55:883-95.

[49] Feng Z, Steel R, Packer S, David SA. Friction Stir Welding of API Garde 65 Steel Pipes. Asme Pressure Vessels & Piping Conference2009.

[50] Cui L, Fujii H, Tsuji N, Nogi K. Friction stir welding of a high carbon steel. Scripta Materialia 2007;56:637-40.

[51] Mostafapour A, Ebrahimpour A, Saeid T. Numerical and experimental study on the effects of welding environment and input heat on properties of FSSWed TRIP steel. The International Journal of Advanced Manufacturing Technology 2016;90:1131-43.

[52] Toumpis A, Galloway A, Cater S, McPherson N. Development of a process envelope for friction stir welding of DH36 steel – A step change. Materials & Design (1980-2015) 2014;62:64-75.

[53] Hermenegildo TFC, Silva ACS, Torres EA, Santos TFA, Ramirez AJ. Desenvolvimento dos Parâmetros do Processo de Soldagem por Atrito com Pino Não Consumível para o Aço de Alta Resistência e Baixa Liga ISO 3183 X80M. Soldagem & Inspeção 2017;22:129-38.

[54] J.H. Record, J.L. Covington, T.W. Nelson, C. D. Sorensen, and B. W. Webb. A Look at the Statistical Identification of Critical Process Parameters in Friction Stir Welding [J]. Welding Journal, 2007: 97-103.

[55] Álvarez AI, Cid V, Pena G, Sotelo J, Verdera D. Assisted Friction Stir Welding of Carbon Steel: Use of Induction and Laser as Preheating Techniques2013.

[56] Álvarez AI, García M, Pena G, Sotelo J, Verdera D. Evaluation of an induction-assisted friction stir welding technique for super duplex stainless steels. Surface & Interface Analysis 2015;46:892-6.

[57] Mehta M, Chatterjee K, De A. Monitoring torque and traverse force in friction stir welding from input electrical signatures of driving motors. Science and Technology of Welding and Joining 2013;18:191-7.

[58] Nandan R, Roy GG, Lienert TJ, Debroy T. Three-dimensional heat and material flow during friction stir welding of mild steel. Acta Materialia 2007;55:883-95.

[59] Roth A, Hake T, Zaeh MF. An Analytical Approach of Modelling Friction Stir Welding. Procedia CIRP 2014;18:197-202.

[60] Schmidt H, Hattel J, Wert J. An analytical model for the heat generation in friction stir welding. Modelling and Simulation in Materials Science and Engineering 2004;12:143-57.

[61] Essa ARS, Ahmed MMZ, Mohamed A-KYA, El-Nikhaily AE. An analytical model of heat generation for eccentric cylindrical pin in friction stir welding. Journal of Materials Research and Technology 2016;5:234-40.

[62] International Bureau of Weights and Measures (2006), The International System of Units (SI) (PDF) (8th ed.), ISBN 92-822-2213-6.

[63] De A, Bhadeshia HKDH, DebRoy T. Friction stir welding of mild steel: tool durability and steel microstructure. Materials Science and Technology 2014;30:1050-6.

[64] Xiang Wan, Wenqian Wang, Jiming Liu. Estimating the sample mean and standard deviation from the sample size, median, range and_or interquartile range. BMC Medical Research Methodology 2014; 14: 135-47.

[65] Welding Handbook, Chapter 4: Gas Metal Arc Welding: 178-188.

[66] Hu Y, Liu H, Fujii H. Improving the mechanical properties of 2219-T6 aluminum alloy joints by ultrasonic vibrations during friction stir welding. Journal of Materials Processing Technology 2019;271:75-84.

[67] Liu FC, Hovanski Y, Miles MP, Sorensen CD, Nelson TW. A review of friction stir welding of steels: Tool, material flow, microstructure, and properties. Journal of Materials Science & Technology 2018;34:39-57.

[68] Cui L, Fujii H, Tsuji N, Nakata K, Nogi K, Ikeda R, et al. Transformation in Stir Zone of Friction Stir Welded Carbon Steels with Different Carbon Contents. ISIJ International 2007;47:299-306.

[69] Fujii H, Cui L, Tsuji N, Maeda M, Nakata K, Nogi K. Friction stir welding of carbon steels. Materials Science and Engineering: A 2006;429:50-7.

[70] Cho H-H, Kang SH, Kim S-H, Oh KH, Kim HJ, Chang W-S, et al. Microstructural evolution in friction stir welding of high-strength linepipe steel. Materials & Design 2012;34:258-67.

[71] Shah, Shital, et al. "Airsim: High-fidelity visual and physical simulation for autonomous vehicles." Field and service robotics. Springer, Cham, 2018.

[72] Nicholas Carlevaris-Bianco, Arash K. Ushani, and Ryan M. Eustice, University of Michigan North Campus Long-Term Vision and Lidar Dataset, International Journal of Robotics Research, 2016.